Navier-Stokes simulations of airflow in rooms and around a human body

Author: M.Sc. Lars Køllgaard Voigt

International Centre for Indoor Environment and Energy
Department of Energy Engineering
Technical University of Denmark, DTU
ET- 2000-??
ISBN ???????

Preface

This dissertation, which is submitted as a part of the requirement for the PhD degree, documents the author's research carried out at the Fluid Mechanics Section and at the International Centre for Indoor Environment and Energy (ICIEE), at the Department of Mechanical Engineering, Tecnical University of Denmark. The research has been carried out in the period August 1998 to September 2001. The work was supervised by Associate Professor Jens Nørkær Sørensen. I would like to give my gratitude to my supervisor for his continuous support and qualified help, despite a tremendous workload of his own. I would also like to acknowledge my co-supervisors Professor Peter V. Nielsen and Associate Professor Arsen Melikov.

I wish to thank Dan Nørtoft Sørensen for many fruitful discussions and for his support. I thank Poul Scheel Larsen, Morten Brøns, Jørn Toftum, Lars Davidson, Claus Topp and Rikke K. Byskov for valuable discussions. For guidance in the *EllipSys* code I would like to thank Jess A. Michelsen, Niels N. Sørensen, Lisbeth Myllerup and Wen Zhong Shen.

I thank Jakob M. Pedersen, Zbigniew Popiolek, Rasmus L. Jensen and Jan Holsøe for providing me with their experimental data. Further, I thank Lars Davidson for a wonderful stay at the Department of Thermo and Fluid Dynamics, Chalmers University of Technology during the spring of 1999 and Peter V. Nielsen for a nice stay at Ålborg University in November 1999. I thank my colleagues at the Department of Mechanical Engineering for the open and social atmosphere and all the people who have read and commented parts of this dissertation. I would also like to thank the High-Performance Computing Center (HPC), UNI-C and UNI-C databar support. Without whom the computations presented in this dissertation would never have been possible.

Thanks to Professor Povl Ole Fanger who made this work possible. The work has been supported by the Danish Technical Research Council (STVF) as a part of the research programme of the ICIEE established at DTU for the period 1998-2007.

Technical University of Denmark
Copenhagen, October 1st, 2001

Lars P. Køllgaard Voigt

Abstract

Computational Fluid Dynamics (CFD) has proven to be a strong tool for prediction of airflows in indoor environment. Despite that CFD is widely used for commercial purposes, many basic issues, such as turbulence models, discretization schemes, etc, need further investigation and development.

Basic properties of flows in indoor environments were studied by an existing Navier-Stokes solver. Five existing turbulence models of the Reynolds Averaging Navier-Stokes method were validated for two-dimensional calculations of indoor airflows. Moreover, a new model was developed. Except for one of the models, the obtained results were found to be in reasonable agreement with LDA measurements. Topological aspects of two-dimensional airflows in rooms were described. The turbulence models were further evaluated for three-dimensional calculations of airflows in rooms. The models showed differences in the laminar regions were the tested models are known to have problems. In these regions, neither of the models were able to reproduce the flow pattern found in PIV measurements. Furthermore, topological aspects of three-dimensional airflows in rooms were described.

The Navier-Stokes solver was prepeared for Large Eddy Simulation (LES). A subgrid scale model was implemented and validated for a two-dimensional channel flow. The capabilities of the LES method were demonstrated, by calculating the airflow in a room. Comparing calculated and measured frequency spectra, the agreement was found to be good for the largest scales, while an improvement of the subgrid scale model would probably improve the agreement for the smallest scales. Comparing mean velocity profiles obtained by a Reynolds Averaging Navier-Stokes model and LES, the former results showed the best agreement with experiments. In LES, the profiles of turbulent kinetic energy were affected by internal stretching.

The airflow in a room with a complex inlet geometry was calculated. The inlet was represented by a rectangular opening. Isothermal computations showed good agreement with measured velocity profiles, but the velocity decay in the jet was too low. In case of non-isothermal flow, the steady solution procedure had convergency problems for some of the used air exchange rates. Bifurcation diagrams based on measurements and computations were constructed, but the available measurements and computations were too limited for a detailed comparison of the diagrams. The level of percentage dissatisfied (PD) based on computations was found, and the ventilation situation was concluded to be satisfying.

With a laser scanning an exact representation of a thermal manikin was obtained,

and the geometry was used for computations of the airflow around a human body. This geometry is the most detailed ever used. The two-equation turbulence models had problems with predicting the airflow around a person sitting in stagnant air, and a constant eddy viscosity model was used instead. With this model, the calculated values of the convective heat transfer coefficients were in reasonable agreement with measurements, while the velocity and temperature profiles in the boundary layer would probably improve with a better turbulence model.

Contents

Notation

A_{Du}	DuBois area	[m^2]
A_{geom}	Geometrical supply area	[m^2]
A_{proj}	Projected supply area	[m^2]
Ar	Archimedes number	[$-$]
a_1	Constant in $k-\omega$ SST model	[$-$]
d_h	Hydraulic diameter	[m]
C_μ	Empirical constants in the $k-\epsilon$ model	[$-$]
$C_{\epsilon 1}, C_{\epsilon 2}, C_{\epsilon 3}$	Empirical constants in the $k-\epsilon$ model	[$-$]
C_m	Empirical constant in the mixed scale model	[$-$]
C_{res}	Dry respiration heat loss	[W/m^2]
c_p	Specific heat of air	[$J/(kg \cdot K)$]
$\mathcal{D}$	Correction term for the Launder & Sharma $k-\epsilon$ model	[m^2/s^3]
$\mathcal{D}_k$	Diffusion of k	[m^2/s^3]
$\mathcal{D}_v$	Viscous diffusion of ϵ	[m^2/s^4]
$\mathcal{D}_\epsilon$	Turbulent diffusion of ϵ	[m^2/s^4]
ΔE_{st}	Energi stored in a control volume	[W]
E_g	Energi generated in a control volume	[W]
E_{in}	Energi applied to a control volume	[W]
E_{out}	Energi leaving a control volume	[W]
E_{dif}	Heat loss by water vapour diffusion	[W/m^2]
E_{sw}	Heat loss by evaporation of sweat	[W/m^2]
E_{res}	Latent respiration heat loss	[W/m^2]
e	Internal energy	[m^2/s^2]
F_1	Blending function in the baseline $k-\omega$ model	[$-$]
F_n	Angle factor	[$-$]
f_{cl},	Clothing area factor	[$-$]
f_{eff},	Effective radiation area factor	[$-$]
f_μ, f_1, f_2	Viscous damping functions	[$-$]
G_k	Buoyancy term in the turbulence models	[m^2/s^3]
g_i	Acceleration due to gravity	[m/s^2]
H	Internal heat production	[W/m^2]
h_c,	Convective heat transfer coefficient	[$W/(m^2 \cdot K)$]
$h_{c,free}$,	Convective heat transfer coefficient for free convection	[$W/(m^2 \cdot K)$]
$h_{c,mixed}$,	Convective heat transfer coefficient for mixed convection	[$W/(m^2 \cdot K)$]
h_r,	Radiative heat transfer coefficient	[$W/(m^2 \cdot K)$]
K, K_1	Constants appearing in grid generator	[$-$]

k	Turbulent kinetic energy	$[\ m^2/s^2\ ]$
k	Thermal conductivity	$[\ W/(m \cdot K)\ ]$
k_{sgs}	Subgrid scale kinetic energy	$[\ m^2/s^2\ ]$
l	Turbulent length scale	$[\ m\ ]$
n	Air exchange rate	$[\ h^{-1}\ ]$
ny	Number of grid points	$[\ -\ ]$
P	Mean pressure	$[\ Pa\ ]$
$\mathcal{P}_k$	Production of k	$[\ m^2/s^3\ ]$
$\mathcal{P}_\epsilon$	Production of ϵ	$[\ m^2/s^4\ ]$
PD	Percentage dissatisfied	$[\ \%\ ]$
p	Pressure	$[\ Pa\ ]$
p'	Fluctuating part of pressure	$[\ Pa\ ]$
p_{da}	Water vapour pressure at air temperature	$[\ Pa\ ]$
p_{ds}	Water vapour pressure at skin temperature	$[\ Pa\ ]$
q_i	Heat flux by conduction	$[\ W/m^2\ ]$
q	Total power	$[\ W\ ]$
Re_t	Turbulent Reynolds number	$[\ -\ ]$
Re_h	Reynolds number based on inlet height	$[\ -\ ]$
Re_m	Reynolds number based on u_m	$[\ -\ ]$
Re_τ	Reynolds number based on wall friction velocity	$[\ -\ ]$
r	Latent heat of vapourization of water	$[\ J/kg\ ]$
S_{ij}	Strain rate tensor	$[\ 1/s\ ]$
S_0, S_1	Height of first cell from the wall	$[\ m\ ]$
T	Average Temperature	$[\ ^oC\ ]$
$\mathcal{T}_u$	Integral time scale	$[\ -\ ]$
Tu	Turbulence intensity	$[\ \%\ ]$
t	Time	$[\ s\ ]$
t	Temperature	$[\ ^oC\ ]$
Δt	Time step	$[\ s\ ]$
Δt^*	Dimensionless time step	$[\ -\ ]$
t_a	Air temperature	$[\ ^oC\ ]$
t_{cl}	Clothing temperature	$[\ ^oC\ ]$
t_{exh}	Temperature of exhaled air	$[\ ^oC\ ]$
t_n	temperature of surface n	$[\ ^oC\ ]$
$\overline{t}_r$	Mean radiant temperature	$[\ ^oC\ ]$
t_{sk}	Skin temperature	$[\ ^oC\ ]$
U_i	Mean velocity	$[\ m/s\ ]$
U, V, W	Mean velocity	$[\ m/s\ ]$
u^+	Streamwise velocity scaled with wall friction velocity	$[\ -\ ]$
u_c	Streamwise velocity in center plane	$[\ m/s\ ]$
u_i	Velocity	$[\ m/s\ ]$
u_i'	Fluctuating part of velocity	$[\ m/s\ ]$
u_m	Streamwise velocity averaged over cross section	$[\ m/s\ ]$
u_τ	Wall friction velocity	$[\ m/s\ ]$
$\mathcal{V}_k$	Effect of molecular viscosity	$[\ m^2/s^3\ ]$

V_{lung}	Pulmonary lung ventilation	[$kg/(s \cdot m^2)$]
x_i	Position	[m]
v_a	Air velocity	[m/s]
v_{floor}	Velocity at floor level	[m/s]
Δx^+,Δz^+	Dimensionless cell distance	[$-$]
x_a	Humidity ratio of air	[kg/kg]
x_{exh}	Humidity ratio of exhaled air	[kg/kg]
x_i	Position	[m]
x, y, z	Position	[m]
y^+	Sublayer scaled distance to the wall	[$-$]
Δy	Distance to the nearest point from the wall	[m]
y_0, y_1	Start and end position for grid	[m]

Greek

α	Thermal diffusivity	[m^2/s]
α	Constant in the mixed scale model	[$-$]
α_t	Turbulent thermal diffusivity	[m^2/s]
β	Thermal expansion coefficient	[$1/K$]
β^*, β_1, β_2	Constants in $k-\omega$ model	[$-$]
δ_{ij}	Kronecker delta	[$-$]
Δ	Filter size	[m]
η	Kolmogorov micro scale	[m]
ϵ	Dissipation of turbulent kinetic energy	[m^2/s^3]
ϵ,	Emissivity	[$-$]
Φ_ϵ	Dissipation of ϵ	[m^2/s^4]
γ_1, γ_2	Constants in $k-\omega$ model	[$-$]
κ	von Karman constant	[$-$]
κ	Wavenumber	[m]
λ	Spatial Taylor micro scale	[m]
λ	Temporal Taylor micro scale	[s]
ν	Kinematic viscosity	[m^2/s]
ν_t	Eddy viscosity	[m^2/s]
ν_{sgs}	Subgrid scale viscosity	[m^2/s]
ω	Specific dissipation rate	[$1/s$]
ω_{ij}	Vorticity	[$1/s$]
ω	Frequency	[Hz]
ρ	Density	[kg/m^3]
σ_k	Turbulent Prandtl number in transport equation for k	[$-$]
σ_ϵ	Turbulent Prandtl number in transport equation for ϵ	[$-$]
$\sigma_{\omega 1}$,$\sigma_{\omega 2}$	Turbulent Prandtl numbers in transport equation for ω	[$-$]
σ,	Stefan-Boltzmann's constant	[$W/(m^2K^4)$]
τ_{ij}	Stress tensor	[N/m^2]

τ_w	Wall shear stress	[N/m^2]
τ	Time difference	[s]
θ	Temperature	[K]
Θ	Mean temperature	[K]
θ_{ref}	Reference temperature	[K]

Subscripts

0	At inlet condition
i	1,2,3
j	1,2,3
k	1,2,3
exp	Experiments
rms	Root-mean-square
tot	Total
out	Outlet
dim	Dimensionless

Superscripts

$'$	Temporal fluctuation
$''$	Spatial fluctuation

overbar

$\bar{}$	Time average quantity
$\bar{}$	Filtered quantity
$\tilde{}$	Test filtered quantity
$< >$	Time average

Abbreviations

BSL	BaSeLine
BSLREV	BaSeLine REVised
C	Centre
CDS	Central Differencing Scheme
CFD	Computational Fluid Dynamics
CFL	Courant Friedrichs Lewy
DES	Detached Eddy Simulation

DNS	Direct Numerical Simulation
LDA	Laser Doppler Anemometry
LES	Large Eddy Simulation
LS	Launder & Sharma
HI RE	HIgh REynolds number
ORG	ORiGinal
PDF	Probability Density Function
PIV	Particle Image Velocimetry
RANS	Reynolds Averaged Navier-Stokes
rms	Root-mean-square
S	Saddle
SGS	SubGrid Scale
SS	Stable Spiral
SST	Shear Stress Transport
SUDS	Second-order Upwind Differencing Scheme
UDS	Upwind Differencing Scheme
UN	Unstable Node
US	Unstable Spiral

Chapter 1

Introduction

In the industrialized part of the world, humans typically spend 80-90 % of their lifetime in indoor environments. A major part of this will be at home, at work or in means of transport. Exposures in the indoor environment may cause symptoms such as headache, fatigue and may generally affect occupants health and performance. More serious effects of poor human exposure to indoor environments include asthma and allergy. Design of an optimal indoor environment is a multiparameter study. The well being of humans are governed by parameters like activity level, clothing insulation, air temperature, mean radiant temperature, air velocity, air humidity, pollutants in the air and noise. This dissertation focus on air velocity and air temperature.

Computational Fluid Dynamics (CFD) provides a strong tool for predicting air velocity, distribution of temperature, radiation, humidity, pollutants and noise. Thus, CFD is an obvious choice for improving our understanding of indoor airflows. Moreover, CFD can be a valuable tool for the design of indoor environments. In CFD the main objective is the solution of the governing equations, which for isothermal flows are the continuity equation and the Navier-Stokes equations. With a sufficient fine computational grid the governing equations will provide the necessary information about the turbulent scales existing in the flow. This method is called Direct Numerical Simulation (DNS). With present available computers it is not possible to use computational grids which are fine enough to resolve all the turbulent scales occurring in indoor airflows, and thus some modelling is needed. Most commonly the governing equations are time averaged, and the fluctuations are modelled. The result of this averaging is termed Reynolds Averaged Navier-Stokes (RANS) equations and several different types of RANS models exist. A physically more correct, but also more expensive method is Large Eddy Simulation (LES). In this transient method, the largest scales are resolved, while the smallest scales, the subgrid scales (SGS), are modelled. Different SGS models have been proposed over the years. Development and validation of different RANS and SGS models are still important issues in CFD.

During the past three decades CFD have evolved concurrently with increasing avail-

able computer resources. Several authors have presented calculations of airflow and temperature distribution in two-dimensional room geometries, see Nielsen [79], Nielsen *et al* [80], Anderson *et al* [3], Peng *et al* [90], Chen [17], Xu & Chen [112] and Xu *et al* [113]. Most of these papers focus on validation and development of turbulence models. A review of different solution strategies was given in Nielsen [84].

Reliable calculations of the airflow in three-dimensional room geometries have been possible only during the last ten years. The experience is therefore more limited than for the two-dimensional room geometries. Calculations of airflow and temperature distribution in three-dimensional room geometries have been presented by e.g Davidson [20], Chen & Xu [18], Emvin & Davidson [30], Fontaine *et al* [36], Davidson & Nielsen [24] and Bennetsen [8]. For these calculations the aim was to validate the methods for calculating indoor airflows.

The $k-\epsilon$ turbulence model has been accepted as a reliable turbulence model for calculations of indoor airflows. This conclusion is based on the aforementioned studies among others. Therefore focus has changed from development of turbulence models to other important tasks related to CFD in indoor environments. One of these tasks is how the geometrical representation of persons can be optimized. For comparison with measurements, it is desirable to get a representation of the human body as close as possible to a real person. This, however, makes the calculations very time consuming, if possible at all. More simple geometries, such as cylinders and boxes have been used over the years, e.g Brohus & Nielsen [13]. The cylindrical geometry was refined to a more human like geometry by Murakami *et al* [73], but still no accurate representation of the human body have been used.

In the 90ties the development of the flow solver *EllipSys*, Michelsen [67], was initiated at the Technical University of Denmark. So far the work with this code has mainly concentrated on external flows, e.g. Sørensen [103]. The code can handle a complex geometry such as the human body. Several RANS models are already available in the code, and moreover the code is efficient in terms of computational costs. This should lead to reasonable computational time even for fine grids. This code is therefore an obvious choice for calculations of indoor airflows.

The objectives in this dissertation falls into two categories, namely validation of turbulence models in the CFD code and calculation of the airflow close to a human subject. In the first category, the objectives were:

- to validate the turbulence models existing in the *EllipSys* code for two-dimensional calculations of isothermal airflows in rooms. Two of these have not before been evaluated for such calculations
- to validate the turbulence models in the *EllipSys* code for three-dimensional calculations of isothermal airflows in rooms
- to implement a SGS model in order to prepare *EllipSys* for LES

- to demonstrate the feasibility of LES to provide statistical information of airflows
- to validate the temperature equation for non-isothermal indoor airflows

In the second category the objectives were:

- to obtain an accurate representation of the human body as input to CFD calculations
- to study the boundary layer close to a human body placed in a stagnant environment and compare the results with measurements

This dissertation is organized as follows: In chapter 2 the mathematical background for the governing equations are presented. A comparison of different turbulence models for two-dimensional calculations of isothermal airflows in the annex 20 test case is presented in chapter 3. Moreover, topological aspects for two-dimensional calculations of airflows for this case are presented. In chapter 4 the tested turbulence models are evaluated for three-dimensional calculations of isothermal airflows in the annex 20 test case. Furthermore, topological aspects for three-dimensional calculations for this case are presented. A validation of the implemented SGS model is carried out in chapter 5. In this chapter the test case is a two-dimensional channel flow. LES results for isothermal airflows in the annex 20 test case are presented in chapter 6. The temperature equation is validated for the annex 20 test case with a heated wall in chapter 7. In chapter 8 an accurate surface description of the geometry of a human body, as input for CFD codes, is presented. Moreover, chapter 8 contains calculations of the airflow around a person located in a stagnant environment. Finally, conclusions are drawn in chapter 9. The dissertation contains several appendices, which are mainly included to justify the accuracy of the CFD solutions presented in chapter 3 to 7. Furthermore, the appendices contains a presentation of the grid generator used, a derivation of the k and ϵ transport equations, a derivation of the temperature equation, and a validation of the laminar temperature equation.

Chapter 2

Mathematical background and numerics

In this chapter an introduction to calculations of indoor airflows by numerical techniques is given. In fluid mechanics the physical phenomena are modelled by the continuum mechanics that describes scales larger than the mean free path between molecules. Applying mass conservation and Newton's 2nd law on an infinitisemal fluid volume results in the continuity and Navier-Stokes equations for describing fluid motions. As these equations only in some simple cases can be solved analytically, one has to resort to numerical modelling.

If the numerical model is able to take into account all spatial and temporal scales, the solution is of maximum quality. This is termed Direct Numerical Simulation (DNS), see figure 2.1.

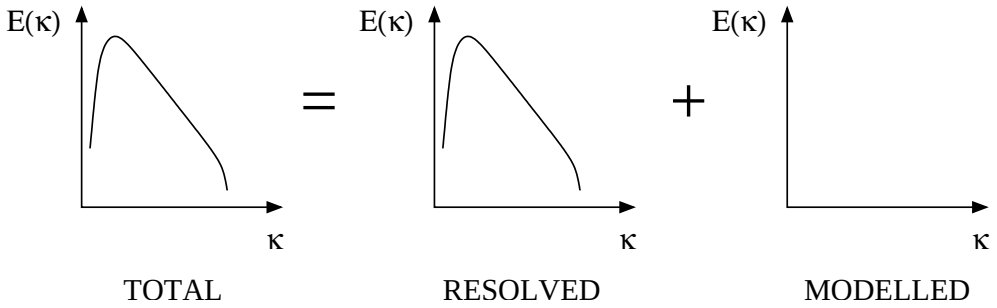

Figure 2.1: Decomposition of frequency spectrum for DNS. κ is the wavenumber and $E(\kappa)$ is the energy contained in the eddies with wavenumber κ.

Due to computational costs it is generally impossible to carry out DNS in practical applications. Thus, some modelling is needed. Time averaging the Navier-Stokes equations, and solving these with a steady solution procedure is referred to as Reynolds Averaged Navier-Stokes (RANS). The method, which is illustrated in figure 2.2, contains several assumptions, but leads to surprisingly correct results for many practical problems. Since the RANS is very fast compared to DNS, it is today

the prevailing method in engineering applications.

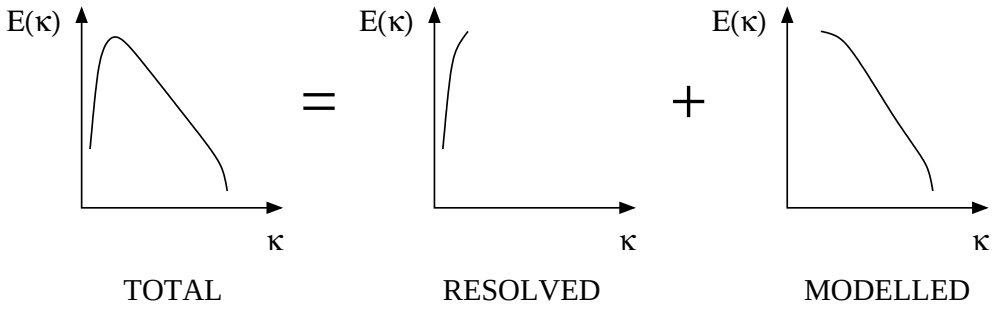

Figure 2.2: Decomposition of frequency spectrum for RANS. κ is the wavenumber and $E(\kappa)$ is the energy contained in the eddies with wavenumber κ.

A method which is physically more accurate than the RANS method is Large Eddy Simulation (LES). With this transient procedure, the low-frequency modes are resolved, while the high-frequency modes are modelled, see figure 2.3. Computationally, this method is more expensive than RANS, but it provides significantly more information about the flow. The use of LES in practical applications is still limited by computer power.

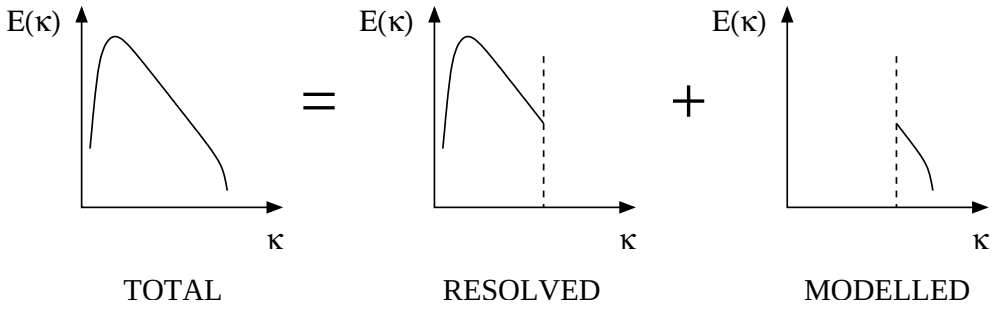

Figure 2.3: Decomposition of frequency spectrum for LES. κ is the wavenumber and $E(\kappa)$ is the energy contained in the eddies with wavenumber κ.

Both RANS and LES will be treated in this work.

2.1 RANS

In RANS, the governing equations are the time averaged continuity and Navier-Stokes equations combined with a model for the fluctuations. Several models for the fluctuations exist, e.g. zero-equation models, one-equation models, two-equation models, Reynolds stress models, etc. This study focus on the two-equation models, which are the prevailing models in calculations of indoor airflow. The $k-\epsilon$ and the $k-\omega$ models were used, but others exist. For the $k-\epsilon$ model, transport equations for the two quantities turbulent kinetic energy k, and dissipation of turbulent kinetic

energy ϵ need to be solved. When non-isothermal calculations are carried out, an additional transport equation for the temperature needs to be solved. The Einstein summation convention is used when presenting the equations. Assuming that the flow is incompressible, the continuity equation and the Navier-Stokes equations read

$$\frac{\partial u_i}{\partial x_i} = 0, \tag{2.1}$$

$$\frac{\partial u_i}{\partial t} + u_j \frac{\partial u_i}{\partial x_j} = -\frac{1}{\rho}\frac{\partial p}{\partial x_i} + \frac{\partial}{\partial x_j}\left[\nu\left(\frac{\partial u_i}{\partial x_j} + \frac{\partial u_j}{\partial x_i}\right)\right] + g_i\beta(\theta - \theta_{ref}), \tag{2.2}$$

where x_i, u_i, p, ρ, ν, θ, θ_{ref}, β and t are position in space, velocity, pressure, density, kinematic viscosity, temperature, reference temperature, thermal expansion coefficient and time, respectively. The flow quantities, f_i, are decomposed into

$$f_i(x_i, t) = F_i(x_i) + f_i'(x_i, t_i), \tag{2.3}$$

where $F_i(x,t)$ is the time average and $f_i'(x_i, t_i)$ the fluctuating part of the quantity. The time average of the quantity is defined by

$$F_i(x) = \lim_{\Delta t \to \infty} \frac{1}{\Delta t} \int_{t_0}^{t_0 + \Delta t} f_i(x_i, t_i) dt, \tag{2.4}$$

see e.g Tennekes & Lumley [105]. In this dissertation f_i is either the velocity u_i, the pressure p or the temperature θ. When introducing equation (2.3) and time averaging using definitions (2.4), equation (2.1) becomes

$$\frac{\partial U_i}{\partial x_i} = 0. \tag{2.5}$$

Equation (2.3) is introduced into (2.2), then time-averaging and thus equation (2.2) becomes

$$\frac{\partial U_i}{\partial t} + U_j \frac{\partial U_i}{\partial x_j} = -\frac{1}{\rho}\frac{\partial P}{\partial x_i} + \frac{\partial}{\partial x_j}\left[\nu\left(\frac{\partial U_i}{\partial x_j} + \frac{\partial U_j}{\partial x_i}\right) - \overline{u_i' u_j'}\right] + g_i\beta(\Theta - \Theta_{ref}). \tag{2.6}$$

The term $\overline{u_i' u_j'}$ is a result of the non-linear convective terms, and is referred to as the Reynolds stresses. This term needs to be modelled in order to solve equation (2.6).

The full Reynolds stress tensor is symmetric, and consequently it contains six new unknowns. Deriving transport equations for $\overline{u_i' u_j'}$ from the Navier-Stokes equations gives rise to third order products of the fluctuating velocities. As a consequence, the number of unknowns compared to the number of equations cannot be reduced this way. This is known as the closure problem. The problem is circumvented by applying the Boussinesq approximation, assuming proportionality between the deviatoric part of the Reynolds stress tensor and the strain rate tensor

$$-\overline{u_i' u_j'} + \frac{1}{3}\delta_{ij}\overline{u_k' u_k'} = 2\nu_t S_{ij} = \nu_t\left(\frac{\partial U_i}{\partial x_j} + \frac{\partial U_j}{\partial x_i}\right), \tag{2.7}$$

which defines the eddy viscosity, ν_t. The strain rate tensor is given by

$$S_{ij} = \frac{1}{2}\left(\frac{\partial U_i}{\partial x_j} + \frac{\partial U_j}{\partial x_i}\right). \tag{2.8}$$

A more thorough description of the physical interpretation of the tensors can be found in Arpaci & Larsen [4]. Inserting equation (2.7) into equation (2.6) yields

$$\frac{\partial U_i}{\partial t} + U_j\frac{\partial U_i}{\partial x_j} = -\frac{1}{\rho}\frac{\partial P}{\partial x_i} + \frac{\partial}{\partial x_j}\left[(\nu+\nu_t)\left(\frac{\partial U_i}{\partial x_j} + \frac{\partial U_j}{\partial x_i}\right)\right] + g_i\beta(\Theta - \Theta_{ref}), \tag{2.9}$$

where the term $\frac{1}{3}\delta_{ij}\overline{u_k' u_k'}$ is included in P.

Various models exist for modelling the eddy viscosity, ν_t, in equation (2.9). These range from the simple constant eddy viscosity models to the two-equation models. Focusing on the latter type of model, dimensional analysis gives

$$\nu_t \propto \frac{k^2}{\epsilon}, \tag{2.10}$$

where k is the turbulent kinetic energy and ϵ is the dissipation of turbulent kinetic energy. In appendix B the transport equations for the two turbulent quantities k and ϵ are derived. For the Launder & Sharma model [56], the transport equations are

$$\frac{\partial k}{\partial t} + u_j\frac{\partial k}{\partial x_j} = \nu_t\left(\frac{\partial u_i}{\partial x_j} + \frac{\partial u_j}{\partial x_i}\right)\frac{\partial u_i}{\partial x_j} + \frac{\partial}{\partial x_j}\left(\nu + \frac{\nu_t}{\sigma_k}\right)\frac{\partial k}{\partial x_j} - \epsilon - D + G_k \tag{2.11}$$

$$\begin{aligned}\frac{\partial \epsilon}{\partial t} + u_j\frac{\partial \epsilon}{\partial x_j} &= c_{\epsilon 1} f_1\left(\left(\frac{\partial u_i}{\partial x_j} + \frac{\partial u_j}{\partial x_i}\right)\frac{\partial u_i}{\partial x_j} + c_{\epsilon 3}G_k\right)\frac{\epsilon}{k} \\ &+ \frac{\partial}{\partial x_j}\left(\nu + \frac{\nu_t}{\sigma_\epsilon}\right)\frac{\partial \epsilon}{\partial x_j} - c_{\epsilon 2}f_2\frac{\epsilon^2}{k} + E.\end{aligned} \tag{2.12}$$

Except for G_k and $c_{\epsilon 3}$ the constants and damping functions are given in appendix D. The buoyancy term, G_k, appearing in (2.11) and (2.12) is modelled by

$$G_k = -\frac{\nu_t}{\sigma_t} g_i \beta \frac{\partial \Theta}{\partial x_i}, \tag{2.13}$$

where σ_t is the turbulent Prandtl number, g_i is acceleration due to gravity, β is the thermal expansion coefficient, and Θ is the time averaged temperature. The turbulent Prandtl number $\sigma_t = 0.9$ was chosen for wall bounded flows, see Meyer [66]. It should be mentioned that the constant $C_{\epsilon 3}$ is a matter of some discussion. However, no consensus was found in the literature and thus $C_{\epsilon 3} = 1$ was used for simplicity.

The transport equation for the time averaged temperature, Θ, was derived in appendix C and reads

$$\frac{\partial \Theta}{\partial t} + u_i\frac{\partial \Theta}{\partial x_i} = \frac{\partial}{\partial x_i}\left[(\alpha + \alpha_t)\frac{\partial \Theta}{\partial x_j}\right], \tag{2.14}$$

where α is the thermal diffusivity and α_t is the turbulent thermal diffusivity.

2.2 LES

The equations governing the flow in LES, see e.g. Sagaut [95], shall be described. The large scale quantities, denoted by an overbar, are defined by the filter operator

$$\overline{f}(\vec{x}) = \int_D f(\vec{x}')G(\vec{x},\vec{x}'')d\vec{x}. \tag{2.15}$$

In the physical space, the box filter

$$G_i(x,x'') = \begin{cases} 1/\Delta, & |x_i - x_i''| < \Delta_i/2 \\ 0, & \text{otherwise,} \end{cases} \tag{2.16}$$

where $\Delta = (\Delta x \Delta y \Delta z)^{1/3}$, is commonly used. Applying the operator (2.15) to the continuity equation and the Navier-Stokes equations gives

$$\frac{\partial \overline{u}_i}{\partial x_i} = 0, \tag{2.17}$$

and

$$\frac{\partial \overline{u}_i}{\partial t} + \frac{\partial \overline{u_i u_j}}{\partial x_j} = -\frac{1}{\rho}\frac{\partial \overline{p}_i}{\partial x_i} + \nu \frac{\partial^2 \overline{u}_i}{\partial x_j \partial x_j}. \tag{2.18}$$

Writing out the term $\overline{u_i u_j}$, gives

$$\overline{u_i u_j} = \overline{\overline{u}_i \overline{u}_j} + \overline{\overline{u}_i u_j''} + \overline{u_i'' \overline{u}_j} + \overline{u_i'' u_j''}, \tag{2.19}$$

where $u_i'' = u_i - \overline{u}_i$. A further decomposition gives

$$\overline{u_i u_j} = \underbrace{\overline{\overline{u}_i \overline{u}_j} - \overline{u}_i \overline{u}_j}_{\mathcal{L}_{ij}} + \underbrace{\overline{\overline{u}_i u_j''} + \overline{u_i'' \overline{u}_j}}_{\mathcal{C}_{ij}} + \overline{u_i'' u_j''} + \overline{u}_i \overline{u}_j, \tag{2.20}$$

where $\mathcal{L}_{ij}$ is the Leonard stress tensor, $\mathcal{C}_{ij}$ is the cross term stress tensor. The box filter is a Reynolds operator and thus,

$$\overline{\overline{f}} = \overline{f}, \quad \overline{\overline{f}\, f''} = \overline{\overline{f}}\ \overline{f''}, \quad \overline{f''} = 0, \tag{2.21}$$

Bearing equation (2.21) in mind, equation (2.20) reduces to

$$\overline{u_i u_j} = \overline{u_i'' u_j''} + \overline{u}_i \overline{u}_j, \tag{2.22}$$

Introducing equation (2.22) into equation (2.18), yields

$$\frac{\partial \overline{u}_i}{\partial t} + \frac{\partial \overline{u}_i \overline{u}_j}{\partial x_j} = -\frac{\partial \tau_{ij}}{\partial x_j} - \frac{1}{\rho}\frac{\partial \overline{p}_i}{\partial x_i} + \nu \frac{\partial^2 \overline{u}_i}{\partial x_j \partial x_j}, \tag{2.23}$$

where $\tau_{ij} = \overline{u_i'' u_j''}$ is the SGS stresses. The SGS stresses need to be modelled.

As for the modelling of the Reynolds stresses in the RANS equations, a broad spectrum of models exist for the SGS stresses. The most simple of these, SGS

models, are the eddy viscosity models, which are based on the assumption that the SGS stresses and rate of strain are aligned

$$-\tau_{ij} + \frac{1}{3}\delta_{ij}\tau_{kk} = 2\nu_{sqs}\overline{S}_{ij} = \nu_{sgs}\left(\frac{\partial \overline{u}_i}{\partial x_j} + \frac{\partial \overline{u}_j}{\partial x_i}\right), \tag{2.24}$$

where

$$\overline{S}_{ij} = \frac{1}{2}\left(\frac{\partial \overline{u}_i}{\partial x_j} + \frac{\partial \overline{u}_j}{\partial x_i}\right) \tag{2.25}$$

and ν_{sqs} is the SGS viscosity which needs to be modelled. By dimensional analysis it may be reasoned that the SGS viscosity is a product of a length scale and a velocity scale.

Before introducing the SGS model, some physical properties which should be contained in the SGS model are mentioned. The effect of the SGS model should be that energy is drained from the smallest resolved scales, i.e the model is dissipative. Physically, however, it is possible that energy is locally transferred from smaller to larger scales, see Piomelli *et al* [92]. It is desirable to incorporate this backscatter, into the SGS model. Further, the model should vanish in fully resolved flows (DNS) and in laminar flows. Finally, the near-wall behaviour should be modelled correctly. In some SGS models, this is done by resolving the boundary layer, which is expensive from a computational point of view. Alternatively, the law-of-the wall approximation is used.

It was chosen to use the mixed scale model by Loc *et al* [60]. The SGS viscosity is calculated from

$$\nu_{sgs} = C_m \Delta^{1+\alpha} k_{sgs}^{\frac{1-\alpha}{2}} |\overline{\omega}_{ij}|^{\alpha}, \tag{2.26}$$

where $C_m = 0.02$ is a constant, $\Delta = (\Delta x \Delta y \Delta z)^{1/3}$ is the filter length, k_{sgs} is the SGS kinetic energy, α is a constant which should be between 0 and 1, and $|\overline{\omega}_{ij}|$ is the absolute value of vorticity based on the resolved scales. In this study $\alpha = 0.5$ is used. The SGS kinetic energy is

$$k_{sgs} = \frac{1}{2}\overline{u_i'' u_i''} \approx \frac{1}{2}(\tilde{\overline{u}}_i - \overline{u}_i)(\tilde{\overline{u}}_i - \overline{u}_i), \tag{2.27}$$

where the filtering $\tilde{\overline{u}}_i$ is the velocity for a test filter with the size $\tilde{\Delta} = 2\Delta$. No second filtering of the governing equations is required, since $\tilde{\overline{u}}_i$ is calculated from the volumetric average

$$\tilde{\overline{u}}_i = \frac{1}{4}(\overline{u}_{i-1} + 2\overline{u}_i + \overline{u}_{i+1}). \tag{2.28}$$

Generally, it is assumed that energy from the smallest resolved scales is mainly transferred to the largest unresolved scales and further that the largest unresolved scales are assumed to be the most energetic. Physically this justifies the calculation of SGS kinetic energy using the smallest resolved scales.

An advantages of the chosen model is that a wall-law modelling is rendered superfluous, since ν_{sgs} goes to zero at walls. Furthermore, ν_{sgs} vanishes in laminar and

fully resolved flows and finally the model is rather easy to implement. The implementation of the model is described in details in e.g Byskov [15]. The model is not capable of predicting backscatter.

2.3 Solution procedure

The numerical code is a finite volume code in general curvilinear coordinates, based on the *Basis* platform developed by Michelsen [68] and Sørensen [103]. The governing equations are solved using block structured grids in a cell centered, non-staggered arrangement. The solution procedure is based on the predictor-corrector method. In the predictor step the momentum equations are solved using a guessed pressure field, and in the corrector step continuity is enforced by adjusting the pressure. For the RANS calculations, the predictor-corrector method used is the SIMPLE algorithm, see Patankar [87], while for the LES calculations, the PISO algorithm by Issa [50] is used. The former one uses one corrector step, while the latter uses two corrector steps. Several discretisation schemes for the convective terms are available in the *EllipSys* code. In the present study it was chosen to use the second-order accurate Second-order Upwind Difference Scheme (SUDS) for the RANS calculations. For the LES calculations, the Central Differencing Scheme (CDS) was used. It is generally accepted that CDS should be used for RANS and LES, respectively. However it was not possible to obtain a converged solution with CDS and thus, the SUDS was employed. The transport equations are solved using a TDMA solver in alternating direction. Under relaxation was employed to improve the convergence, and pressure decoupling is avoided applying the Rhie/Chow interpolation technique, see Rhie [94]. The residual of the flow quantities are calculated from a 1-norm. This imply taking the absolute value of the difference from iteration number $n-1$ to iteration number n of a flow quantity in each grid point. The sum of the differences scaled with total difference in the first iteration defines the 1-norm.

Chapter 3

Validation of turbulence models and topological aspects for two-dimensional calculations of the airflow in the annex 20 case

3.1 Introduction

The flow in empty ventilated spaces has been studied both experimentally and numerically in the past twenty years. Experiments were carried out in 1978 by Nielsen *et al* [80], using Laser Doppler Anemometry (LDA). In 1990 one of the experimental setups was used as a standard configuration for validation of numerical codes, Nielsen [82]. Recently, experiments in a water scale model of this geometry were carried out by Pedersen & Meyer [88], using Particle Image Velocimetry (PIV). The numerical codes used to reproduce these experiments are often based on the solution of the RANS equations. Although many different turbulence models exist, most interest has been paid to two-equation models, such as the low Reynolds number $k-\epsilon$ model by Launder & Sharma [56], the $k-\omega$ model by Wilcox [110] and the $k-\omega$ models by Menter [64]. These models are used in this chapter. Further descriptions can be found in Voigt [108].

The purpose of this chapter is first and foremost to validate the turbulence models existing in the *EllipSys* code for two-dimensional indoor airflow calculations. Two-dimensional calculations of the airflow in the annex 20 room, see Nielsen [82], were carried out using the in-house developed flow solver *EllipSys*. Five different turbulence models, the standard high-Reynolds number $k-\epsilon$ model using wall laws, the low Reynolds number model by Launder & Sharma, [56], the original $k-\omega$ model by Wilcox [110], the $k-\omega$ baseline model by Menter [64], and the $k-\omega$ shear stress transport model by Menter [64], were tested. The two latter are zonal versions of the original $k-\omega$ model. Further, a new model, the revised $k-\omega$ baseline model, was developed. In this model the switch occurring in the $k-\omega$ baseline model was altered, based on numerical tests, to give a more correct behaviour of the turbulence

model.

Velocity profiles obtained with the tested models, were compared with the LDA measurements of Nielsen [82]. Applying theory for a two-dimensional wall jet, LDA measurements of the turbulent kinetic energy are compared with calculated results. It is a matter of course, that the best agreement is expected in the wall jet, due to the parabolic nature of jet flows. The standard high-Reynolds number $k-\epsilon$ model was used to test the grid layout and the results therefore included when comparing with LDA measurements. However, since this dissertation focus on the low Reynolds number models, only these were used in the remaining studies. For the low Reynolds number models, the size of the recirculation zone appearing in the lower left corner of the room is compared with PIV measurements of Pedersen & Meyer [88]. Finally, the level of the eddy viscosity, ν_t, predicted by the low Reynolds number models was compared.

3.2 Test case

In this chapter the test case to be used in the numerical calculations is defined in terms of its geometry and inlet conditions. Since previous measurements have been gathered and the test case serves as a benchmark for room air distribution, it is suitable for the purpose of this chapter. The two-dimensional isothermal test case described in Nielsen [82] is considered.

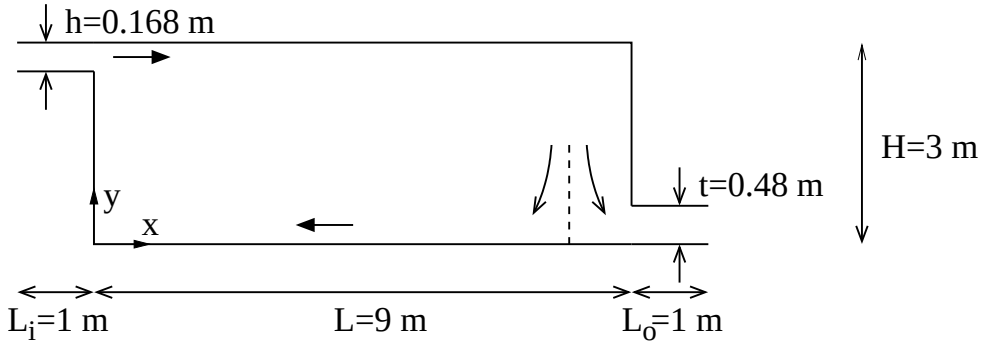

Figure 3.1: The annex 20 2-D isothermal test case. The inlet and the outlet was not included in the original test case, Nielsen [82].

In figure 3.1 the dimensions are

$$H = 3.0\ m,\ L = 9.0\ m,\ L_i = 1.0\ m,\ L_o = 1.0\ m,$$
$$h = 0.168\ m \text{ and } t = 0.48\ m, \tag{3.1}$$

which denotes height of the room, length of the room, length of the inlet, length of the outlet, height of the inlet and height of the outlet, respectively. In the annex 20 room, illustrated in figure 3.1, the air is supplied in the upper left corner and

exhausted through the opening to the lower right. The inlet velocity

$$U_0 = 0.455 \ \frac{m}{s}, \tag{3.2}$$

and the kinematic viscosity $\nu = 15.3 \cdot 10^{-6} \ m^2/s$ are used. This leads to the Reynolds number

$$Re_h = \frac{hU_0}{\nu} = 5000, \tag{3.3}$$

based on the conditions at the supply opening.

According to Nielsen [82], the turbulent length scale is estimated from

$$l_0 = \frac{h}{10} = 0.0168 \ m. \tag{3.4}$$

A turbulent intensity $Tu \equiv \sqrt{\overline{u_i'^2}}/U_0 = 4\%$ is chosen. From these values an estimate of the inlet conditions are

$$k_0 = \frac{3}{2}(Tu \cdot U_0)^2 \approx 4.97 \cdot 10^{-4} \ \frac{m^2}{s^2} \tag{3.5}$$

for the turbulent kinetic energy, and

$$\epsilon_0 = \frac{k_0^{1.5}}{l_0} \approx 6.60 \cdot 10^{-4} \ \frac{m^2}{s^3} \tag{3.6}$$

for the dissipation of turbulent kinetic energy, respectively. The inlet condition for the specific dissipation rate ω is specified using the relation

$$\omega_0 = \frac{\epsilon_0}{0.09 k_0} \approx 15 \ \frac{1}{s}. \tag{3.7}$$

Equation (3.7) is derived by equating the eddy viscosity for the standard $k-\epsilon$ model to the eddy viscosity for the $k-\omega$ model. The definition of the eddy viscosity for these two models can be found in appendix D. In the input file for the flow solver, the inlet conditions specified are k_0 and either ϵ_0 or ω_0, for the $k-\epsilon$ and $k-\omega$ models, respectively.

An example of a representative computational grid, obtained with the grid generator presented in appendix A.1, is shown in figure 3.2.

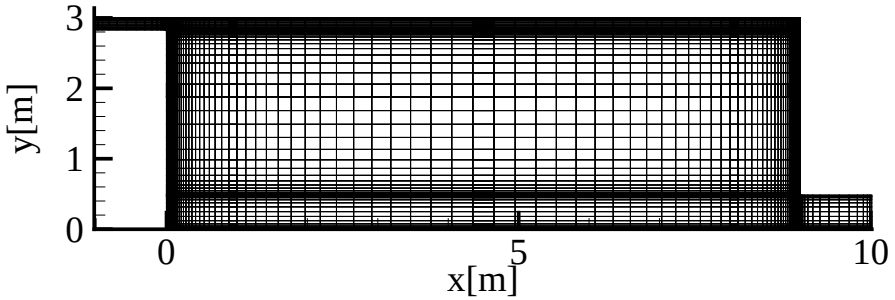

Figure 3.2: A representative computational grid obtained with the grid generator presented in appendix A.1. The grid was build from blocks of 16×16 cells using 6 blocks in the horizontal direction and 4 blocks in the vertical direction. Two extra blocks were added to include the inlet and outlet, respectively.

LDA measurements, Nielsen [82], are available along two vertical lines,

$$x = 3.0\ m \text{ and } x = 6.0\ m, \tag{3.8}$$

and two horizontal lines,

$$y = 0.084\ m \text{ and } y = 2.916\ m. \tag{3.9}$$

In appendix E, the solution for four different grids was evaluated in terms of mean velocity profiles. The different grids was generated from blocks of 8×8, 16×16, 32×32 and 48×48 grid points, respectively and the solutions were obtained using the low Reynolds number $k - \epsilon$ model. Based on the results presented in appendix E, it is assumed that for a low Reynolds number model, a grid consisting of 32×32 cells in each block gives a solution independent of grid size. A convergence criterion of 10^{-5} was used. However, for one of the calculations, the solution was converged to 10^{-14}. Since no diffences between the velocity profiles existed for a solution converged to 10^{-5} and a solution converged 10^{-14}, it was assumed that the former was a satifying convergence criterion.

3.3 Results and discussion

The numerical results obtained, using the six different turbulence models for the test case presented in chapter 3.2 are presented. The two-equation turbulence models introduced in appendix D, are abbreviated as follows

$$\begin{aligned}
k-\epsilon \text{ HI RE} &: \text{Standard high Reynolds number } k-\epsilon \\
k-\epsilon \text{ LS} &: \text{Low Reynolds number } k-\epsilon \text{ Launder \& Sharma, [56]} \\
k-\omega \text{ ORG} &: k-\omega \text{ original, Wilcox [110]} \\
k-\omega \text{ BSL} &: k-\omega \text{ baseline, Menter [64]} \\
k-\omega \text{ SST} &: k-\omega \text{ shear stress transport, Menter[64]} \\
k-\omega \text{ BSLREV} &: k-\omega \text{ baseline revised}
\end{aligned} \tag{3.10}$$

3.3.1 Comparison of turbulence models

In figure 3.3 and 3.4 computed velocities at the positions $x = 3.0\ m$ and $x = 6.0\ m$ are compared with measurements. At $x = 3.0\ m$, figure 3.3(left) and figure 3.4(left), the low Reynolds number models tend to overpredict the velocity close to the ceiling, while the standard $k-\epsilon$ model is in good agreement. Near $y = 2.5\ m$ all the models slightly underpredict the velocity, worst for the $k-\omega$ SST model. Close to the floor the two $k-\epsilon$ models and the $k-\omega$ BSLREV model show good accordance with measurements, while the $k-\omega$ ORG model and the $k-\omega$ BSL model underpredict the velocity. The velocity computed with $k-\omega$ SST model has the wrong sign.

At the position $x = 6.0\ m$, figure 3.3(right) and figure 3.4(right), the standard $k-\epsilon$ model underpredicts the velocity close to ceiling. The low Reynolds number models show good agreement here. At $y = 2.5\ m$ all the models show better accordance with measurements than for the same position at $x = 3\ m$. Though a relative strong discrepancy has now occurred close to $y = 1\ m$. Since the same deviation is predicted by all the models, it is reasonable to believe that the phenomenon is a three-dimensional effect. So could be the case for $x = 3\ m$ and $y = 2.5\ m$. Except from the $k-\omega$ SST model all the models fit the measurements well close to the floor.

In figures 3.5 and 3.6 computed velocities are compared with measurements at the positions $y = 0.084\ m$ close to the floor, and $y = 2.916\ m$ close to the ceiling. Close to the ceiling, figure 3.5(upper) and 3.6(upper), the agreement between measurements and computations is reasonable for all the models. However, a clear discrepancy between measurements and computations is found close to the boundary of the recirculation zone in the upper right corner of the room. The phenomenon is common for all the models, but it seems as if the passage from the main flow to the small recirculation zone is predicted best by the $k-\epsilon$ LS model and the $k-\omega$ BSLREV model. Close to the floor, figure 3.5(lower) and figure 3.6(lower), the standard $k-\epsilon$ model shows better agreement with measurements than the low Reynolds number models. The $k-\omega$ SST model shows very poor accordance with measurements close to the floor. From figure 3.6(lower), it is observed that the $k-\omega$ ORG model and the $k-\omega$ BSL model predict a steep drop in the velocity at $x \approx 2.5\ m$. This phenomenon is observed neither in the $k-\epsilon$ models and the $k-\omega$ BSLREV model nor in the measurements.

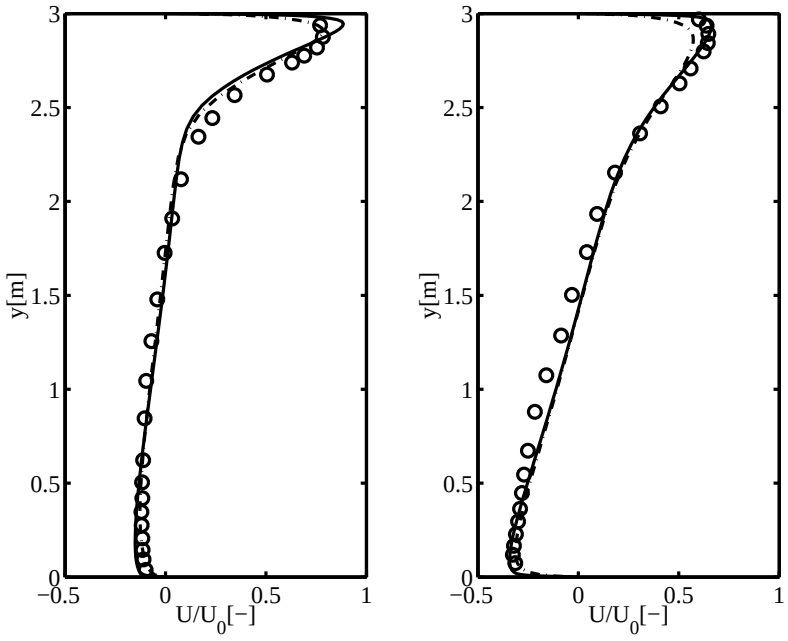

Figure 3.3: Comparison of velocities U/U_0 along two vertical lines for the $k-\epsilon$ models. Left: $x = 3\ m$. Right: $x = 6\ m$. $-\cdot-\cdot-$:$k-\epsilon$ HI RE, ——:$k-\epsilon$ LS. ∘: Measurements, Nielsen [82].

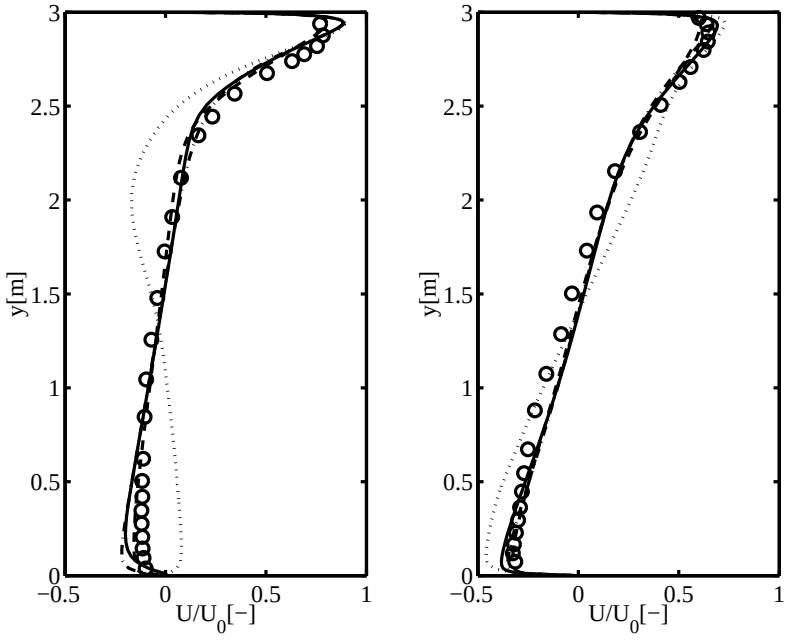

Figure 3.4: Comparison of velocities U/U_0 along two vertical lines for the $k-\omega$ models. Left: $x = 3\ m$. Right: $x = 6\ m$. $-\cdot-\cdot-$:$k-\omega$ ORG. ——:$k-\omega$ BSL. ·····: $k-\omega$ SST. $-\ -\ -\ -$: $k-\omega$ BSLREV. ∘: Measurements, Nielsen [82].

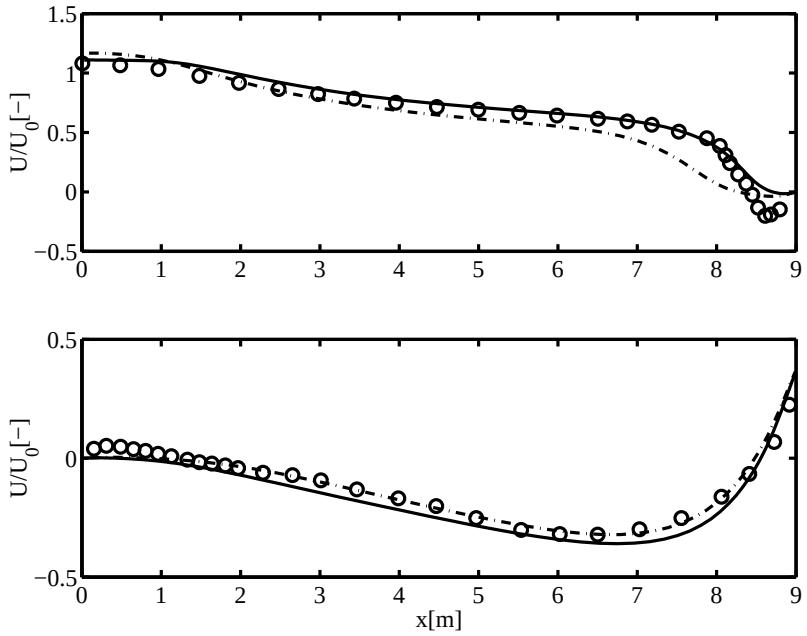

Figure 3.5: Comparison of velocities U/U_0 along two horizontal lines for the $k-\epsilon$ models. Bottom: $y = 0.084\ m$. Top: $y = 2.916\ m$. Symbols, see figure 3.3.

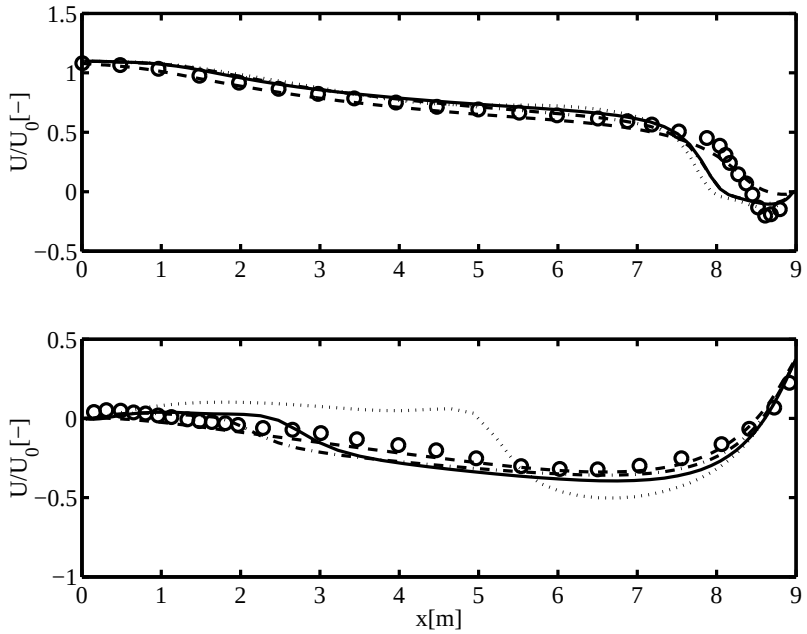

Figure 3.6: Comparison of velocities U/U_0 along two horizontal lines for the $k-\omega$ models. Bottom: $y = 0.084\ m$. Top: $y = 2.916\ m$. Symbols, see figure 3.4.

The turbulent kinetic energy is an important quantity to assess the validity of the turbulence models. A comparison of this quantity is troublesome, since measurements are in one direction only. According to Nielsen [81], the correlation between the normal stresses in a two-dimensional wall jet is given by

$$\overline{u_2'^2} \approx 0.6\,\overline{u_1'^2} \quad \text{and} \quad \overline{u_3'^2} \approx 0.8\,\overline{u_1'^2}. \tag{3.11}$$

Introducing (3.11) in the definition for the turbulent kinetic energy gives

$$\sqrt{k} \approx 1.1\,\sqrt{\overline{u_1'^2}}. \tag{3.12}$$

If instead, the flow is considered as a boundary layer on a flat plate, a different correlation between the normal stresses is measured by Klebanoff, see Schlichting [97]. Using this correlation the factor 1.1 in (3.12) would take both higher and lower values throughout the boundary layer. In general, only an increase of this constant would improve the agreement between computations and measurements, see figures 3.7-3.10. For simplicity the relation (3.12) is used.

In figure 3.7-3.10 calculated values of $\sqrt{k}/1.1U_0$ are compared with measurements of $\sqrt{\overline{u_1'^2}}/U_0$ for the various turbulence models. Except from the $k-\omega$ SST model, the models give almost similar distribution of the turbulent kinetic energy. The models tend to underpredict the turbulent kinetic energy, except in the wall jet, i.e. $2.5\ m < y < 3\ m$ in figure 3.7(left) and figure 3.8(left), and a small region close to $y = 1.5\ m$. Since equation (3.12) is only valid for a jet it was expected that the agreement between measurements and calculations would be best in the jet. No further conclusions are drawn due the uncertainty on comparing calculated values of turbulent kinetic energy with one-dimensional measurements. An interesting task for future studies is to carry out measurements in more than one direction. This would make it possible to evaluate the expression (3.12) and to conclude further on the performance of the turbulence models.

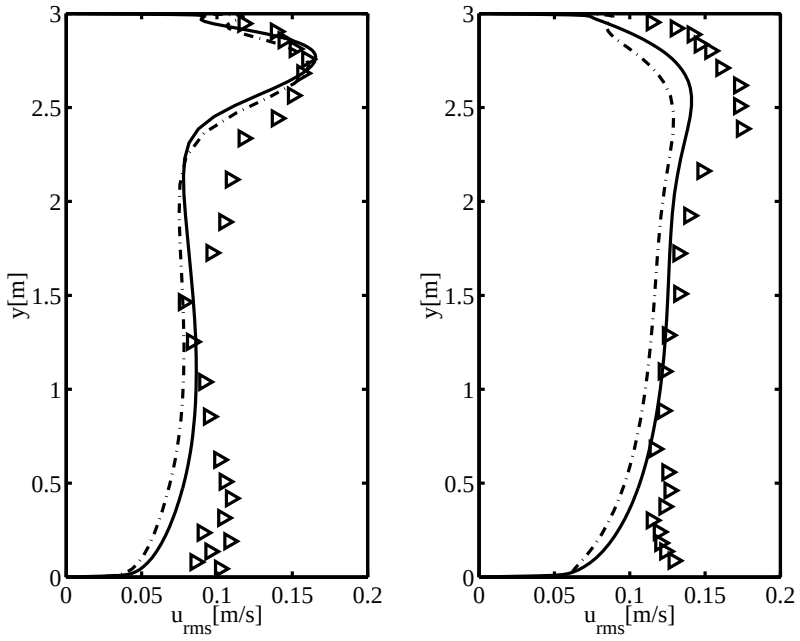

Figure 3.7: Comparison of turbulent kinetic energy, $\sqrt{k}/1.1u_o$, along two vertical lines for the $k-\epsilon$ models. Left: $x = 3\ m$. Right: $x = 6\ m$. $-\cdot-\cdot-\cdot$:$k-\epsilon$ HI RE, ——:$k-\epsilon$ LS. $\triangleright$: Measurements of $\sqrt{\overline{u_1'^2}}/U_0$, Nielsen [82].

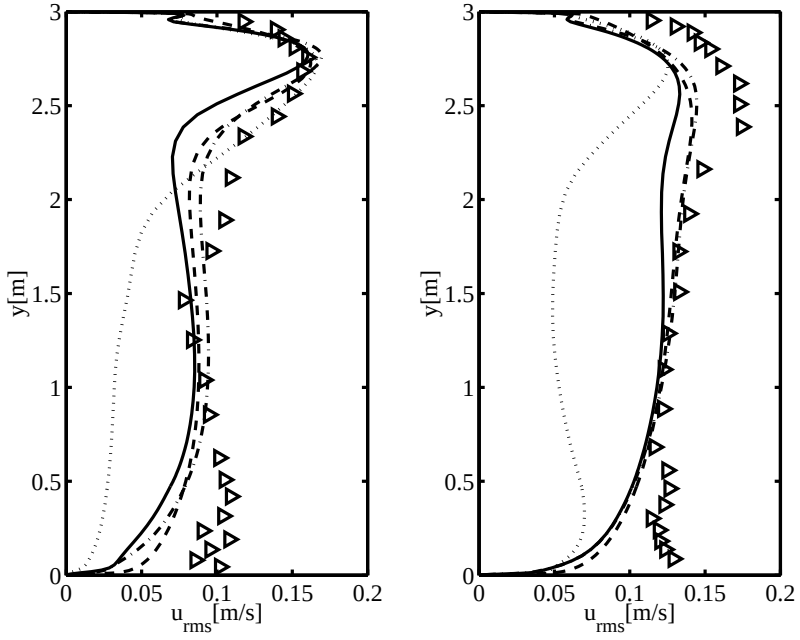

Figure 3.8: Comparison of turbulent kinetic energy, $\sqrt{k}/1.1U_0$, along two vertical lines for the $k-\omega$ models. Left: $x = 3\ m$. Right: $x = 6\ m$. $-\cdot-\cdot-\cdot$:$k-\omega$ ORG. ——:$k-\omega$ BSL. $\cdots\cdots$: $k-\omega$ SST. $-\ -\ -\ -$: $k-\omega$ BSLREV. $\triangleright$: see figure 3.7.

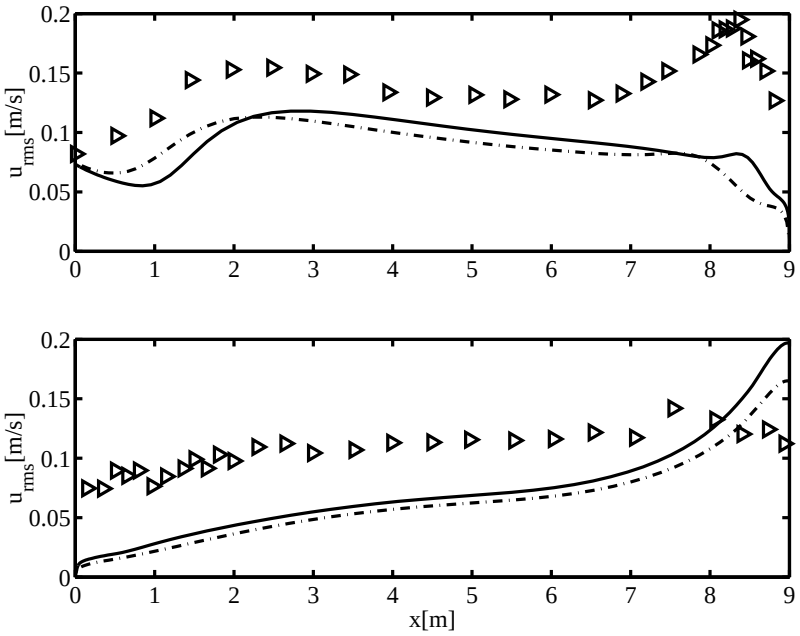

Figure 3.9: Comparison of turbulent kinetic energy, $\sqrt{k}/(1.1U_0)$, along two horizontal lines for the $k-\epsilon$ models. Bottom: $y = 0.084\ m$. Top: $y = 2.916\ m$. Symbols, see figure 3.7.

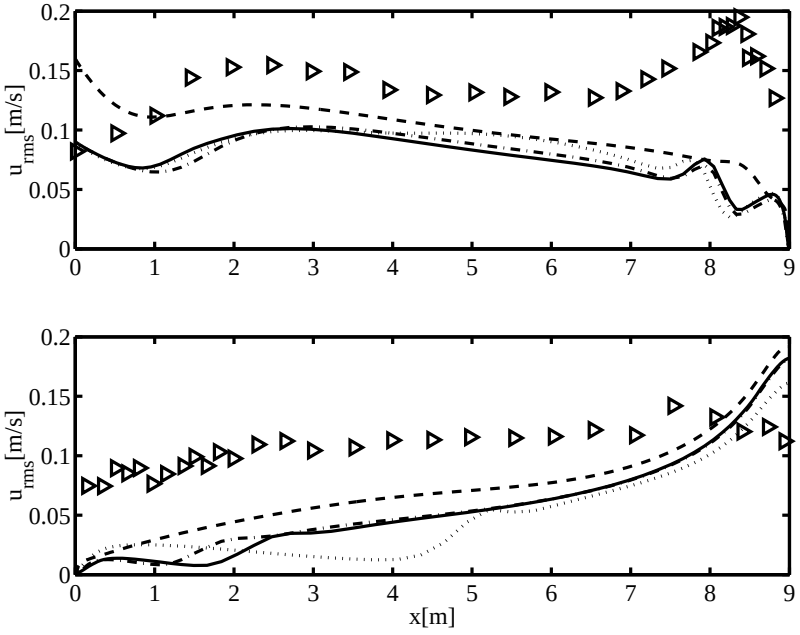

Figure 3.10: Comparison of turbulent kinetic energy, $\sqrt{k}/(1.1U_0)$, along two horizontal lines for the $k-\omega$ models. Bottom: $y = 0.084\ m$. Top: $y = 2.916\ m$. Symbols, see figure 3.8.

3.3.2 Topological aspects

To further challenge the turbulence models it was chosen to compare the size of the recirculating zone appearing in the lower left corner. It was chosen to focus on this part of the flow because experimental results exist, see Pedersen & Meyer [88]. However, the region is also interesting, since the mean velocities are close to zero and the turbulence models therefore expected to be most sensitive in this area.

Figure 3.11-3.15 shows selected contour lines of the stream function for the five low Reynolds number models tested. Figure 3.11 shows that the $k-\epsilon$ LS model predicts a size of the recirculation zone which is in good agreement with the size obtained using commercial software, see Bennetsen [7]. However, comparing the location of the separation point and the attachment point with experiments, see table 3.1, the size of the recirculation zone is severely underpredicted. Using the less dissipative[1]. $k-\omega$ ORG model the size of the recirculation zone increases, see figure 3.12. The computed location of the separation and attachment point varied less than 10 %.

Using the $k-\omega$ BSL model the recirculation zone further increases, see figure 3.13, indicating that the model is less dissipative than the $k-\omega$ ORG model. This is inconsistent with the fact that this model is a blending of the $k-\omega$ model and the $k-\epsilon$ model, for which reason a model more dissipative than the $k-\omega$ ORG model was anticipated. This is explained considering the contour plot in figure 3.16, illustrating the blending between the $k-\omega$ model and the $k-\epsilon$ model. Clearly the $k-\omega$ model is used in most of the domain, and the intension of letting the blending from a $k-\omega$ model to a $k-\epsilon$ model take place throughout the boundary layer fails. Using the $k-\omega$ BSLREV model the blending is defined in such a way that the model changes from the $k-\omega$ model to the $k-\epsilon$ model at a user defined distance from the wall. The choice of blending function in the $k-\omega$ BSLREV model is by no means optimal, since it is independent of any flow variables, but the results gave the expected results. Considering figure 3.14 the $k-\omega$ BSLREV model predicts a recirculation zone with the same size as predicted by the $k-\epsilon$ LS model.

Finally, the $k-\omega$ SST model which is the least dissipative model of the tested models is found to predict a recirculation zone covering almost half of the room length. To explain this, it was investigated in what regions the $k-\omega$ SST model accounts for transport of principal shear stress, i.e. when the $k-\omega$ SST model is used instead of the $k-\omega$ BSL model, see figure 3.17. The $k-\omega$ SST model accounts for principal shear stress in the shear layer caused by the mixing of the inlet jet with the almost stagnant room air. It seems physically reasonable to account for principal shear stress in this part of the flow, while accounting for principal shear stress in the stagnant core of the room air is more difficult to explain. Accounting for principal shear stress has a tremendous effect on the predicted eddy viscosity, see figures 3.18-3.20. The $k-\epsilon$ LS model finds maximum values of the eddy viscosity which is approximately 860 times the kinematic viscosity, while for the $k-\omega$ ORG

[1] The more dissipative a model is the higher values of the modelled viscosity ν_t.

model this value is 897. The $k-\omega$ BSL model takes of course values very similar to those of the $k-\omega$ ORG model, while accounting for principal shear stress reduces the maximum ratio of the eddy viscosity to the kinematic viscosity with a factor of three. Since a more thorough analysis is needed for improving the $k-\omega$ SST model, and very good agreement between the $k-\omega$ ORG model and measurements was obtained, the recent observations are left without further comments.

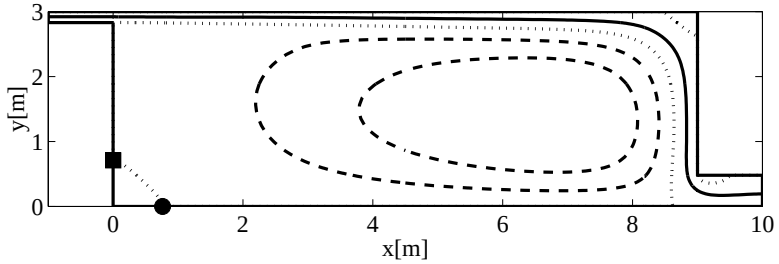

Figure 3.11: Flow structure using the $k-\epsilon$ LS model. The lines are isolines of the stream function. $\cdots\cdots$: contour levels [0 ; 0.0932568], $-\ -\ -\ -$: contour levels [-0.05 ; -0.1] ——: contour level [0.05]. Separation point on floor is indicated by • and attachment on wall is indicated by ■.

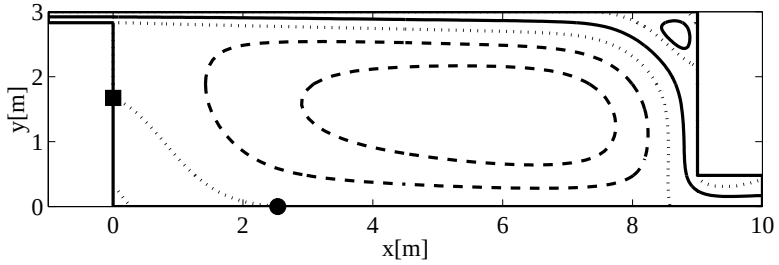

Figure 3.12: Flow structure using the $k-\omega$ ORG model. Interpretation of symbols, see figure 3.11.

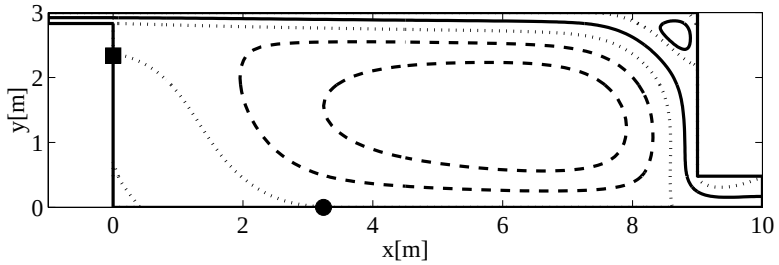

Figure 3.13: Flow structure using the $k-\omega$ BSL model. Interpretation of symbols, see figure 3.11.

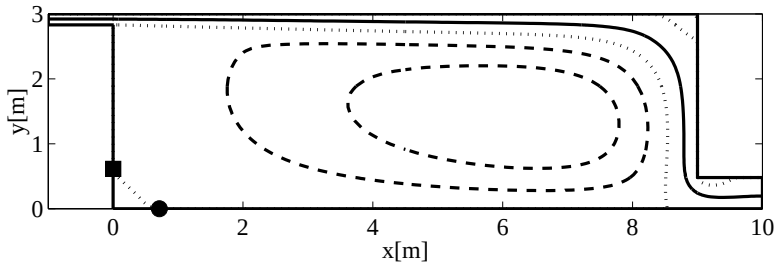

Figure 3.14: Flow structure using the $k-\omega$ BSLREV model. Interpretation of symbols, see figure 3.11.

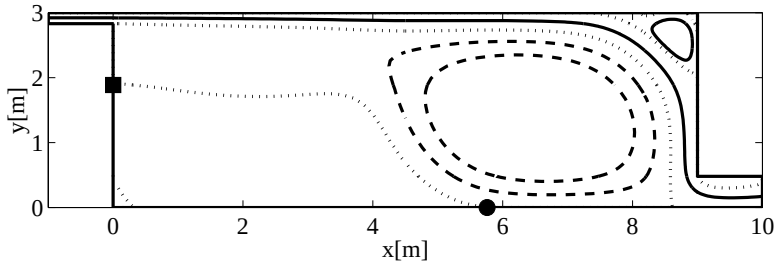

Figure 3.15: Flow structure using the $k-\omega$ SST model. Interpretation of symbols, see figure 3.11.

Model	Separation	Deviation	Attachment	Deviation
	$x[m]$	%	$y[m]$	%
Measurements	2.78	0	1.82	0
$k-\epsilon$ LS	0.76	-73	0.71	-61
$k-\omega$ ORG	2.54	-9	1.67	-8
$k-\omega$ BSL	3.24	17	2.34	29
$k-\omega$ SST	5.76	107	1.89	4
$k-\omega$ BSLREV	0.71	-74	0.61	-66

Table 3.1: Comparison of the separation point and the attachment point for the recirculation zone appearing in the lower left corner, see figure 3.11-3.15. First column is the x coordinate for the separation point on the floor, second column is the deviation from the separation point found by PIV measurements, third column is the y coordinate for the reattchment point on the left wall and fourth column is the deviation from the attachment point found by PIV measurements.

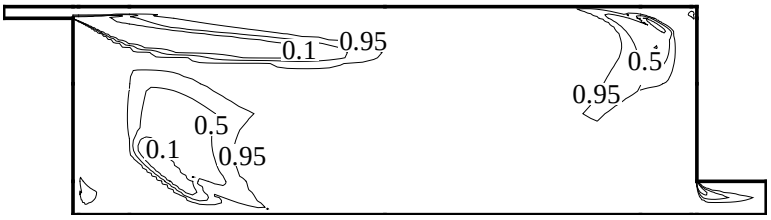

Figure 3.16: Contour plot of the blending function F_1 for the $k-\omega$ BSL model. 0 corresponds to an unblended $k-\epsilon$ model and 1 corresponds to an unblended $k-\omega$ model. The unblended $k-\omega$ model is used in most of the domain.

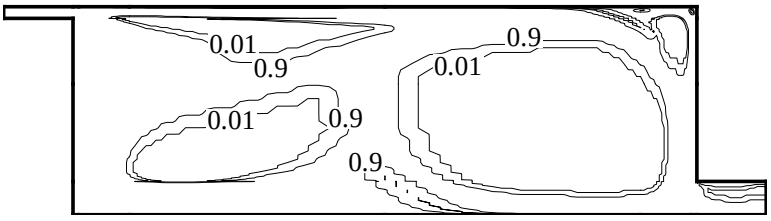

Figure 3.17: Contour plot of the limiter used when calculating the viscosity for the $k-\omega$ SST model. 0 corresponds to the $k-\omega$ SST model and 1 corresponds to the $k-\omega$ BSL model.

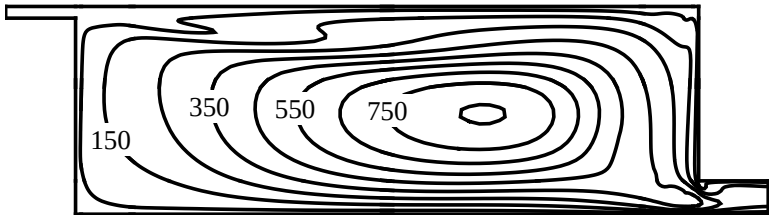

Figure 3.18: Contour plot of the eddy viscosity to the kinematic viscosity, ν_t/ν, for the $k-\epsilon$ LS model. Contourlevels are [50;150;250;350;450;550;650;750;850] and the maximum value is ν_t/ν=858.

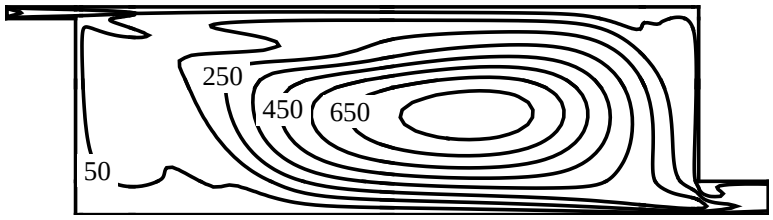

Figure 3.19: Contour plot of the eddy viscosity to the kinematic viscosity, ν_t/ν, for the $k-\omega$ ORG model. Contourlevels are [50;150;250;350;450;550;650;750] and the maximum value is ν_t/ν=897.

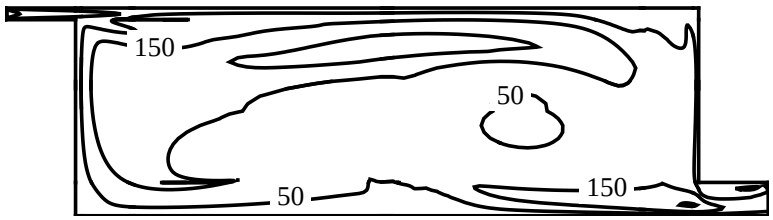

Figure 3.20: Contour plot of the eddy viscosity to the kinematic viscosity, ν_t/ν, for the $k-\omega$ SST model. Contourlevels are [50;150;250] and the maximum value is ν_t/ν=298.

3.4 Summary

In this chapter the turbulence models existing in the flow solver *EllipSys* was validated for two-dimensional calculations of the airflow in the annex 20 room. Furthermore, topological aspects for two-dimensional airflows was described.

Five existing turbulence models, the standard $k-\epsilon$ model, the low Reynolds number $k-\epsilon$ model by Launder & Sharma, the $k-\omega$ model by Wilcox, the $k-\omega$ baseline model by Menter and the $k-\omega$ shear stress transport by Menter were evaluated. Further, a new model, the revised $k-\omega$ baseline model, was developed. Except for the $k-\omega$ shear stress transport model, the models are almost equally good and leads to results in reasonably good agreement with LDA measurements.

The models were further compared with PIV measurements from which positions of the separation point on the floor and the attachment point on the left wall are available. Deviations less than ten percent from the measurements were obtained using the $k-\omega$ model by Wilcox. This was found to be superior to the remaining models, which in some cases led to discrepancies of more than hundred percent.

The blending function of the $k-\omega$ baseline model by Menter, which is designed to change from zero to one throughout the boundary layer fails for this flow. The blending function was found to be one in most of the domain. The revised $k-\omega$ baseline model, uses a new ad hoc blending function which circumvents this problem on the expense of a less physical model.

The poor performance of the $k-\omega$ shear stress transport model was investigated. This model was found to account for principal shear in parts of the domain were this was not physically expected. This reduces the maximum ratio of the eddy viscosity to the kinematic viscosity with a factor of three compared to the original $k-\omega$ model.

Thus it is concluded that for two-dimensional calculations, the turbulence models in the *EllipSys* code are able to give velocity profiles in agreement with LDA measurements for the annex 20 test case. Further good agreement with recent PIV measurements for the same test case can be obtained with one of the tested models.

Chapter 4

Validation of turbulence models and topological aspects for three-dimensional calculations of the airflow in the annex 20 case

4.1 Introduction

When validating and developing turbulence models for three-dimensional indoor airflows, the most widely used test case is the 2-D annex 20 room, see Nielsen [82]. Since this test case was originally used for validation of two-dimensional calculations it has been termed 2-D. This assumption was investigated in the present chapter and it was found that it is not valid. This new insight was attained by challenging the used turbulence models not only by means of velocity profiles, but also on the location and classification of stagnation points appearing in the symmetry plane.

The limited amount of literature treating the three-dimensional computations of the 2-D annex 20 room is, attributed to two reasons. First, the amount of computer power needed for accurate three-dimensional calculations is large, and, second, that model calibration is typically carried out in two dimensions. However, recently model calibration for the airflow in three dimensional room geometries has been initiated, see Chen & Xu [18]. Here a zero-equation model based on a local mean velocity scale and a length scale was developed. The model converged 10 times faster then the $k-\epsilon-$model due to fewer grid points used, a reduced amount of differential equations and the non-linear coupling between the k and ϵ equation was avoided. Similar arguments are used when introducing a constant eddy viscosity model in a later chapter of this dissertation. A thorough validation of different turbulence models for three-dimensional indoor airflows was carried out by Bennetsen [7].

The purpose of this chapter is first and foremost to validate the turbulence models existing in the *EllipSys* code for three-dimensional indoor airflow calculations. Most attention was paid to the low Reynolds number $k-\epsilon$ model, which today is

the prevailing turbulence model for calculations of indoor airflows. The previous chapter, however, questions whether this is reasonable. It was therefore chosen to continue using and testing the $k-\omega$ models as well. Velocity profiles obtained with the tested models, were compared with the LDA measurements of Nielsen [82]. The flow pattern in the symmetry plane deviates from the two-dimensional solution. This necessitated a more thorough investigation of the differences between two- and three-dimensional calculations of indoor airflows.

The procedure for validating the turbulence models is described in the following. First a two-dimensional grid was generated with the grid generator presented in appendix A.1, a converged solution for the used models was obtained, and the location of the stagnation points related to the recirculation zone appearing below the inlet depicted. The grid was expanded to three dimensions, and periodic boundary conditions were employed in the spanwise direction. The $k-\epsilon$ model had severe convergence problems and the grid was altered slightly using less stretching. This improved the convergence properties. The stagnation points were located and compared with the two-dimensional solution. Adding wall boundary conditions in the spanwise direction changed the flow pattern below the inlet.

Finally it was chosen to classify the stagnation points appearing in the symmetry plane of the flow. In two-dimensional calculations a low Reynolds number $k-\epsilon$ model was tested. In three-dimensional calculations a high Reynolds number and a low Reynolds number $k-\epsilon$ model were evaluated. Based on the classification of the stagnation points, the topologies were established and compared with recently published experiments, see Pedersen & Meyer [88].

4.2 Test case

The test case considered is the 2-D isothermal annex 20 geometry expanded to three dimensions, see figure 4.1. The dimensions are

$$\begin{aligned} H &= 3.0\ m,\ L = 9.0\ m,\ L_i = 1.0\ m,\ L_o = 1.0\ m,\ W = 3.0\ m, \\ & h = 0.168\ m \text{ and } t = 0.48\ m, \end{aligned} \tag{4.1}$$

which denotes height of the room, length of the room, length of the inlet, length of the outlet, width of the room, height of the inlet and height of the outlet, respectively. The inlet velocity is specified in order to obtain $Re = 5000$ based on inlet height and mean inlet velocity. Turbulent kinetic energy and dissipation of turbulent kinetic energy are specified from the values given in the previous chapter, see equation (3.5) and equation (3.6). The inlet and outlet were not a part of the test case specified in Nielsen [82].

Two kinds of boundary conditions were used for the spanwise direction, i.e. the z-direction, either periodic boundary conditions or wall boundary conditions.

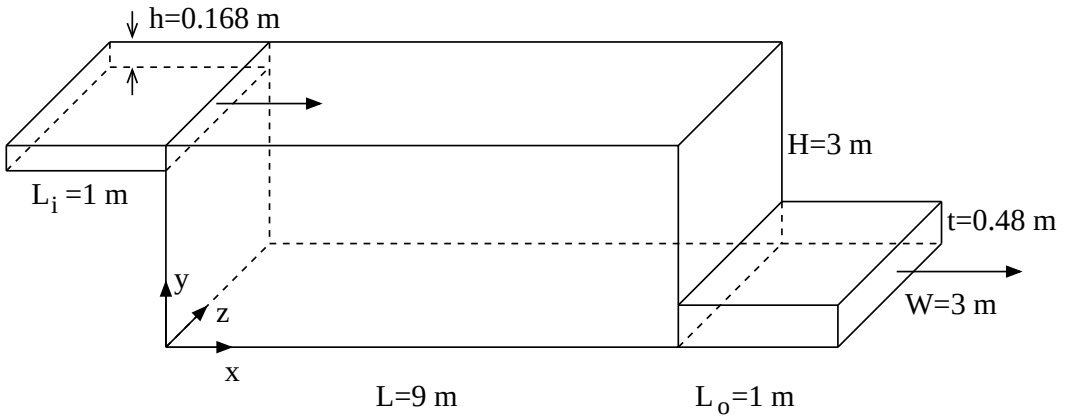

Figure 4.1: The annex 20 2-D isothermal test case in three dimensions.

The grid was generated from blocks of $16 \times 16 \times 16$ cells. The grid layout in the center plane is shown in appendix A.1, and a grid study was carried out in appendix F.

4.3 Results and discussion

The results obtained using three of the turbulence models presented in appendix D is presented. The tested models and used abbreviations are

$k-\epsilon$ LS	:	Low Reynolds number $k-\epsilon$ Launder & Sharma, [56]
$k-\omega$ ORG	:	$k-\omega$ original, Wilcox [110]
$k-\omega$ BSLREV	:	$k-\omega$ baseline revised.

4.3.1 Comparison of turbulence models

In figure 4.2 and figure 4.3, three dimensional computations using wall boundary conditions in the spanwise directions are compared with measurements, Nielsen [82] It was not possible to obtain a converged solution for the $k-\omega$ ORG model. The results should further be evaluated against the two-dimensional computations presented in figure 3.3 and figure 3.4 in the previous chapter. Considering first the results for $x = 3\ m$, figure 4.2(left), the used models tend to overpredict the velocity close to the ceiling. A similar deviation from measurements were observed in the two-dimensional calculations. The computed velocities close to $y = 2.5\ m$ and near the floor are slightly lower than in the measurements. This was also observed for the two-dimensional computations. For the $k-\epsilon$ LS model the velocity is underpredicted more for the three-dimensional computation than in the two-dimensional calculation. This could be an effect from either the walls or from the numerics.

For $x = 6\ m$, figure 4.2(right) the velocities show discrepancies from measurements similar to those found from the two-dimensional calculations. The used models all

show very good agreement with measurements in the wall jet. Close to the floor the accordance with measurements is good for the $k-\epsilon$ LS model, while it is less evident for $k-\omega$ BSLREV model. A significant deviation between measurements and computations exists close to $y = 1\ m$ for both of the used models. The most obvious reason for this discrepancy, which was also observed for the two-dimensional calculations, is that some three-dimensional effects exist in the measurements.

The calculations were compared to measurements close to the floor, figure 4.3(lower), and measurements close to the ceiling, figure 4.3(upper). Near the ceiling, figure 4.3(upper), the agreement with measurements is good except close to the recirculation zone appearing at the wall above the outlet. It is interesting to notice that for the two-dimensional calculations, the $k-\epsilon$ LS model predicted the passage from the main flow to this recirculation zone better than the remaining models. In the three-dimensional calculations the $k-\omega$ BSLREV model performs best of the two models in this region. Close to the floor some deviation from the two-dimensional calculations was also observed. The velocities for $2\ m < x < 8\ m$ are underpredicted more in the three-dimensional calculations than in the two-dimensional calculations. For $x < 2\ m$, the $k-\omega$ BSLREV model overpredicts the velocity found by measurements, while the agreement between the $k-\epsilon$ LS model and the measurements is quite good.

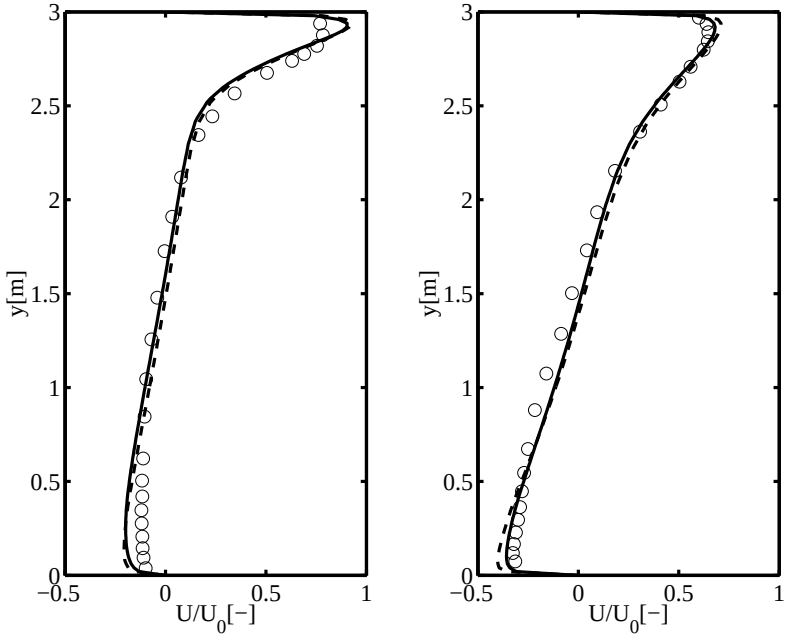

Figure 4.2: Dimensionless velocities U/U_0 along two vertical lines in the symmetry plane. Left: $x = 3\ m$. Right: $x = 6\ m$. Symbols are: ——: $k-\epsilon$ LS. $-\ -\ -\ -$: $k-\omega$ BSLREV. o: Measurements by Nielsen [82].

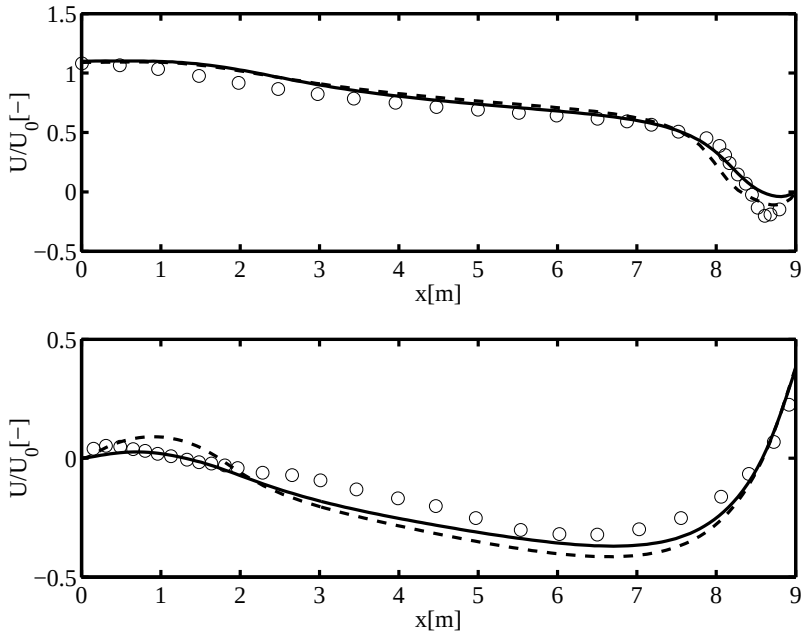

Figure 4.3: Dimensionless velocities U/U_0 along two horizontal lines in the symmetry plane. Lower: $y = 0.084\ m$. Upper: $y = 2.916\ m$. Symbols see figure 4.2.

4.3.2 Topological aspects

In the light of recent experiments, Pedersen & Meyer [88], it was interesting to compare the location of the stagnation points belonging to the recirculation zone occurring below the inlet. A considerable influence from the walls was observed, why it was chosen to further compare the entire vector plots in the symmetry plane. For the three-dimensional calculations, the location of stagnation points, streamlines and vector plots are based on sectional data, i.e the x and y component of the velocity. The stagnation points on the floor are determined as the point at which the x component of the velocity changes sign at the first grid line parallel to the floor. Similarly, is the stagnation point at the wall is determined as the point in which the y component of the velocity changes sign at the first grid line parallel to the wall. The streamlines occurring in figure 4.4 to figure 4.7 are integrated from the grid point next to the stagnation point at the floor. For the two-dimensional calculation this line should theoretically coincide with the streamline with value zero, on the assumption that the level of the stream function is chosen such that it is zero at the floor.

In figure 4.4 vector plots for the two-dimensional calculations are shown. The exact location of the two stagnation points is given in table 4.1. The small deviations from the two-dimensional results presented in figure 3.11, figure 3.12, figure 3.13, figure 3.14 and table 3.1, are presumably caused by the different grids. Comparing the two-dimensional results, figure 4.4, with three-dimensional results using periodic boundary conditions, figure 4.5, only small deviations are found. The $k-\epsilon$ LS model

predicts a smaller recirculation zone for the three-dimensional calculation than for the two-dimensional calculation, while the opposite appears for the $k-\omega$ models, see also table 4.1. From figure 4.6 it is observed that applying the wall boundary conditions has a dramatic effect on the recirculation zone and the location of the stagnation points. The recirculation zone is no longer closed, but the streamline emanating from the stagnation point on the floor continues to the lower part of the jet. The recirculation zone take a very open structure. In the PIV measurements by Pedersen & Meyer, [88], the recirculation zone is open, see figure 4.7, but the structure is more closed than in the calculation presented in figure 4.6. The location of the stagnation points in the calculations and in the measurements are summarized in table 4.1.

Based on the experiences from the previous chapters it was reasonable to believe that the models are not dissipative enough in the region where the recirculation zone exists. For the steady calculations, the convective terms were discretized to second order accuracy using SUDS and a convergence criterion of 10^{-4} was used. Using the first order upwind difference scheme(UDS) reduced the calculation time to obtain a converged solution, on the expense of a less accurate solution. To ensure that effects from the used convergence criterion was negligible, the calculation using UDS was converged to 10^{-8}. No effects from the convergence criterion seemed to exist. The UDS is known to introduce false diffusion in the solution. Thus, it was chosen to use the results obtained with this discretization scheme to give an indication of whether a more dissipative turbulence model would change the structure of the recirculation below the inlet. The results are not shown in this dissertation and will only be described briefly. For the calculation with the UDS, the region between the streamline emanating from the stagnation point at the floor and the wall below the inlet became more narrow. Moreover, the stagnation point on the floor was displaced more to the left. However, the recirculation zone still had the open structure.

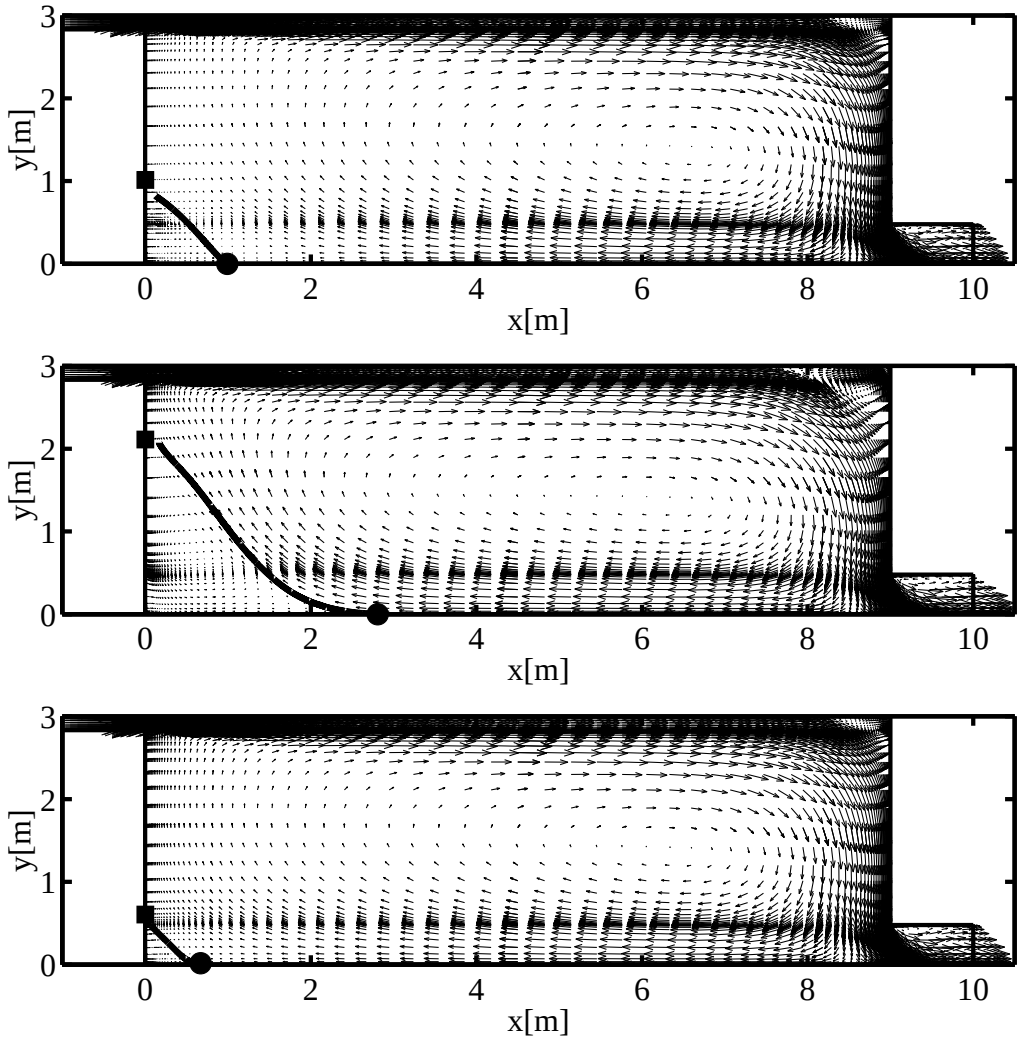

Figure 4.4: Comparison of vector plots for two-dimensional calculations of the flow in the 2-D annex 20 room. Upper: $k-\epsilon$ LS model. Middle: $k-\omega$ ORG model. Lower: $k-\omega$ BSLREV model. The vectors are scaled with a factor 6. The stagnation point on the floor is indicated by $\bullet$ and the stagnation on the wall is indicated by $\blacksquare$.

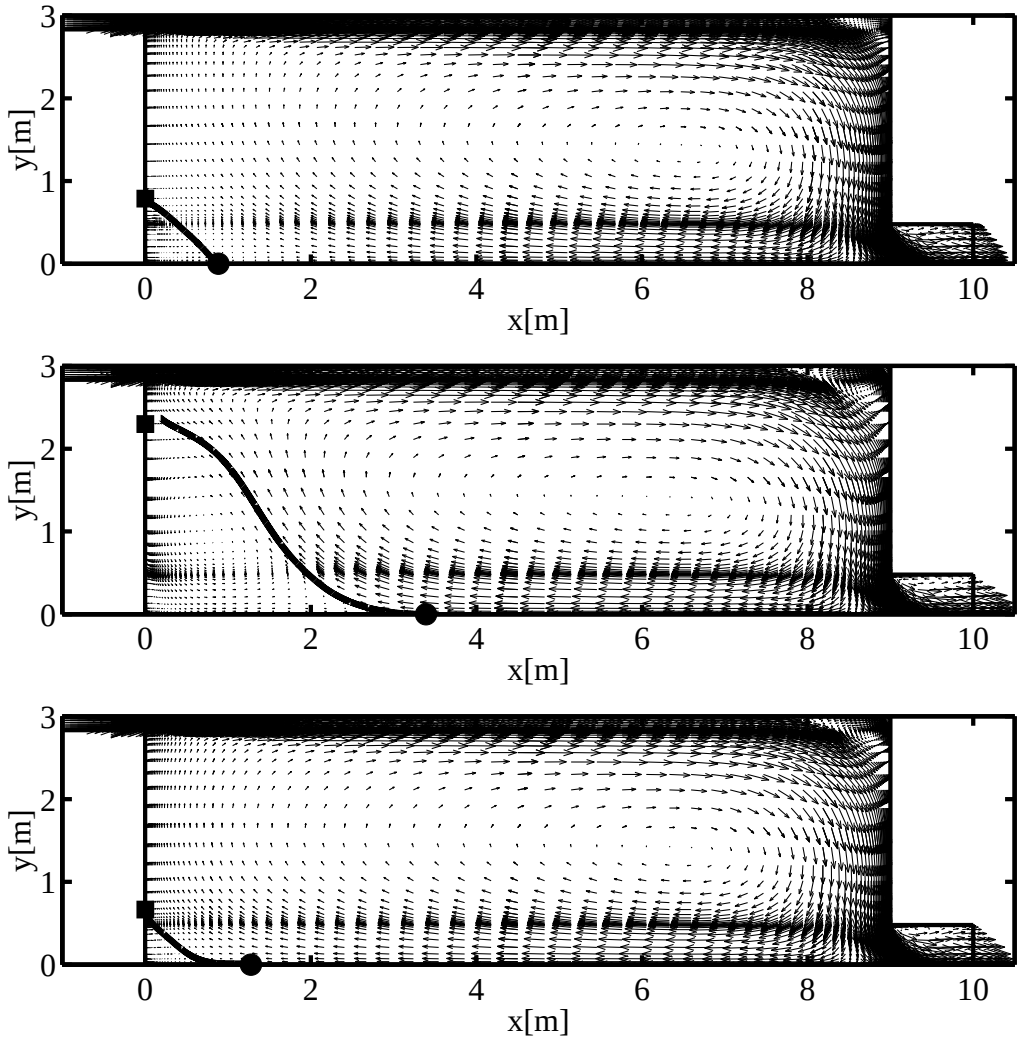

Figure 4.5: Comparison of vector plots for three-dimensional calculations of the flow in the 2-D annex 20 room. The width is 1 m and periodic boundary conditions are employed in the spanwise direction. Upper: $k-\epsilon$ LS model. Middle: $k-\omega$ ORG model. Lower: $k-\omega$ BSLREV model. The vectors are scaled with a factor 6. The stagnation point on the floor is indicated by • and the stagnation point on the wall is indicated by ■.

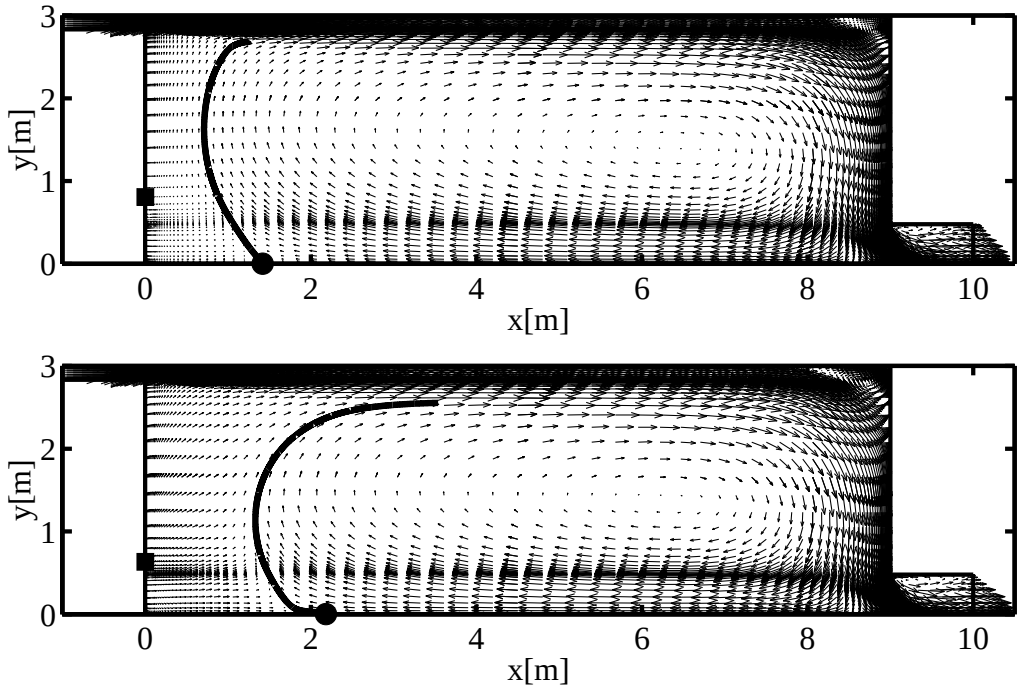

Figure 4.6: Comparison of vector plots for three-dimensional calculations of the flow in the 2-D annex 20 room. The width is 3 m and wall boundary conditions are employed in the spanwise direction. Upper: $k-\epsilon$ LS model. Lower: $k-\omega$ BSLREV model. The vectors are scaled with a factor 6. The stagnation point on the floor is indicated by • and the stagnation point on the wall is indicated by ■.

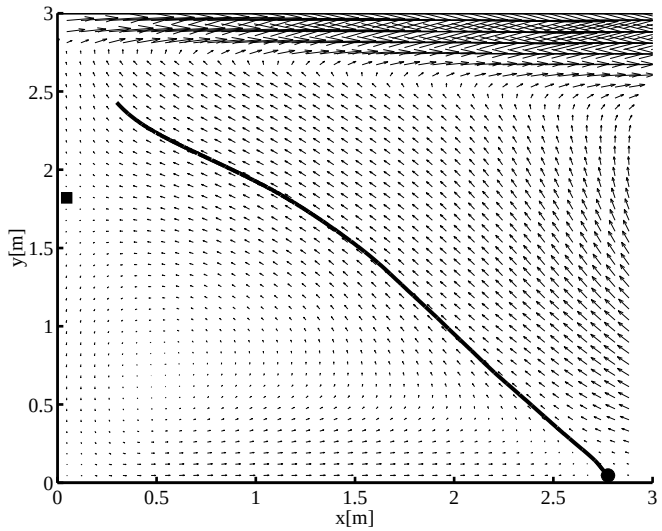

Figure 4.7: PIV measurements of flow in a water scale model of the 2-D annex 20 room, see Pedersen & Meyer [88]. The vectors are scaled with a factor 6. The stagnation point on the floor is indicated by • and the stagnation point on the wall is indicated by ■.

Model	Floor	Deviation	Wall	Deviation
	$x[m]$	%	$y[m]$	$[m]$
Measurements	2.78	0	1.82	0
2-D $k-\epsilon$ LS	0.99	-64	1.01	-45
2-D $k-\omega$ ORG	2.81	1	2.11	16
2-D $k-\omega$ BSLREV	0.67	-76	0.61	-66
3-D $k-\epsilon$ LS (periodic)	0.89	-68	0.79	-57
3-D $k-\omega$ ORG (periodic)	3.40	22	2.30	26
3-D $k-\omega$ BSLREV (periodic)	1.28	-54	0.67	-63
3-D $k-\epsilon$ LS (walls)	1.42	-49	0.81	-55
3-D $k-\omega$ BSLREV (walls)	2.18	-22	0.63	-65

Table 4.1: Comparison of the location of the stagnation point on the floor and the stagnation point on the wall. Both are related to the recirculation zone appearing below the inlet jet, see figure 3.11-3.15. First column is the x coordinate for the stagnation point on floor, second column is the deviation between the experimental and the calculated location of the stagnation point on the floor, third column is the y coordinate for the stagnation point on the wall below the inlet and fourth column is the deviation between the experimental and the calculated location of the stagnation point on the wall.

Comparing the location of stagnation points on the wall provided a new criterion for evaluating the turbulence models. However, the problem of the actual flow pattern below the inlet jet was not clarified. In order to evaluate the turbulence models further, and to get a better insight in the differences between two-dimensional and three-dimensional calculations, the stagnation points appearing in the symmetry plane of the flow were classified. To achieve this, selected streamlines for various calculations are presented in figures 4.8-4.12, and the full topology in the symmetry plane is presented in figure 4.13. The stagnation points are classified using the theory of non-linear differential equations, see e.g. Grimshaw [39].

In figure 4.8, selected streamlines for a two-dimensional calculation using the low Reynolds number $k-\epsilon$ model is presented. Figure 4.8(upper) indicates that closed trajectories exist around $(x, y) \approx (6.5\ m, 1.5\ m)$. Thus, this point can be characterized as a **centre**. From figure 4.8(middle), it is clear that a trajectory emanates from the lower edge of the inlet. The trajectory is an **unstable manifold** from the point where the wall below the inlet and the lower wall of the inlet coincide. The point is characterized as a **saddle point**. The lower wall of the inlet and the wall below the inlet are **stable manifolds**. A saddle for which the unstable manifold emanates into the flow and the stable manifolds exist on the floor, wall or ceiling is referred to as a **separation point**, see Hartnack [42]. A trajectory, which is a stable manifold, approaches a point at $(x, y) \approx (8.5\ m, 0\ m)$, see figure 4.8(middle). This point is a saddle. Two unstable manifolds exist on the floor one on each side of the saddle. This is termed an **attachment point**, see Hartnack [42]. In the lower left corner of the symmetry plane, see 4.8(lower left), a separation point exists at $(x, y) \approx (1\ m, 0\ m)$. The presence of an attachment point is found in $(x, y) \approx (0\ m, 0.9\ m)$. Moreover,

the closed trajectory indicates the presence of a centre at $(x, y) \approx (0.3\ m, 0.4\ m)$. In the upper right corner of the symmetry plane, figure 4.8(lower right), a separation point exists at the ceiling in $(x, y) \approx (8.3\ m, 3\ m)$, while an attachment point is located at $(x, y) \approx (9\ m, 2.6\ m)$. The closed trajectory indicates the presence of a centre at $(x, y) \approx (8.8\ m, 2.8\ m)$. The qualitative topology for the two-dimensional calculation is presented in figure 4.13(A). The saddle points are connected by trajectories. The argument for this is to be found in the Hamiltonian properties of the stream function. The discussion is beyond the scope of this dissertation. Further information can be found in Grimshaw [39].

Figure 4.9 shows selected streamlines in the symmetry plane for a three-dimensional calculation using the low Reynolds number $k-\epsilon$ model and periodic boundary conditions in the spanwise direction. The flow pattern is identical to the flow pattern obtained in the two-dimensional calculation. A centre exists at $(x, y) \approx (6.5\ m, 1.5\ m)$, see figure 4.9(upper). A separation point exists at the lower edge of the inlet, $(x, y) = (0\ m, 2.832\ m)$, and an attachment point is located at $(x, y) \approx (8.5\ m, 0\ m)$, see figure 4.9(middle). In the lower left corner of the symmetry plane, figure 4.9(lower left), a separation point exists at the floor and an attachment point exists at the wall. Further, the presence of a centre in $(x, y) \approx (0.3\ m, 0.4\ m)$ is observed. In the upper right corner of the symmetry plane, figure 4.9(upper right), an attachment point exists at the wall and a separation point exists at the ceiling. Finally, a centre is located at $(x, y) \approx (8.8\ m, 2.8\ m)$. The topologies corresponds to the two-dimensional topology, see figure 4.13(A).

Using the low Reynolds number $k-\epsilon$ model and applying wall boundary conditions changes the flow pattern in the symmetry plane significantly, see figure 4.10. The trajectory emanating from a point in the vicinity of $(x, y) \approx (6.5\ m, 1.5\ m)$ is found to spiral away from this point, see figure 4.10(upper). The point $(x, y) \approx (6.5\ m, 1.5\ m)$ is therefore classified as an **unstable spiral point**. A closed trajectory is surrounding the core of the flow, see figure 4.10(upper). Since trajectories are spiralling towards this trajectory from both inside and outside, the trajectory is called a **stable limit cycle**. A separation point exists at the lower edge of the inlet, $(x, y) = (0\ m, 2.832\ m)$, and at the floor an attachment point appears in $(x, y) \approx (8.5\ m, 0\ m)$, see figure 4.10(middle). In the lower left corner of the symmetry plane a separation point is found to exist on the floor at $(x, y) \approx (1.4\ m, 0\ m)$. From a point at the wall trajectories emanate in all directions covering a total angle of 180^o. Such a point is termed an **unstable node**. A centre is no longer present in this part of the flow. In the upper right corner, figure 4.10(lower left), a separation point exists at the ceiling. Further, an attachment point is located at the wall. Trajectories are attracted to the point $(x, y) \approx (8.8\ m, 2.8\ m)$. Thus, this point is termed a **stable spiral point**. With this information the topology in the symmetry plane was sketched in figure 4.13(B). For three-dimensional calculations it is unlikely that the two saddles are connected by a trajectory, since a stream functions with Hamiltonian properties no longer exists.

The high Reynolds number $k-\epsilon$ model was used to illustrate another possible topology in the symmetry plane, see figure 4.11. An unstable spiral point exists at $(x, y) \approx (6.5\ m, 1.5\ m)$, see figure 4.11(upper). This was observed for the low Reynolds number $k-\epsilon$ model also. However, in contrast to the low Reynolds number $k-\epsilon$ model no stable limit cycle is surrounds the core region of the flow. A separation point exists at $(x, y) = (0\ m, 2.832\ m)$, see figure 4.11(middle). Further, an attachment point exists at the floor for $(x, y) \approx (9.5\ m, 0\ m)$. In the lower left corner of the symmetry plane, 4.11(lower left), a separation point is present on the floor at $(x, y) \approx (2\ m, 0\ m)$. Moreover, an attachment point exists at the wall in $(x, y) \approx (0\ m, 1.5\ m)$. Finally, a stable spiral point exists at $(x, y) \approx (0.5\ m, 0.35\ m)$. In the upper right corner, see figure 4.11(lower right), a separation point exists on the ceiling at $(x, y) \approx (8.2\ m, 3\ m)$. At the wall at $(x, y) \approx (9\ m, 2.4\ m)$, an unstable node exists. The topology in the symmetry plane using the high Reynolds number $k-\epsilon$ model is sketched in figure 4.13(C).

Selected streamlines for the PIV measurements is shown in figure 4.12. For the measurements data for $0\ m \leq x \leq 3\ m$ and $0\ m \leq y \leq 3\ m$ are available. In this region, a separation point exists at the floor in $(x, y) \approx (2.8\ m, 0\ m)$. Further, an attachment point exists on the wall at $(x, y) \approx (0\ m, 1.8\ m)$. Finally, an unstable spiral point exists at $(x, y) \approx (0.5\ m, 0.7\ m)$. The topology is shown in 4.13(D). As a final remark it should be mentioned that the exact location of the saddle points on the walls, floor and ceiling could be found in a way similar to that used for determining the location of the stagnation points in table 4.1.

From figure 4.13 it is clear that the airflow pattern predicted in empty spaces is influenced by the type of calculation. Using two-dimensional calculations will result in closed trajectories only, since the stream function is a Hamiltonian function. Further, the only stagnation points occurring will be centres and saddles and the saddles will be connected by a trajectory. For three-dimensional calculation the solutions are no longer restricted by the Hamiltonian properties. Thus, a variety of different stagnation points can occur, e.g stable spiral points, unstable centres, saddles and unstable nodes. All the mentioned types were found in this work, but others exist. Further, a stable limit cycle was observed in one of the three-dimensional calculations. The choice of turbulence model have a significant impact on the flow pattern. Figure 4.13(B) and figure 4.13(C) shows the obvious differences on the obtained flow pattern using a low Reynolds number $k-\epsilon$ model and a high Reynolds number $k-\epsilon$ model. It is impossible to conclude if one of the turbulence models is superior to another, since both disagree with measurements, see figure 4.13(D). In this dissertation different turbulence models were evaluated. In the future other parameters such as discretisation scheme and steady/unsteady solution procedure should be evaluated.

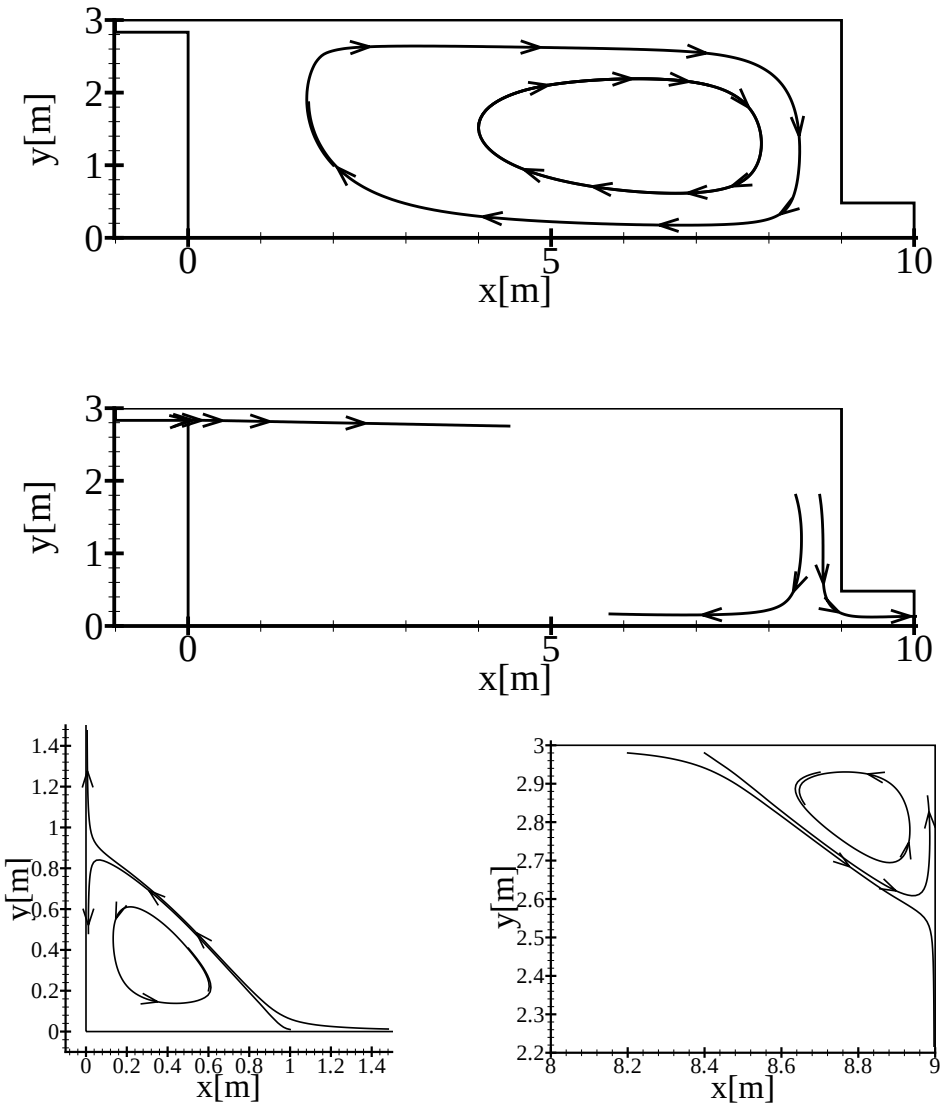

Figure 4.8: Streamlines for a two-dimensional calculation using a low Reynolds number $k - \epsilon$ model.

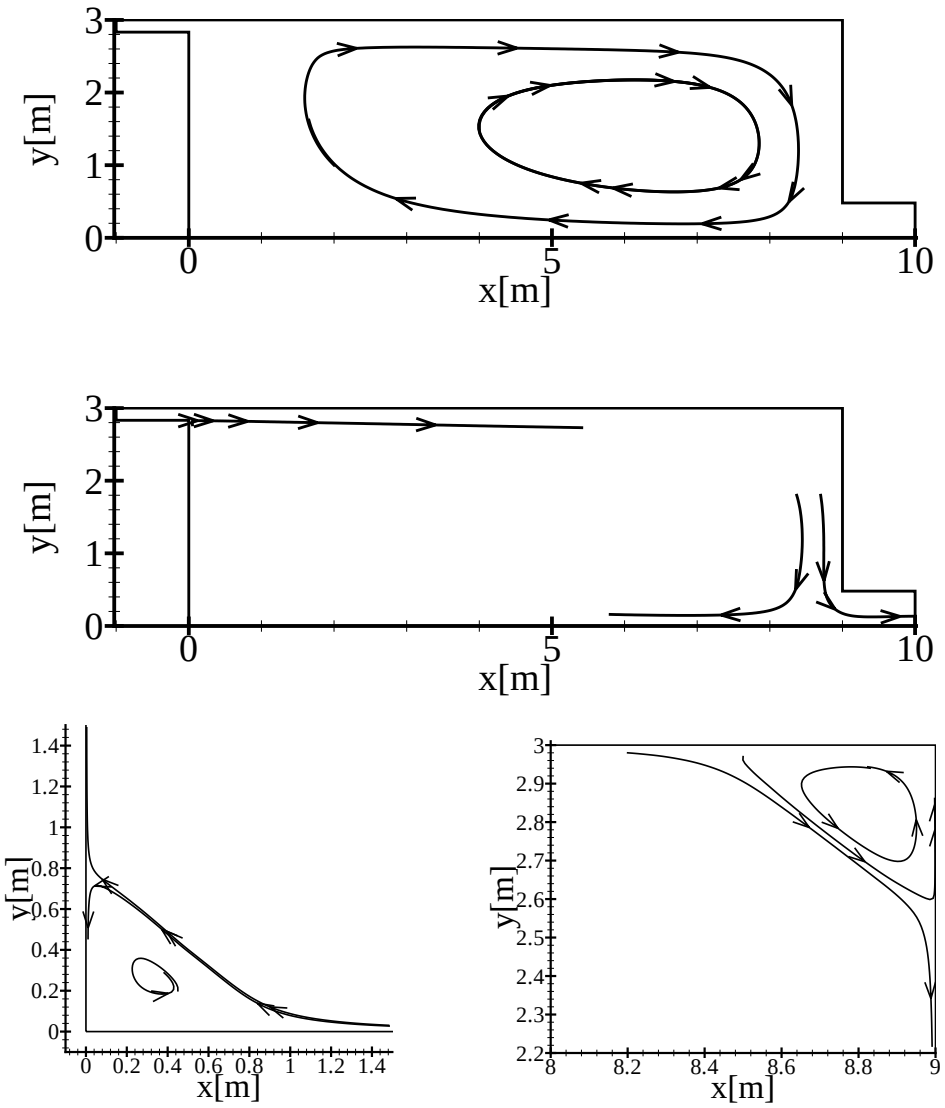

Figure 4.9: Streamlines for a three-dimensional calculation using a low Reynolds number $k-\epsilon$ model and periodic boundary conditions at the walls in the spanwise directions. The plots are from the symmetry plane, $z = 1.5\ m$.

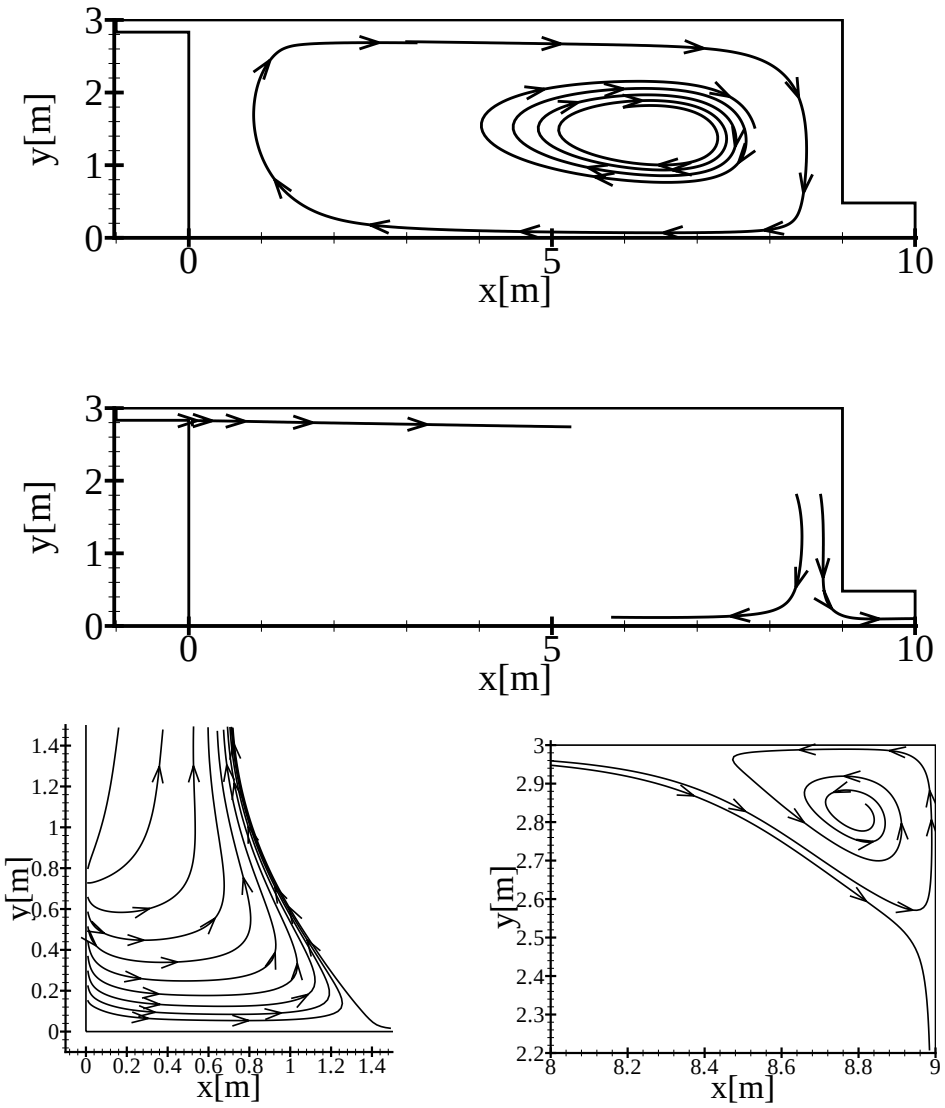

Figure 4.10: Streamlines for a three-dimensional calculation using a low Reynolds number $k-\epsilon$ model and no-slip boundary conditions at the walls in the spanwise directions. The plots are from the symmetry plane, $z = 1.5\ m$.

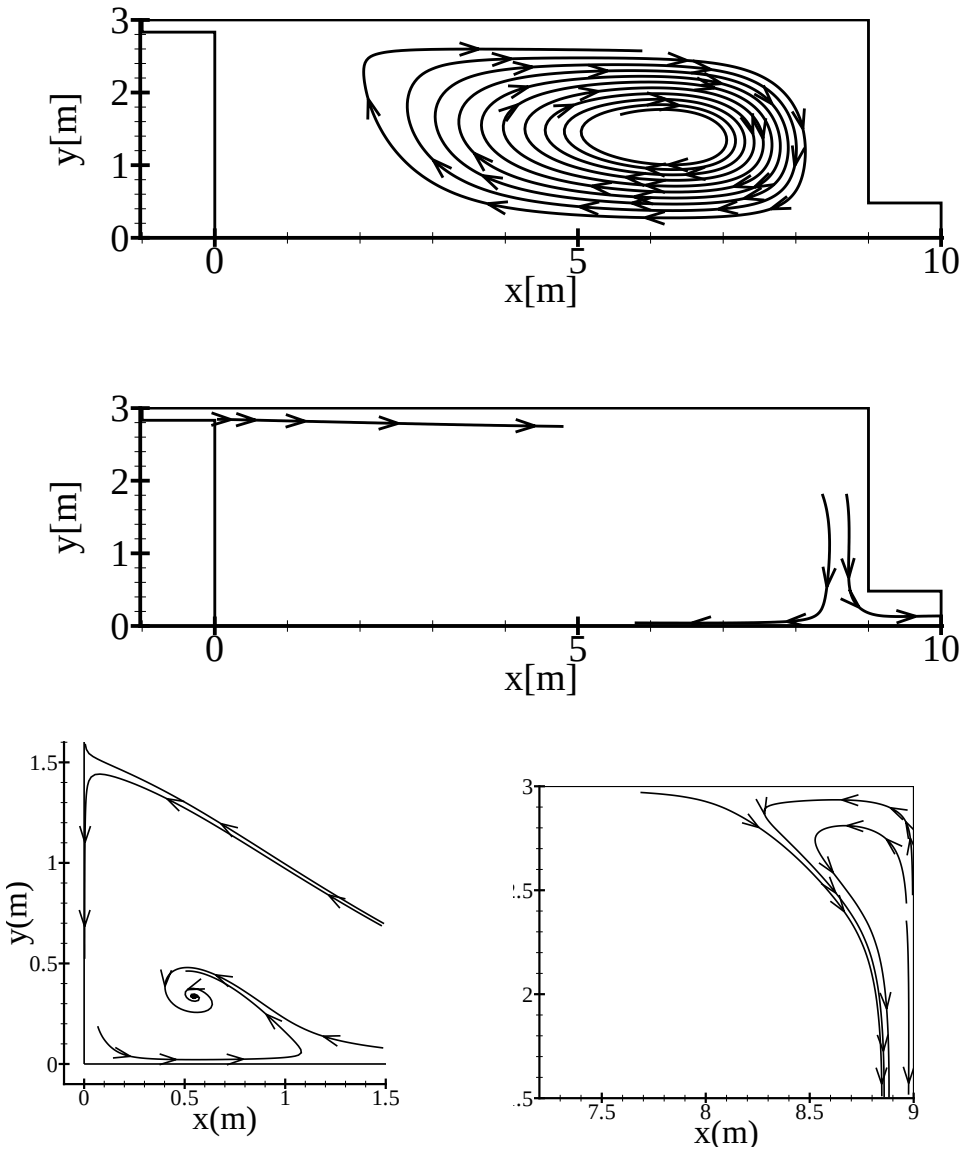

Figure 4.11: Streamlines for a three-dimensional calculation using a high Reynolds number $k-\epsilon$ model and no-slip boundary conditions at the walls in the spanwise directions. The plots are from the symmetry plane, $z = 1.5\ m$.

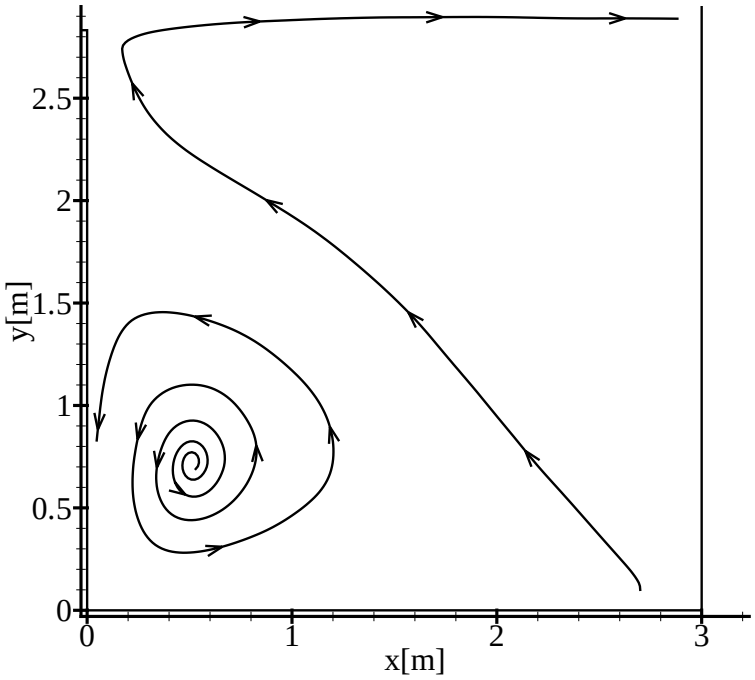

Figure 4.12: Streamlines in the symmetry plane, $z = 1.5\ m$, from PIV data, Pedersen & Meyer [88]. The region covers $0\ m \leq x \leq 3\ m$ and $0\ m \leq y \leq 3\ m$.

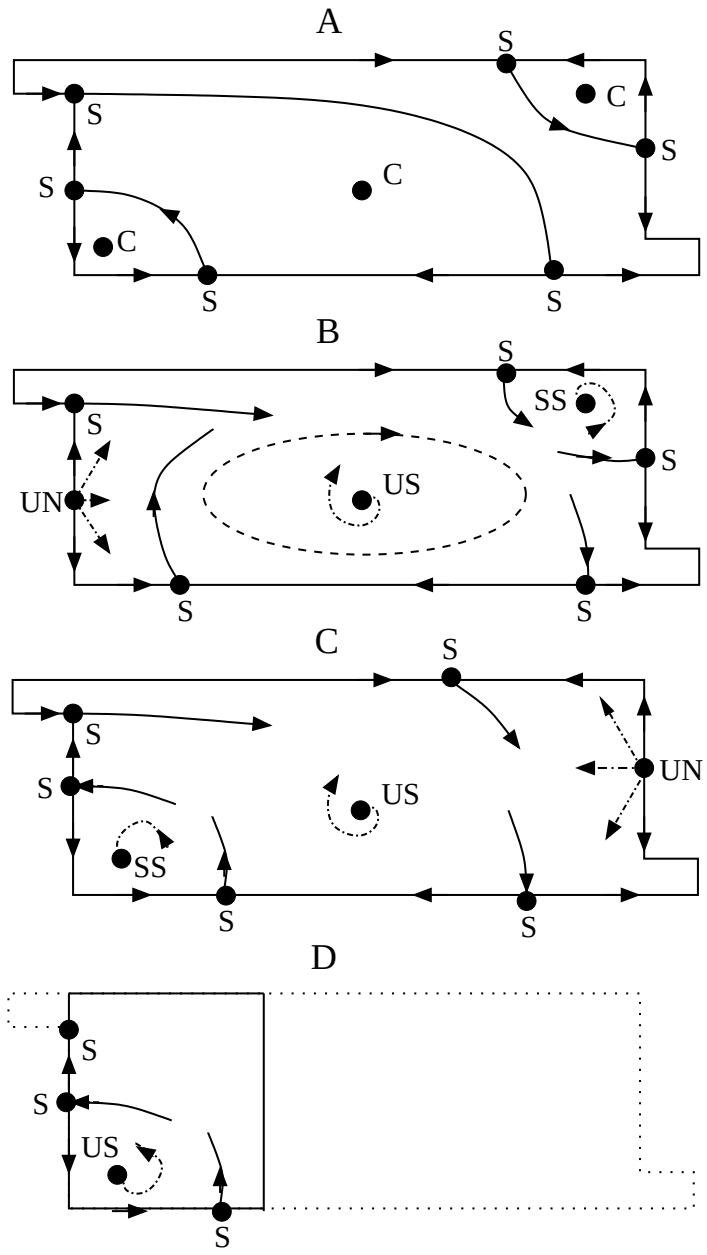

Figure 4.13: Topologies in the symmetry plane, $z = 1.5$. A: Topology for a two-dimensional calculation or a three-dimensional calculation using periodic boundary conditions in the spanwise direction. B: Topology for a three-dimensional calculation using wall boundary conditions in the spanwise direction and a low Reynolds number $k - \epsilon$ model. C: Three-dimensional calculation using wall boundary conditions in the spanwise direction and a high Reynolds number $k - \epsilon$ model. D: Measurements for $0\ m \leq x \leq 3\ m$ and $0\ m \leq y \leq 3\ m$. S : Saddle, C : Centre, SS : Stable spiral, US : Unstable spiral, UN : Unstable node. ———: Separatrices from saddles. – – – –: Limit cycle. – · – · –: Streamlines emanating or approaching spirals or nodes.

4.4 Summary

This chapter contains a thorough validation of the turbulence models, existing in the *EllipSys* code, for indoor air calculations using the 2-D annex 20 test case. Furthermore, topological aspects for three-dimensional airflows was described.

The existing low Reynolds number models were tested. It was only possible to obtain a converged solution for the $k-\epsilon$ model and the revised $k-\omega$ baseline model. In terms of the mean velocity profiles, the two tested models showed good agreement with LDA measurements by Nielsen [82].

In the light of recent PIV experiments by Pedersen & Meyer [88], it was chosen to focus on the flow pattern in the symmetry plane of the room. Two new criteria for evaluating the performance of a turbulence model is thus possible. First the ability of the turbulence model to predict the location of stagnation points can be used as a criterion. Second the ability of the turbulence model to reproduce the flow pattern near the stagnation point, i.e predict the correct type of the stagnation point, is a way of evaluating the turbulence model. Using the first new criterion, the location of the stagnation points related to the recirculation zone appearing below the inlet jet were compared for two-dimensional calculations and three-dimensional calculations using either periodic boundary conditions or wall boundary conditions in the spanwise direction. The agreement with measurements was poor. In general the discrepancies between measurements and calculations were 20-70 % for the location of the stagnation points. Only for the two-dimensional calculation using the original $k-\omega$ model the agreement was reasonable. The original $k-\omega$ model was the least dissipative of the models tested in this chapter.

The second new criterion was to classify the stagnation points. For the calculations, this was carried out for all stagnation points appearing in the symmetry plane even though experiments were only available for one third of the length. The classification of stagnation points revealed some interesting differences between the turbulence models. For the two-dimensional calculations the trajectories are closed and saddles were connected by a trajectory due to the Hamiltonian property of the stream function. Further, only centres and saddles will occur. In three-dimensional calculations the solution of the Navier-Stokes equations are no longer restricted by the Hamiltonian property. A variety of new types of stagnation points therefore exist. The very open structure of the recirculation zone occurring below the inlet is related to the fact that the stagnation point on the wall below the inlet is not a saddle but an unstable node. This was observed for the low Reynolds number $k-\epsilon$ model. For the high Reynolds number $k-\epsilon$ model the stagnation point occurring at the wall below the inlet is a saddle. Thus, the recirculation took a more closed structure. However, the centre related to the recirculation zone was stable, while this centre was observed to be unstable in the experiments. Thus, none of the calculations were able to reproduce the topology obtained from the experiments. Moreover, the calculated topologies had obvious differences.

All together it is concluded that for the three-dimensional calculations, the turbulence models in the *EllipSys* code is able to give velocity profiles in agreement with LDA measurements for the annex 20 test case. However, by comparing with recent PIV measurements for the same test case, it is obvious that a further development and validation of existing turbulence models for three-dimensional calculations are required.

Chapter 5

LES for two-dimensional channel flow

5.1 Introduction

For the development of the Large Eddy Simulation (LES) technique, the plane channel flow has been one of the most important test cases used in the past decades. This flow has been important not only for understanding and further improve the LES technique, but also for the understanding of numerous related fields, e.g Direct Numerical Simulation (DNS) and Proper Orthogonal Decompositition (POD).

In 1970 Deardorff [27] presented his LES calculation of a channel flow using a Smagorinsky SGS model and only 6720 cells. The viscous sublayer was not resolved in the calculations. This was assumed to reasonable, since the Reynolds number was large. Applying the SGS model, the accuracy of the averaged turbulence intensities were improved significantly compared to using no model. Already in this work it was emphasized that for near wall flows a SGS model that accounts for anisotropy is necessary. Later, Moin & Kim [70] presented their calculation of a channel flow using LES. Besides presentation of numerous statistics for the flow, the paper discusses the appropriate dimensions of the computational domain when using periodic boundary conditions. The component of turbulence intensity perpendicular to the wall is transferred to the component parallel to the wall. This is termed the 'impingement effect' and were described in the paper by Moin & Kim [70].

Piomelli *et al* [91] used the channel flow for evaluating combinations of filters and SGS models. It was found that the filter and the SGS model should carry the same length of information. Hence the Smagorinsky model based on only one length scale, normally the grid size, should not be coupled with the Gaussian filter where a broad range of scales contributes to the SGS velocity. The SGS modelling was further investigated by Horiutu [49] who experienced that inclusion of the SGS cross stress term improves prediction of the statistical values for the channel flow. Härtel & Kleiser [40] made a numerical study of the channel flow for different low Reynolds numbers $115 < Re_\tau < 300$. Special emphasis was put on the inverse cascade occurring in the buffer layer, $5 < y^+ < 30$, using DNS. By means of *a priori* testing it was found that this reverse energy flux, often referred to as 'backscatter', could not be

represented by any of the employed SGS models, including a dynamic model. The *a posteriori* test, i.e an actual LES simulation, showed that the impact of not representing 'backscatter' has a stronger effect on the core flow for the lower Reynolds numbers due to a stronger coupling to the near wall flow. These two flow regions would essentially be decoupled in flows with turbulence in equilibrium, i.e the turbulence is not affected by past and surrounding events. The treatment of the wall boundary condition has been discussed in several papers since this region often contains stretching of the grid. Belaras *et al* [5] suggested that LES were to be used only to the first point from the wall. Then the boundary layer equations were solved for a very fine grid between the first grid point and the wall. This approach is in some sense similar to the use of the wall law. The problem of anisotropic grids were circumvented by Zahrai *et al* [115], replacing the scalar function of grid spacings in the Smagorinsky model with a matrix. Furthermore, the use of stretched grids in the near wall region has also been treated by use of Detached-Eddy Simulation (DES), see e.g. Schu *et al* [101].

Several databases are available on DNS results for plane channel flow. The database AGARD [1] holding DNS data for several test cases was used for comparison. It should be noted that a database containing similar information for the same Reynolds numbers can be found in Moser *et al* [71].

This chapter describes a validation of the implementation of the SGS model described in chapter 2.2. Simulations with and without the use of a SGS model were carried out, referred to as LES and coarse DNS, respectively. Considering the maximum ratio of the SGS viscosity-to-kinematic viscosity, the empirical constant, C_m, involved in the mixed scale model was calibrated.

Mean velocity profiles obtained with LES and coarse DNS were compared with existing DNS data. Lower order statistics were compared with both DNS data and experiments. Profiles of the standard deviation of the three velocity components were compared with DNS. Furthermore, the ratio of the standard deviation to the velocity at the centeraxis was calculated and compared with experiments by Durst *et al.* [28].

Higher order statistics were investigated pointwise and the PDFs were obtained in these points. In a boundary layer point, $y/\delta = 0.01$, an approximate integral time scale and an estimated temporal Taylor microscale were determined.

Finally, the temporal spectra of each velocity component in the boundary layer point were obtained. The spectra for coarse DNS and LES were compared.

5.2 Test case

The computational domain for the two-dimensional channel is shown in figure 5.1 that illustrates the two parallel plates and the two homogeneous streamwise and spanwise direction. Periodic boundary conditions are used in these two directions, which is valid if the computational domain contains the largest eddies of the flow. This can normally be evaluated from a two-point correlation of an experiment, see Moin & Kim [70]. Originally it was chosen to validate the implementation of the SGS model against DNS data by Kim *et al* [54], and therefore the computational domain was chosen as

$$2\delta = 2\ m,\ L = 4\pi\delta = 12.57\ m,\ \ W = 2\pi\delta = 6.28\ m, \tag{5.1}$$

see figure 5.1.

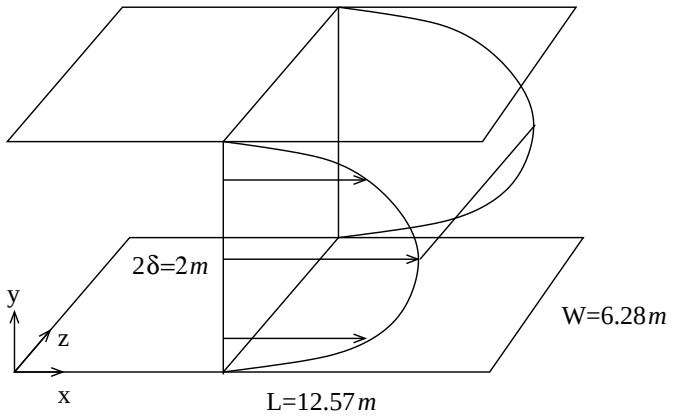

Figure 5.1: The channel used for evaluating the code for large-eddy simulation.

However, with the Re used by Kim *et al* [54] the flow became laminar in the present calculation. Using the test case in AGARD [1], the computational domain could have been reduced in the streamwise and spanwise directions. It was, however, decided to continue with the original domain despite the fact that AGARD [1] uses a computational box of $2\delta,\ L = 2\pi\delta,\ W = \pi\delta$.

The mesh used was $48 \times 64 \times 48$ cells, equally distributed in the streamwise and spanwise direction, but stretched away from the plates. The distribution of points in the vertical direction was obtained by the stretching function presented in appendix A.1, using a distance from the lower plate to the first grid point of $0.000192\ m$. The same distance was specified from the upper plate to the first grid point. A $Re_\tau = u_\tau\delta/\nu = 395$ gives $\Delta x^+ = u_\tau\Delta x/\nu \approx 103$ and $\Delta z^+ = u_\tau\Delta z/\nu \approx 51$. Further, the stretching ensures that $y^+ = 0.076$ at the first grid point and that there are 16 points within $y^+ < 10$. For reliable LES results the requirements, $\Delta x^+ < 80$, $\Delta z^+ < 30$ and at least 3 points in the sublayer $0 < y^+ < 10$, listed by Zang [116], should apply. These requirements are almost fulfilled for the present grid.

The time step was $\Delta t = 0.002\ s$, which implies a non-dimensional time step of $\Delta t^* = u_\tau \Delta t/\delta = 0.002$. This is almost twice the non-dimensional time step suggested by Vanka & Tafti [104] for their calculation of rotating channel flow. However, the time step ensures that the CFL number is below $CFL = u\Delta t/\Delta x < 0.31$ in the entire domain and the time resolution is therefore assumed to be satisfactory. Since the flow is streamwise and spanwise homogeneous, statistical averaging was carried out in these two directions.

In the calculation the desired Re_τ was obtained by specifying the mean pressure gradient. Considering the balancing of forces shown in figure 5.2 gives

$$\tau_w = -\delta \frac{\partial p}{\partial x}. \tag{5.2}$$

The mean pressure gradient

$$\frac{\partial p}{\partial x} = -1\ N/m^3. \tag{5.3}$$

was fixed, which implies

$$\tau_w = 1\ N/m^2. \tag{5.4}$$

Insertion in the definition for the wall shear velocity, $u_\tau = \sqrt{(\tau_w/\rho)}$, and fixing $\rho = 1\ kg/m^3$ yields

$$u_\tau = 1\ m/s. \tag{5.5}$$

In the specification of the test case $Re_\tau = 395$ and thus

$$\nu = \frac{u_\tau \delta}{Re_\tau} = \frac{1\ m^2/s}{395} = 2.53 \cdot 10^{-3}\ m^2/s. \tag{5.6}$$

The total force F_{tot} from the pressure drop is

$$F_{tot} = \int_V -\frac{dp}{dx} \partial V = -V, \tag{5.7}$$

where V is the volume of the computational domain.

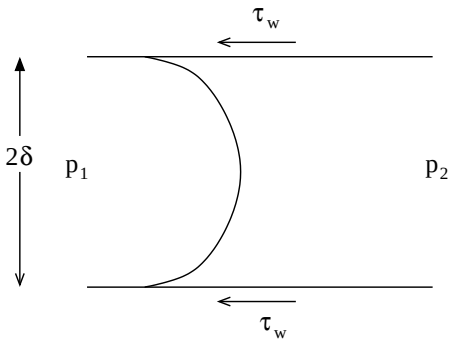

Figure 5.2: Forces to be in equilibrium when calculating the flow in a plane channel .

For the boundaries of the computational domain, periodicity is imposed in streamwise and spanwise directions, while no slip wall boundary conditions are imposed at the upper and lower plate. With this choice of boundary conditions the channel is infinitely long and wide, and the flow should therefore be invariant to the specified initial condition. However, to trigger turbulence, it was chosen to apply a random perturbation to a solution of mean fields obtained with a $k-\omega$ turbulence model and use this as initial condition.

The governing equations are solved using a time marching scheme with underrelaxation. The convective terms are discretized using central differencing scheme (CDS), and the PISO algorithm is used for the pressure correction. The time stepping was carried out using a backward Euler scheme, which is first order accurate. One subiteration was carried out in each time step. Subiterations imply that the time stepping is repeated a user specified number of times in order to get a more accurate solution of pressure field from the corrector step. The use of subiterations stabilizes the time stepping, and for some flows accurate solutions have been obtained with CFL numbers of up to 200, see Jameson [51]. Normally the time step is limited by a CFL number of one. In the present calculation subiterations were not necessary since the timestepping is numerically stable and the CFL number everywhere less than one. However, the subiterations ensures that the residual of velocities and pressure are converged to at least 10^{-2} at every time step. To rule out rounding errors occurring from convergence it is proposed to use more subiterations in future calculations. This gives a higher accuracy for the pressure distribution at every time step.

In each grid point, the velocities, pressure, SGS viscosity and the square of the velocities are summed up over every time step during the calculation. With the knowledge of the number of iterations taken in the calculation, the mean horizontal velocity component in a grid point, (x, y, z), is estimated from

$$< \overline{u}(x,y,z) >= \frac{1}{N}\sum_{i=0}^{i=N} \overline{u}(x,y,z,t_i), \tag{5.8}$$

where N is the number of iterations and $\overline{u}(x,y,z,t_i)$ is the horizontal filtered velocity component in point (x,y,z) at the time corresponding to iteration i. The standard deviation is estimated from

$$\overline{u}_{rms} = \sqrt{< \overline{u}(x,y,z)'^2 >} = \sqrt{\frac{1}{N}\sum_{i=0}^{i=N} \overline{u}(x,y,z,t_i)^2 - < \overline{u}(x,y,z) >^2}, \tag{5.9}$$

where $< \overline{u}(x,y,z) >$ is estimated from equation (5.8). The same formulas are used for estimating the mean velocity and standard deviation for the wall normal and spanwise direction. Further, the mean SGS viscosity is calculated in a way similar to equation (5.8). The flow has two homogeneous directions, the streamwise and spanwise, respectively. Thus spatial averaging was carried out in these two direction. E.g. for the horizontal component of the mean velocity this implies that

all horizontal mean velocities appearing for a constant $y-$plane is added and divided by the total number of grid points existing for that plane. The profiles shown in figures 5.3-5.6 are obtained in this way. The friction velocity, $\overline{u}_\tau$, was calculated in each time step and approximated from $\overline{u}_\tau =< \sqrt{\nu \overline{u}_1/\Delta y} >$, where $\overline{u}_1$ is velocity in the the first cell center from the wall and Δy is the distance to the first cell center from the wall. The friction velocity is only evaluated close to the lower wall, and was averaged over the streamwise and spanwise direction. When the friction velocity had stabilized near 1 m/s, which implies a $Re_\tau \approx 395$, the averaging of velocities was initiated. From the above mentioned temporal and spatial average of the streamwise velocity component, a one-dimensional velocity profile is obtained. Integration over this profile determines the mean velocity, $\overline{u}_m$, of the channel flow. The time average of friction velocity was, $< \overline{u}_\tau >= 0.99\ m/s$, for the LES calculation, while the time average of the mean velocity was $< \overline{u}_m >= 20.3\ m/s$.

5.3 Results and discussion

Particular attention is given to quantities that justify a correct implementation of the SGS model. Further, statistical results, which are assumed to be relevant for future LES calculations of indoor airflows, are presented.

First, the constant, C_m, involved in the mixed scale model was calibrated against results obtained with similar SGS models. It was found that using a value of 0.02 resulted in a maximum peak value of the SGS viscosity-to-kinematic viscosity of $< \nu_{sgs} > /\nu = 1.4$. In Byskov [15] this ratio was reported to be approximately one. Thus, the value of C_m was decreased to 0.01, and the maximum value of $< \nu_{sgs} > /\nu$ reduced to approximately 0.85, see figure 5.3. This value was assumed to be satisfactory for the present calculations. From the ratio of the SGS viscosity-to-kinematic viscosity it is found that the grid is fine for a LES, since reliable results can be obtained for larger ratios of $< \nu_{sgs} > /\nu$, see Davidson *et al* [25].

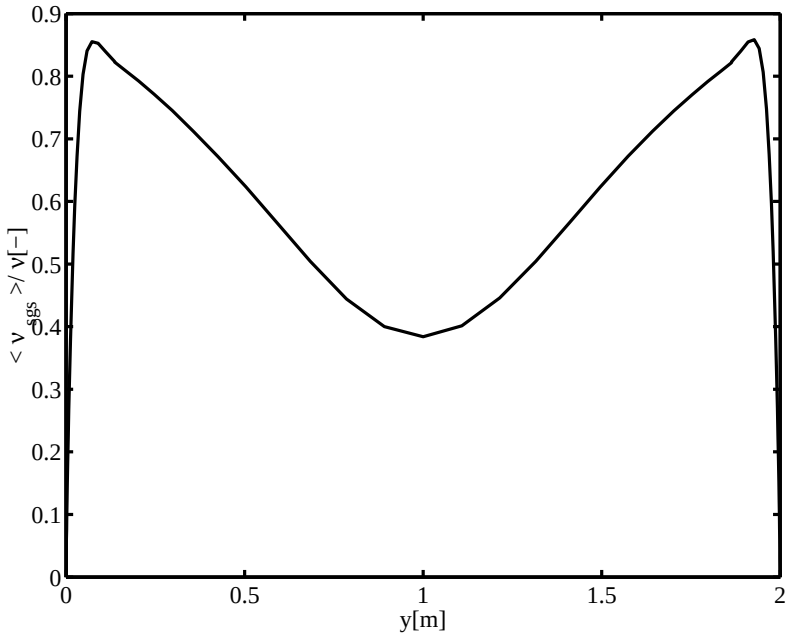

Figure 5.3: Ratio between SGS viscosity and kinematic viscosity.

Comparing mean velocity profiles, see figure 5.4, a clear discrepancy between LES and coarse DNS is observed. Modelling the SGSs in the LES improves the agreement with unfiltered DNS data, especially in the core flow. The LES model therefore leads to a more correct value of the center velocity, which was also observed by Byskov [15]. Considering the same quantity in the near wall region, see figure 5.5, it is found that both the LES and coarse DNS closely follow the DNS profile in the viscous sublayer for $y^+ < 2$. This was expected since u_τ are identical in all three cases. For larger y^+, coarse DNS tends to overpredict and LES tends to underpredict the velocity obtained by DNS. At y^+ larger than 20 both coarse DNS and LES overpredicts the velocity obtained by DNS, and hence also the velocity predicted by the log-law is overestimated. It therefore seems as if the implemented SGS model leads to excessive damping in the region $1 < y^+ < 20$. In the studies by Zahrai *et al* [115], an increased spanwise resolution in LES was found to improve the agreement with velocity profiles obtained by DNS.

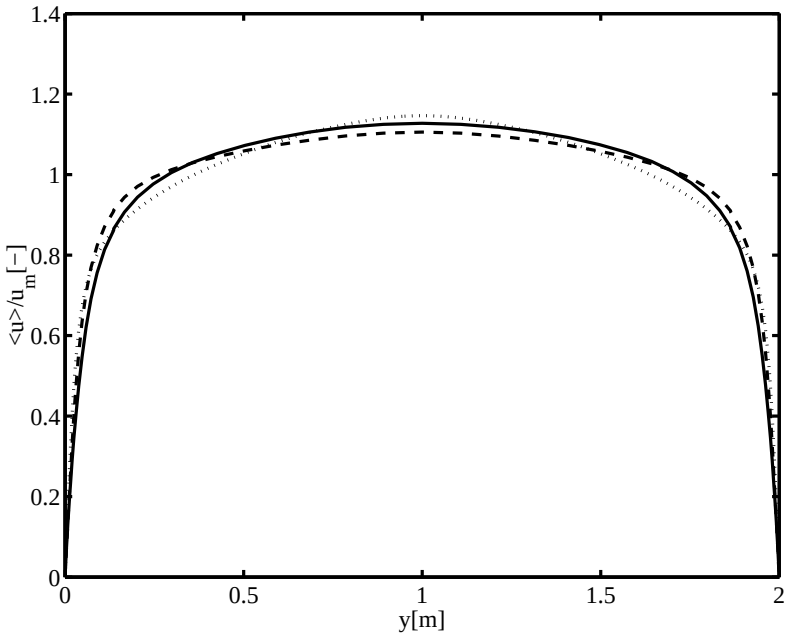

Figure 5.4: Averaged mean velocity profiles.———: LES. · · · · ··: DNS. – – – –: Coarse DNS

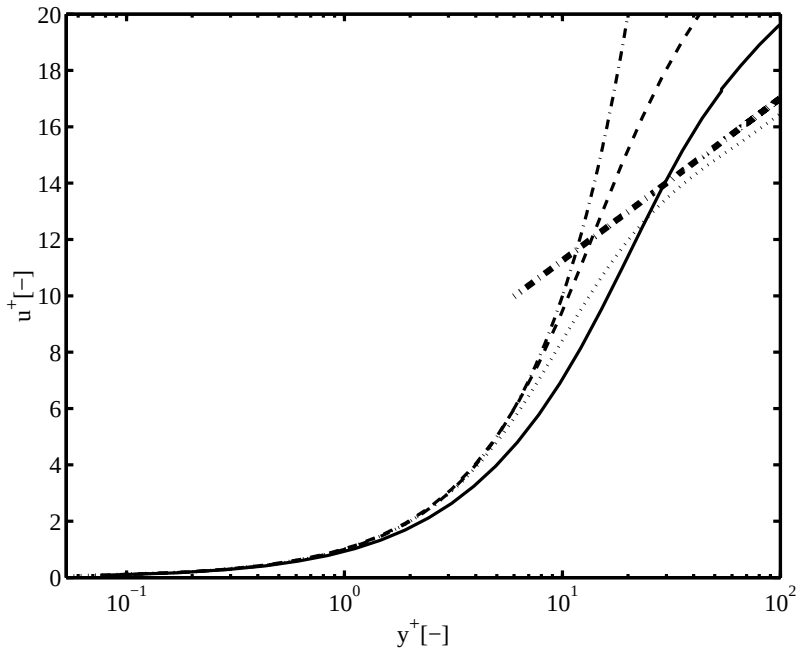

Figure 5.5: Averaged mean velocity profiles in the near wall region. ———: LES. · · · · ··: DNS. – – – –: Coarse DNS. –·–·–·–: $u^+ = y^+$. –·–·–·– (heavy):$u^+ = 2.5\ln(y^+) + 5.5$.

The observations concerning the friction velocity and the mean velocity are quantified in table 5.1. It was found that Re_τ for LES and coarse DNS deviates less

than 1 % from the fixed $Re_\tau = 395$. This is slightly better than the discrepancies of the order of 3 % obtained by Byskov [15]. However, the deviation of Re_m for DNS and coarse DNS was 33 %, which diminishes to 17 % using LES. This agrees well with the above findings of an improved prediction of the core flow velocity, when modelling the SGSs. Comparing the ratio of the centerline velocity and the mean flow velocity, $< u_c > / < u_m >$, the deviation from DNS was 2 % and 3 % for coarse DNS and LES respectively. This order of magnitude was also reported by Byskov [15]. The good agreement for Re_τ and the poor agreement for Re_m can be explained by the used pressure gradient. This was fixed to get the correct friction velocity. An alternative way of applying the pressure gradient would be to correct this in every time step to fix the mean velocity. This would lead to a prediction of Re_m, which is in better agreement with DNS, but the prediction of Re_τ is expected to be less accurate.

Calculation	Re_τ	Re_m	$< u_c > / < u_m >$
DNS	395	6873	1.15
Coarse DNS	396	9125	1.11
LES	391	8019	1.13

Table 5.1: Comparison of Reynolds numbers and velocities for calculations of channel flow. $Re_\tau = \delta < u_\tau > /\nu$. $Re_m = \delta < u_m > /\nu$.

In figure 5.6 the lower order statistics, i.e. the standard deviation, of the three velocities are compared with DNS data. The appearance of the standard deviation profiles obtained using LES is in reasonable agreement with the curves obtained by DNS. The mutual location of the curves for v_{rms} and w_{rms} are correct, in the sense that the peak of v_{rms} has a smaller value than w_{rms}. This indicates that the spanwise velocity is more fluctuating than the velocity in the wall normal direction. Further, the curves for v_{rms} and w_{rms} obtained with LES have peak values lower than the curves based on DNS, while the peak value of u_{rms} is larger than DNS. These results are to some extent substantiated by the findings of Zahrai *et al* [115]. Their LES results showed similar mutual location of the standard deviation profiles for $Re_\tau = 180$. The fact that the peak value of u_{rms} from the LES was in excess of the DNS peak was ascribed to a Reynolds number effect. In the studies of Zahrai *et al* [115] the discrepancy of the profiles for the standard deviation obtained with LES and DNS diminished as the spanwise grid resolution was increased. It should be mentioned that in the calculation by Byskov [15] the mixed scale models tended to underpredict the turbulent kinetic energy, which disagrees with the present findings. Since the spanwise resolution for the present calculation is similar to the resolution used by Byskov [15] it is believed that the discrepancy is attributed to the maximum value of the SGS viscosity-to-kinematic viscosity found to be 1 in Byskov [15] and 0.85 in the present computations. It should be mentioned that the calculation of the SGS kinetic energy was based on the strain rate in the studies by Byskov [15], while it is based on vorticity in the present computations.

Finally it is found that the peak value of u_{rms} using LES is located at $y^+ \approx 30$, whereas DNS give $y^+ \approx 14$. This discrepancy was also found for the mixed scale models used by Byskov [15], and it relates to the differences also found in the velocity distribution.

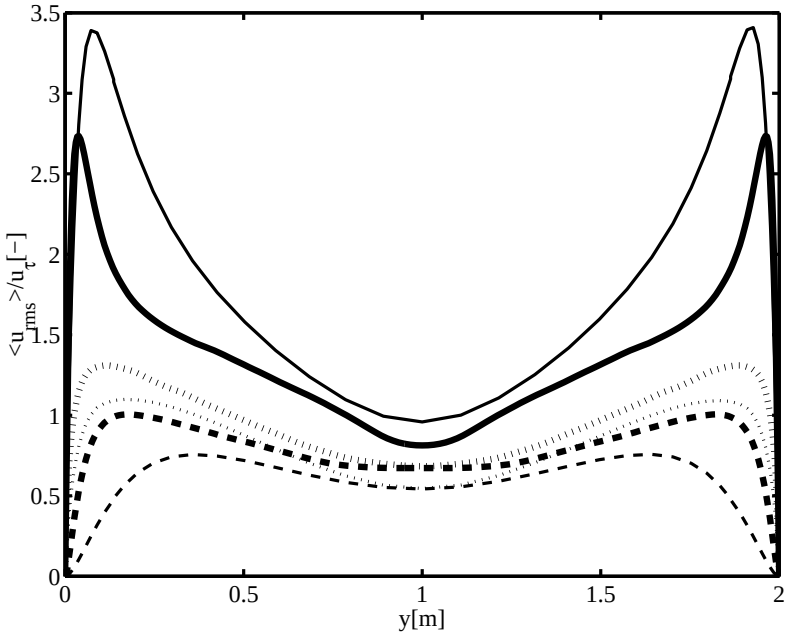

Figure 5.6: Standard deviation of velocity fluctuations from LES normalized by friction velocity. ——: u. – – – – : v · · · · · : w. Heavy lines are DNS results.

The standard deviation can be compared with experiments. Durst *et al.* [28] observed that the ratio of the standard deviation and the velocity at the centeraxis scales with the Reynolds number. They obtained the empirical relation

$$\frac{< u_{c,rms} >}{< u_c >} \approx 0.13 Re_c^{-\frac{1}{8}}, \tag{5.10}$$

where $< u_{c,rms} >$ is the time averaged standard deviation, $< u_c >$ is the mean velocity and $Re_c = \delta < u_c > /\nu$, evaluated at a point on the centeraxis. Insertion of data from the present LES calculation, using a time series of the velocities taken at a point close to the centerline, yields

$$\frac{< \overline{u}_{c,rms} >}{< \overline{u}_c >} = 0.0455, \tag{5.11}$$

while (5.10) gives

$$0.13 \left(\frac{\delta < \overline{u}_c >}{\nu} \right)^{-\frac{1}{8}} = 0.0416.$$

The difference between these results is less than 10 %, which is within the accuracy of the measurements.

The evoluation of the third and fourth order moments, normally referred to as skewness, S, and kurtosis (flatness), K, were only carried out at two distinct points despite that profiles of the former are available in the DNS database. It was chosen to consider two monitor points, a point close to the wall, $(x_w, y_w, z_w) = (3.36\ m, 0.01\ m, 1.66\ m)$, and a point close to the centerline $(x_c, y_c, z_c) = (10.83\ m, 1.11\ m, 1.66\ m)$. The time history of streamwise velocity component $\overline{u}_w$ is shown in figure 5.7. The four central moments of the time history of the three velocity components at the two monitor points are listed in table 5.2.

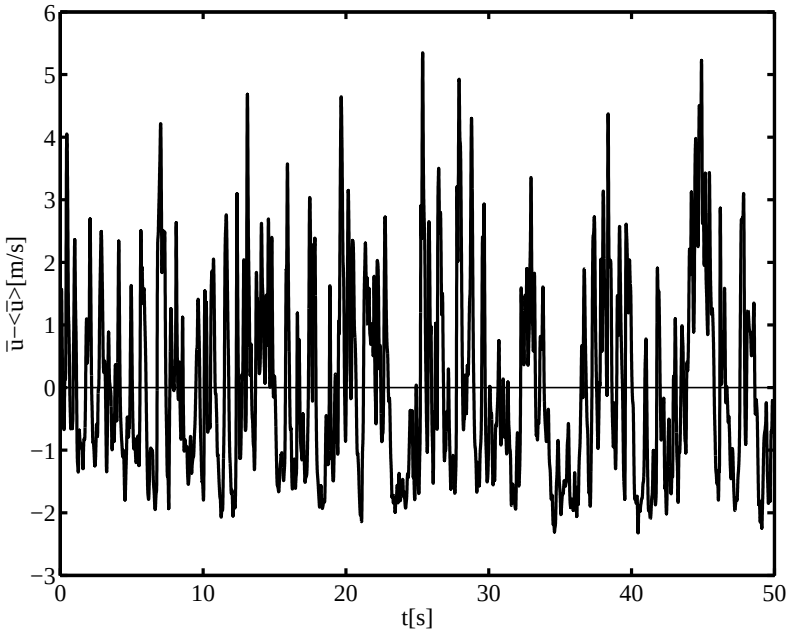

Figure 5.7: Time history of $\overline{u}_w - < \overline{u}_w >$ velocity at point $(x_w, y_w, z_w) = (3.36\ m, 0.01\ m, 1.66\ m)$, which is located in the boundary layer, $y^+ = 3.95$. Velocity components at this point are denoted $(\overline{u}_w, \overline{v}_w, \overline{w}_w)$ for streamwise, wall normal and spanwise direction, respectively

Velocity	Mean $[m/s]$	Standard deviation$[m/s]$	Skewness [-]	Kurtosis [-]
$\overline{u}_w$	4.3797	1.5005	0.7793	2.959
$\overline{v}_w$	$-3.8296 \cdot 10^{-4}$	0.0196	0.2135	3.9938
$\overline{w}_w$	-0.0015	0.4870	0.0858	3.7415
$\overline{u}_c$	22.6338	1.0444	0.0575	3.0554
$\overline{v}_c$	0.0632	0.5091	0.0234	3.4666
$\overline{w}_c$	-0.0577	0.5530	0.2715	3.1189

Table 5.2: Central moments for channel flow. Subscript w refers to the point located near the wall and subscript c refers to the point located close to the centeraxis

Table 5.2 shows that except for the streamwise direction the mean values are close

to zero. The mean value of the spanwise component was expected to be zero due to the zero pressure gradient in this direction, while the mean value of the wall normal component should be zero since the mean flow is parallel. The skewness, S, and kurtosis, K, factors are used for evaluating if the turbulence is isotropic, in which case the two quantities attain the values $S = 0$ and $K = 3$, see Durst *et al*, [28]. From table 5.2 the skewness and kurtosis is in the correct order of magnitude. To investigate the isotropy further, the Probability Density Functions (PDFs) are shown in figures 5.8-5.10. For isotropy the PDFs should be Gaussian.

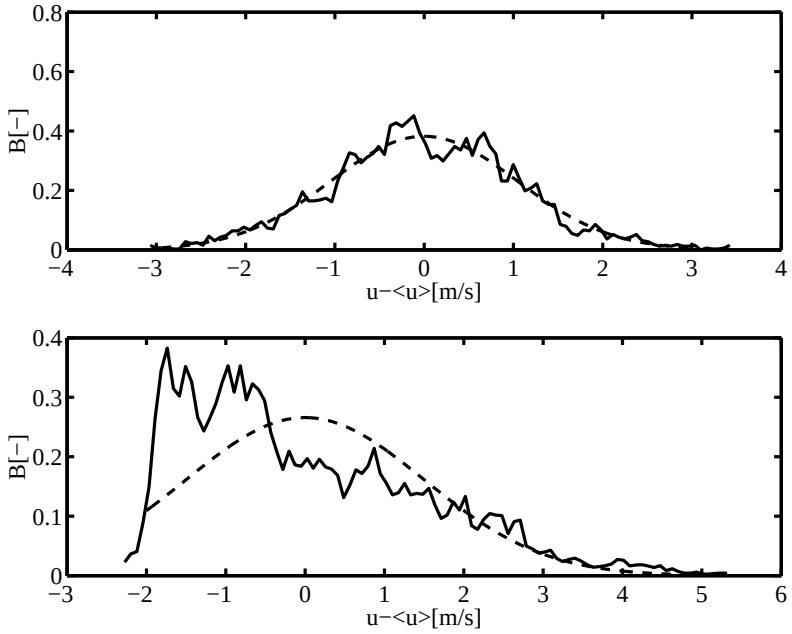

Figure 5.8: PDF for $\overline{u} - < \overline{u} >$ velocity fluctuations. ——: PDF based on LES data, $- - - -$: Gaussian distribution based on mean value and the standard deviation for the time series used to generate the PDF. Lower: PDF based on a time series from a point located in the boundary layer, $y^+ = 3.95$. Upper: PDF based on a time series from a point located near the center of the channel, $y^+ = 352$.

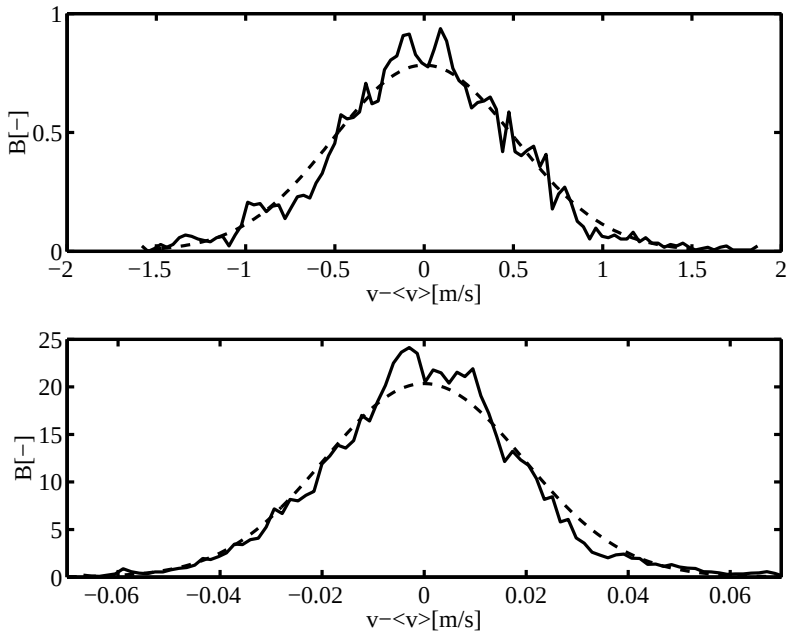

Figure 5.9: PDF for $\overline{v} - < \overline{v} >$ velocity fluctuations. Interpretation of lines, see figure 5.8. Lower: PDF for a point located in the boundary layer, $y^+ = 3.95$. Upper: PDF for a point located near the center of the channel, $y^+ = 352$.

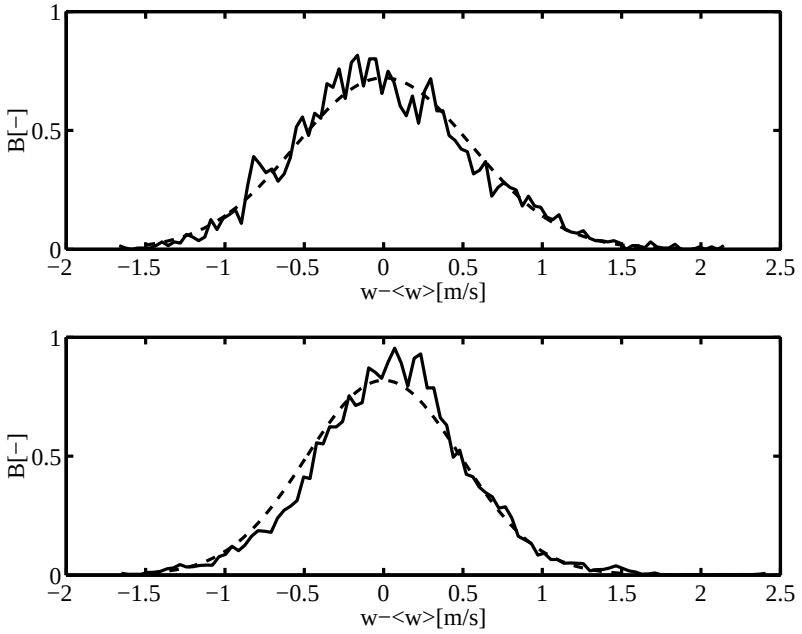

Figure 5.10: PDF for $\overline{w} - < \overline{w} >$ velocity fluctuations. Interpretation of lines, see figure 5.8. Lower: PDF for a point located in the boundary layer, $y^+ = 3.95$. Upper: PDF for a point located near the center of the channel, $y^+ = 352$.

The comparison of the PDF for the streamwise velocity component and a Gaussian distribution with the same mean value and standard deviation, see figure 5.8, coincides very well for the point located close to the center of the flow. On the other hand, the PDF for the point located in the boundary layer shows significant skewness. This high positive skewness, is also found in table 5.2. Further, a high positive skewness indicates a tendency of the time series to have more frequent large positive peaks than negative peaks. Figure 5.7 shows an example of a time series with large positive skewness. For the wall normal direction, see figure 5.9, the agreement with the Gaussian distribution is reasonable for both the point located close to the center and for the point located close to the wall. Finally, the agreement between the PDF and the Gaussian distribution is found to be reasonable for the spanwise velocity component in both the center of the flow and in the boundary layer, see figure 5.10. Thus, it is only for the streamwise component of the velocity in the boundary layer that the PDF does not have the shape of the Gaussian distribution.

To evaluate if the time period of averaging used to obtain the mean values and higher order statistics was appropriate, the autocorrelation for the streamwise velocity component in the boundary layer was calculated, see figure 5.11. The figure shows the autocorrelation coefficient ρ versus time difference $\tau = t' - t$. The first intersection point with zero is used to define the integral time scale, $\mathcal{T}_u$, found to be approximately 1.1 s for the present time series. This quantity gives a measure of the interval over which the velocity is correlated with itself. The averaging was carried out over 50 s, and therefore approximately 45 uncorrelated samples were used. The theoretical relative error estimates for the point located in the boundary layer is

$$\frac{s_w(<\overline{u}_w>)}{<\overline{u}_w>} = \frac{\sqrt{<\overline{u}_w'^2>}}{<\overline{u}_w>\sqrt{N}} = \frac{1.5}{4.38\sqrt{45}} = 5\% \tag{5.13}$$

and

$$\frac{s_w(<\overline{u}_w'^2>)}{<\overline{u}_w'^2>} = \frac{<\overline{u}_w'^2>}{<\overline{u}_w'^2>}\sqrt{\frac{2}{N}} = \frac{2.25}{2.25}\sqrt{\frac{2}{45}} = 21\% \tag{5.14}$$

for the mean velocity, $<\overline{u}_w>$, and standard deviation, $<\overline{u}_w'^2>$, respectively. For the wall normal direction and the spanwise direction, the relative error on the mean velocity will be several thousands percent due to the low mean velocities in these directions. For the point located close to the center axis, the theoretical relative error estimates are very similar those obtained in the boundary layer.

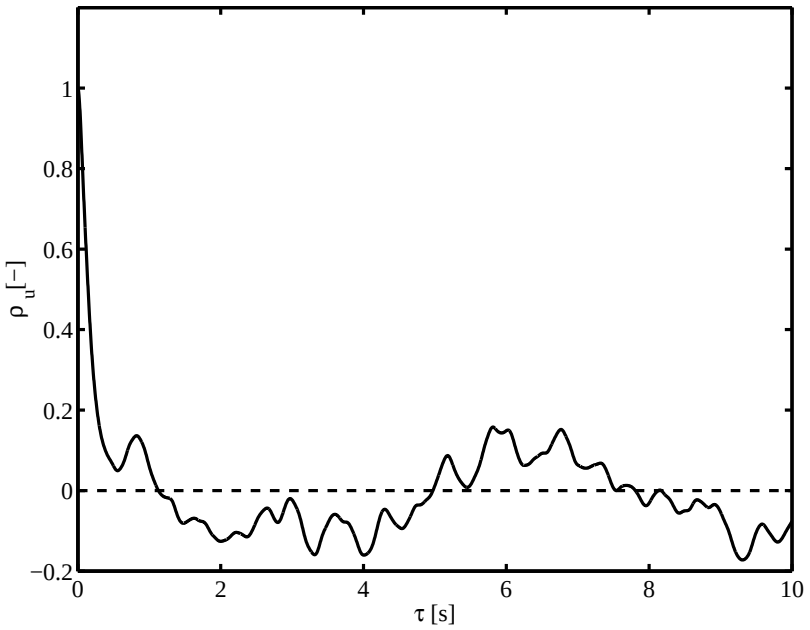

Figure 5.11: Autocorrelation for the streamwise velocity in the point $(x, y, z) = (3.36\ m, 0.01\ m, 1.66\ m)$. The figure indicates an integral time scale of $\mathcal{T}_u = 1.13\ s$.

The autocorrelation coefficient is defined as

$$\rho(\tau) \equiv \frac{< u'(t)u'(t-\tau) >}{< u'^2 >}, \tag{5.15}$$

see Tennekes & Lumley [105]. Further, the temporal Taylor microscale, λ, is defined as the curvature of the autocorrelation coefficient at the origin

$$\left.\frac{d^2\rho}{d\tau^2}\right|_{\tau=0} \equiv -\frac{2}{\lambda^2}. \tag{5.16}$$

From equation (5.15) and equation (5.16) it is possible to derive the relation

$$\left\langle \left(\frac{du'}{dt}\right)^2 \right\rangle = \frac{< 2u'^2 >}{\lambda^2}, \tag{5.17}$$

see Tennekes & Lumley [105]. Using the time series of the streamwise velocity component of the point located in the boundary layer, the temporal Taylor micro scale thus becomes

$$\lambda = 0.12\ s \tag{5.18}$$

This is approximately a factor 10 less than the integral time scale of 1.1 s.

The integral time scale gives a measure of time within which the velocity is correlated with itself, while the temporal Taylor microscale gives a measure of the time scale

related to the smallest scales. From Tennekes and Lumley [105] an estimate of the spatial Taylor microscale is

$$\lambda = l\left(\frac{15}{A}\right)^{1/2} Re_l^{-1/2} = \delta\left(\frac{15}{A}\right)^{1/2}\left(\frac{\delta < u_{rms} >}{\nu}\right)^{-1/2} \approx 0.32\ m, \tag{5.19}$$

where l is a length scale chosen to be δ, A is of the order one and the velocity scale is approximated with $< u_{rms} >= \sqrt{< u_w'^2 >}$ found in table 5.2. The spatial Taylor microscale, which gives a measure of the size of the smallest eddies, is of the same order as the cell size, which is 0.27 m based on 48 grid points equally distributed over $L = 12.57\ m$. The Kolmogorov micro scale is estimated from

$$\eta = \lambda\left(\frac{225}{A}\right)^{-1/4} Re_l^{-1/4} = 0.32\left(\frac{225}{1}\right)^{-1/4} 592^{-1/2} \approx 0.0034\ m, \tag{5.20}$$

see Tennekes & Lumley, [105].

Finally the time spectra for the time series taken in the boundary layer is shown in figure 5.12. Since the point is fixed the obtained time spectra are Eulerian, and hence the the energy decay at the inertial subrange $E(\omega)$ is proportional to $\omega^{-\frac{5}{3}}$. The time spectrum can be understood from the cascade concept, described in Tennekes & Lumley [105], if large wavenumbers correspond to high frequencies. From figure 5.12 it is observed that the highest energy content is found for the streamwise direction, and the lowest energy content was found in the wall normal direction. Considering figure 5.6, this was expected since the streamwise direction has the largest fluctuations and the wall normal direction has the smallest fluctuations. The energy content was generally found to cover from 3 to 6 decades, while the frequency covers approximately 4 decades. An inertial subrange was found to be between 1 and 10, but the width of this range varies with the velocity component. The time spectra for LES and coarse DNS showed very similar behaviour. This is probably due to the fine grid resolution, which diminishes the effect of modelling the SGSs.

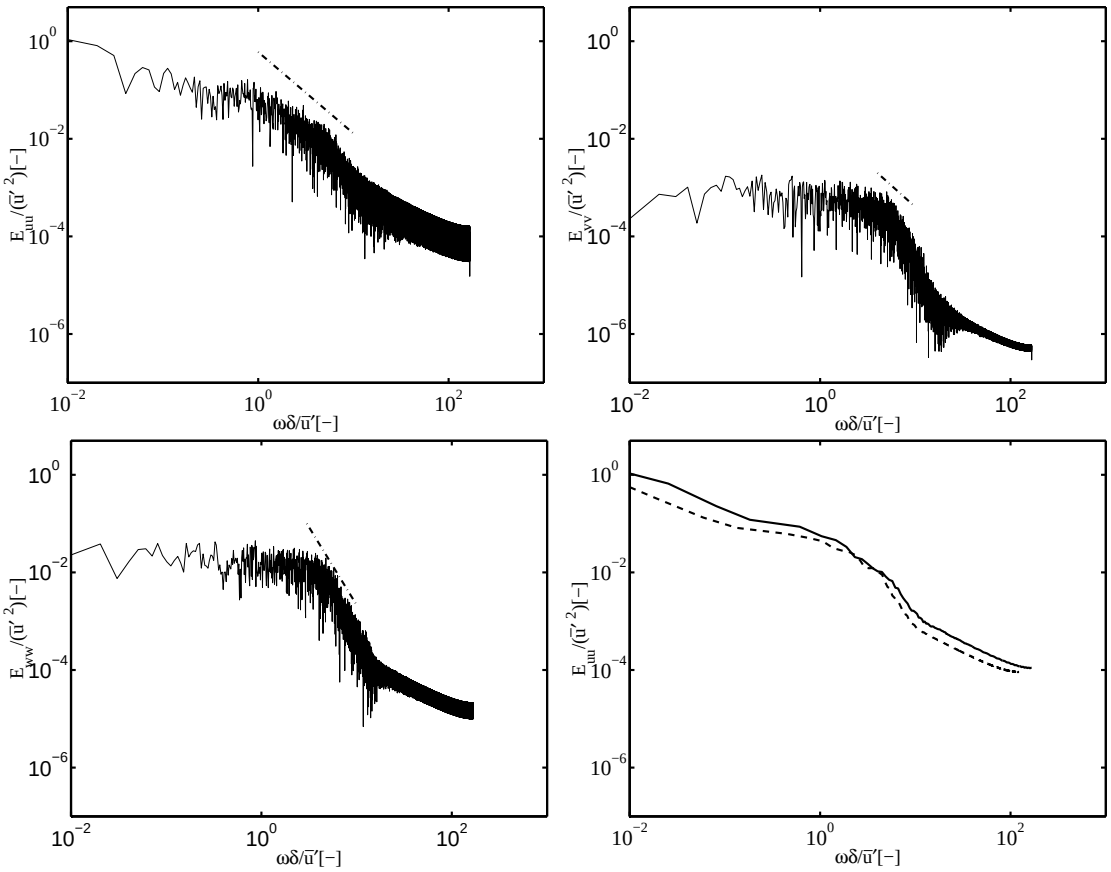

Figure 5.12: The Eulerian time spectrum of turbulence based on a time series for the point located in the boundary layer, $y^+ = 3.95$. ——: LES, – – – – : Coarse DNS, $-\cdot-\cdot-\cdot$:$E(\omega) \propto \omega^{-\frac{5}{3}}$.

5.4 Summary

The present chapter contains a validation of the implementation of the SGS model described in chapter 2.2. First and foremost the empirical constant, C_m, involved in the mixed scale model was calibrated against computations with a similar model. Using $C_m = 0.02$ a maximum ratio of the SGS viscosity-to-kinematic viscosity of approximately 1.4 was obtained, while decreasing the value to 0.01 led to a maximum ratio of the SGS viscosity-to-kinematic viscosity of approximately 0.85. It was chosen to use the latter value, since earlier presented results showed that the ratio of the SGS viscosity-to-kinematic viscosity should be approximately 1.

Comparing the mean velocity profile obtained by LES and coarse DNS with an existing DNS profile showed that the LES represented the DNS profiles better than the coarse DNS profile. This was of course expected. Focusing on the behaviour of the mean profiles close to the wall shows that the mean profile obtained with the implemented SGS model overpredicts the wall law when y^+ exceeds 30. Similar

results have been reported elsewhere. This discrepancy was amplified when using coarse DNS. The LES underpredicted the mean velocity in the region $1 < y^+ < 20$. This behaviour has been reported elsewhere. A comparison of the three simulations, i.e. LES, coarse DNS and existing DNS, showed that the Re_τ agreed within 1 %, which is satisfactory. The deviation of the Re_m is significantly larger since the volume force was imposed to fix Re_τ. The discrepancy from DNS data was reduced from 33 % to 17 % using LES instead of coarse DNS, which agreed with previous findings of an improved mean velocity profiles using LES instead of coarse DNS. Comparing the ratio of the centerline velocity to the mean velocity, the deviation from DNS was 2% and 3% for LES and coarse DNS, respectively. The LES results were compared with experimental data, which showed that the ratio of the standard deviation to the velocity at the centerline, scaled with the Reynolds number based on the centerline velocity. Insertion of LES data in the empirical relation found by Durst *et al* [28], yielded a difference of less than 10 % which was within the accuracy of the experiments.

The lower order statistics, i.e the standard deviation, of the velocity fluctuations for LES were compared with DNS. The best agreement was found near the centerline of the flow, while the SGS model dampens the fluctuations in the boundary layer. This was observed for the wall normal direction and the spanwise direction, while the streamwise component showed the opposite. Physically, this ambiguity was not quite clear.

To elucidate the isotropy behaviour of the flow, the higher order statistics, skewness and kurtosis, were determined. These quantities were calculated for a point in the boundary layer and a point close to the centerline, respectively. It was chosen to consider the three velocity components and compare the values with the PDFs. Values for skewness were found to be between 0.0234 and 0.7793, while values of kurtosis were between 2.959 and 3.9938. The PDFs were Gaussian distributed except for the streamwise velocity component in the boundry layer.

For the time series of the streamwise component of the velocity in the boundary layer an integral time scale of approximately 1.1 s was found. This value was a factor of 10 larger than the estimated temporal Taylor microscale of 0.12 s. The integral time scale gives a measure of time within which the velocity is correlated with itself, while the temporal Taylor microscale gives a measure of the time scale related to the smallest scales. The spatial Taylor microscale, which gives a measure of the size of the smallest eddies was estimated to 0.32 m.

Finally, the Eulerian time spectra of the three velocity components of the point in the boundary layer were considered. The energy spectra were found to cover 3 to 6 decades and the inertial subrange existed for frequencies between 1 and 10. The streamwise direction was the most energetic, while the lowest energy content was found for the wall normal direction. This coincides well with the mutual location of the profiles for the standard deviation. The energy spectrum from LES was

compared with the energy spectrum from coarse DNS. These spectra were very similar, which is probably due to the fine grid resolution used.

It is concluded that the implementation of the SGS model is correct in the sense, that the calculation of the flow in a plane channel is in good agreement with DNS and experiments.

Chapter 6

LES of the airflow in the annex 20 case

6.1 Introduction

With increasing computer power the LES method is becoming a realistic alternative to the RANS method, which has most often been used in indoor air movement. Still the experience with LES is limited, though some results have been published.

Davidson [23], used the LES method for the annex 20 2-D test case. Different SGS models were tested. He concluded that a dynamic approach were preferable, since the Smagorinsky SGS model, requires time consuming calibration of the involved constant. The mean velocity profiles showed some dependency of the grid resolution, while they were rather unaffected by the averaging period. Further, results for the same test case were presented by Davidson & Nielsen [24], using both a Smagorinsky SGS model and a dynamic SGS model. In terms of the mean velocity profiles the Smagorinsky SGS model was found to depend strongly on the choice of constant, while the dynamic SGS model performed well without calibration of a constant. Moreover, PDFs for two points near the floor and two points in the jet were shown. The PDFs indicated the existence of a well defined horizontal mean velocity in the jet, while no well defined mean velocity existed close to the floor. This is interesting because regions without a well defined mean velocity are known to cause problems for the two-equation turbulence models, see Davidson & Nielsen, [24]. Finally Davidson & Nielsen [24] presented a time spectrum from the wall jet indicating an inertial subrange close to 0.2, which agrees with experimental findings by Sandberg [96]. Bennetsen [8] tested a mixed scale SGS model with promising result. The results were similar to those obtained by Davidson & Nielsen [24]. Finally, Emmerich & McGrattan [29] have presented LES results for the annex 20 2-D test case. They reported, that the averaged values of the flow quantities, for an averaging period of 100 s, were affected by the averaging period. However, averaging longer than 500 s was sufficient for obtaining results which were unaffected by the averaging period. The averaged results showed some dependency on the grid size. It was concluded, that the Smagorinsky SGS model leads to trustworthy predictions of indoor airflows.

In terms of mean velocities for the annex 20 2-D test case it is generally accepted that LES performs worse than the RANS approach. This fact is substantiated in the present study. However, for flows with low Reynolds numbers, LES is the best alternative. Davidson *et al* [25] investigated a flow with low Reynolds number using an unsteady laminar approach, RANS and LES. They concluded, that only LES provided results in agreement with measurements. In ventilated rooms low Reynolds number effects will often occur, see Davidson *et al* [25].

An important advantage of LES is that information on the statistical properties of the flow is provided with this method. This is a valuable information, since the turbulent characteristics of the flow is known to have a significant impact on human sensation of draught, see Fanger *et al* [34]. Their investigations of turbulence intensities ranging from 12% to above 55%, showed that the discomfort due to draught increased with increasing turbulence intensity.

In this chapter the LES approach using a mixed scale SGS model was conducted for the annex 20 2-D test case. Mean velocity and turbulent kinetic energy was calculated and compared with results obtained with the RANS approach using the low Reynolds number $k-\epsilon$ model. Further, the modelled viscosities and isovelocities for LES and RANS were evaluated. The results were in agreement with previous findings. For seven points in the occupied zone, the time spectra based on LES were compared with time spectra obtained from measurements by Melikov, [63].

6.2 Test case

The test case is the 2-D annex 20 geometry. The dimensions and a sketch of the geometry can be found in chapter 4, see figure 4.1. To reduce the amount of grid points, periodic boundary conditions were employed in the spanwise direction. Two different grids were employed, a coarse grid of $72 \times 48 \times 36$ and a fine grid of $96 \times 64 \times 48$. The grid points were equally distributed in the spanwise direction, and stretched towards the walls appearing in the remaining directions. For the fine grid, the grid layout in a plane with constant z can be found in appendix A.1. To minimize grid effects, the comparison of averaged quantities were carried out with results obtained using the fine grid. In order to use a maximum length of the time series, the coarse grid was used for generation of the time spectra. An evaluation of grid effects and the averaging period can be found in appendix G.

Previously, see chapter 4, it was found that periodic boundaries in the spanwise direction generates the two-dimensional flow field in each cross section of constant z using RANS. In contrary to RANS, the LES calculation will lead to a fully three-dimensional flow field. To ensure that the flow field is three-dimensional in the entire domain, a random perturbation needs to be superimposed at the inlet boundary. Therefore, for the LES calculations, the inlet boundary conditions, $\overline{u}_0$, $\overline{v}_0$ and $\overline{w}_0$,

were specified in the following way

$$\overline{u}_{in} = U_0 + random \cdot u'_{exp}, \quad \overline{v}_{in} = random \cdot u'_{exp}, \quad \overline{w}_{in} = random \cdot u'_{exp},$$

where U_0 is the velocity specified in order to get $Re_h = 5000$ (air exchange rate $n = 10\ h^{-1}$) , $0 \leq random \leq 1$ is a random function called at three different times for $\overline{u}_{in}$, $\overline{v}_{in}$ and $\overline{w}_{in}$, respectively. This ensures uncorrelated fluctuations. Finally, $u'_{exp} = Tu \cdot U_0 = 0.04 \cdot 0.455\ m/s = 0.0182\ m/s$ is the magnitude of velocity fluctuations in the inlet. Tu is the turbulence intensity measured in the inlet, see Nielsen [82]. The velocities with the superimposed fluctuations were scaled to ensure the correct mass flux. As initial condition for the LES calculations, a RANS solution with a small perturbation superimposed was used.

6.3 Results and discussion

6.3.1 Comparison of RANS and LES

To provide a better insight into the differences between RANS and LES, a thorough comparison of the two methods was carried out. The RANS model used was the low Reynolds number $k - \epsilon$ model, see appendix D, and the SGS model used was the mixed scale model by Loc *et al* [60] see chapter 2.2. Mean velocity profiles for measurements, RANS and LES at two values of x in the center plane, $z = 1.5\ m$, is shown in figure 6.1. For $x = 3\ m$, figure 6.1(left) the velocity in the jet is slightly overpredicted by RANS, while LES underpredicts the velocity in this region. For $y = 2.5\ m$ the opposite is observed, RANS shows velocities lower than measurements, while LES takes higher values. For y lower than $2\ m$ the accordance between RANS and measurements is very good, while LES underpredicts the velocity for $0.2\ m < y < 1.5\ m$. In contrary to RANS and measurements, the velocities based on LES are positive very close to floor. The latter might be an effect from the grid. Davidson & Nielsen [24] carried out LES for the same flow using the Smagorinsky SGS model using two different model constants, 0.14 and 0.18, respectively. The velocity profile obtained with the present LES model, is very similar to the profile obtained by Davidson & Nielsen [24] using the Smagorinsky SGS model with model constant 0.14. The only significant difference is, that for $y \approx 2.5\ m$ velocities are overpredicted with the present model, while it was underpredicted in the results presented by Davidson & Nielsen [24]. Their results improved when the model constant was increased to 0.18. For this reason it seems reasonable, that increasing the model constant in the present SGS model would improve the LES results. However, due to computer limitations, these calculations were not done.

For $x = 6\ m$, figure 6.1(right), the accordance between measurements and RANS is very good in the jet, while the velocities are underpredicted by LES. Further, the maximum velocity in the jet using LES is located lower than the maximum for RANS. For $0.5\ m < y < 2.5\ m$, RANS and LES show velocities lower than measurements, however, lowest for LES. Close to the floor, LES and RANS are in good

agreement with measurements. Comparing with the LES results obtained by Davidson & Nielsen [24] the profile agrees well with their results for the Smagorinsky SGS model using the model constant of 0.14. Their results for $x = 6\ m$ improved when the model constant was increased to 0.18. This substantiates that an increase of the constant in the present model would improve the agreement between LES and measurements.

RANS, LES and measurements are compared for two horizontal velocity profiles appearing in the center plane, $z = 1.5\ m$, see figure 6.2. For the velocity profile $y = 2.916\ m$, 6.2(upper), LES underpredicts the velocities for almost all values of x, while the agreement between RANS and measurements is good. Thus, the velocity in the jet decays too fast in LES. For the measurements the velocity changes from positive to negative at $x \approx 8.4\ m$, while for LES the velocity changes sign at a lower value $x \approx 7.7\ m$. This indicates that the size of the recirculation appearing in the upper right corner is overpredicted by LES. It is believed, that an increase of the model constant in the present model would probably lead to an improved agreement between LES and measurements.

For $y = 0.084\ m$, figure 6.2(lower), the agreement between RANS, LES and measurements is rather good for $x < 4\ m$. For $x > 4$ the agreement between RANS and measurement is good, while the agreement between LES and measurements is not. One explanation could be that for $x < 4\ m$ the flow is almost laminar, and the influence of the SGS model therefore small compared to more turbulent regions of the flow. At $x = 4\ m$ LES predicts a steep drop in the velocity. A similar trend was observed for the $k - \omega$ models tested in chapter 3 and chapter 4. The good agreement between LES, RANS and measurements found close to the floor for $x = 6\ m$, figure 6.1(right), does not seem to be general for the flow in this region. From figure 6.2(lower) it is clear, that to the left of this value LES underpredicts the measured velocity, while to the right the velocities are overpredicted.

In figure 6.3 and 6.4, rms profiles of the horizontal velocity component for RANS, LES and measurements are compared. The definition of rms values for LES and measurements are identical, $\sqrt{< u'^2 >}/U_0$, while for RANS the values are estimated from the turbulent kinetic energy according to the relations presented in chapter 3, equation (3.12). RANS and LES represents the shape of the measured vertical profiles of rms well, see figure 6.3. For $x = 3\ m$, the results obtained with RANS agree with measurements in the jet and in the central part of the flow, see figure 6.3(left). For the remaining values of y, the measured rms values are underpredicted. For $x = 6\ m$, figure 6.3(right), the agreement between RANS and measurements is good in the central part of the flow only, while RANS underpredicts the rms values for the remaining $y-$values. The discrepancies between LES and measurements is more contradictory. For $x = 3\ m$ and y above approximately $1.5\ m$, figure 6.3(left), the rms values are overestimated by LES. For y below $1.5\ m$ the accordance between LES and measurements has improved. Close to $y = 2.832\ m$ and $y = 0.48\ m$ an undesirable local extremum of the LES profiles exists. This stems from the internal

stretching of the grid. This is stretched towards $y = 2.832\ m$ and $y = 0.48\ m$ in order to resolve the boundary layers appearing at the lower wall of the inlet and the upper wall of the outlet. Close to these lines the value of the SGS viscosity decreases compared to the adjacent cells located above and below, see figure 6.5(lower). This diminishes the effect of the SGS model, since the smallest scales are represented better than for larger cells at higher and lower values of y. For $x = 6\ m$, figure 6.3(right), LES tends to underestimate the rms values, except in the regions close to $y = 0.48\ m$ and $y = 2.832\ m$. This indicates, that an improved SGS model or a finer grid would result in a better accordance between measurements and LES.

For $y = 2.916\ m$, figure 6.4(upper), it was observed, that LES overestimates the rms-values in the initial part of the jet (x less than $4\ m$), This might be due to the grid, the used SGS model or some effect of the chosen inlet boundary conditions exists. If the problem is caused by the latter, it could be circumvented by using a fully developed channel flow as inlet condition alternatively to superimposing random fluctuations. For $4\ m < x < 6\ m$ the agreement between LES and measurements is relatively good. For $x > 6\ m$, the rms profile based on LES shows a behaviour similar to experiments, except that the peak is located close to $x \approx 6.5\ m$ for LES and $x \approx 8.5\ m$ for measurements. A possible explanation is that the size of the recirculation zone is overestimated by LES, and the location of the peak therefore located at a too low value of x. Changing the model constant would probably improve the SGS model, and the size of the recirculation zone in the upper right corner be diminished. The effect might be that the peak predicted by LES is displaced to a higher value of x. Close to the floor at $y = 0.084\ m$, see figure 6.4(lower), LES generally underpredicts the rms values.

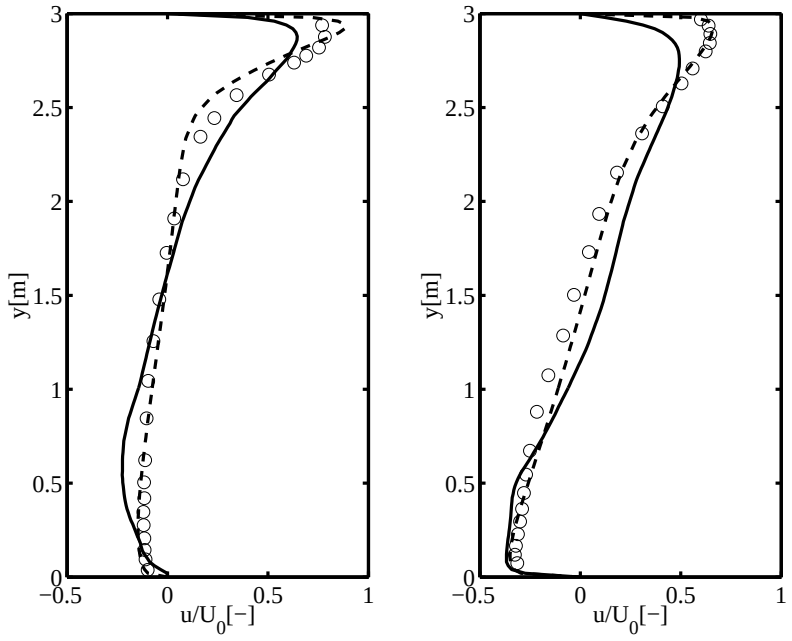

Figure 6.1: Velocity profiles of horizontal velocity component. ——–: LES. – – – – : RANS. o: Measurements by Nielsen [82]. Left: $x = 3\ m$. Right: $x = 6\ m$.

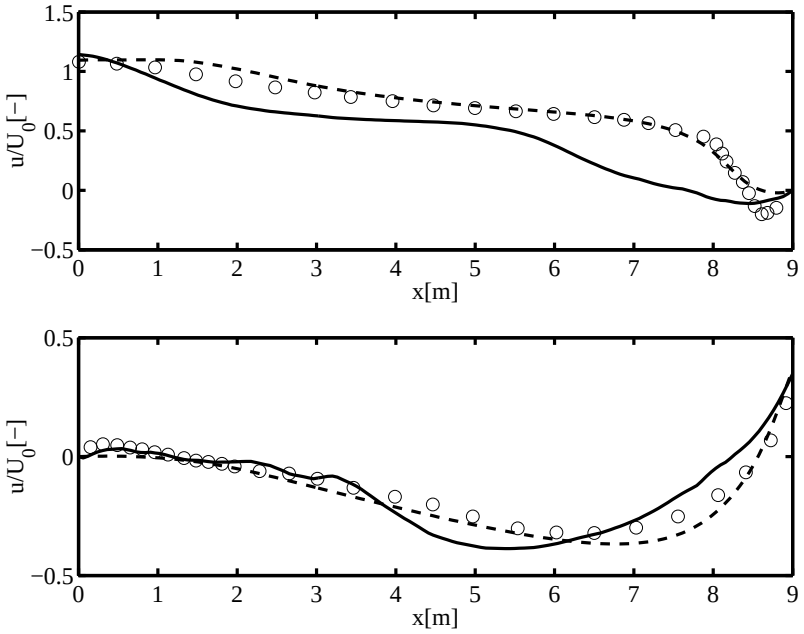

Figure 6.2: Velocity profiles of horizontal velocity component. ——–: LES. – – – – : RANS. o: Measurements by Nielsen [82]. Lower: $y = 0.084$. Top: $y = 2.916\ m$.

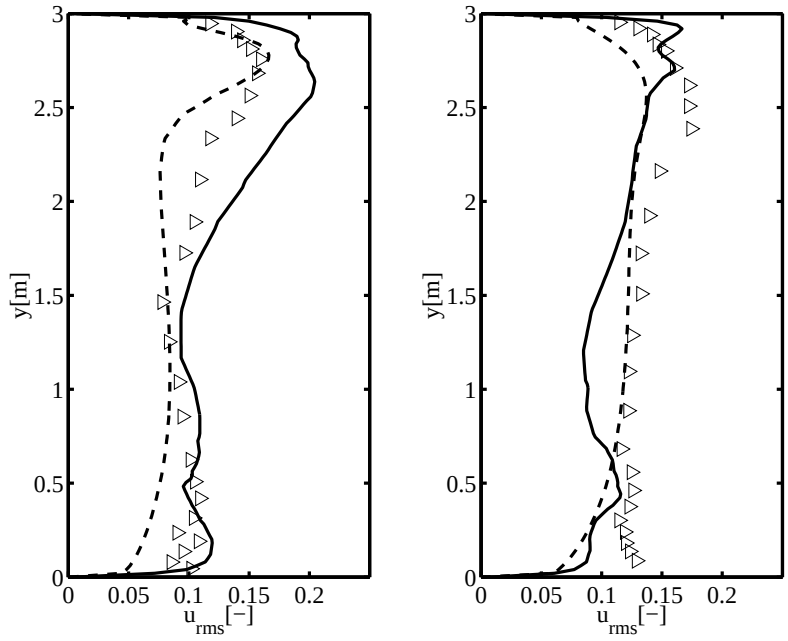

Figure 6.3: Standard deviation of horizontal velocity component. ——: LES. – – – – : RANS. ▷: Measurements by Nielsen [82]. Left: $x = 3\ m$. Right: $x = 6\ m$.

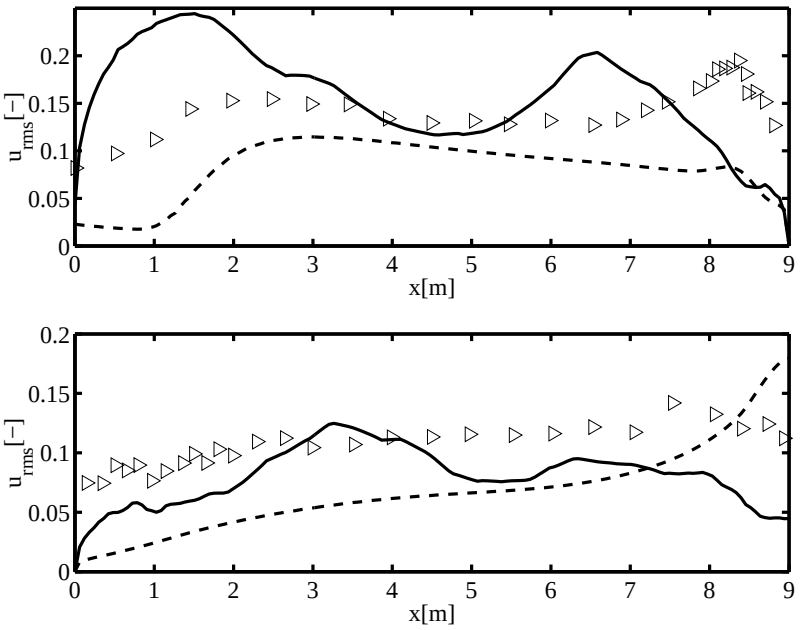

Figure 6.4: Standard deviation of the horizontal velocity component. ——: LES. – – – – : RANS. ▷: Measurements by Nielsen [82]. Lower: $y = 0.084\ m$. Top: $y = 2.916\ m$.

To shed further light on the differences between LES and RANS, the ratio of the modelled viscosities to the kinematic viscosity is shown in figure 6.5. Figure 6.5(upper) shows the ratio of the eddy viscosity to the kinematic viscosity predicted by the RANS model, while figure 6.5(lower) shows the same quantity obtained by LES. The latter is based on a time average of the modelled viscosity. For the RANS model, the modelled viscosity takes values of approximately 800 times the kinematic viscosity, while the modelled viscosity for LES takes maximum values of only 8 times the kinematic viscosity. The reason is that in LES only a narrow range of scales are modelled, while in RANS a much larger region of scales are modelled. With the used SGS model, the modelled viscosity for the LES calculation is related to the grid size. This effect is in particular obvious when comparing with the grid shown in figure 6.5(middle). The grid is stretched towards the walls and the modelled viscosity decreases. This is desirable, since the need for wall damping functions is then rendered superfluous. However, the grid was stretched towards the line $y = 0.48\ m$ and $y = 2.832\ m$. This leads to an undesirable behaviour of the rms profiles, see figure 6.3, because the value of the modelled viscosities changes dramatic in the interior of the domain. Local stretching of the grid away from walls should therefore be avoided if possible. On the other hand, RANS is unaffected by interior stretched grid lines, and the modelled viscosity only goes to zero close to the walls. This is only determined by the damping functions appearing in the RANS models.

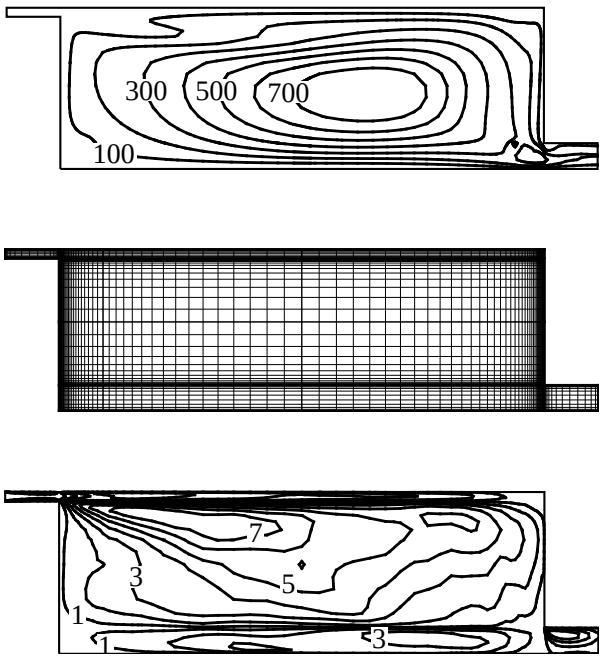

Figure 6.5: Comparison of the ratio of the modelled viscosity to the kinematic viscosity. Top: RANS. Contours are [100;200;300;400;500;600;700]. Middle: Computational grid. Lower: LES. Contours are [1;2;3;4;5;6;7]. All plots are from the center plane, $z = 1.5\ m$.

The three-dimensionality of the flow is illustrated in figure 6.6. From this figure RANS, figure 6.6(upper), indicates a smooth uniform isovelocity. Contrasting this, an instant isovelocity plot for LES, figure 6.6(lower), indicates a clear three-dimensional behaviour.

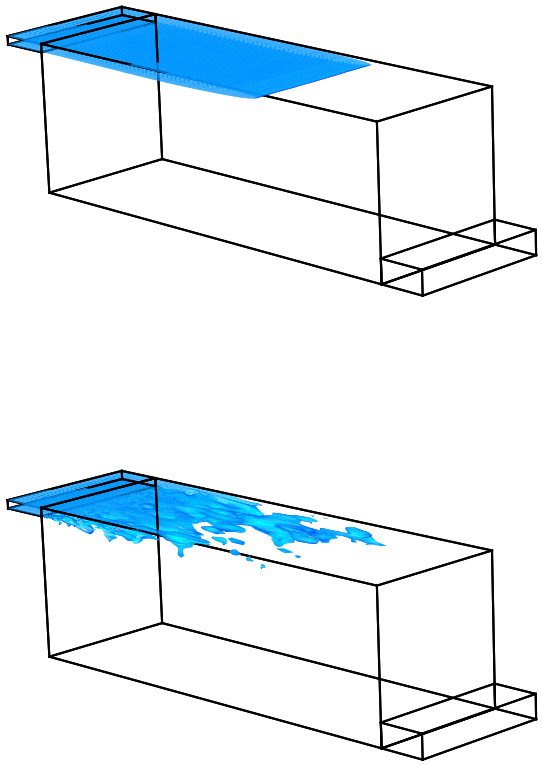

Figure 6.6: Upper: Isovelocity, $U = 0.3\ m/s$, using the RANS method. The smooth surface is constant in time. Lower: Instantaneous isovelocity $\overline{u} = 0.3\ m/s$ using LES. The isovelocity changes in every timestep.

6.3.2 Time spectra for room airflow

In Melikov [63], measurements in several empty and furnished spaces were presented. One of these took the dimensions length $L_e = 7\ m$, height $H_e = 2.8\ m$ and the width was $W_e = 4.4\ m$, see figure 6.7.

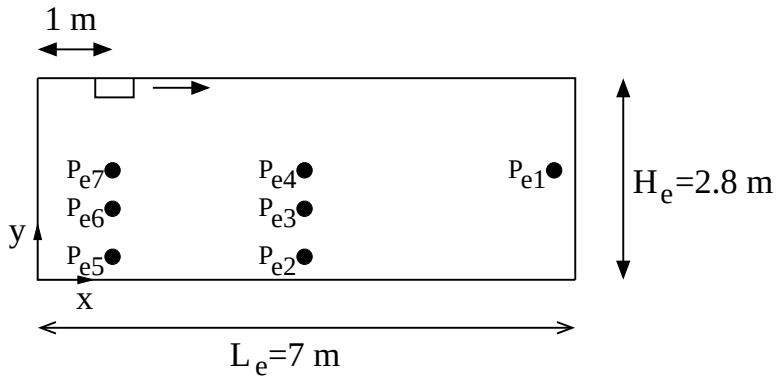

Figure 6.7: Geometry used in the experiments carried out by Melikov, [63]. The width of the room was $W_e = 4.4\ m$, and the figure shows the plane $z = 2.2\ m$.

Thus, the dimensions are very similar to the dimensions of the annex 20 2-D test case. Measurements are available for an air exchange rate of 10 h^{-1}. Despite that the geometry is not exactly the same as the annex 20 2-D case, see figure 6.8, the test case was the best available for comparing time spectra.

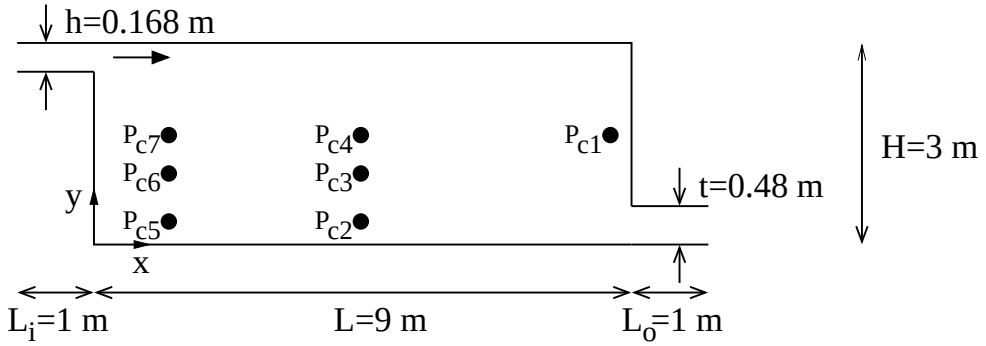

Figure 6.8: Geometry of the used in the calculations. The width of the room was $W = 3\ m$, and the figure shows the plane $z = 1.5\ m$.

For the measurements, all points are located in the center plane and the non-dimensionalized coordinates are determined as specified in table 6.1. Using the dimensionless distances found in table 6.1, the monitor points used in the calculation are found as specified in table 6.2.

Point nr.	$x[-]$	$y[-]$	$z[-]$
P_{e1}	$(L_e - 0.1)/H_e = 2.46$	$1.7/H_e = 0.61$	$(W_e/2)/W_e = 0.5$
P_{e2}	$(L_e/2)/L_e = 0.5$	$0.1/H_e = 0.04$	$(W_e/2)/W_e = 0.5$
P_{e3}	$(L_e/2)/L_e = 0.5$	$1.1/H_e = 0.39$	$(W_e/2)/W_e = 0.5$
P_{e4}	$(L_e/2)/L_e = 0.5$	$1.7/H_e = 0.61$	$(W_e/2)/W_e = 0.5$
P_{e5}	$1.0/H_e = 0.36$	$0.1/H_e = 0.04$	$(W_e/2)/W_e = 0.5$
P_{e6}	$1.0/H_e = 0.36$	$1.1/H_e = 0.39$	$(W_e/2)/W_e = 0.5$
P_{e7}	$1.0/H_e = 0.36$	$1.7/H_e = 0.61$	$(W_e/2)/W_e = 0.5$

Table 6.1: Monitor points where measured time series of the three velocity components are available, see Melikov [63] and figure 6.7.

Point nr.	$x[m]$	$y[m]$	$z[m]$
P_{c1}	$L - 2.46H = 7.39$	$0.61 \cdot 3 = 1.82$	$W/2 = 1.5$
P_{c2}	$L/2 = 4.50$	$0.04 \cdot 3 = 0.11$	$W/2 = 1.5$
P_{c3}	$L/2 = 4.50$	$0.39 \cdot 3 = 1.18$	$W/2 = 1.5$
P_{c4}	$L/2 = 4.50$	$0.61 \cdot 3 = 1.82$	$W/2 = 1.5$
P_{c5}	$0.36 \cdot 3 = 1.07$	$0.04 \cdot 3 = 0.11$	$W/2 = 1.5$
P_{c6}	$0.36 \cdot 3 = 1.07$	$0.39 \cdot 3 = 1.18$	$W/2 = 1.5$
P_{c7}	$0.36 \cdot 3 = 1.07$	$0.61 \cdot 3 = 1.82$	$W/2 = 1.5$

Table 6.2: Monitor points where computational time series of the three velocity components are stored, see figure 6.8.

The time spectra for the horizontal velocity component obtained by measurement and LES were compared, see figure 6.9-6.12. For the large scales, i.e. scales with a wave number of approximately 50 m^{-1}, the accordance between measurements and LES is good. At higher wave number, the discrepancy between measurements and LES increases with increasing wave number. A wave number of 50 m^{-1} corresponds to a length scale of $2\pi/(50m^{-1}) \approx 0.125\ m$. The grid in the x direction consisted of 72 points distributed over 9 m and thus, the filter size is of the order $9/72 = 0.125\ m$. A wave number of approximate 50 m^{-1} is therefore related to the filter size, and discrepancies between computations and measurements for wave numbers above 50 m^{-1} is probably caused by the SGS model.

For wavenumbers larger than 50 m^{-1}, the deviation between measurements and calculations increases gradually. One explanation could be that the SGS kinetic energy is calculated from the filter and a test filter, see equation (2.27). Therefore the scales closest to the filter size are represented best in the model. This explains why the agreement for the SGS wave numbers is best close to the resolved scales, and the discrepancy grows for increasing wave number. In order to bring the LES results in better agreement with measurements the grid should be refined or the SGS model improved.

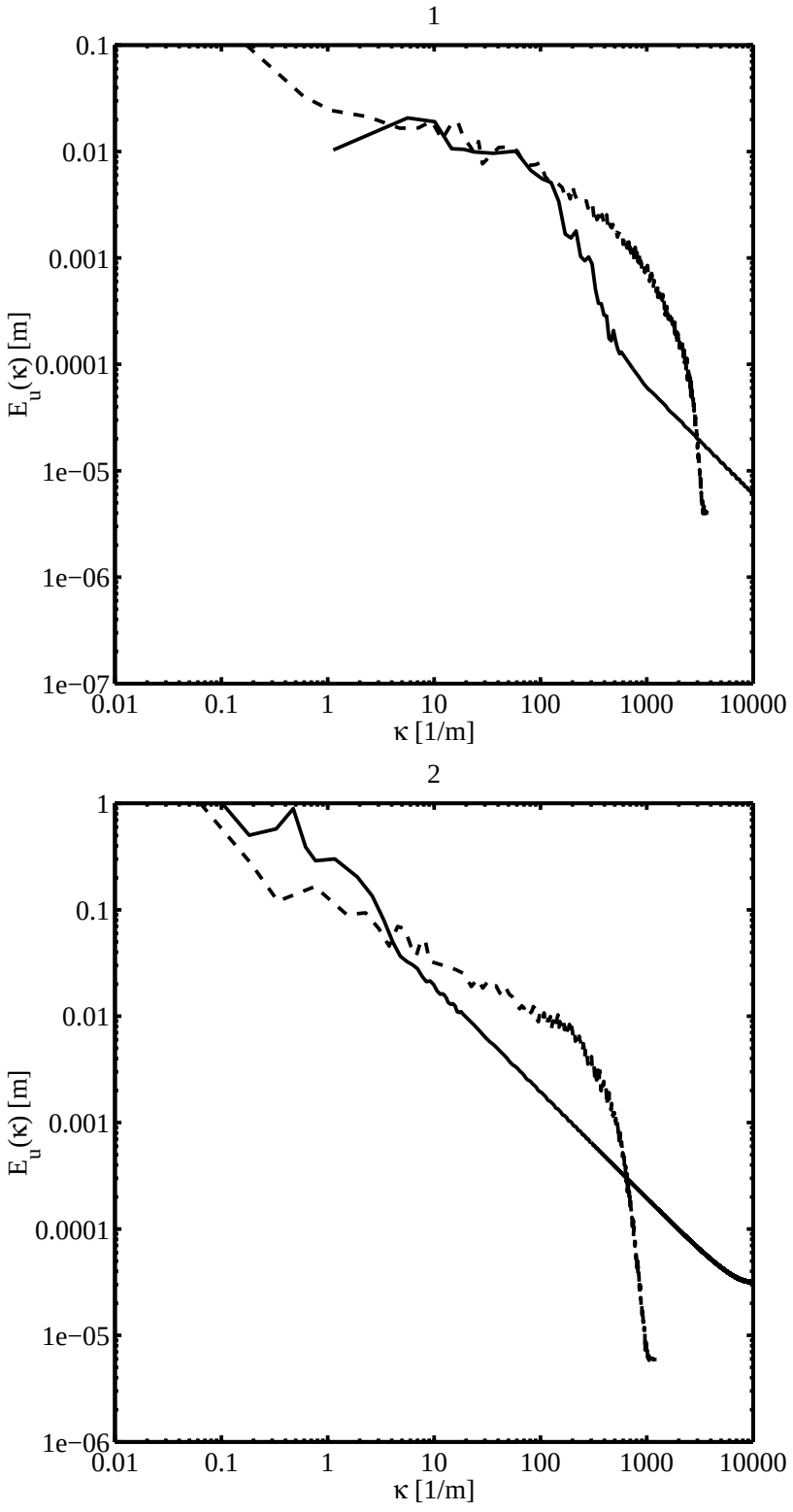

Figure 6.9: Time spectra the horizontal velocity components. Upper: ——: P_{c1}. – – – –: P_{e1}, Melikov [63]. Lower: ——: P_{c2}. – – – –: P_{e2}, Melikov [63]. The wave number, κ is related to the frequency ω using $\kappa = 2\pi\omega / < \overline{u} >$ and the energy content $E_u(\omega)$ is scaled to give $E_u(\kappa) =< \overline{u} > \cdot E_u(\omega)/(4 \cdot < \overline{u}'^2 >)$, see Hinze [46]. With the chosen scaling, the integral timescale is can be determined from $\mathcal{T}_u = E_u(\kappa = 0)/ < \overline{u} >$.

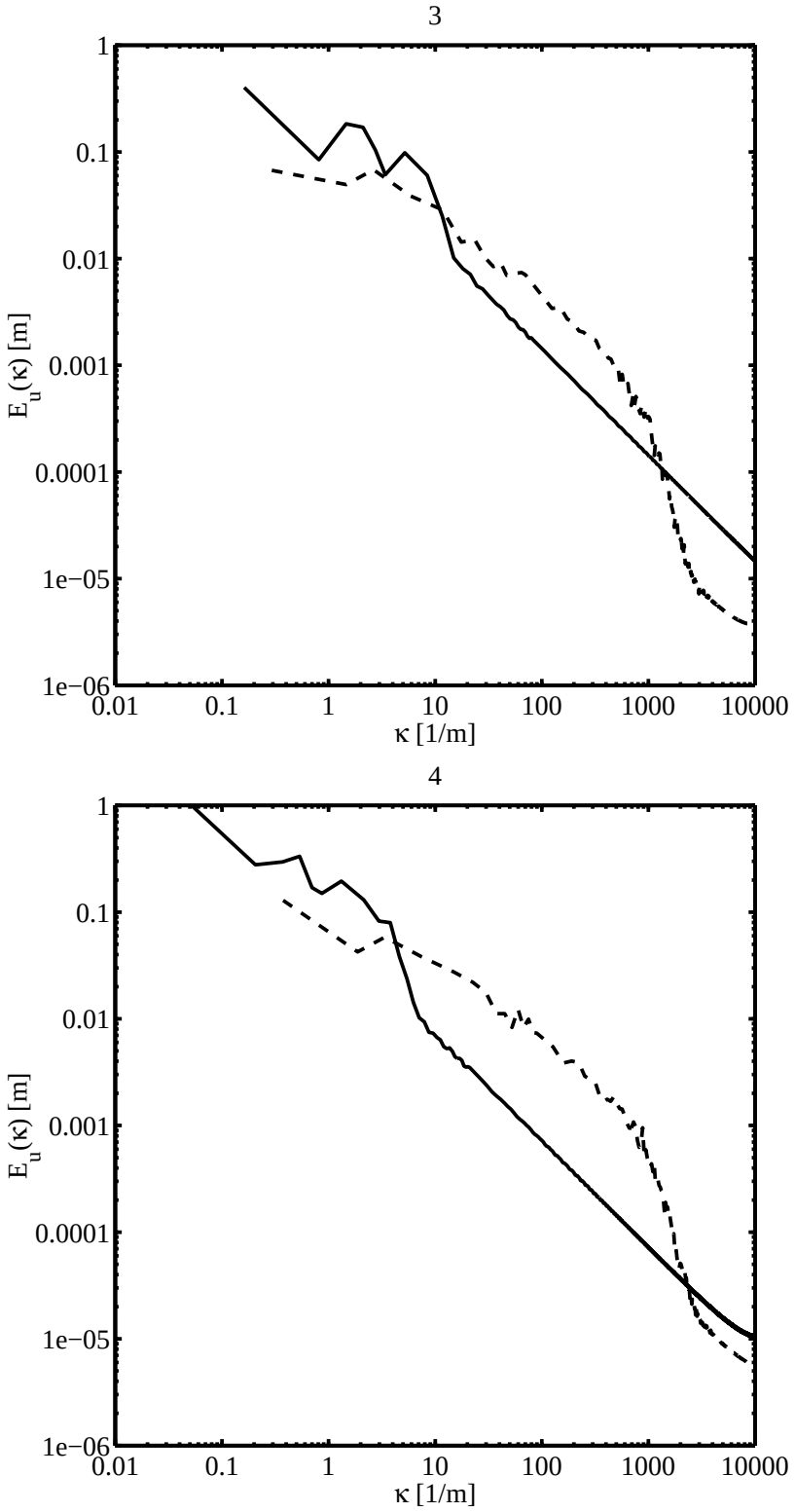

Figure 6.10: Time spectra the horizontal velocity components. Upper: ———: P_{c3}. – – – –: P_{e3}, Melikov [63]. Lower: ———: P_{c4}. – – – –: P_{e4}, Melikov [63]. Scaling of the axes, see figure 6.9.

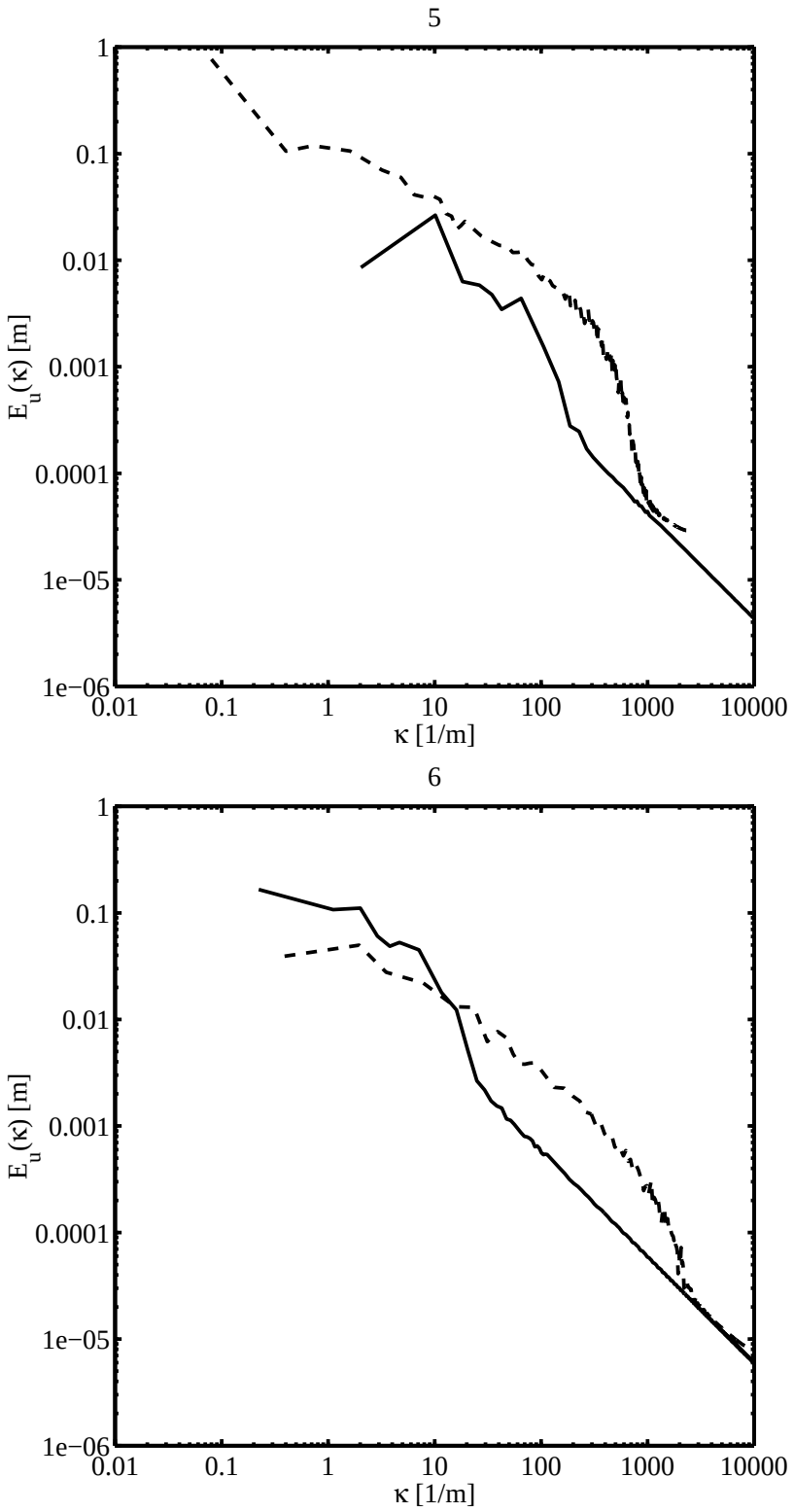

Figure 6.11: Time spectra the horizontal velocity components. Upper: ———: P_{c5}. – – – –: P_{e5}, Melikov [63]. Lower: ———: P_{c6}. – – – –: P_{e6}, Melikov [63]. Scaling of the axes, see figure 6.9.

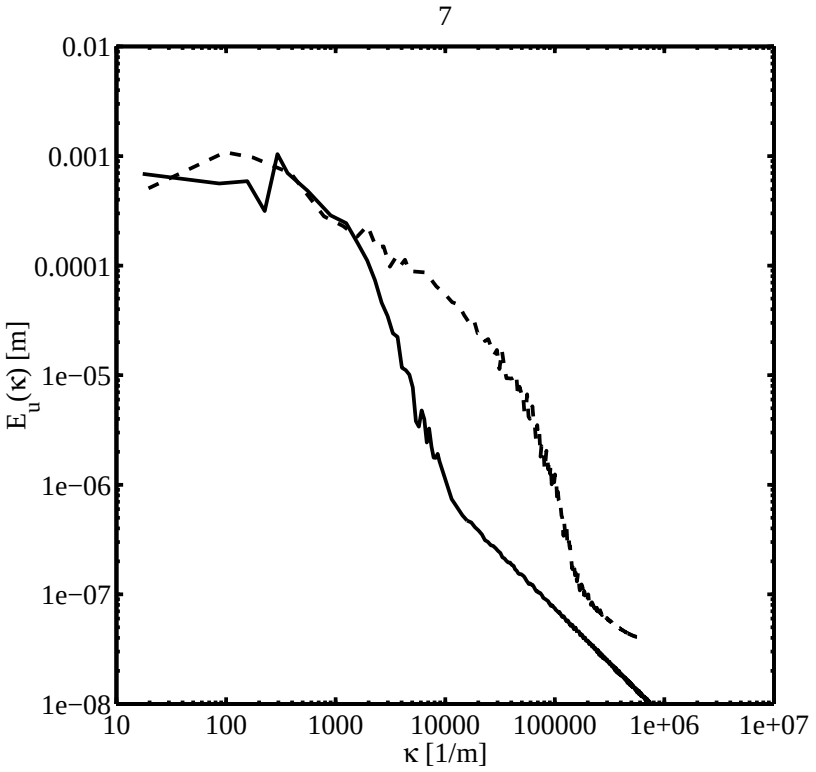

Figure 6.12: Time spectra the horizontal velocity components. ——: P_{c7}. – – – –: P_{e7}, Melikov [63]. Scaling of the axes, see figure 6.9.

Finally, three time scales appearing in the flow is shown in figure 6.13. The first time scale occurs in the almost laminar region in the occupied zone, see figure 6.13(upper left). The fluctuations are very slow in this region, with only four large positive peaks within 300 s. In the jet the time scale is clearly different, see figure 6.13(lower left). The behaviour of the time series is much more turbulent, and the distance between the peaks is in order of a few seconds. The third time scale is associated with the small fluctuations applied to the inlet, see figure 6.13(upper right), and the zoom of one second of this time series, figure 6.13(lower right). From the latter figure, the superimposed fluctuations are obvious.

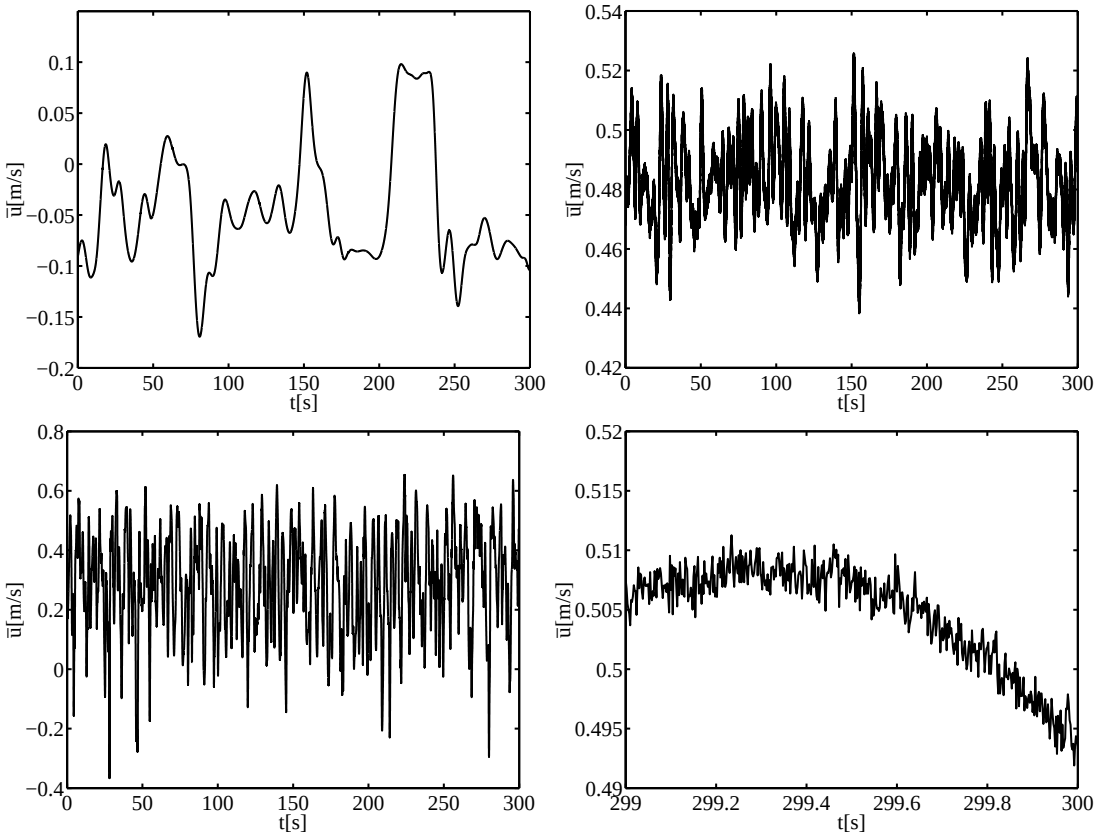

Figure 6.13: Calculated times series of the horizontal velocity component in three different points. These illustrate three time scales appearing in the flow. Top left: $(x, y, z) = (2.84, 0.21, 0.21)$, $0\ s < t < 300\ s$. Top right: $(x, y, z) = (-0.86, 2.91, 1.50)$, $0\ s < t < 300\ s$. Lower left: $(x, y, z) = (0.22, 2.83, 1.50)$, $0\ s < t < 300\ s$. Lower right: $(x, y, z) = (-0.86, 2.91, 1.50)$, $299\ s < t < 300\ s$.

6.4 Summary

In this chapter LES in the annex 20 2-D test case was conducted. In order to reduce the amount of grid points periodic boundary conditions were employed in the spanwise direction. This gave the two-dimensional solution in each cross section using RANS, while LES provided a fully three-dimensional flow field.

A thorough comparison of RANS and LES was carried out. In terms of mean velocity profiles, the RANS method performed better than LES. By comparing with previously presented results, the need for calibrating the constant appearing in the used SGS model was obvious. It was suggested that the constant should be increased. Comparing rms values, the RANS method tended to underpredict measurements, while LES predictions were contradictory. LES predicted rms values which were both higher and lower than measurements. Stretching of the grid in the inner domain led to a local minimum of rms profiles based on LES, which was explained by

the modelled viscosity. The magnitude of the SGS viscosity reduced as the size of the grid cells were reduced. This was a desirable feature close to the walls, since this renders wall functions superfluous. However, using local stretching away from walls causes local effects in the rms values, and thus local stretching away from walls should be avoided. The maximum ratio of the modelled viscosity to the kinematic viscosity was found to be 100 times larger for RANS than in LES. The reason was that in RANS the range of scales which had to be modelled was much larger than in LES.

The time spectra based on calculations and measurements were compared. The experiments, Melikov [63], were carried out in a room geometry almost similar to the annex 20 2-D case, and time spectra were compared for seven points located in the occupied zone. The agreement between LES and measurements was good for wave numbers less than approximately 50 m^{-1}, which corresponded to the smallest resolved scales. The deviation for wave numbers higher than 50 m^{-1} was thus believed to be attributed to the SGS modelling. The SGS kinetic energy is calculated from the velocity difference of the filter and a test filter. Therefore, the largest unresolved scales are better represented than the smallest unresolved scales. This explains why the deviation between measurements and LES increased for wave numbers increasing above the wave number related to the smallest resolved scales.

Finally, three time scales appearing in the flow were shown. The first time scale was related to low Reynolds number region in the lower part of the room, the second appeared in the turbulent jet, and the final timescale was associated with the random perturbation superimposed at the inlet boundary.

It is concluded that a LES model for indoor airflows is now available in *EllipSys*, but further calibration of the SGS model is necessary. The calibration was not carried out due to computational limitations.

Chapter 7

Calculation of the airflow in the annex 20 case with a heated wall

7.1 Introduction

Temperature is an important comfort parameter for humans. A summer situation with cooling is a typical scenario where an accurate knowledge of the temperature distribution is desirable. The test case specified by Heikkinen [43] is suitable for validating calculations of non-isothermal airflows. The test case is characterized by a cold jet supplied through a complex diffuser geometry in one end wall of the room, and a heated window at the opposite end wall. This test case has been the objective of several experimental and numerical studies of which a thorough review is given in Whittle [109].

The flow in the aforementioned test case is complicated for two reasons, namely the complexity of the inlet and the heated wall. This is reflected in the literature, where especially the former has been treated thoroughly. The three most popular models for the complex inlet diffuser are the basic model, the box model and the prescribed velocity model. The basic model uses a rectangular opening to model the inlet. In the box model, Nielsen [83], a velocity is prescribed on the surface of an imaginary box in front of the diffuser, and in the prescribed velocity model, Gosman *et al* [38], analytical or experimental velocities are prescribed in a volume in front of the inlet, excluding calculations of velocities in this region. Computations were carried out by Skovgaard & Nielsen [99], and the modelling of the inlet was emphasized. The basic model and the prescribed velocity model were evaluated in terms of the jet emanating from the inlet, and the latter was found to represent measurements best. Chen & Moser [16] calculated the airflow using different models for the inlet. The basic model and two refinements of the basic model, consisting of 12 and 84 rectangular slots were evaluated. Compared to measurements, the velocity decay was too rapid using the basic model and the model with 12 slots. It was therefore recommended to use the model with 84 slots. Emvin & Davidson [30] carried out a further numerical study of the inlet boundary conditions. The basic model tended to overpredict the penetration depth of the jet for diffusers with small ratios of nozzle-to-diffuser area.

Huo *et al* [19] provided the jet main region specification model. This is based on the box model, Nielsen [83], but analytical data are applied to the box. Further, a guideline for selection of the box was given. This model has the advantage that no measurements are needed.

The basic model consisting of one rectangular opening was the most simple of the described models. Therefore, this model was used in the following.

Several measurements are available for the test case, see e.g. Fossdal [37], Blomqvist [12], Fontaine *et al* [36] and Jensen & Pedersen [52]. Isothermal measurements for four different air exchange rates ranging from 2 to 6 h^{-1} were presented by Blomqvist [12]. Non-isothermal measurements using air exchange rates ranging from 1.5 to 6 h^{-1} and a window temperature of approximately 10^oC above room air temperature, were presented by Fossdal [37]. The aforementioned measurements were full scale experiments, while more recent Fontaine *et al* [36] presented water scale experiments for studying isothermal wall jets. In the latter, experiments were carried out using a diffuser with 84 nozzles and the basic diffuser. The flow was symmetric using the complex diffuser with 84 nozzles, while the flow was asymmetric using the basic diffuser. They substantiated their measurements by simulations. Finally, experiments were presented by Jensen & Pedersen [52], who carried out isothermal and non-isothermal measurements of the flow using air exchange rates between 1.5 and 6 h^{-1}. The latter measurements will be used for comparison with simulations in this chapter.

In appendix I, the *EllipSys* code was evaluated for a laminar temperature driven cavity flow. It is the main objective of the present chapter to validate the *EllipSys* code for three-dimensional non-isothermal turbulent indoor airflow calculations. Isothermal calculations were carried out for an air exchange rate of 6 h^{-1}. Velocity profiles and the velocity decay in the jet were compared with measurements by Jensen & Pedersen [52]. For the non-isothermal calculations, the same grid and the same model for the inlet geometry were used. The numerical solution turned out to be unstable when using a steady state solution procedure, while increasing the air exchange rate to 9.7 h^{-1} stabilized the solution.

Considering flow patterns in the center plane of the room, an assumed bifurcation diagram, showing the flow pattern as a function of the inverse Archimedes number, was constructed. Moreover, an experimental and computational bifurcation diagram were established. However, for a more thorough comparison of the two latter diagrams the information was too limited.

The air exchange rate of 9.7 h^{-1} was used for a comparison with experiments for an air exchange rate of 6 h^{-1}. Finally, the ventilation situation was evaluated in terms of Percentage Dissatisfied (PD).

7.2 Test case

The annex 20 geometry used in this chapter is more complicated than the three-dimensional 2-D annex 20 geometry used in the previous chapters. The reason is that a more complex inlet geometry is used, and further a heated wall is introduced. The geometry used for the computations is sketched in figure 7.1, taking the dimensions

$$H = 2.5\ m,\ L = 4.2\ m,\ W = 3.6\ m, h_i = 0.0182\ m,\ w_i = 0.68\ m,$$
$$h_o = 0.2\ m,\ w_o = 0.3\ m, h_w = 1.6\ m,\ w_w = 2.0\ m.$$

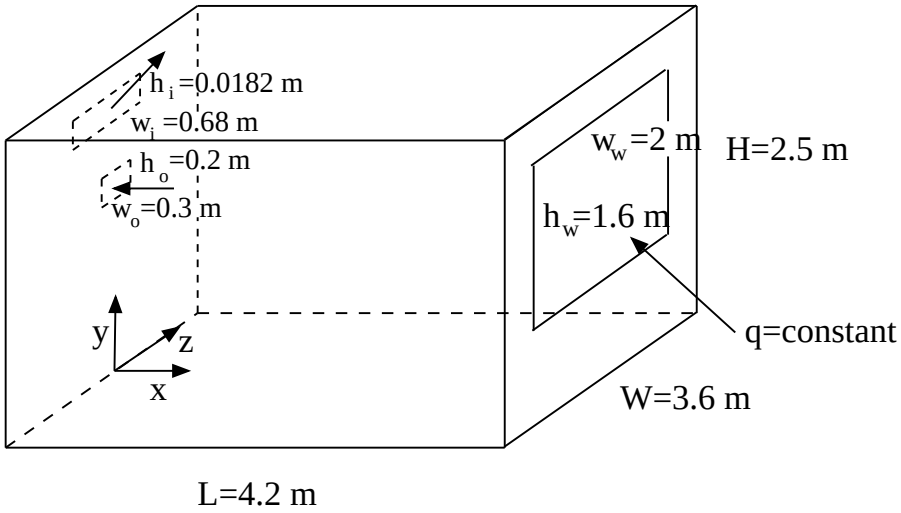

Figure 7.1: The annex 20 test case with a heated wall. In the present calculation q is 0 for isothermal conditions and 500 W for non-isothermal conditions. Notice, that the origin of the coordinate system is located in the center plane of the room

The inlet has been a matter of discussions in various publications. As a first approach, the inlet is modelled by the basic model, representing the diffuser by an opening in the wall. The diffuser used in the experiments consists of 84 round nozzles with a geometrical area of

$$A_{geom} = 84\frac{\pi}{4}0.012^2 = 0.0095\ m^2. \tag{7.1}$$

With an inlet angle of 40^o this area can, by simple geometric considerations, be projected to a vertical area of

$$A_{proj} = \frac{0.0095}{cos(40)} = 0.0124\ m^2, \tag{7.2}$$

see figure 7.2.

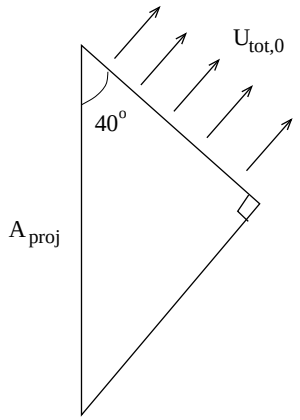

Figure 7.2: Sketch of a vertical cut through a the simplified inlet.

Using a width of the inlet $w_{in} = 0.68\ m$, which corresponds to the width of the diffuser, the inlet height $h_{in} = 0.0182\ m$ follows immediately bearing equation (7.2) in mind. For the air exchange rate of 6 h^{-1} and an inlet area of 0.0124 m^2, the air should be supplied with a velocity of $U_{tot,0} = 6.63\ m/s$. When the boundary conditions are applied in the calculation, the velocity is split into two components

$$U_0 = 6.63\cos(40) = 5.08\ \frac{m}{s} \text{ and } \quad V_0 = 6.63\sin(40) = 4.26\ m/s. \tag{7.3}$$

Based on the results presented in the previous chapters, it was chosen to use the low Reynolds number $k-\epsilon$ model Launder & Sharma, [56]. Therefore, the turbulent quantities k and ϵ need to be specified. The relation

$$k_0 = 0.01(U_0^2 + V_0^2) = 0.44\ m^2/s^2, \tag{7.4}$$

is used for the turbulent kinetic energy, and for the dissipation the relation

$$\epsilon_0 = 0.00016\frac{(U_0^2 + V_0^2)^{1.5}}{d_h} = 0.02\ m^2/s^3, \tag{7.5}$$

with the hydraulic diameter $d_h = 0.035\ m$ is used. Equation (7.4) and (7.5) were used by Emvin & Davidson [31]. For the non-isothermal calculation a total power, $q = 500\ W$ is applied to the heated surface, see figure 7.1, while the remaining walls take the adiabatic no-slip boundary condition. The temperature in the inlet, T_0, is fixed at 15^oC.

The calculations are carried out on both a coarse and a fine mesh. The coarse mesh consists of $40 \times 72 \times 48$ cells, while the fine mesh consists of $80 \times 144 \times 96$ cells in the x, y and z direction, respectively. For the fine mesh the inlet is represented by 8 cells in the $y-$direction and 32 cells in the $z-$direction. For the isothermal calculation on the fine mesh y^+ is less than 5 almost everywhere, but take values up to 8 in a small region above the inlet and in the outlet. The solution is therefore NOT fully grid independent, since this would require y^+ less than one everywhere.

The results presented in the next section are all based on calculations carried out on the fine grid, for which a plane with constant z is shown in figure 7.3. The grid was generated with *ICEM* using the 'BiGeometric' meshing law with default values, which implies that the distance between grid points will be constant on an edge of a block. At the block boundaries this leads to rather large aspect ratios of adjacent cells, see figure 7.3. The problem could easily be circumvented by stretching the grid. However, in the next chapter the 'BiGeometric' meshing law are used in parts of the domain when generating the grid around a human body. In that case it is not a straight forward matter to introduce stretching everywhere in the domain, due to the large amount of blocks. Therefore, it is relevant to know how the *EllipSys* code handles the large aspect ratios between some cells. Due to convergence problems for the coarse grids, a small rectangular channel was added to the outlet, see figure 7.3. Details on influence from the grid and convergence histories can be found in appendix H.

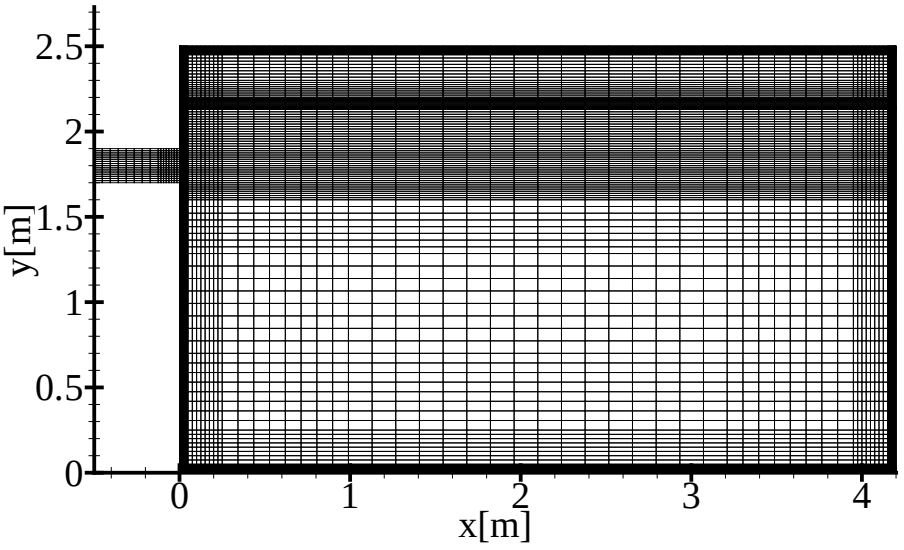

Figure 7.3: Mesh for constant z for fine mesh consisting of $80 \times 128 \times 96$ cells.

This concludes the presentation of the test case.

7.3 Results and discussion

7.3.1 Isothermal calculation

The isothermal calculations, with an air exchange rate of 6 h^{-1} is now presented. It was later experienced, that the air exchange rate in the isothermal experiments, Jensen & Pedersen [52], was only 5.8 h^{-1}. To compensate for this, the velocities are nondimensionalized by the inlet velocity. The velocity profiles in the center plane $z = 0\ m$ are shown in figure 7.4, where the upper row is the velocity profiles close to the ceiling, $y = 2.5\ m$, and the lower row is the velocity profiles close to the floor, $y = 0\ m$.

Considering first the velocity profiles close to the ceiling, figure 7.4(upper), it is observed that close to the inlet, $x = 0.6\ m$, calculations and measurements coincide well, and the largest deviation is found close to the ceiling.. Further downstream from the inlet, at $x = 1.4\ m$, $x = 2.2\ m$ and $x = 3.0\ m$, the agreement between calculations and experiments is very good. At these three positions, the largest discrepancies are found close to the ceiling. At $x = 3.5\ m$ the deviation between calculations and measurements is larger than for $x = 4.0\ m$, which is difficult to explain. The calculated and measured velocities are almost identical close to the floor, figure 7.4(lower). For $x = 1.8\ m$, $x = 2.4\ m$, $x = 3.0\ m$, $x = 3.6\ m$, the calculated velocities agree almost perfectly with the measured velocities. However, for $x = 1.2\ m$, the deviation between calculation and experiments is more significant. This is probably due to the used turbulence model, which in chapter 4 was found to have problems in regions with very low turbulence.

Finally, it was chosen to examine the decay of the maximum velocity in the jet, see figure 7.5. Compared to measurements, the maximum velocity in the jet is overpredicted by the calculations. Thus, the basic model gives a too low velocity decay in the jet. This is contrary to the findings of Topp *et al* [106] who found that the basic model provides a correct velocity decay in the jet. Topp *et al* [106] used approximately 200.000 cells in their calculation, while approximately 1.100.000 cells were used in the present calculation. This indicates that the calculation of Topp *et al* [106] was not fully grid independent and that the basic model might be insufficient to predict the correct velocity decay in the jet.

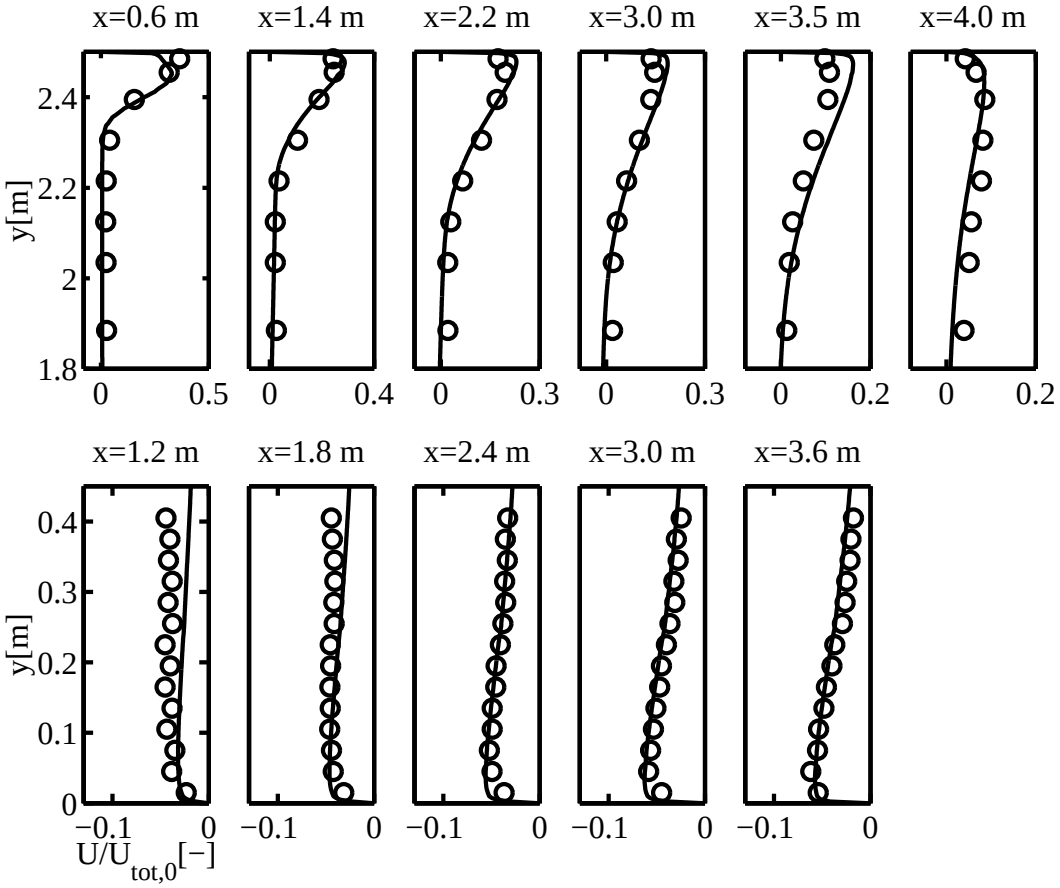

Figure 7.4: Comparison of experiments and computations of isothermal airflow in the annex 20 geometry. ——: computations with an air exchange rate of 6 h^{-1} and o: experiments with an air exchange rate of 5.8 h^{-1}.

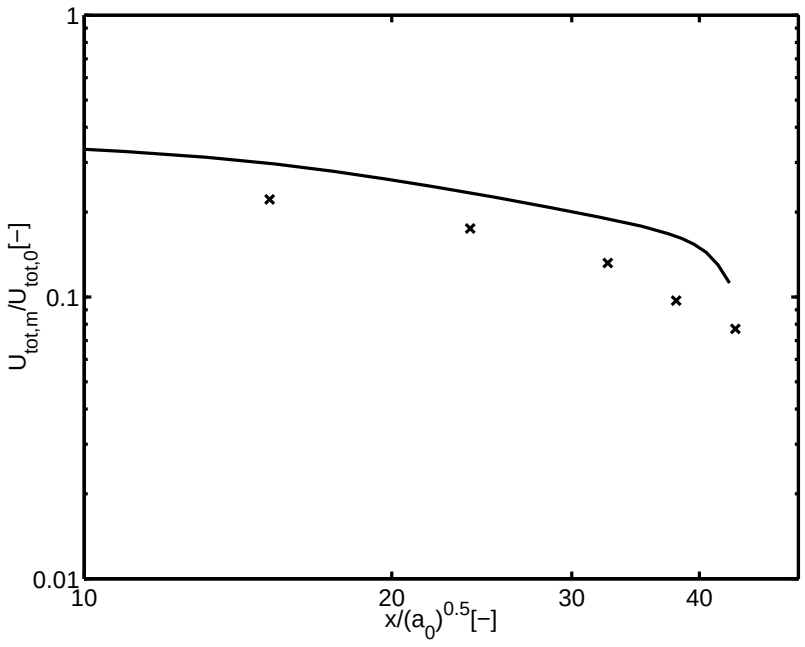

Figure 7.5: Decay of maximum velocity. x is distance from the inlet. $a_0 = 0.0085\ m^2$ is the measured effective area of the diffuser, Jensen & Pedersen [52]. $U_{tot,m} = \max((\sqrt{U^2+V^2+W^2})$ and $U_{tot,0} = 7.15\ m/s$ and $U_{tot,0} = 6.63\ m/s$ for measurement and calculations, respectively.

7.3.2 Non-isothermal calculation

For ventilation systems where a momentum driven and a buoynacy driven flow counteracts, a stability problem arises. The governing parameter in this situation is the Archimedes number

$$Ar = \frac{\beta g \sqrt{A_{geom}} \Delta T}{U_{tot,0}^2}, \tag{7.6}$$

where β is the thermal expansion coefficient, g is acceleration due to gravity, a_{geom} is the geometric area of the diffuser, $\Delta T = T_{out} - T_0$ is the temperature difference between outlet and inlet, and $U_{tot,0}$ is the velocity at the inlet. In the present case, the problem is related to whether momentum from the inlet or buoyancy from the heated surface dominates the flow. If the latter is the case, Ar will be large and the flow in the center plane of the room act like sketched in figure 7.6 A). It should be mentioned that this is a two-dimensional interpretation of the flow field. If the momentum from the inlet dominates the flow, Ar will be small, and the flow in the center plane will behave like shown in figure 7.6 C). Between situation A) and C) in figure 7.6, some equilibrium between momentum from the inlet and buoyancy from the heated surface exists. This gives the flow pattern shown in figure 7.6 B). From a CFD point of view, the flow is very different in the three cases sketched in figure 7.6. In particular it is interesting whether the flow is steady or not. In this chapter only a steady solution procedure were employed.

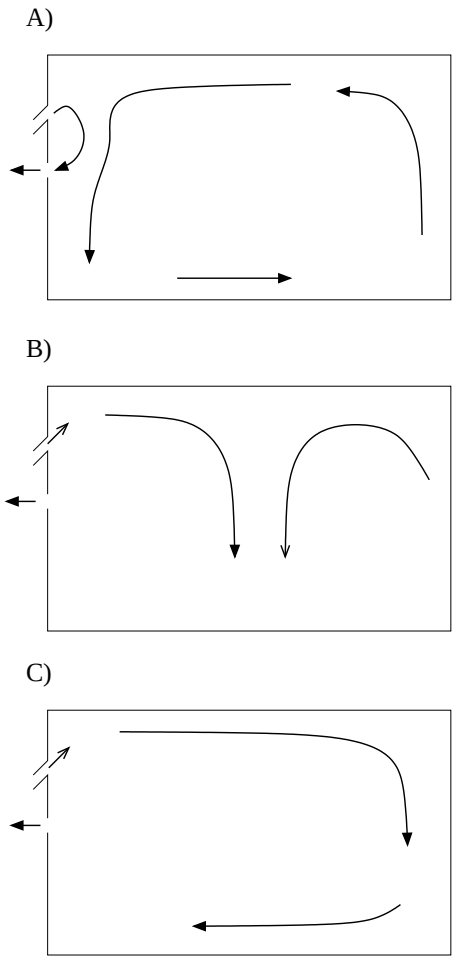

Figure 7.6: Flowpatterns occurring at different air exchange rates. Situation A) occur for large Archimedes numbers. Situation C) appear for small Archimedes numbers and situation B) occurs for Archimedes numbers between those related to A) and C).

Based on the three flow situations sketched in figure 7.6 the bifurcation diagram shown in figure 7.7 was assumed to exists. The bifurcation diagram shows the flow pattern in center plane for different values of $1/Ar$. The bifurcation points, •, indicates values of $1/Ar$ where the flow pattern changes. The exact location of the bifurcation points is not known.

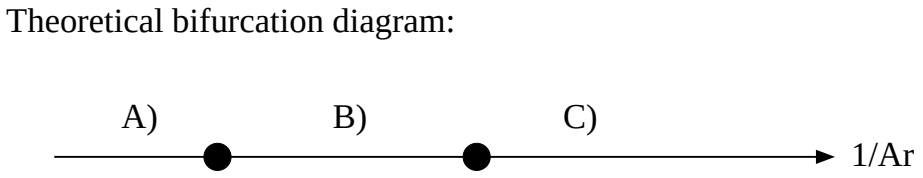

Figure 7.7: Assumed bifurcation diagram for a ventilated room with a heated surface. A), B) and C) refers to figure 7.6. •: Points where the flow pattern changes.

Experiments at three different air exchange rates were carried out by Jensen & Pedersen [52]. Based on these experiments, they sketched the flow pattern in the center plane. From this information, the experimental bifurcation diagram shown in figure 7.8 is constructed.

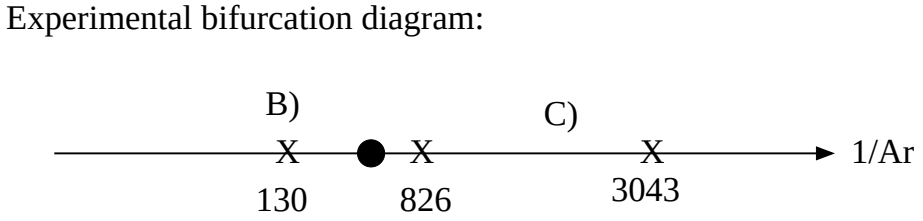

Figure 7.8: Experimentally determined bifurcation diagram for a ventilated room with a heated surface. A), B) and C) refers to figure 7.6. x: Points where measurements are available. •: Points where the flow pattern changes.

In the non-isothermal calculations, the same grid as for the isothermal calculations was used, and a total power of $q = 500\ W$ was applied to the end wall. With an air exchange rate of 6 h^{-1}, this corresponds to $Ar = 5.5 \cdot 10^{-4}$. It was not possible to obtain a converged solution. The variation of the velocity components in a point $(x, y, z) = (4.0, 2.2, 0.6)$ is shown in figure 7.9(left) and clearly no steady region is reached with the 25.000 iterations. The flow pattern in the center plane of the flow was varying periodically with the iteration number. At a given iteration the flow pattern corresponded to situation C) in figure 7.6, while at a later iteration number the flow pattern was more similar to situation B). Results from a calculation based on a steady solution procedure should therefore be interpreted carefully.

The air exchange rate was increased to 9.7 h^{-1}, corresponding to an $Ar = 4.4 \cdot 10^{-4}$. This stabilized the solution. The residuals was converged to below 10^{-3} and the velocity components in the monitor point $(x, y, z) = (4.0, 2.2, 0.6)$, see figure 7.9(right), stabilized after 15.000 iterations. The flow in the center plane behaved as illustrated in figure 7.6 C). Based on the calculations a bifurcation diagram using steady state solutions of the RANS equations is shown in figure 7.10.

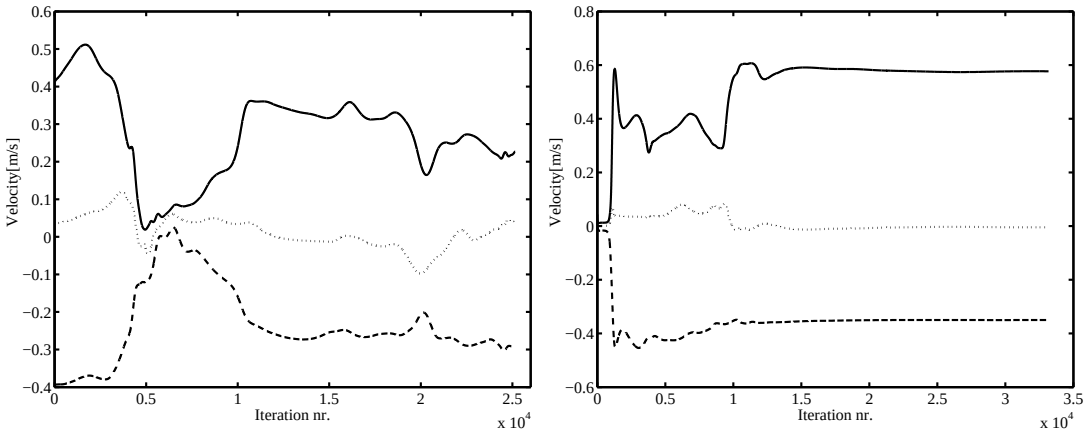

Figure 7.9: The time series taken in the point $(x, y, z) = (4.0, 2.2, 0.6)$. Left: $n = 6\ h^{-1}$. Right: $n = 9.7\ h^{-1}$. ——: u, $-\ -\ -\ -$:v, $\cdots\cdots$:w.

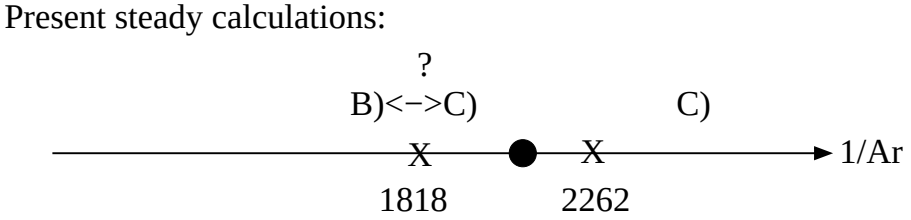

Figure 7.10: Numerically determined bifurcation diagram for a ventilated room with a heated surface. Only a steady solution procedure were employed. A), B) and C) refers to figure 7.6. x: Points where calculations are available. •: Points where the flow pattern changes. ? indicates that the steady state solution procedure had convergence problems in this region and the result might be wrong.

Contour plots of the temperature distribution in the center plane were compared in figure 7.11. It is difficult to make a quantitative comparison between the results since the experiments are carried out at an air exchange rate of $n = 6\ h^{-1}$, while the computations are carried out at an air exchange rate of $n = 9.7\ h^{-1}$. However, figure 7.11 illustrates very well the intension of this chapter, namely to compare temperature distribution based on measurements and calculations. In the present case, when the jet is supplied into a warmer region, a narrow cold region appears below the ceiling, see figure 7.11. Comparing figure 7.11(upper) and figure 7.11(lower), the penetration length of this cold zone is shorter in measurements than in computations. This is most likely to be due the different air exchange rates used.

When the temperature and velocity distributions are known, the Percentage Dissatisfied (PD) can be estimated from Fanger *et al* [34],

$$PD = (34 - t_a)(U_{tot} - 0.05)^{0.62}(0.37 \cdot U_{tot} \cdot Tu + 3.14), \tag{7.7}$$

where t_a is the air temperature, U_{tot} is the velocity and Equation (7.7) is fitted from data in the range: $20 < t_a < 26\ ^oC$, $0.05 < U_{tot} < 0.4\ m/s$ and $0 < Tu < 70\ \%$. Fanger *et al* [34] suggested to insert $U_{tot} = 0.05\ m/s$ in equation (7.7) if $U_{tot} < 0.05\ m/s$ and to use $PD = 100\ \%$ if equation (7.7) gives $PD > 100\ \%$. For predicting PD based on computations, Skovgaard & Nielsen [99] used

$$PD = (34 - t_a)(U - 0.05)^{0.62}(0.37 \cdot U \cdot Tu + 3.14), \tag{7.8}$$

where t_a is the air temperature, U is the horizontal component of velocity and the turbulence intensity is estimated from $Tu = \sqrt{k}/(1.1U) \cdot 100\%$. In the computations, negative values of U occurs in the lower part of the room. Therefore,

$$PD = (34 - t_a)(||U| - 0.05|)^{0.62}(0.37 \cdot U \cdot Tu + 3.14), \tag{7.9}$$

was used when calculating PD in the present dissertation. The turbulence intesity is was estimated from $Tu = \sqrt{k}/(1.1U) \cdot 100\%$ and if $U < 0.05\ m/s$ the value $U = 0.05\ m/s$ was inserted. Based on the computation with an air exchange rate of $n = 9.7\ h^{-1}$ the contour plot for PD, using equation (7.9), is shown in figure 7.12. It is recommended that PD should be below 10 % in occupied rooms, see e.g. Hansen *et al* [41]. Considering figure 7.12, this is fulfilled in most of the occupied zone for the examined ventilation situation. In this case, PD is typically between 0 % and 10 % except close to the floor for $1\ m < x < 4\ m$. In this region values of PD reaches 15 to 20 %. It is therefore concluded that in terms of PD, the relative high air exchange will not lead to a poor ventilation situation.

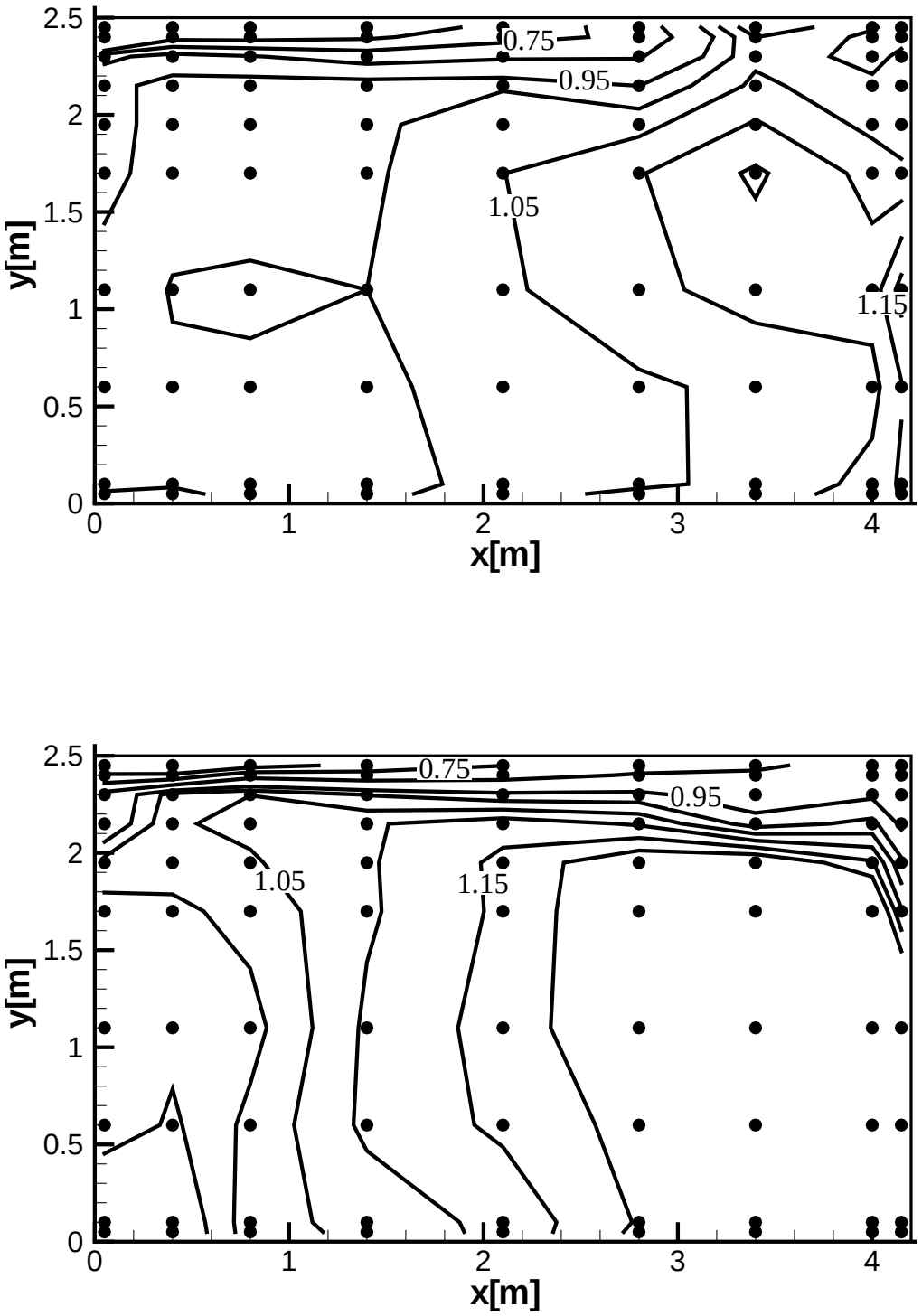

Figure 7.11: Comparison of dimensionless temperature, $(T - T_i)/(T_{out} - T_i)[-]$, for $z = 0\ m$, i.e the center plane of the room. The dimensionless temperatures shown are [0.65;0.75;0.85;0.95;1.00;1.05;1.10;1.15;1.20] based on values in the points indicated by •. Top: experiments for an air exchange rate of $n = 6\ h^{-1}$. Lower: computation for an air exchange rate of $n = 9.7\ h^{-1}$.

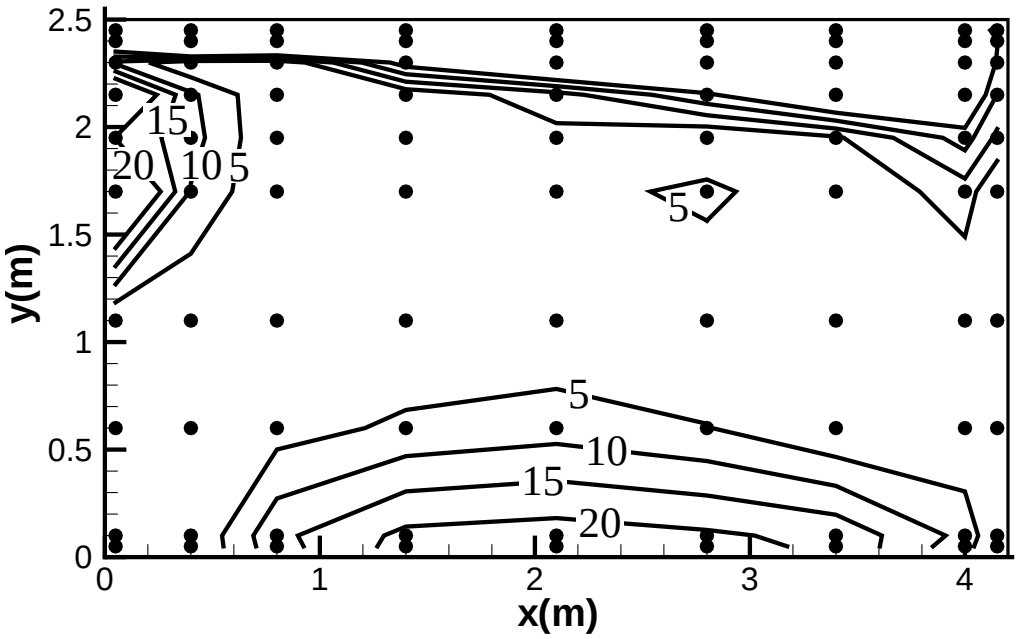

Figure 7.12: Contour plot of PD calculated from equation (7.9).

7.4 Summary

In this chapter it has been documented, that the *EllipSys* code is capable of handle and predict velocity and temperature distribution in turbulent indoor airflows. Modelling of complex inlet diffuser geometries requires further investigation.

Comparing isothermal calculation and measurements for an air exchange rate of 6 h^{-1}, good agreement was found in the center plane. The velocity decay in the jet was examined and the basic model showed a lower velocity decay than measurements.

For a non-isothermal flow with a cold inlet jet and a heated wall, the possible flow patterns in the center plane of the room were sketched. Further, an assumed bifurcation diagram, indicating where the flow patterns will occur as a function of the inverse Archimedes number, was established. From existing experiments, Jensen & Pedersen [52], an experimental bifurcation diagram was found.

With a steady state solution procedure, it was not possible to obtain a stable solution for an air exchange rate of 6 h^{-1} corresponding to the measurements. Thus, the air exchange was increased to 9.7 h^{-1}, which gave a stable solution. Based on

the limited information, a computational bifurcation diagram was obtained.

Temperature distribution for measurements with an air exchange rate of 6 h^{-1} and calculations with an air exchange rate 9.7 h^{-1} were compared. When the air was supplied into the room, a cold zone arose below the ceiling. As expected, the penetration length of this zone was shorter for the low air exchange rate than for the high air exchange rate.

For the computations with an air exchange rate 9.7 h^{-1} the PD was calculated. This showed that the requirement of less than 10 % dissatisfied was fulfilled in most of the occupied zone for this ventilation situation.

Chapter 8

Calculation of airflow around a thermal manikin

8.1 Introduction

Numerical predictions of the thermal sensation for individuals typically necessitates a mathematical representation of the human body. The models are used to investigate quantities which are important for thermal comfort, and thus it is important to know how parameters e.g as the convective heat transfer of the model relates to a real human subject. The most simple of the mathematical models is the rectangle, see e.g Brohus & Nielsen [13], while a more advanced geometry with the shape of a human was used by Murakami *et al* [73]. In this dissertation a mathematical model with the highest level of details seen in the literature is presented.

In CFD for room airflows one of the objectives is to predict the flow phenomena close to the person. This requires a high degree of detail when representing the human geometry. Due to limitations of computational time and memory as few grid points as possible around the person should be used. Increasing the degree of detail, increases the amount of grid points needed for a valid CFD calculation. For this reason it is desirable to use a simple representation of the person. Therefore, the commonly used shapes for representing persons are spheres, cylinders and rectangular geometries. To investigate ventilation efficiency and concentration profiles in a room with a moving person, Mattsson *et al* [62] carried out experiments with a simple and a detailed full scale person simulator. The former was a cylinder, while the latter was a manikin with the shape of a real person. Concentration profiles of a pollutant source were qualitatively the same for the two person geometries, but the levels were different. Brohus & Nielsen [13] used three models constructed of rectangular shapes. The models ranged from a rectangular box to a model with legs and head. CFD calculations of these geometries placed in a wind tunnel with a pollution source located upstream were carried out. The study showed that the legs have a significant impact on the exposure level for a pollutant source located below 0.75 m. Bjørn & Nielsen [11] used the rectangular geometries to perform a CFD study of the contaminant transport between two breathing persons. Varying

the distance between the persons, CFD provide results physically realistic, i.e. the exposure decreases with increasing distance between the persons. However, the level of exposure was different from full scale experiments by Bjørn & Nielsen, [10].

Murakami *et al* [73] studied opportunities for refinements of the cylindrical geometry. The developed geometry, the computational manikin, was used in various other studies. In Murakami *et al* [74], the computational manikin was placed in a ventilated room. Five environments were studied. In the first, the computational manikin was placed in stagnant air, in the second and third it was placed in a horizontal flow of low air velocity (0.25 m/s), with 6 % or 29 % turbulence intensity. The two remaining cases had upward and downward low velocity airflow. For the stagnant flow the $k-\epsilon$ model had problems reproducing the transition from laminar to turbulent flow in the boundary layer. Murakami *et al* [74] circumvented the problem by adding an extra source term, to the k and ϵ equation. For the horizontal airflow case, the flow showed a level of turbulent kinetic energy which was significant higher than for the stagnant airflow case. In Murakami *et al* [75], the computational manikin was placed in environments covering stagnant air, low air velocity (0.25 m/s) with varying turbulence intensities, high air velocity (2.5 m/s), and interaction between two manikins placed beside each other in a low air velocity flow field. In all cases the air approached the manikin in the horizontal direction. The results compared were velocity distribution, pressure distribution and the convective heat transfer coefficient. For the stagnant environment the velocity boundary layer thickness increased with height similar to the boundary layer along a vertical plate and a thin layer of heated air covers the body. The heat transfer coefficient ranges from 3 to 4 $W/(m^2K)$, but reaches 7 $W/(m^2K)$ at feet level. At low air velocities, the thin layer of heated air vanishes and the convective heat transfer coefficient increases with a factor of 2-3.

The numerical simulations of flow field and temperature field were coupled with radiation and moisture transport in Murakami *et al* [76]. In this case their computational manikin was placed in a stagnant environment simulating a person standing in a room with displacement ventilation. The boundary conditions at the surface of the computational manikin was determined in accordance with a thermo-physiological model, and then radiation between surfaces was calculated to obtain temperatures at the walls. With the obtained boundary conditions CFD was used for calculating flow, temperature and moisture fields. The results showed that of the heat released, 29.0 % was released by convection, 38.1 % by radiation, 24.2 % by evaporation and 8.7 % by respiration. The convective heat transfer coefficient ranged from 2 to 8 W/m^2K, and was highest at feet level due to the thin boundary layer at this height. The radiant heat transfer rate was distributed uniformly between 30 and 40 W/m^2. At feet level the radiant heat transfer rate was only 20 W/m^2. The evaporative heat transfer rate was modest at the legs, but increased to approximately 20 W/m^2 at the torso and reached 30 W/m^2 at the shoulders. The heat loss by respiration was fixed at 8.7 W/m^2.

The purpose of this chapter is to present calculations of the flow field and temper-

ature field around a sedentary person and compare the results with measurements made with a thermal manikin in the laboratory, Holsøe [47]. To improve the understanding of how the present calculations can be used in indoor environment, a thorough presentation of Fanger's comfort equation [32] is given. Further, a literature study on convective heat transfer is presented. The experimental and numerical setups are then described before the results are presented.

8.2 Fanger's comfort equation

In this section the comfort equation in the form presented by Fanger, [32] is introduced.

The heat balance expresses that for a person with a constant metabolic heat rate and a constant internal body temperature, the heat production equals the heat loss. The heat balance may be expressed as

$$H - E_{dif} - E_{sw} - E_{res} - C_{res} = R + C, \tag{8.1}$$

where H is internal heat production, E_{dif} is heat loss by water vapour diffusion through the skin, E_{sw} is heat loss by evaporation of sweat from the surface of the skin, E_{res} is latent respiration heat loss, C_{res} is the dry respiration heat loss, R is radiation heat loss from the outer surface of the clothes and C is heat loss by convection at the outer surface of the clothes.

The internal heat production can be attributed to two contributions

$$H = M - W, \tag{8.2}$$

where M is metabolic heat rate and W is external work load. The first term can be found tabulated for typical activities in Fanger [33], while the latter can be neglected for many types of work.

Three thermophysiological variables appear in the heat balance: the internal heat production H, the skin temperature, t_{sk}, and the sweat secretion, E_{sw}. At a certain metabolic rate a balance between t_{sk} and E_{sw} will be reached for persons feeling thermally neutral. Measurements of t_{sk} and E_{sw} as a function of metabolic heat rate for occupants in thermal comfort can be found in Fanger [33], from which linear regression leads to

$$t_{sk} = 35.7 - 0.0275H \tag{8.3}$$

and

$$E_{sw} = 0.42(H - 58). \tag{8.4}$$

The latter equation is used to represent the heat loss by sweating in equation (8.1).

From Fanger [32] the diffusion of water vapour through the skin can be calculated from

$$E_{dif} = 0.31(p_{ds} - 0.01p_{da}), \tag{8.5}$$

where p_{ds} is the saturated water vapour pressure in Pa at skin temperature and p_{da} is the water vapour pressure at room air temperature. From tables Hansen *et al* [41], assuming the skin temperature $27^oC < t_{sk} < 35^oC$, linear regression gives

$$p_{ds} = 2.56t_{sk} - 33.7. \tag{8.6}$$

Now inserting (8.6) into (8.5) yields

$$E_{dif} = 0.31(2.56t_{sk} - 33.7 - 0.01p_{da}). \tag{8.7}$$

Diffusion through the skin, is a passive process occurring also while no sweating takes place. Thus, diffusion through the skin is not a part of the termoregulatory control, but it is a part of the heat balance, see Fanger [32].

When air is inhaled and passes through the respiratory tract to the lungs, heat and water vapour is transferred by convection and evaporation. When reaching the alveoli the air will be close to deep body temperature and be saturated. As the air is exhaled some heat and water is returned to the body, but exhaled air has an increased contents of heat and water vapour compared to the inhaled air. The latent heat loss can be related to the pulmonary ventilation by

$$E_{res} = V_{lung}(x_{exh} - x_a)r, \tag{8.8}$$

where x_{exh} is the humidity ratio of exhaled air, x_a is humidity ratio of inhaled air, V_{lung} is the pulmonary ventilation and $r = 2406 \cdot 10^3 J/kg$ is latent heat of vapourization of water at 35^oC. The pulmonary ventilation is estimated using the metabolic heat rate

$$V_{lung} = 0.00143 \cdot 10^{-3} M. \tag{8.9}$$

obtained from a literature study by Liddell [59]. Assuming the subject to be thermally neutral, the difference in humidity ratio between exhaled and inhaled air can be estimated from

$$x_{exh} - x_a = 0.0277 + 0.000065t_a - 0.80x_a \approx 0.029 - 0.8x_a, \tag{8.10}$$

assuming the air temperature constant at 20^oC. The expression was found by McCutchan & Taylor [61]. Generally $p_{da} << p$ for atmospheric pressure, and therefore the water content in the room air can be approximated by

$$x_a = 0.622\frac{p_{da}}{p - p_{da}} \approx 6.14 \cdot 10^{-6} p_{da}, \tag{8.11}$$

which substituted into (8.10) yields

$$x_{exh} - x_a = 0.029 - 4.96 \cdot 10^{-6} p_{da}. \tag{8.12}$$

Finally, substituting (8.12) and (8.9) into (8.8) yields

$$E_{res} = 0.0017M(58.7 - 0.01p_{da}). \tag{8.13}$$

The last term occurring on the left hand side of the heat balance (8.1), the dry respiration heat loss, is calculated from the temperature difference between exhaled and inhaled air

$$C_{res} = V_{lung} c_p (t_{exh} - t_a). \tag{8.14}$$

Taking into account that the dry respiration heat loss is small compared to the other heat losses, t_{exh} is assumed constant, 34^oC. The specific heat of air, c_p, takes the value 1010 $J/(kg \cdot K)$. Accordingly, equation (8.14) reduces to

$$C_{res} = 0.0014M(34 - t_a). \tag{8.15}$$

The two terms appearing on the right hand side of the heat balance (8.1) are heat loss by radiation and convection, respectively. The heat loss by radiation may be expressed from

$$R = f_{eff} f_{cl} \epsilon \sigma ((t_{cl} + 273)^4 - (\overline{t}_r + 273)^4), \tag{8.16}$$

where f_{eff} is the effective radiation area factor typically taken to be 0.7 for the human body, f_{cl} is the ratio of the surface area of the clothed body to the nude body, ϵ is the emissivity often taken to be 0.95, σ is Stefan-Boltzmann's constant, t_{cl} is the temperature of the clothing and $\overline{t}_r$ is the mean radiant temperature defined by

$$\overline{t}_r = F_1 t_1 + F_2 t_2 + ... + F_n t_n. \tag{8.17}$$

In equation (8.17), F_n is the angle factor from person to surface n and t_n is temperature of surface n. The heat loss by convection can be estimated from

$$C = f_{cl} h_c (t_{cl} - t_a), \tag{8.18}$$

where $h_c = 12.1 v_a^{0.5}$ for forced convection, $h_c = 2.4(t_{cl} - t_a)^{0.25}$ for free convection, t_a is the air temperature and v_a is the air velocity. The convection, equation (8.18), will be discussed in the following.

8.3 Convective heat transfer

The investigation and understanding of convective heat transfer from a human subject is an important issue when designing indoor climate. On referring to the heat balance equation (8.1) it shall be describe how the heat loss by convection can be determined. Basically, three approaches with different advantages and disadvantages can be used. The heat loss by convection can be obtained using a human subject, a thermal manikin or a computational manikin.

For a human subject in a typical office environment the terms appearing in equation (8.1) are all different from zero. These terms can, however, be determined in laboratory experiments. In Nielsen & Pedersen [78] the terms were determined as follows: The heat production M was found by measuring the O_2 consumption, which can be directly related to the heat production. Furthermore, the change in body heat content was determined as the change of body temperature multiplied by

weight and specific heat of body tissue. Finally, the heat loss by evaporation, E_{res}, was calculated from the weight loss corrected for respiratory metabolism. These quantities represent the left hand side of equation (8.1). The heat loss by radiation can be found by having an air temperature equal to the temperature of the clothes, while the convective heat transfer can be found by using a mean radiant temperature which is equal to the temperature of the clothes. It is obvious that several uncertainties occur using this approach for finding the heat loss by radiation and convection. First of all, the determination of the terms on the left hand side of equation (8.1) involves errors in the measurements. The surface temperature of the clothing cannot be kept completely constant. Furthermore, small movements of the person during the experiments implies that the effective radiation area changes. The small movements of the person also seem to affect the measurements of the heat loss by convection, see Nielsen & Pedersen [78]. The described method is the one closest to a real life situation, but it suffers from being quite laborious.

Some of the problems can be circumvented using a thermal manikin. For a thermal manikin, see among others Nielsen & Pedersen [78], the left hand side of equation (8.1) vanishes, and therefore several uncertainties introduced in the measurements of these terms are avoided. Instead the surface temperature of the the manikin is kept constant and the supplied electrical effect is a measure of the left hand side of equation (8.1). The effective radiation area still has to be determined, but will be kept constant since the thermal manikin is not allowed to move. The effect of small movements on the measurement of heat loss by convection is also avoided.

Using a computational manikin is rather similar to the use of a thermal manikin. The advantages of a computational manikin are the same as for the thermal manikin. Furthermore, it is possible to isolate the contribution for radiation and convection, respectively. For the computational manikin, it is advantageous that the heat loss by convection can be found in several points in one calculation. This is important for evaluation of e.g. draft risk [34]. The need for measuring equipment inside the room is also avoided for the computational manikin. The main disadvantage is that limited computer resources often necessitates a simplification of the person geometry. Therefore, the person is often modelled by boxes, cylinders, etc.

Several formulas for the heat loss by convection have been proposed over the years. The formula

$$C = 5.06(t_{cl} - t_a)^{1.21} \tag{8.19}$$

for a human subject was suggested by Nielsen & Pedersen [78]. This is valid for "still" air (free convection), corresponding to air velocities lower than 0.1 m/s. Later Fanger [32] suggested

$$h_c = \begin{cases} 2.4(t_{cl} - t_a)^{0.25} & \text{if } 2.4(t_{cl} - t_a)^{0.25} > 10.4\sqrt{v_a} \\ 10.4\sqrt{v_a} & \text{if } 2.4(t_{cl} - t_a)^{0.25} < 10.4\sqrt{v_a} \end{cases}, \tag{8.20}$$

for the convective heat transfer coefficient. Here h_c for the former is valid for free convection while the latter, originally stated by Winslow *et al* [111], is valid for forced

convection. To obtain the heat loss by convection, equation (8.20) in combination with

$$C = A_{Du} f_{cl} h_c (t_{cl} - t_a) \tag{8.21}$$

gives the heat transfer by convection. In equation (8.21) A_{Du} is the DuBois area (area of the nude body). Introducing equation (8.20), the calculation of the convective heat transfer coefficient for a broad temperature and air velocity range has been encompassed into one formula. Furthermore, by introducing equation (8.21), the heat loss by convection is corrected for both the size of the subject and the clothing of the subject.

Using an abrupt transition from free to forced convection introduced in equation (8.20), the calculation of h_c in the region where a combination of free and forced convection co-exists (mixed convection) should be interpreted cautiously. This mixed region was examined by Rapp [93] and was found to have a significant impact on the convective heat transfer coefficient. The three regions, forced, free and mixed, are governed by the parameters v_a, ΔT and $v_a^2/\Delta T$, respectively, where v_a is the velocity and ΔT is the difference between the surface temperature and the air temperature. For human subjects, Rapp [93] found that forced convection exists for $v_a > 0.2\ m/s$, free convection for $v_a < 0.05\ m/s$ and mixed convection between these limits. It was argued by Klyachko [55] that $h_{c,mixed}$ in the mixed convection region for a sphere should be $h_{c,free}$, which is constant in the free convection region, corrected with a term involving the governing parameter $v_a^2/\Delta T$ and thus the equation

$$h_{c,mixed} = C_1 \Delta T^{0.25} (1 + C_2 \frac{v_a^2}{\Delta T})^{0.2}, \tag{8.22}$$

was derived. Rapp [93], used a 0.75 m sphere to determine h_c. This is a rough geometric simplification of a person, but it leads to h_c in the correct order of magnitude. Using the sphere Rapp [93] determined $C_1 = 1.26$ and $C_2 = 3.17$. Therefore, a correlation for heat loss by convection exists in the mixed convection region, but the correlation is based on a rough geometrical simplification.

Measurements of the convective heat transfer coefficient for a rectangular heated manikin in still air was performed by Homma & Yakiyama [48]. The convective heat transfer coefficient was measured to be approximately 8 $W/(m^2K)$ at the feet level. Increasing the height, the convective heat transfer coefficient decreased rapidly to 3-4 $W/(m^2K)$. This value was measured for the remaining height. De dear [26] placed a 16 segment thermal manikin in a wind tunnel and exposed it to seven different wind speeds in the forced convection region. Convection heat transfer regression models were found for the whole body as well as for the individual segments. The regression model for the whole body of the seated manikin was

$$h_c = 10.1 v_a^{0.51}, \tag{8.23}$$

where v_a is the speed of the approaching wind.

In future investigations, the computational manikin presented in this chpater should

be used to obtain expressions for the convective heat transfer coefficient as a function of velocity and temperature.

8.4 Experimental setup

To understand the formulation of boundary conditions described in the next section, the experiments, Holsøe [47], shall be described briefly. The thermal manikin, see figure 8.2, was placed in an enclosure of the dimensions 2.95 m $\times$ 2.95 m $\times$ 2.40 m, see figure 8.1.

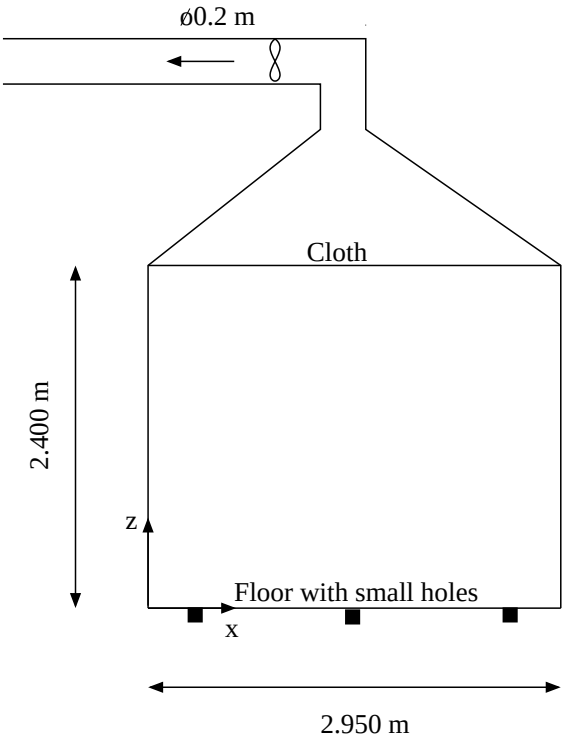

Figure 8.1: Sketch of the enclosure used in the experiments.

Figure 8.2: Picture of the breathing thermal manikin used in the experiments by Holsøe [47].

The air was supplied from the surrounding room through holes in the floor and exhausted through the ceiling. The air temperature was measured at four locations, two at the floor and two at the ceiling, see table 8.1. The vertical air velocity at the floor was measured at several locations and in several series of experiments. The air velocity at the floor was found to be in the interval of

$$0.01\ m/s < w_{floor} < 0.04\ m/s \tag{8.24}$$

and the $rms-$values were

$$u_{rms} = 0.01\ m/s, \quad w_{rms} = 0.02\ m/s. \tag{8.25}$$

It was assumed that $v_{rms} = 0.01$. The diameter of the circular holes in the floor was $0.003\ m$.

Location	Floor	Floor	Ceiling	Ceiling
Temperature $[^oC]$	18.2	19.1	19.3	19.2

Table 8.1: Air temperature measured at four location.

During the experiments the skin temperature and the heat loss were measured at five distances from the floor. The results are summerized in table 8.2.

$z[m]$	$T_{\mathrm{sk}}[^oC]$	$Q[\frac{W}{m^2}]$
0.15	30.4	89.3
0.24	30.5	99.4
0.38	30.0	89.3
0.75	31.3	111.6
0.95	30.9	101.6
Average	30.6	98.2

Table 8.2: The skin temperatures and heat losses measured at five distances from the floor. The temperatures at $z = 0.15\ m$, $z = 0.24\ m$ and $z = 0.38\ m$ were measured at the lower leg, while the temperatures at $z = 0.75\ m$ and $z = 0.95\ m$ were measured at the torso (symmetry plane of the manikin).

8.5 Numerical setup

In order to carry out numerical predictions of the flow field and temperature field, a three-dimensional laser scanning of the thermal manikin was carried out[1]. The thermal manikin was divided above the hip, and the lower and upper half were scanned separately. Afterwards, the two existing halves were numerically "glued" together. The accuracy of the laser scanning was 0.5 mm and the surface was closed, i.e there were no "holes" in the surface. The surface geometry, see figure 8.3, consists of approximately 500.000 cells and the length of the edges ranged from 3 to 10 mm. The surface geometry, can be directly imported in the grid generator *ICEM*[2]. The structured grid consists of 2.336.768 cells and was generated around half of the manikin. In the grid generation some details of the surface were modified. The surface of the manikin after the grid generation is shown in figure 8.4, where red lines indicate block boundaries. The grid layout in the symmetry plane of the manikin is shown in figure 8.5 The boundary conditions were specified in accordance with the experimental setup. The surface temperature of the manekin was specified to 30.6 ^oC, see table 8.2. The vertical component of the velocity at the floor was fixed to $W_{floor} = 0.025\ m/s$, which is the average of the minimum and maximum measured values, see equation (8.24). The two remaining velocity components were set to zero. According to table 8.1, the temperature at the floor was set to $T_{floor} = 18.65^oC$, which is the average of the two measured values. The walls were assumed to be adiabatic, which is a reasonable assumption, since the temperature difference between the air in the room and the surrounding air is small. Two different turbulence models, a low Reynolds number $k-\epsilon$ model and a constant eddy viscosity model were used. For the former, values for the turbulent kinetic energy, k_{floor}, and the dissipation of turbulent kinetic energy, ϵ_{floor}, need to be specified at the floor. With the $rms-$values given in equation (8.25) the turbulent kinetic energy becomes $k_{floor} = 0.5((0.01\ m/s)^2 + (0.01\ m/s)^2 + (0.02\ m/s)^2) = 0.003\ m^2/s^2$.

[1]The scanning was carried out by Cascade Computing A/S, www.cascade.dk.

[2]The grid was generated by Icemcfd, www.icemcfd.de.

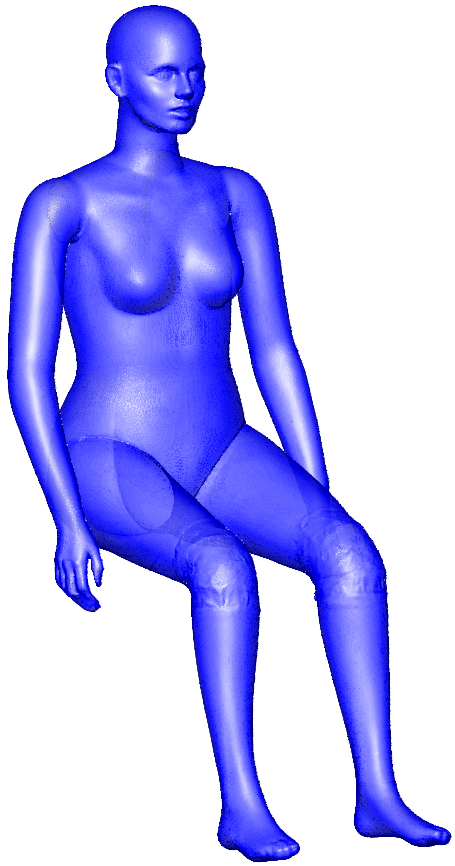

Figure 8.3: The surface geometry of the scanned thermal manikin. A high level of details were preserved during the scanning. The surface consists a approximately 500.000 cells with sidelengths ranging from 3 to 10 mm.

Using the diameter of the holes in floor, $l_{floor} = 0.003\ m$, as the length scale gives $\epsilon_{floor} = k_{floor}^{1.5}/l_{floor} = 1.73 \cdot 10^{-3}\ m^2/s^3$. For the constant eddy viscosity model no additional values need to be specified at the floor.

The low Reynolds number $k - \epsilon$ turbulence model was used, but this did not converge, probably because the flow was laminar in most of the domain. Murakami *et al* [74] reported that the $k - \epsilon$ model had problems with predicting the transition from laminar to turbulent flow in the boundary layer. In their work, the problem was circumvented by adding an extra source to the k and ϵ equations. In the present study a constant eddy viscosity model, $\nu_t = 5\nu$, without modifications near the walls was used. The constant, 5, was calibrated to give a whole-body average convective heat transfer coefficient of $h_c = 6.1\ W/(m^2K)$. This is somewhat larger than the computational whole-body average convective heat transfer coefficient of $h_c = 3.9W/(m^2K)$ for a manikin standing in stagnant air, Murakami *et al* [74]. Decreasing the constant made the computation unstable and led to problems with

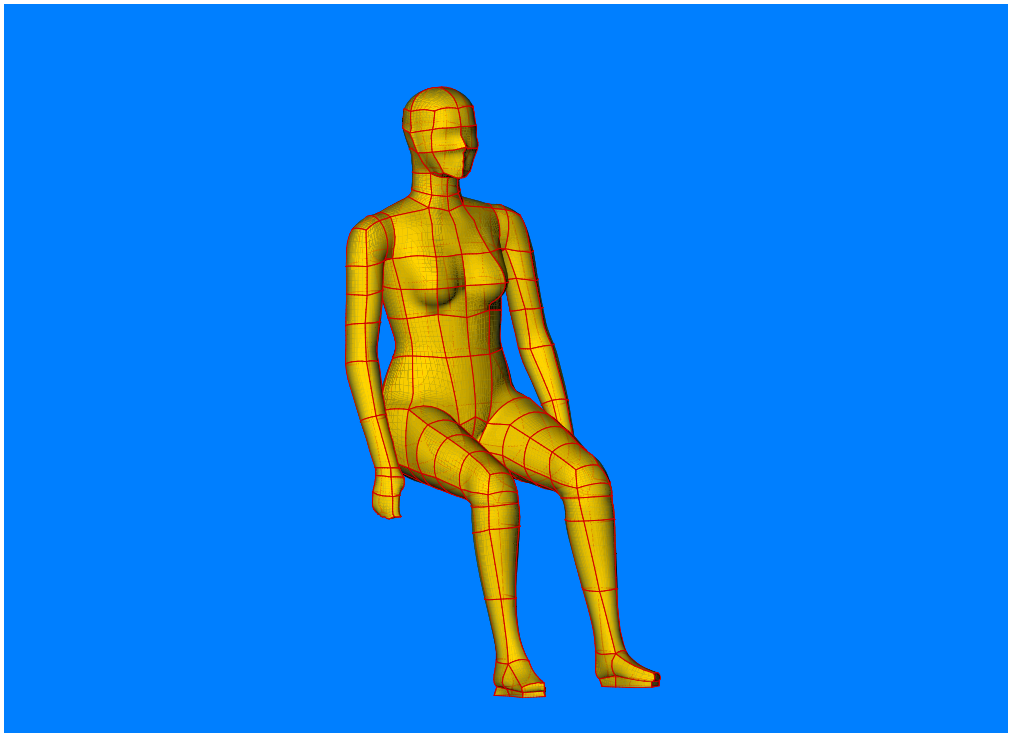

Figure 8.4: The surface for the thermal manikin after the grid generation. Since the number of points to represent the surface has decreased in the grid generation process, some details were modified. The red lines represent the block boundaries, each consisting of 8×8 cells on the surface.

convergence. Increasing the constant involved in the constant eddy viscosity model increased h_c. Thus, a value of 5 was found to be the best choice for the constant. y^+ is kept below 1.0 almost everywhere. In a small region on the arm and at the top of the chest y^+ reaches 1.5. At a few points on the mid chest and on the back y^+ reaches 2.5.

8.6 Results and discussion

In this section, the results obtained using the constant eddy viscosity model is compared with measurements. Table 8.3 contains measurements of the total, radiative and convective heat transfer coefficients for five points on the manikin, three on the lower leg and two on the torso. Furthermore, calculated values of the convective heat transfer coefficient in these points are presented. On the lower leg the convective heat transfer coefficient predicted by the computation is 0.5-1 $W/(m^2K)$ higher than found by the measurements. The most obvious reason for this was that the turbulence model used, suffers from insufficient modelling of the boundary layer, i.e no damping of the eddy viscosity took place near the walls. At the torso, the calculated convective heat transfer coefficient were lower than in experiments. At $z = 0.75\ m$, the calculated convective heat transfer coefficient was approximately

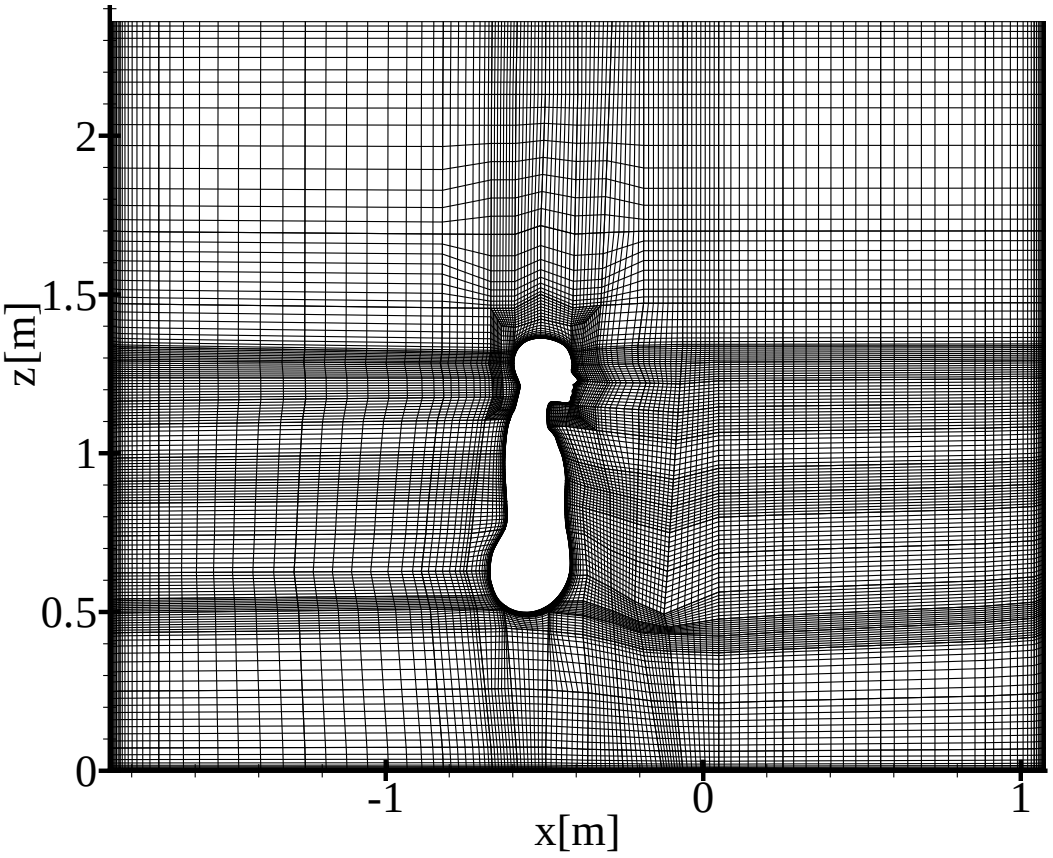

Figure 8.5: A cut through the symmetry plane of the computational grid.

0.1 $W/(m^2K)$ smaller than in the measurements, while calculations underpredicted measurements by approximately 1.2 $W/(m^2K)$ at $z = 0.95\ m$. Again it was most reasonable to ascribe this to the modelling of the boundary layer. The variation of the convective heat transfer coefficient along the computational manikin, is depicted in figure 8.6. As mentioned above, the values of the convective heat transfer coefficient was lower when calculated than when measured. In various other publications, the convective heat transfer coefficient showed peak values of 7-8 $W/(m^2K)$ at the feet level, see e.g Homma & Yakiyama [48] and Murakami *et al* [75]. Such high values was not observed in figure 8.6. However, no data below the ankle was included in this profile, and closer to the floor the present calculation showed values of h_c up to 11 $W/(m^2K)$.

$z[m]$	Body segment	$h_{tot,exp}[\frac{W}{m^2K}]$	$h_{r,exp}[\frac{W}{m^2K}]$	$h_{c,exp}[\frac{W}{m^2K}]$	$h_c[\frac{W}{m^2K}]$
0.15	Lower leg	7.77	4.55	3.22	4.17
0.24	Lower leg	8.57	4.55	4.02	4.54
0.38	Lower leg	8.05	4.54	3.51	4.12
0.60	Torso				4.05
0.75	Torso	9.00	4.57	4.43	4.34
0.95	Torso	8.47	4.65	3.82	2.60
1.10	Torso				5.49

Table 8.3: The first column is the distance to the floor, the second column is the body segment, third column is total measured heat transfer coefficient, fourth column is measured radiative heat transfer coefficient, fifth column is measured convective heat transfer coefficient and sixth column is calculated convective heat transfer coefficient. All results are for a nude thermal manikin.

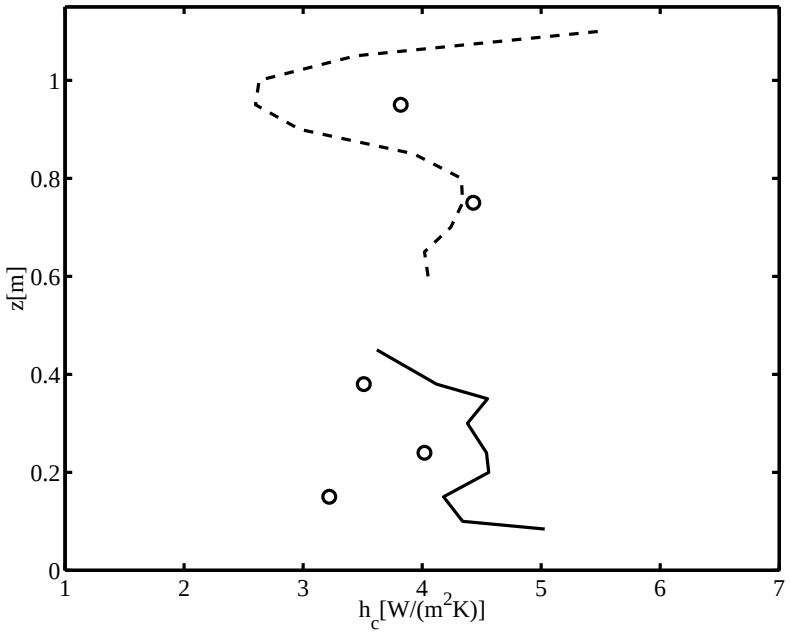

Figure 8.6: Variation of the convective heat transfer coefficient h_c. Calculated values of h_c are extracted in points with a distance of 0.05 m. ——: Lower leg. – – – –: Torso. o: Measurements, Holsøe [47].

For five of the vertical locations listed in table 8.3, horizontal velocity and temperature profiles are available. In figure 8.7, the computed and measured velocity profiles close to the lower leg are compared. Close to the floor, $z = 0.15$ m, the agreement between calculations and measurements are poor. For $x < 8$ mm the calculated velocities are clearly below the measured velocities, while for larger x values the opposite occurs. At $z = 0.24$ m the agreement between measurements and calculations improves close to the manikin, while further away the agreement is still

poor. For $z = 0.38\ m$ measurements and calculations show very similar results for $x < 15\ mm$, while for larger x the agreement is not very good. A dip exists at the calculated profiles for $z = 0.24\ m$ and $z = 0.38\ m$. These occur at $x \approx 5\ mm$ and $x \approx 6\ mm$, for $z = 0.24\ m$ and $z = 0.38\ m$, respectively. The grid was examined in this region and the dip could be caused by too large aspect ratios between adjacent points.

At the torso, figure 8.8, similar observations are made. At $z = 0.6\ m$ and at $z = 0.75\ m$, the agreement between measurements and calculations are poor. Close to the person, x less than approximately 5 mm, the calculations underpredict the measurements, while the opposite occurs for larger x. At $z = 0.95\ m$, measured and calculated velocity profiles have the same shape, but the calculated velocities are consistently larger than in the measurements. For $z = 1.1\ m$ calculations and measurements show rather good agreement, taking into account the simple turbulence model used. It must be concluded that using a constant eddy viscosity model does not lead to an optimal representation of the boundary layer around a computational manikin placed in a stagnant environment, since the agreement with measurement is only satisfying in a few regions. Undoubtful, an improved turbulence model would provide better results.

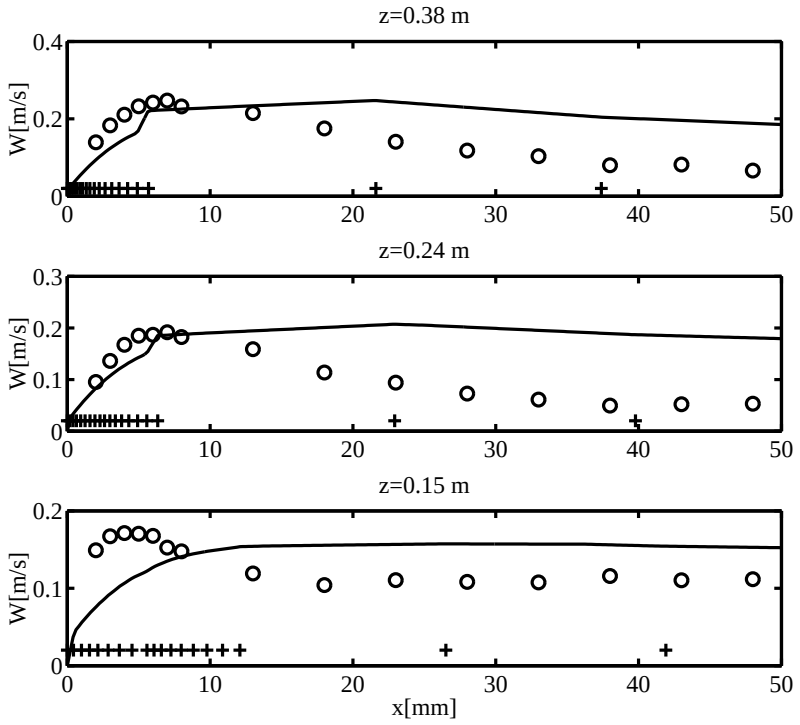

Figure 8.7: Velocity profiles at the lower leg for the nude manikin. ———: Calculation. o: Measurements, Holsøe [47]. +: Location of grid points.

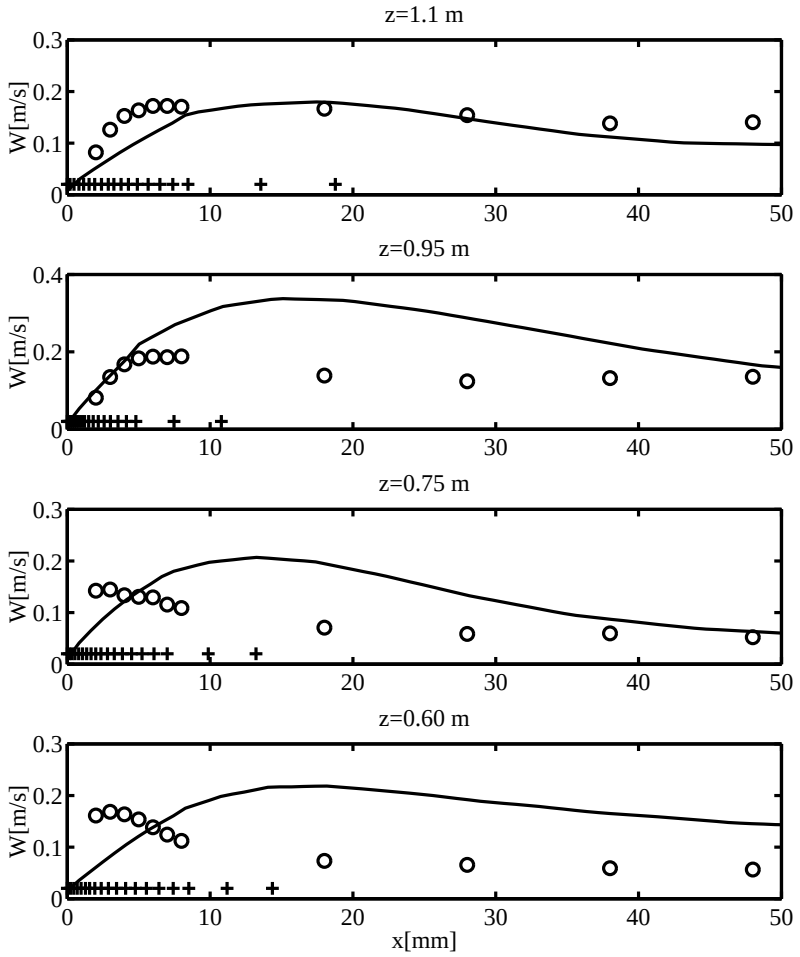

Figure 8.8: Velocity profiles at the torso for the nude manikin. Symbols, see figure 8.7.

Dimensionless temperature profiles in five of the vertical locations listed in table 8.3 are shown in figure 8.9 and 8.10. The discrepancy between calculations and measurements is significant for the vertical distances $z = 0.15\ m$, $z = 0.24\ m$ and $z = 0.38\ m$, see figure 8.9. For these locations, measurements were available for $7\ mm < x < 50\ mm$, calculations predict higher dimensionless temperatures than the measurements. A dip exists at each of the calculated profiles. These occurred at $x \approx 5\ mm$, $x \approx 6\ mm$ and $x \approx 11\ mm$ for $z = 0.15\ m$, $z = 0.24\ m$ and $z = 0.38\ m$, respectively. The dip could be caused by too large aspect ratios between adjacent grid points.

The residual was found to be periodic, using a steady solution procedure. The temperature profiles were evaluated twice during a period, and both predicted the same dip. Moreover, the variation of the velocity, temperature and heat flux near the computational manikin, showed a steady behaviour. Thus, no periodic effect seemed to exist in the flow field or temperature field near the computational manikin. Furthermore, the heat flux released from the computational manikin was stable.

At the torso, figure 8.10, measurements were available for 12 $mm < x < 50$ mm. The agreement between the calculations and measurements is poor, especially near the wall. The dip which occurred in the temperature profiles near the lower leg has vanished on the profiles near the torso.

Figure 8.9 and figure 8.10 indicate that the temperature decay from the computational manikin and throughout the boundary layer was not large enough in the calculations compared to measurements. More investigations are needed to explain this, but it seems reasonable that improving the turbulence model would improve both velocity and temperature profiles.

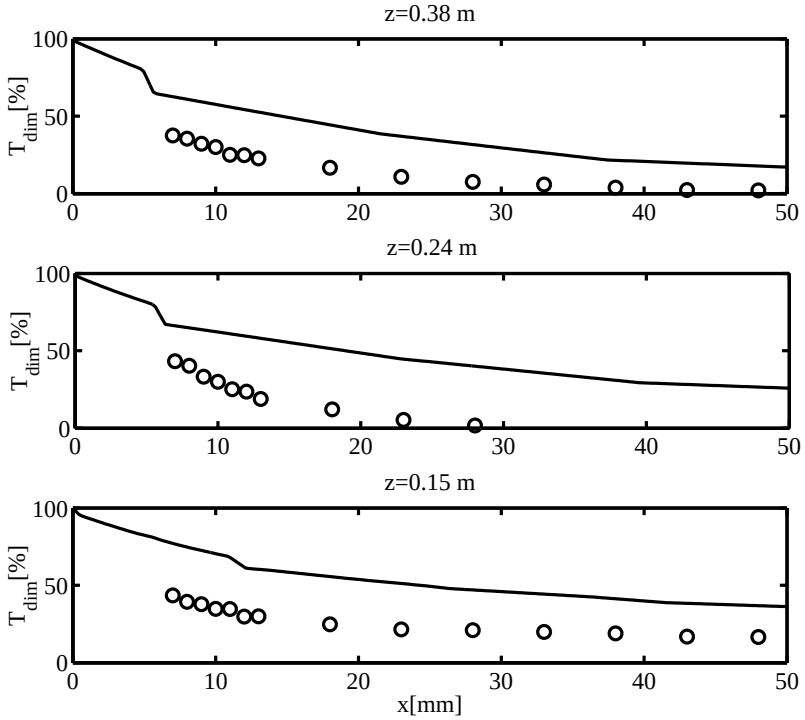

Figure 8.9: Dimensionless temperature profiles, $T_{dim} = (T - T_i)/(T_{sk} - T_i)$, at the lower leg for the nude manikin .

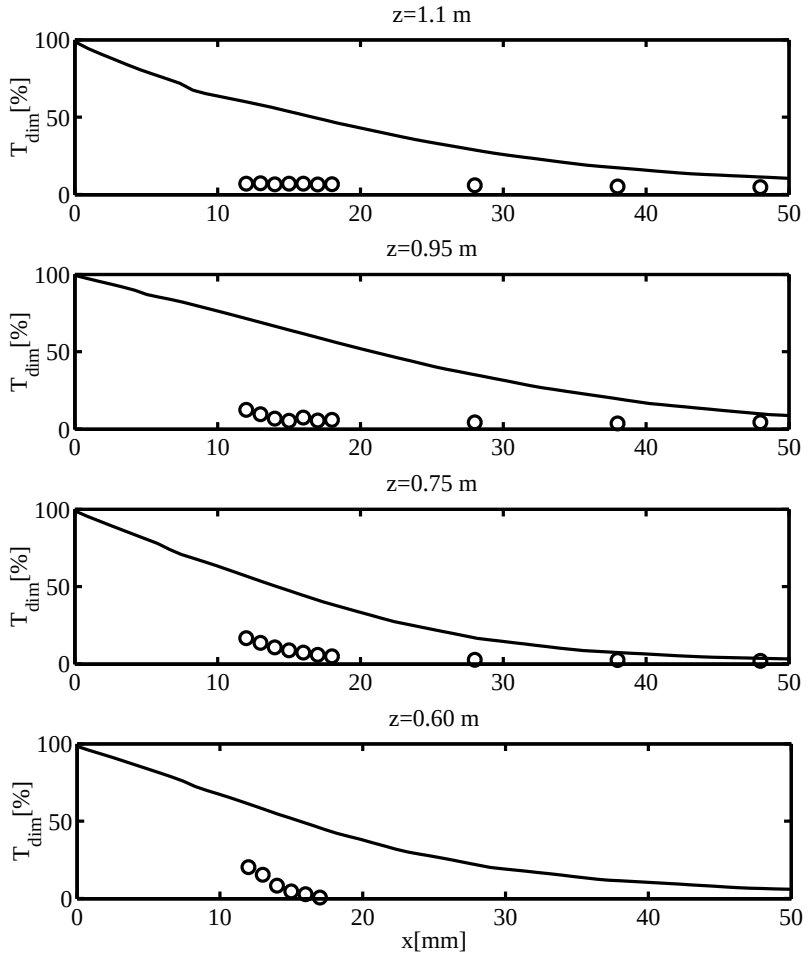

Figure 8.10: Temperature profiles, $T_{dim} = (T - T_i)/(T_{sk} - T_i)$, at the torso for the nude manikin.

8.7 Summary

The present chapter describes the first step in a process which should lead to accurate prediction of velocity and temperature distributions of the airflow around a detailed computational manikin.

A presentation of Fanger's comfort equation and the convective heat transfer coefficient was given in order to clarify how CFD in the future is expected to provide valuable information in the area of indoor climate. A three-dimensional laser scanning of the thermal manikin used in the experiments was obtained and a high level of detail was preserved during this process. A computational grid around the scanned surface of the manikin was obtained. Some details were modified during the grid generation, since the maximum number of grid points was restricted by limited computer resources. The most important modification was that the grid was only generated around half of the scanned manikin, which of course reduced the number

of grid points with 50%.

Boundary conditions which were in agreement with measurements were employed. This implied that the computational manikin with a constant surface temperature of 30.6 ^oC was placed in an almost stagnant environment. Using the low-Reynolds number $k-\epsilon$ model, the calculations would not converge. The reason was probably that the flow was laminar in most of the domain, and further that the $k-\epsilon$ model generally have problems with predicting the transition from laminar to turbulent in the boundary layer. Murakami *et al* [74] circumvented the latter problem by adding an extra source term in the k and ϵ equation. In the present study an alternative approach was taken. A constant eddy viscosity model without modifications near the walls was applied. Using $\nu_t = 5\nu$ gave convective heat transfer coefficients larger than measured values at the lower leg. Contrary to this, the predicted values was smaller than the measured values at the torso. The variation of the the convective heat transfer coefficient along the lower leg and the torso was investigated. Peak values of approximately 11 $W/(m^2K)$ was found near the floor. Elsewhere it was reported that h_c took peak values of 7-8 $W/(m^2K)$ close to the floor.

On comparing calculated and measured velocity profiles close to the lower leg and close to the torso, poor agreement was observed. Close to the computational manikin calculations underpredicted measurements, while further away the opposite occurred. For temperature profiles close to the lower leg and close to the torso, calculations generally overpredicted measurements. Improving the turbulence would probably improve the results. Close to leg the calculation of velocity profiles and temperatur profiles predicted an unexpected dip. It is believed that this is caused by the large aspect ratio of two adjacent grid points here.

Alltogether it is concluded that it was possible to carry out CFD calculations with a highly detailed representation of the thermal manikin used in the experiments. In a stagnant air flow the $k-\epsilon$ model fails to converge, while a simple turbulence model as a constant eddy viscosity model without modifications near the walls is not accurate enough to reproduce the velocity and temperature profiles near the body. In the future, more accurate turbulence models should be used.

Chapter 9

Conclusion

The work presented in this dissertation has focused on CFD for indoor airflows. It was chosen to use the in-house developed CFD code, *EllipSys*, which was efficient in computational costs, and thus reasonable calculations time was expected even for fine grids. The work falls into two categories. The first category was validation of the turbulence models already contained existing in the code, validation of the temperature equation for turbulent indoor airflows, implemention of a SGS model and validation of the code for LES. The other category concerned applications of the code. The code was used to predict different flow structures and different turbulent scales in ventilated rooms. This led to a new insight in the flow for the annex 20 test case. Furthermore, the airflow in a room with a temperature gradient was examined. Finally, calculations of the convective heat transfer, the airflow and the temperature distribution around an exact representation of the human body were carried out. The representation of the human body was the most exact ever used for such studies.

In chapter 3 the turbulence models were validated for two-dimensional calculations of isothermal airflow in the annex 20 test case. Five existing two-equation turbulence models were tested and a new turbulence model, the revised $k-\omega$ baseline model was developed. The results achieved with the standard $k-\epsilon$ model, the low Reynolds number $k-\epsilon$ model by Launder & Sharma, [56], the $k-\omega$ model by Wilcox [110], the $k-\omega$ baseline model by Menter [64] and the revised $k-\omega$ baseline model were almost equally good and led to results in reasonable good agreement with LDA measurements Nielsen [82]. The $k-\omega$ SST model by Menter [64] performed poorly. Furthermore, topological aspects of two-dimensional airflows in room were discussed. The results were compared with PIV measurements, Pedersen $ Meyer [88], from which coordinates for the separation point on the floor and the attachment point on the left wall were available. Deviations of less than ten percent from the measurements were obtained using the $k-\omega$ model by Wilcox [110]. This was found to be superior to the remaining models, which in some cases led to discrepancies of more than hundred percent.

In chapter 4 the turbulence models were validated for three-dimensional calculations of isothermal airflow in the annex 20 test case. The existing low Reynolds number models were tested. It was only possible to obtain a converged solution for the $k-\epsilon$ model and the revised $k-\omega$ baseline model. In terms of the mean velocity profiles, the two tested models showed good agreement with LDA measurements Nielsen [82].

Moreover, topological aspects of three-dimensional airflows in room were discussed. With PIV experiments, Pedersen $ Meyer [88], two new criteria for evaluating the performance of a turbulence model was proposed. First, the ability of the turbulence model to predict the location of stagnation points was used as a criterion. Second the ability of the turbulence model to reproduce the flow pattern near the stagnation point, i.e predict the correct type of the stagnation point, was used. Using the first new criterion, the location of the stagnation points were compared for two-dimensional calculations, three dimensional calculations using periodic boundary conditions and wall boundary conditions in the spanwise direction, respectively. The agreement with measurements was poor and discrepancies between measurements and calculations of 20-70 % were found. Only for the two-dimensional calculations using the original $k-\omega$ model the agreement was reasonable. The second new criterion was to classify the stagnation points. For the calculations, this was carried out for all stagnation points appearing in the center plane, even though experiments were only available for one third of the room. The classification of stagnation points revealed some interesting differences between the turbulence models used. For the two-dimensional calculations the trajectories were closed and saddles were connected by a trajectory due to the Hamiltonian property of the stream function. Moreover, only centres and saddles will occur. In the three dimensional calculations, the solution of the Navier-Stokes equations were no longer restricted by the Hamiltonian property. A variety of new types of stagnation points therefore exists. Two-dimensional calculations and three-dimensional calculations with periodic boundary conditions in the spanwise directions showed similar topologies. Applying wall boundary conditions in the spanwise direction, the recirculation zone occurring below the inlet took a very open structure. This was related to the fact that the stagnation point on the wall below the inlet was not a saddle but an unstable node. This was observed for the low Reynolds number $k-\epsilon$ model. For the high Reynolds number $k-\epsilon$ model the stagnation occurring at the wall below the inlet was a saddle. Thus, the recirculation zone took a more closed structure. However, none of the calculations, two-dimensional calculation using a low Reynolds number $k-\epsilon$ model, three-dimensional calculation using a low Reynolds number $k-\epsilon$ model or three-dimensional calculation using high Reynolds number $k-\epsilon$ model, were able to reproduce the topology obtained from experiments. It was concluded that the turbulence models for three-dimensional flows in room need further validation.

Chapter 5 contains a validation of the implemented SGS model. The constant involved in the SGS model was calibrated to 0.01. Comparing the mean velocity profile obtained with LES and coarse DNS with an existing DNS profile showed that LES

represented the DNS profile better than the coarse DNS profile. The LES results were compared with experimental data. These data show that the ratio of the standard deviation to the velocity at the centerline scales with the Reynolds number based on the centerline velocity. Insertion of LES data in the empirical relation found by Durst *et al* [28], yielded a difference of less than 10 % which was within the accuracy of the experiments. The standard deviation from the mean velocity for LES and DNS was compared. The agreement was best in the central part of the flow. For a time series of the streamwise component of the velocity in the boundary layer, an integral time scale of approximately 1.1 s was found. This value was a factor of 10 larger than the estimated temporal Taylor microscale of 0.12 s. The spatial Taylor microscale, which gives a measure of the size of the smallest eddies was estimated to 0.32 m. It was concluded that the implementation of the SGS model was correct in the sense that the calculation of the flow in a plane channel was in good agreement with DNS and experiments.

In chapter 6 a comparison of RANS and LES was carried out. In terms of the mean velocity profiles, the RANS method performed better than LES for the annex 20 test case. A comparison with previously presented results indicates the need for calibrating the constant appearing in the used SGS model. It was suggested that the constant should be increased. Comparing the $rms-$values, the RANS method tended to underpredict measurements, while LES predicted $rms-$values which were both higher and lower than measurements. Stretching of the grid in the inner domain led to a local minimum of $rms-$profiles based on LES. Therefore, local stretching away from walls should be avoided if possible. The maximum ratio of the modelled viscosity to the kinematic viscosity was found to be 100 times larger for RANS than for LES. Finally, the time spectra in seven points were generated and compared with time spectra based on measurements, Melikov [63]. The agreement between LES and measurements was good for wavenumbers less than approximately 50 m^{-1}. The deviation for wavenumbers larger than approximately 50 m^{-1} was believed to be attributed to the SGS modelling. It was concluded that the LES model was able to predict the airflow in rooms.

In chapter 7 the test case was the annex 20 room with a heated wall and a complex diffuser geometry. In the computations, the diffuser was modelled as a rectangular opening. For an air exchange rate of 6 h^{-1}, the computed velocity profiles were in good agreement with measurements by Jensen & Pedersen [52]. However, the velocity decay in the jet was underpredicted with the basic model. For a non-isothermal flow with a cold inlet jet and a a heated wall, the possible flow patterns which can occur in the center plane of the room were sketched. Further, an assumed bifurcation diagram, indicating where the different flow patterns occur as a function of the inverse Archimedes number, was constructed. From existing experiments, Jensen & Pedersen [52], a experimental bifurcation diagram was found. With a steady state solution procedure, it was not possible to obtain a stable solution with the air ex-

change rate of 6 h^{-1}. Increasing the airflow rate to 9.7 h^{-1} a steady solution was found and hereafter a computational bifurcation diagram was established. Due to the few measurements and computations available, it was difficult to compare the bifurcation diagram. The temperature distribution obtained by measurements with an air exchange rate of 6 h^{-1} and computations with an air exchange rate of 9.7 h^{-1} was compared. As expected the penetration length of the cold zone emanating from the inlet was shorter for the low air change rate than for the high air change rate. For the computations with air exchange rate of 9.7 h^{-1} the PD was calculated. For this case, the requirement of less than 10 % dissatisfied was fulfilled in most of the occupied zone. It was concluded that calculations of the airflow in the annex 20 test case need further investigations.

Chapter 8 contains calculations of the airflow around a computational manikin placed in a stagnant environment. The chapter describes the first step in a process which should lead to accurate predictions of velocity and temperature distributions in the airflow around a detailed computational manikin. A three-dimensional laser scanning of the thermal manikin used in the corresponding experiments, Holsøe [47], was carried out. A high degree of details was captured in this process. A grid was generated around the very complex geometry, and some details were modified during this process. The low Reynolds number $k-\epsilon$ model failed to converge and a constant eddy viscosity model without modifications near the walls was applied. Using $\nu_t = 5\nu$ gave convective heat transfer coefficients larger than the measured values at the lower leg. Contrary to this, the predicted values were smaller than the measured values at the torso. The variation of the convective heat transfer coefficient along the lower leg and the torso was investigated. Peak values of approximately 11 $W/(m^2K)$ was found near the floor. Comparing calculated and measured velocity profiles and temperature profiles close to the lower leg and close to the torso showed poor agreement. It was therefore concluded that it was possible to carry out CFD calculations with a highly detailed representation of the thermal manikin used in the experiments. However, in a stagnant airflow a simple turbulence model consisting of a constant eddy viscosity without modifications near the walls was not accurate enough to reproduce the velocity and temperature profiles near the body. In the future more accurate turbulence models should be used.

Even though this study improved the understanding of CFD for calculations of airflows in rooms, many questions were left open. It was not explained why the turbulence models in RANS calculations are not able to capture the experimental topology. Neither was it explained why RANS performs better LES for the annex 20 test case. A converged solution for the flow in the annex 20 test case with a heated wall was not obtained for the air exchange rate for which measurements are available. Finally, the choice of turbulence model for calculations of the airflow around a person sitting in a stagnant environment needs further investigations.

References

[1] (1998) *A Selection of Test Cases for the Validation of Large-Eddy Simulations of Turbulent Flows.*, AGARD advisory report 345.

[2] (2001) *Performance Optimization and Parallelization on Sun Systems.*, Notes for training by Sun Microsystems, Technical University of Denmark, February 13-15.

[3] Anderson, H.I., Braseth, A.O. and Holmedal, B. (1993) *Computation of the inlet wall jet in a rectangular enclosure.*, Comp. Fluid Dyn., vol. 1, 217-232.

[4] Arpaci, V.S. & Larsen, P.S (1984) *Convection Heat Transfer.* Prentice-Hall, Inc. New Jersey.

[5] Balaras, E., Benocci, C. and Piomelli, U. (1996) *Two-layer Approximate Boundary Conditions for Large-Eddy Simulation.*, AIAA Journal, Vol.34, No.6, June, 1111-1119.

[6] Behnia, M., Reizes, J.A. and de Vahl Davis, G. (1990) *Combined Radiation and Natural Convection in an Rectangular Cavity with a Transparent Wall and Containing a Non-participating Fluid.*, Int. J. for Num. Methods in Fluids, vol. 10, 305-325.

[7] Bennetsen, J.C. (1999) *Numerical Simulation of Turbulent Airflow in Livestock Buildings.*, Ph.D. dissertation, Department of Mathematical Modelling, DTU and Department of Agricultural Engineering, Research Centre Bygholm, Danish Institute for Agricultural Sciences.

[8] Bennetsen, J.C., Sørensen, J.N., Søgaard, H.T. and Christiansen, P.L. (1996) *Numerical simulation of turbulent airflow in a livestock building.*, ROOMVENT 1996, vol. 2, 169-176.

[9] Bird, R.B., Stewart, W.E. & Lightfoot, E.N. (1960) *Transport phenomena.*, John Wiley & Sons, 60-111, 243-264 & 310-352.

[10] Bjørn, E. and Nielsen, P.V. (1996) *Exposure due to interacting air flows between two persons.*, ROOMVENT 1996, vol. 1, 107-114.

[11] Bjørn, E. and Nielsen, P.V. (1998) *CFD simulation of contaminant transport between two breathing persons.*, ROOMVENT 1998, vol. 2, 133-140.

[12] Blomqvist, C. (1991) *Measurements of testcase B (forced convection, isothermal).*, IEA Annex 20, Research Item 1.16.

[13] Brohus, H. and Nielsen, P.V. (1996) *CFD models of persons evaluated by full-scale wind channel experiments.*, ROOMVENT 1996, vol. 2, 137-144

[14] Bowles, A. and Cheesewright, R. (1989) *Direct Measurements of the Turbulence Heat Flux in a Large Rectangular Air Cavity.*, Experimental Heat Transfer, vol. 2, 59-69.

[15] Byskov, R.K. (2000) *Large Eddy Simulation of Flow Structures in a Centrifugal Pump Impeller, Part II*, Ph.D dissertation, Ålborg University, ISBN 87-89179-30-5.

[16] Chen, Q. & Moser A. (1991) *Simulation of a multiple-nozzle diffuser.*, AIVC Conference on Air Movement and Ventilation Control within Buildings, Ottawa, Canada, September.

[17] Chen, Q. (1995) *Prediction of room air motion by Reynolds-stress models.*, Building and Environment, vol. 31, no. 3, 233-244.

[18] Chen, Q. and Xu, W. (1998) *A zero-equation turbulence model for indoor airflow simulation.*, Energy and Buildings 28, 137-144.

[19] Huo, Y., Haghighat, F., Zhang, J.S. and Shaw, C.Y. (2000) *A systematic approach to describe the air terminal device in CFD simulation for room air distribution analysis.*, Building and Environment 35, 563-576.

[20] Davidson, L. (1989) *Ventilation by displacement ventilation in a three dimensional room - a numerical study.*, Building and Environment, vol. 24, no. 4, 363-372

[21] Davidson, L. (1990) *Calculation of the turbulent buoyancy-driven flow in a rectangular cavity using an efficient solver and two different low Reynolds number* $k-\epsilon$ *turbulence models.*, Numerical Heat Transfer, Part A, vol. 18, 129-147.

[22] Davidson, L. (1990) *Second-order corrections of the* $k-\epsilon$ *model to account for non-isotropic effects due to buoyancy.*, Int. J. Heat and Mass Transfer, vol. 33, No. 12, 2599-2608.

[23] Davidson, L. (1996) *Implementation of a Large Eddy Simulation method applied to recirculating flow in a ventilated room..*, Department of Building Technology and Structural Engineering, Ålborg University, ISSN 1395-7953 R9611, 1-28.

[24] Davidson, L. and Nielsen, P. (1996) *Large Eddy Simulation of the Flow in a Three - Dimensional Ventilated Room.*, ROOMVENT 1996, vol. 2, 161-168.

[25] Davidson, L., Nielsen, P.V. and Topp, C.(2000) *Low-Reynolds number effects in ventilated rooms: a numerical study.*, ROOMVENT 2000, vol.1, 307-312.

[26] de Dear, R.J., Arens, E. and Hui, Z. (1997) *Convective and Radiative Heat Transfer Coefficients for Individual Human Body Segments.*, Int. J. Biometeorol, vol. 40, 141-156.

[27] Deardorff, J.W. (1970) *A Numerical Study of the Three-Dimensional Turbulent Channel Flow at Large Reynolds Number.*, J. of Fluid Mech., vol 41, 453-480.

[28] Durst, F., Fischer, M., Jovanović and Kikura, H. (1998) *Methods to Set Up and Investigate Low Reynolds Number, Fully Developed Turbulent Channel Flows.*, Journal of Fluids Engineering, vol. 120, 496-503.

[29] Emmerich S.J. and McGrattan (1998) *Application of a Large Eddy Simulation Model to Study Room Air Flow.*, ASHRAE Transactions, vol 104, issue 1, part B, 1128-1140.

[30] Emvin, P. and Davidson, L. (1996) *A numerical comparison of three inlet approximations of the diffuser in the case E1 Annex20.*, ROOMVENT 1996, vol. 1, 219-226.

[31] Emvin, P. and Davidson, L. (1997) *A local mesh refinement algorithm applied to turbulent flow*, International journal for numerical methods in fluids, vol. 24, 519-530.

[32] Fanger, P.O. (1967) *Calculation of Thermal Comfort: Introduction of a Basic Comfort Equation.*, ASHRAE Transactions, vol. 73, part II.,1-20.

[33] Fanger, P.O. (1970) *Thermal comfort.*, Danish Technical Press, Copenhagen.

[34] Fanger, P.O., Melikov, A.K., Hanzawa H. and Ring, J. (1988) *Air turbulence and sensation of draught.*, Energy and Buildings, 21-39.

[35] Farhangnia, M., Biringen, S. and Peltier, L.J. (1996) *Numerical Simulation of Two-dimensional Buoyancy-driven Turbulence in a Tall Rectangular Cavity.*, Int. J. for Num. Methods in Fluids, vol. 23, 1311-1326.

[36] Fontaine, J.R., Biolley, F., Rapp, R., Sérieys and Cunin, J.C. (1994) *Analysis of a three-dimensional validation flow: Experimental validation on a water scale model of numerical simulations.*, Numerical Heat Transfer, Part A, vol. 26, 431-451.

[37] Fossdal, S. (1990) *Measurements of testcase E (mixed convection, summer cooling).*, IEA Annex 20, Research Item 1.17.

[38] Gosman, A.D., Nielsen, P.V., Restivo, A. and Whitelaw, J.H. (1980) *The flow properties of rooms with small ventilation openings.*, Journal of Fluids Engineering, vol. 102, 316-323.

[39] Grimshaw, R. (1990) *Non-linear ordinary differential equations.,* Blackwell scientific publications.

[40] Härtel, C. and Kleiser, L. (1998) *Analysis and Modelling of Subgrid-scale motions in Near-wall Turbulence.*, J. of Fluid Mech., vol 356, 327-352.

[41] Hansen, H.E., Kjerulf-Jensen, P. & Stampe, O.B. (1997) *Varme- og klimateknik DANVAK*, 2. udgave. (in Danish)

[42] Hartnack, J.N (1999) *Streamline topologies near a fixed wall using normal forms.*, Acta Mechanica, vol. 136, issue 1, 55-75.

[43] Heikkinen, J. (1989) *Specification of Test case B.*, Appendix to IEA, RID no. 1.13.

[44] Henkes, R.A.W.M., van der Vlugt, F.F. and Hoogendoorn, C.J. (1991) *Natural-convection flow in a square cavity calculated with low-Reynolds-number turbulence models.*, Int. J. Heat and Mass Transfer, vol. 34, No. 2, 377-388.

[45] Henkes, R.A.W.M., and Hoogendoorn, C.J. (1993) *Scaling of the laminar natural-convection flow in a heated square cavity.*, Int. J. Heat and Mass Transfer, vol. 36, No. 11, 2913-2925.

[46] Hinze, J.O. (1975) *Turbulence.*, McGraw-Hill, Inc.

[47] Holsøe, J. (2001) *Personalized ventilation: Air movement around the human body.*, Private communication.

[48] Homma, H. and Yakiyama, M. (1988) *Examination of the Free Convection Around Occupants Body Caused by its Metabolic Heat Rate.*, ASHRAE Transactions, vol. 94, part 1, 104-124.

[49] Horiutu, K. (1989) *The Role of the Bardina Model in Large Eddy Simulation of Turbulent Flow.*, Brief Communications, Physics of Fluids, vol. 1, num. 2, February, 426-428.

[50] Issa, R.I. (1986) *Solution of the Implicitly Discretised Fluid Flow Equations by Operator-Splitting.*, J. Comput. Phys., Vol. 62, 40-65.

[51] Jameson, A. (1991) *Time Dependent Calculations Using Multigrid, with Applications to Unsteady Flows Past Airfoils and Wings.*, AIAA paper 91-1596, 1-8.

[52] Jensen, R.L. and Pedersen, D.N. (2000) *Strømningsforhold i opblandingsventileret kontorrum.*, Private communication.

[53] Johansson, P. and Davidson, L. (1995) *Modified collocated SIMPLEC algoritm applied to buoyancy-affected turbulent flow using a multigrid solution procedure*, Numerical Heat Transfer, Part B, vol. 28, 39-57.

[54] Kim, J., Moin, P and Moser, R. (1987) *Turbulence Statistics in Fully Developed Flow at Low Reynolds Number.*, J. of Fluid Mech., vol 177, 133-166

[55] Klyachko, L.S. (1963) *Heat Transfer Between a Gas and a Spherical Surface with the Combined Effect Action of Free and Forced Convection.*, ASME, Series C, J. Heat Transfer 85, 355-357.

[56] Launder, B.E. & Sharma, B.I. (1974) *Application of the Energy Dissipation Model of Turbulence to the Calculation of Flow Near a Spinning Disk.* Letters in Heat and Mass Transfer, Vol.1, No.2.

[57] Le Quéré, P. (1991) *Accurate Solutions to the Square Thermally Driven Cavity at High Rayleigh Number.* Comput. Fluids, 20, 29-41.

[58] Leong, W.H., Hollands, K.G.T. and Brunger, A.P. (1999) *Experimental Nusselt Numbers for a Cubical-cavity Benchmark Problem in Natural Convection.*, Int. J. Heat and Mass Transfer, vol. 42, 1979-1989.

[59] Liddell, F. D. K. (1963) *Estimation of energy expenditure from expired air.*, J. Appl. Physiol. 18, I, 25-29.

[60] Loc, T.P., Lardat, T., Coutanceau, M., Pineau, G. (1994) *Recherce er analyse de modéles de turbulence de sous maille adaptés aux écoulements instationnaires décollés.*, Rapport intermédiaire No. 2 de Contract DRET/LIMSI No 93074.

[61] McCutchan, J.W. and Taylor, C.L. (1951) *Respiratory heat exchange with varying temperatures and humidity of inspired air.*, J. Appl. Physiol. 4, 121-135.

[62] Mattsson, M., Bjørn, E., Sandberg, M. and Nielsen, P.V. (1997) *Simulating people moving in displacement ventilated rooms.*, Proceedings of Healthy Buildings/IAQ '97, Washington DC, USA, 1997, vol. 1, 495-500.

[63] Melikov, A.K. (1997) *Calibration and requirements for accuracy of thermal anemometers for indoor velocity measurements.*, REPORT-ET-IE9701.

[64] Menter, F.R., (1993) *Zonal Two Equation $k-\omega$ Turbulence Models for Aerodynamical Flows.* AIAA Paper No. 93-2906, 24th Fluid Dynamics Conference, Florida, 1-21.

[65] Menter, F.R. (1994) *Two-Equation Eddy-Viscosity Turbulence Models for Engineering Applications.* AIAA Journal, Vol.32, No.8, August, 1598-1605.

[66] Meyer, K.E., (1993) *Models for turbulent heat transfer.*, AFM 93-04, Department of Fluid Mechanics, 1-21, DTU.

[67] Michelsen, J.A., (1989) *Solution of the Navier-Stokes equations on general non-orthogonal meshes.*, AFM 89-08, Department of Fluid Mechanics, DTU.

[68] Michelsen, J.A., (1992) *Basis3D - a Platform for Development of Multiblock PDE Solvers.*, AFM 92-05, Department of Fluid Mechanics, DTU.

[69] Michelsen, J.A. (2000) *Implementation of a temperature equation.*, Private Communication.

[70] Moin, P. and Kim, J. (1982) *Numerical Investigation of Turbulent Channel Flow.*, J. of Fluid Mech., vol 118, 341-377.

[71] Moser, R., Kim, J. and Mansour, N.N. (1999) *Direct Numerical Simulation of Turbulent Channel Flow.*, Physics of Fluids, vol. 11, num. 4, April, 943-945.

[72] Myllerup, L. (2000) *Turbulence Models for Complex Flows.*, ET-PHD 2000-03, Department of Energy Engineering, Fluid Mechanics Section., 1-104.

[73] Murakami, S., Kato, S. and Zeng, J. (1995) *Development of a computational thermal manikin - CFD analysis of thermal environment around human body.*, Proc. Tsinghua-HVAC-95, Beijing, 349-354.

[74] Murakami, S., Kato, S. and Zeng, J. (1997) *Flow and temperature fields around human body with various room air distribution, Part 1 - CFD study on computational thermal manikin.*, ASHRAE Transactions, 103(1), 3-15.

[75] Murakami, S., Zeng, J., Hayashi, T. (1999) *CFD analysis of wind environment around a human body.*, Journal of Wind Engineering and Industrial Aerodynamics, 83, 393-408.

[76] Murakami, S., Kato, S. and Zeng, J. (2000) *Combined simulation of airflow, radiation and moisture transport for heat release from a human body.*, Building and Environment, 35, 489-500.

[77] Newell, M.E. and Schmidt, F.W. (1970) *Heat tranfer by laminar natural convection within rectangular enclosures.*, ASME, J. of Heat Transfer, February, 159-168.

[78] Nielsen, M. and Pedersen, L. (1952) *Studies on the Heat Loss by Radiation and Convection from the Clothed Human Body.*, From the Zoophysiological Laboratory, University of Copenhagen and from the Technological Institute, Copenhagen.,272-294.

[79] Nielsen, P.V. (1973) *Berechnung der luftbewegung in einem zwangsbelüfteten raum*, Gesundheits-Ingeneieur, 94, 299-302.

[80] Nielsen, P.V., Restivo, A. and Whitelaw, J.H. (1978) *The velocity characteristics of ventilated rooms.*, Journal of Fluids Engineering, vol.100, September, 291-298.

[81] Nielsen, P.V. (1989) *Airflow Simulation Techniques - Progress and Trends.*, 10th AIVC Conference on Progress and Trends in Air Infiltration and Ventilation Research, vol.1, 203-223, ISBN o 946075 45x, The Air Infiltration and Ventilation Centre, Coventry

[82] Nielsen, P.V. (1990) *Specification of a Two-dimensional Test Case.*, International Energy Agency, Annex 20: Air Flow Pattern Within Buildings., Department of Building Technology and Structural Engineering, Ålborg University, ISSN 0902-7513 R9040, 11-15.

[83] Nielsen, P.V (1992) *Description of supply openings in numerical models for room air distribution.*, ASHRAE Trans., vol. 98, part 1, 963-971.

[84] Nielsen, P.V (1998) *The selection of turbulence models for prediction of room air flow.,* ASHRAE Trans., vol. 104, part 1B, 1119-1127.

[85] Nielsen, P.V., Jensen, R.L, Pedersen, D.N, Topp, C. (2001) *Air distribution in a room and design considerations of mixing ventilation by flow elements.*, Accepted for publication in the proceedings of IAQVEC 2001, The 4th International Conference On Indoor Air Quality, Ventilation and Energy Conservation in Buildings, Changsha, Hunan, China.

[86] Paolucci, S. (1990) *Direct numerical simulation of two-dimensional turbulent natural convection in an enclosed cavity.*, J. of Fluid Mech., vol 215, 229-262.

[87] Patankar, S.V. (1980) *Numerical Heat Transfer and Fluid Flow.*, Hemisphere Publishing Corporation, Taylor & Francis Group, New York.

[88] Pedersen, J.M. and Meyer, K.E.,(2001) *Analysis of Flow Structures in an Annex 20 Room.*, To appear on 4th International Symposium on Particle Image Velocimetry, Göttingen, Germany, September 17-19.

[89] Peng, S. and Davidson, L. (1997) *Computation of turbulent buoyant flows in enclosures with low-Reynolds-number $k-\omega$ models.*, Doktorsavhandlingar vid Chalmers Tekniska Hogskola, 1391, 1-23.

[90] Peng, S, Davidson, L. and Holmberg S. (1997) *A modified low-Reynolds number $k-\omega$ model for recirculating flow.*, ASME Journal of fluids engineering, vol. 119, 867-875.

[91] Piomelli, U., Moin, P. and Ferziger, J.H. (1988) *Model Consistency in Large Eddy Simulation of Turbulent Channel Flows.*, Physics of Fluids, vol. 31, num. 7, July, 1884-1891.

[92] Piomelli, U., Cabot, W.H., Moin, P. and Lee S. (1991) *Subgrid Scale backscatter in turbulent and transtitional flows.*, Physics of Fluids A, vol. 3, num. 7, July, 1766-1771.

[93] Rapp, G.M. (1973) *Convective Heat Transfer and Convective Coefficients of Nude Man, Cylinders and Spheres at Low Air Velocities.*, ASHRAE Transactions, vol. 79, part 1, 75-87.

[94] Rhie, C.M., (1981) *A numerical study of the flow past an isolated airfoil with separation.* Ph.D. thesis, University of Illinois, Urbane- Champaign.

[95] Sagaut, P. (2001) *Large eddy simulation for incompressible flows.,* Springer-Verlag, Berlin Heidelberg.

[96] Sandberg, M. (1987) *Velocity characteristics in mechanically ventilated office rooms.*, ROOMVENT 1987, vol. 2a, 1-14.

[97] Schlichting, H., (1968) *Boundary-Layer Theory.* McGraw-Hill Book Company.

[98] Schmidt, Jens J., (1997) *Experimental and numerical investigation of separated flows.*, ET-PHD 97-01, Department of Energy Engineering, Fluid mechanics Section, DTU, 105-163.

[99] Skovgaard, M. & Nielsen P.V. (1991) *Modelling complex inlet geometries in CFD - applied to airflow in ventilated room.*, AIVC Conference on Air Movement and Ventilation Control within Buildings, Ottawa, Canada, September.

[100] Speziale, C.G., Ridha, A., Anderson, E.C., (1992) *Critical Evaluation of Two-Equation Models for Near-Wall Turbulence.* AIAA Journal, Vol.30, No.2, February, 324-331.

[101] Shur, M., Spalart, P.R., Strelets, M. and Travin, A. (1999) *Detached-eddy simulation of an airfoil at high angle of attack.*, Engineering Turbulence Modelling and Experiments 4, 669-678.

[102] Sørensen, D.N., (1999) *Development of a grid generator based on a hyperbolic tangent function.*, Private communication.

[103] Sørensen, N.N., (1995) *General Purpose Flow Solver Applied to Flow over Hills.* Ph.D. Thesis, Risø National Laboratory, Roskilde, Denmark, Risø-R-827(EN).

[104] Tafti, D.K. and Vanka, S.P. (1991) *A Numerical Study of The Effects of Spanwise Rotation on Turbulent Channel Flow.*, Physics of Fluids, vol. 3, num. 4, April, 642-656.

[105] Tennekes, H. & Lumley, J.L, (1972) *A First Course in Turbulence.,* The MIT Press Design Department.

[106] Topp, C., Jensen, R.L, Pedersen, D.N, Nielsen, P.V (2001) *Validatin of boundary conditions for CFD simulations on ventilated rooms.*, Accepted for publication in the proceedings of IAQVEC 2001, The 4th International Conference On Indoor Air Quality, Ventilation and Energy Conservation in Buildings, Changsha, Hunan, China.

[107] de Vahl Davis, G. (1983) *Natural Convection of Air in a Square Cavity: a Benchmark Numerical Solution.*, Int. J. for Num. Methods in Fluids, vol. 3, 249-264.

[108] Voigt, L.P.K (2000) *Comparison of turbulence models for numerical calculation of airflow in an Annex 20 room.*, ET-AFM 2000-01, Department of Energy Engineering, Fluid Mechanics Section, International Centre for Indoor Environment and Energy, 1-39, DTU.

[109] Whittle, G.E. (1991) *Presentation of results from measurements and simulations of test cases B, D, E, F and 2D.* IEA, Report E.

[110] Wilcox, D.C., (1988) *Reassessment of the Scale-Determining Equation for Advanced Turbulence Models.* AIAA Journal, Vol.26, No.11, November, 1299-1310.

[111] Winslow, C.-E.A., Gagge, A.P and Herrington, L.P. (1939) *The Influence of Air Movement Upon Heat Losses from the Clothed Human Body.*, Jour. Physiology, Vol. 127,505-518.

[112] Xu, W and Chen, Q.(2001) *A two-layer turbulence model for simulating indoor airflow. Part II. Applications.*, Energy and Buildings 33, 627-639.

[113] Xu, W, Chen, Q. and Nieuwstadt, F.T.M (1998)*A new turbulence model for near wall natural convection.,* Int. J. of Heat and Mass Transfer. vol. 41, 3161-3176.

[114] Wu, X., Squires, K.D. and Lund, T.S. (1995) *Large Eddy Simulation of a Spatially-Developing Boundary Layer.*, Preceeding of the ACM/IEEE Supercomputing Conference, vol. 2, 1838-1857.

[115] Zahrai, S., Bark, F.H. and Karlsson, R.I. (1995) *On Anisotropic Subgrid Modelling.*, Eur. J. Mech., B/Fluids 14, num. 4, 459-486.

[116] Zang, T.A. (1991) *Numerical Simulation of the Dynamics of Turbulent Boundary Layers: Perspectives of a Transition Simulator.*, Philosophical Tansactions of the Royal Society, vol. 336, 95-102.

Appendix A

Computational grid

A.1 Hyperbolic grid stretching

In this section a function for stretching based on a hyperbolic tangent function is suggested. The grid generator was developed by Sørensen [102].

Denoting the start and ending points for the grid by y_0 and y_1, respectively, a general function for the distribution of the points may be written as

$$y = y_0 + (y_1 - y_0)f, \tag{A.1}$$

where the function f lies in the interval from zero to one, both included. Using hyperbolic tangent functions, three variations of the function f may be used, depending on the desire to stretch towards both y_0 and y_1, towards y_0 only or towards y_1 only. Applying the information that $f(j = 1) = 0$ and $f(j = ny) = 1$, the three functions can be written as

$$f(j) = \frac{\tanh\left(K\left(\frac{2(j-1)}{ny-1} + K_1\right)\right) - \tanh\left(K \cdot K_1\right)}{\tanh\left(K\left(2 + K_1\right)\right) - \tanh\left(K \cdot K_1\right)}, \tag{A.2}$$

$$f(j) = \frac{\tanh\left(K\left(\frac{j-1-(ny-1)}{ny-1}\right)\right)}{\tanh(K)} + 1, \tag{A.3}$$

and

$$f(j) = \frac{\tanh\left(K\left(\frac{j-1}{ny-1}\right)\right)}{\tanh(K)}, \tag{A.4}$$

respectively. The constants K and K_1 in (A.2) are determined by the required cell heights in the first and last cell, respectively. K in (A.3) is determined by the required cell height in the first cell and K in (A.4) by the cell height in the last cell. The function stretching towards both ends, equation (A.2), is used as an example. The required cell heights in the first and last cell are S_0 and S_1, and followingly the

first and last cell becomes

$$f(2) = \frac{tanh\left(K\left(\frac{2}{ny-1} + K_1\right)\right) - tanh\left(K \cdot K_1\right)}{tanh\left(K\left(2 + K_1\right)\right) - tanh\left(K \cdot K_1\right)} = S_{0,n}, \tag{A.5}$$

and

$$f(ny-1) = \frac{tanh\left(K\left(\frac{2(ny-2)}{ny-1} + K_1\right)\right) - tanh\left(K \cdot K_1\right)}{tanh\left(K\left(2 + K_1\right)\right) - tanh\left(K \cdot K_1\right)} = 1 - S_{1,n}, \tag{A.6}$$

where $S_{0,n}$ and $S_{1,n}$ are the original values of S_0 and S_1 divided by $(y_1 - y_0)$. For use with the Newton-Raphson method, the equations may be rewritten as

$$S_{0,n} - \frac{tanh\left(K\left(\frac{2}{ny-1} + K_1\right)\right) - tanh\left(K \cdot K_1\right)}{tanh\left(K\left(2 + K_1\right)\right) - tanh\left(K \cdot K_1\right)} = 0, \tag{A.7}$$

and

$$1 - S_{1,n} - \frac{tanh\left(K\left(\frac{2(ny-2)}{ny-1} + K_1\right)\right) - tanh\left(K \cdot K_1\right)}{tanh\left(K\left(2 + K_1\right)\right) - tanh\left(K \cdot K_1\right)} = 0. \tag{A.8}$$

Thus, by solving the non-linear system of equations given by (A.7) and (A.8), the coefficients K and K_1 can be found. The solution is performed by standard methods. After determination of K and K_1, the equations (A.1) and (A.2) are used to calculate the grid-point positions. Similar procedures are carried out for the functions stretching towards one end only. Here only one unknown K value exist. An example of distributing eight cells between two horizontal plates, stretching towards both ends is shown in figure A.1

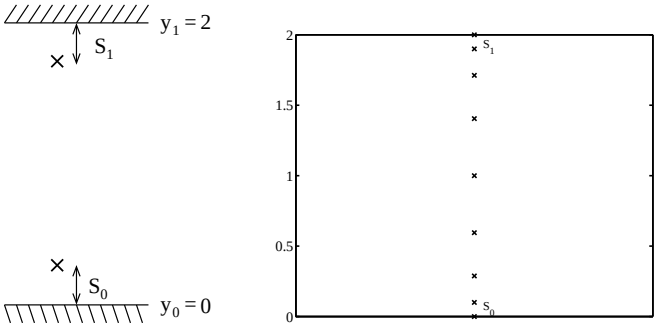

Figure A.1: Distribution of eight cells between two horizontal plates. Left: Input needed by the grid generator distributing the cells. Right: The grid points returned by the grid generator. The stretching results in more narrow cells close to the walls.

With the present grid generator a grid for a two-dimensional room geometry was generated. The block structure is shown in figure A.2, while the grid is illustrated in figure A.3. The grid consists of 96 cells in the horizontal direction and 64 cells in

the vertical direction. The inlet constists of 16×16 cells, and the outlet consists of 16×16 celss.

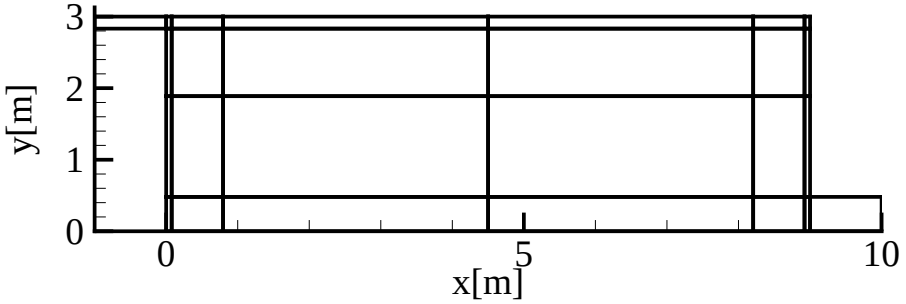

Figure A.2: Block structure for a computational grid generated with the present grid generator. Six blocks are used in the horizontal direction and four blocks are used in the vertical direction. Two extra blocks is added to model the inlet and outlet, respectively.

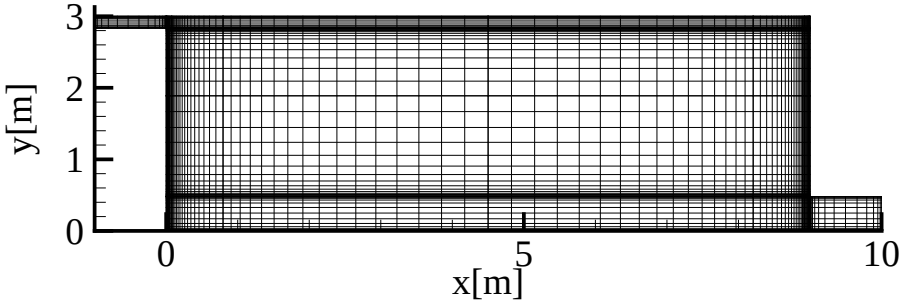

Figure A.3: Computational grid generated with the present grid generator. The block structure shown in figure A.2 was used, and each block consists of 16×16 cells.

A.2 *ICEM* to *EllipSys* interface

When creating a structured grid using the commercial grid generator *ICEM*, none of the output formats available can be directly interpreted by the *EllipSys* code. Thus, it is necessary to develop a translator converting a standard output file from *ICEM* to *EllipSys*. It was chosen to export the grid in the *Multiblock-info* format. This results in two files, the "info.geo" file holding the grid points and the "info.topo" file containing information about boundary conditions and the connectivity between the blocks. The connectivity between the blocks is handled by the *Basis* platform, the preprocessor for the *EllipSys* code, and is therefore not read by the translator. The "info.geo" is read block wise by the translator. After reading each block, the boundary conditions are applied using the relevant information from the "info.topo" file. The output is exported in the *EllipSys* format.

Appendix B

Derivation of $k-\epsilon$ transport equations

B.1 The k equation

The turbulent kinetic energy k, is defined as $k \equiv \frac{1}{2}\overline{u_i' u_i'}$. A transport equation for k is obtained by multiplying the Navier-Stokes equations with u_i' and taking the time average. Physically, this corresponds to requiring conservation of the mechanical energy connected to the velocity fluctuation. Introducing the decomposed quantities,

$$\begin{aligned} u_i'\frac{\partial U_i}{\partial t} + u_i'\frac{\partial u_i'}{\partial t} &+ u_i' U_j \frac{\partial U_i}{\partial x_j} + u_i' U_j \frac{\partial u_i'}{\partial x_j} + u_i' u_j' \frac{\partial U_i}{\partial x_j} + u_i' u_j' \frac{\partial u_i'}{\partial x_j} \\ &= -\frac{1}{\rho}\left(u_i'\frac{\partial P}{\partial x_i} + u_i'\frac{\partial p}{\partial x_i}\right) + \nu\left(u_i'\frac{\partial^2 U_i}{\partial x_j^2} + u_i'\frac{\partial^2 u_i'}{\partial x_j^2}\right) \end{aligned} \tag{B.1}$$

is obtained. Taking the time-average, introducing the identity

$$\overline{u_i'\frac{\partial u_i'}{\partial x_j}} = \frac{\partial\left(\frac{1}{2}\overline{u_i' u_i'}\right)}{\partial x_j} = \frac{\partial k}{\partial x_j} \tag{B.2}$$

together with continuity, leads to the transport equation

$$\frac{\partial k}{\partial t} + U_j\frac{\partial k}{\partial x_j} = \underbrace{-\overline{u_i' u_j'}\frac{\partial U_i}{\partial x_j}}_{\mathcal{P}_k} \underbrace{- \frac{\partial}{\partial x_j}\left(\frac{\overline{p' u_j'}}{\rho} + \frac{1}{2}\overline{u_j' u_i' u_i'}\right)}_{\mathcal{D}_k} + \underbrace{\nu\overline{u_i\frac{\partial^2 u_i'}{\partial x_j^2}}}_{\mathcal{V}_k} \tag{B.3}$$

for the turbulent kinetic energy. In (B.3) $\mathcal{P}_k$ is the production of k, $\mathcal{D}_k$ is interpreted as the diffusion of k, and $\mathcal{V}_k$ is the effect of the molecular viscosity.

Applying the Boussinesq approximation equation (2.7), the production term $\mathcal{P}_k$ is modelled by

$$\begin{aligned} \mathcal{P}_k &= \nu_t\left(\frac{\partial U_i}{\partial x_j} + \frac{\partial U_j}{\partial x_i}\right)\frac{\partial U_i}{\partial x_j} - \frac{2}{3}k\delta_{ij}\frac{\partial U_i}{\partial x_j} \\ &= \nu_t\left(\frac{\partial U_i}{\partial x_j} + \frac{\partial U_j}{\partial x_i}\right)\frac{\partial U_i}{\partial x_j}. \end{aligned} \tag{B.4}$$

The latter reduction occurs due to continuity for the incompressible case. The diffusion term is modelled using a gradient transport hypothesis

$$\mathcal{D}_k = -\frac{\partial}{\partial x_j}\left(\frac{\nu_t}{\sigma_k}\frac{\partial k}{\partial x_j}\right), \tag{B.5}$$

see Speziale *et al* [100]. Here σ_k is the turbulent Prandtl number, normally taken to be unity. Finally, the term due to the effect of the molecular viscosity is rewritten, and thus

$$\begin{aligned}
\mathcal{V}_k &= \nu\overline{u_i'\frac{\partial^2 u_i'}{\partial x_j^2}} \\
&= \nu\frac{\partial}{\partial x_j}\left(\overline{u_i'\frac{\partial u_i'}{\partial x_j}}\right) - \nu\overline{\frac{\partial u_i'}{\partial x_j}\frac{\partial u_i'}{\partial x_j}} \\
&= \nu\frac{\partial}{\partial x_j}\left(\overline{u_i'\frac{\partial u_i'}{\partial x_j}}\right) - \epsilon,
\end{aligned} \tag{B.6}$$

where ϵ denotes the isotropic dissipation of turbulent kinetic energy. Inserting equation (B.4), (B.5) and (B.6) into equation (B.3),

$$\frac{\partial k}{\partial t} + U_j\frac{\partial k}{\partial x_j} = \nu_t\left(\frac{\partial U_i}{\partial x_j} + \frac{\partial U_j}{\partial x_i}\right)\frac{\partial U_i}{\partial x_j} + \frac{\partial}{\partial x_j}\left[\left(\nu + \frac{\nu_t}{\sigma_k}\right)\frac{\partial k}{\partial x_j}\right] - \epsilon. \tag{B.7}$$

is finally obtained.

B.2 The ϵ equation

In the previous section the dissipation of turbulent kinetic energy was defined as $\epsilon \equiv \nu\overline{\frac{\partial u_i'}{\partial x_j}\frac{\partial u_i'}{\partial x_j}}$. By applying the operator $\nu\frac{\partial u_i'}{\partial x_j}\frac{\partial}{\partial x_j}$ to the Navier-Stokes equations, again introducing the decomposed quantities, it is found that

$$\begin{aligned}
&\nu\frac{\partial u_i'}{\partial x_j}\frac{\partial}{\partial x_j}\left[\underbrace{\frac{\partial(U_i+u_i')}{\partial t}}_{I} + \underbrace{(U_j+u_j')\frac{\partial(U_i+u_i)}{\partial x_j}}_{II}\right] \\
= \;& \nu\frac{\partial u_i'}{\partial x_j}\frac{\partial}{\partial x_j}\left[\underbrace{\frac{1}{\rho}\frac{\partial(P+p')}{\partial x_i}}_{III} + \underbrace{\nu\frac{\partial^2(U_i+u_i')}{\partial x_j^2}}_{IV}\right].
\end{aligned} \tag{B.8}$$

From (B.8) the ϵ-equation is derived. To maintain the overview the rigorous procedure used by Schmidt in [98] is followed. Taking the time average and writing the

terms in their full extent it is found that

$$I: \quad \nu\overline{\frac{\partial u_i'}{\partial x_j}\frac{\partial^2 U_i}{\partial x_j \partial t}} + \overline{\frac{\partial u_i'}{\partial x_j}\frac{\partial^2 u_i'}{\partial x_j \partial t}} = 0 + \frac{1}{2}\frac{\partial \epsilon}{\partial t} \tag{B.9}$$

$$\begin{aligned}
II: \quad & \nu\overline{\frac{\partial u_i'}{\partial x_k}\frac{\partial}{\partial x_k}\left(U_j\frac{\partial U_i}{\partial x_j}\right)} + \nu\overline{\frac{\partial u_i'}{\partial x_k}\frac{\partial}{\partial x_k}\left(U_j\frac{\partial u_i'}{\partial x_j}\right)} \\
+ \; & \nu\overline{\frac{\partial u_i'}{\partial x_k}\frac{\partial}{\partial x_k}\left(u_j'\frac{\partial U_i}{\partial x_j}\right)} + \nu\overline{\frac{\partial u_i'}{\partial x_k}\frac{\partial}{\partial x_k}\left(u_j'\frac{\partial U_i}{\partial x_j}\right)} \\
= \; & 0 + \nu\frac{\partial U_j}{\partial x_k}\overline{\frac{\partial u_i'}{\partial x_j}\frac{\partial u_i'}{\partial x_k}} + \nu U_j\overline{\frac{\partial}{\partial x_j}\left[\frac{1}{2}\left(\frac{\partial u_i'}{\partial x_k}\right)^2\right]} \\
+ \; & \nu\frac{\partial U_i}{\partial x_j}\overline{\frac{\partial u_i'}{\partial x_k}\frac{\partial u_j'}{\partial x_k}} + \nu\frac{\partial^2 U_j}{\partial x_j \partial x_k}\overline{u_j'\frac{\partial u_i'}{\partial x_k}} \\
+ \; & \nu\overline{\frac{\partial u_i'}{\partial x_j}\frac{\partial u_i'}{\partial x_k}\frac{\partial u_j'}{\partial x_k}} + \nu\overline{u_j'\frac{\partial}{\partial x_j}\left[\frac{1}{2}\left(\frac{\partial u_i'}{\partial x_k}\right)^2\right]} \\
= \; & \frac{1}{2}U_j\frac{\partial \epsilon}{\partial x_j} + \nu\frac{\partial U_i}{\partial x_k}\left(\frac{\partial u_i'}{\partial x_j}\frac{\partial u_i'}{\partial x_k} + \frac{\partial u_i'}{\partial x_j}\frac{\partial u_k'}{\partial x_j}\right) + \nu\frac{\partial^2 U_j}{\partial x_j \partial x_k}\overline{u_j'\frac{\partial u_i'}{\partial x_k}} \\
+ \; & \nu\overline{\frac{\partial}{\partial x_j}\left[u_j'\frac{1}{2}\left(\frac{\partial u_i'}{\partial x_k}\right)^2\right]} + \nu\overline{\frac{\partial u_i'}{\partial x_j}\frac{\partial u_i'}{\partial x_k}\frac{\partial u_j'}{\partial x_k}}
\end{aligned} \tag{B.10}$$

$$III: \quad -\frac{\nu}{\rho}\left[\overline{\frac{\partial u_i'}{\partial x_j}\frac{\partial^2 P}{\partial x_i \partial x_j}} + \overline{\frac{\partial u_i'}{\partial x_j}\frac{\partial^2 p'}{\partial x_i \partial x_j}}\right] = -\frac{\nu}{\rho}\overline{\frac{\partial}{\partial x_i}\left(\frac{\partial u_i'}{\partial x_j}\frac{\partial p'}{\partial x_j}\right)} \tag{B.11}$$

$$\begin{aligned}
IV: \quad & \nu^2\overline{\frac{\partial u_i'}{\partial x_k}\frac{\partial^3 U_i}{\partial x_j \partial x_j \partial x_k}} + \nu^2\overline{\frac{\partial u_i'}{\partial x_k}\frac{\partial^3 u_i'}{\partial x_j \partial x_j \partial x_k}} \\
= \; & 0 + \nu^2\overline{\frac{\partial u_i'}{\partial x_k}\frac{\partial^3 u_i}{\partial x_j \partial x_j \partial x_k}} \\
= \; & \nu^2\frac{\partial^2}{\partial x_j \partial x_j}\left[\frac{1}{2}\overline{\left(\frac{\partial u_i'}{\partial x_k}\right)^2}\right] - \nu^2\overline{\left(\frac{\partial^2 u_i'}{\partial x_j \partial x_k}\right)^2} \\
= \; & \frac{\nu}{2}\frac{\partial^2 \epsilon}{\partial x_j^2} - \nu^2\overline{\left(\frac{\partial^2 u_i'}{\partial x_j \partial x_k}\right)^2}.
\end{aligned} \tag{B.12}$$

Introducing (B.9)-(B.12) into (B.8) gives

$$\frac{D\epsilon}{Dt} = \mathcal{P}_\epsilon - \Phi_\epsilon - \mathcal{D}_\epsilon + \mathcal{D}_v, \tag{B.13}$$

where

$$\begin{aligned}
\frac{D\epsilon}{Dt} &= \frac{\partial \epsilon}{\partial t} + U_j \frac{\partial \epsilon}{\partial x_j}, \\
\mathcal{P}_\epsilon &= -2\nu \frac{\partial U_i}{\partial x_k} \left(\frac{\partial u_i'}{\partial x_j} \frac{\partial u_i'}{\partial x_k} + \frac{\partial u_i'}{\partial x_j} \frac{\partial u_k'}{\partial x_j} \right) \\
&- 2\nu \overline{\frac{\partial u_i'}{\partial x_j} \frac{\partial u_i'}{\partial x_k} \frac{\partial u_j'}{\partial x_k}} - 2\nu \frac{\partial^2 U_j}{\partial x_j \partial x_k} \overline{u_j' \frac{\partial u_i'}{\partial x_k}}, \\
\Phi_\epsilon &= \nu^2 \overline{\left(\frac{\partial^2 u_i'}{\partial x_j \partial x_k} \right)^2}, \\
\mathcal{D}_\epsilon &= -\frac{2\nu}{\rho} \overline{\frac{\partial}{\partial x_i} \left(\frac{\partial u_i \prime}{\partial x_j} \frac{\partial p'}{\partial x_j} \right)} + \nu \overline{\frac{\partial}{\partial x_j} \left[u_j' \left(\frac{\partial u_i'}{\partial x_k} \right)^2 \right]}, \\
\mathcal{D}_v &= \nu \frac{\partial^2 \epsilon}{\partial x_j^2}.
\end{aligned}$$

The four terms on the right-hand side of (B.13) are respectively production, dissipation, turbulent diffusion and viscous diffusion of the dissipation of turbulent kinetic energy. Due to the complexity of the terms in (B.13), the production and dissipation are modelled by multiplying the corresponding terms in the transport equation for k with $\frac{\epsilon}{k}$, a constant and a damping function. The damping function is introduced to ensure correct behaviour of ϵ near the walls. The turbulent diffusion is modelled using a gradient transport hypothesis similar to that of the k equation. Thus the transport equation (B.13) becomes

$$\frac{D\epsilon}{Dt} = C_{\epsilon 1} f_1 \frac{\epsilon}{k} \left(-\overline{u_i' u_j'} \right) \frac{\partial U_i}{\partial x_j} + \frac{\partial}{\partial x_j} \left[\left(\nu + \frac{\nu_t}{\sigma_\epsilon} \right) \frac{\partial \epsilon}{\partial x_j} \right] - C_{\epsilon 2} f_2 \frac{\epsilon^2}{k}, \tag{B.14}$$

where σ_ϵ is the turbulent Prandtl number.

Appendix C

Derivation of the temperature equation

In this dissertation the temperature equation was only solved in combination with the RANS equations. The temperature equation is derived by considering energy conservation for a control volume. In general terms the first law of thermodynamics is expressed as

$$\Delta E_{st} \equiv E_{in} + E_g - E_{out}, \tag{C.1}$$

where ΔE_{st} is energy stored during the time period Δt, E_{in} is energy applied, E_g is energy generated and E_{out} is energy leaving the control volume. Following Bird *et al.* [9] the differential form of equation (C.1) is

$$\frac{\partial}{\partial t}\rho(e + \frac{1}{2}u_i^2) = -\frac{\partial}{\partial x_i}(\rho u_i(e + \frac{u^2}{2})) - \frac{\partial}{\partial x_i}q_i + \rho u_i g_i - \frac{\partial}{\partial x_i}(pu_i) - \frac{\partial}{\partial x_i}(\tau_{ij}u_j), \tag{C.2}$$

where e is internal energy, $\frac{1}{2}u^2$ is kinetic energy and q_i is heat flux by conduction given by Fourier's law

$$q_i = -k\frac{\partial \theta}{\partial x_i}, \tag{C.3}$$

for an isotropic fluid. In equation (C.3), k is thermal conductivity (not to be mistaken with turbulent kinetic energy) and θ is temperature.

Equation (C.2) is reduced to a transport equation for the thermal energy by subtracting the mechanical energy equation. The mechanical energy equation is found by forming the scalar product of the local velocity u_i and the momentum equation (2.2). This procedure is treated in further details in Bird *et al.* [9]. The thermal energy equation then takes the form

$$\frac{\partial}{\partial t}(\rho e) + \frac{\partial}{\partial x_i}(\rho u_i e) = -\frac{\partial q_i}{\partial x_i} - \frac{\partial p u_i}{\partial x_i} - \nu\left(\frac{\partial u_i}{\partial x_j} + \frac{\partial u_j}{\partial x_i}\right)\frac{\partial u_j}{\partial x_i}. \tag{C.4}$$

Air is considered to be an ideal gas and thus, $e = c_v\theta$, where c_v is specific heat of air. Furthermore, the indoor airflows are assumed incompressible and finally viscous

dissipation is neglected except for special occasions. Thus, equation (C.4) reduces to

$$\frac{\partial \theta}{\partial t} + u_i \frac{\partial \theta}{\partial x_i} = \alpha \frac{\partial}{\partial x_i} \left[\frac{\partial \theta}{\partial x_i} \right], \tag{C.5}$$

where equation (C.3) was introduced in the right hand side and $\alpha = k/(c_v \rho)$ is the thermal diffusivity.

By time averaging equation (C.5) becomes

$$\frac{\partial \Theta}{\partial t} + u_i \frac{\partial \Theta}{\partial x_i} = -\alpha \frac{\partial}{\partial x_i} \left[\frac{\partial \Theta}{\partial x_i} \right] - \frac{\partial \overline{u_i \theta}}{\partial x_i}. \tag{C.6}$$

The turbulent temperature flux $\overline{u_j \theta}$ is unknown and has to be modelled. This is modelled using a gradient transport hypothesis

$$\overline{u_i \theta} = \alpha_t \left(\frac{\partial \Theta}{\partial x_i} \right), \tag{C.7}$$

see e.g. Meyer [66]. The turbulent thermal diffusivity α_t is related to the eddy viscosity through the Reynolds analogy

$$\sigma_t = \frac{\nu_t}{\alpha_t}, \tag{C.8}$$

where $\sigma_t = 0.9$ is the turbulent Prandtl number. The Prandtl number is commonly assumed constant 0.7 for free shear flows and 0.9 for wall bounded flows, see e.g. Meyer [66]. Substituting equation (C.7) into equation (C.6) now yields

$$\frac{\partial \Theta}{\partial t} + u_i \frac{\partial \Theta}{\partial x_i} = \frac{\partial}{\partial x_i} \left[(\alpha + \alpha_t) \frac{\partial \Theta}{\partial x_j} \right]. \tag{C.9}$$

Thus, the transport equation for the time averaged temperature was derived.

Appendix D

Turbulence models

In the following the six two-equation models used in this dissertation are presented. Five of the models are standard models from the literature, while a new one, the revised baseline, is presented.

D.1 Standard $k-\epsilon$ model

For the standard $k-\epsilon$ model the transport equations for the turbulent quantities take the form

$$\frac{Dk}{Dt} = \frac{\tau_{ij}}{\rho}\frac{\partial U_i}{\partial x_j} + \frac{\partial}{\partial x_j}\left[(\nu + \frac{\nu_t}{\sigma_k})\frac{\partial k}{\partial x_j}\right] - \epsilon \tag{D.1}$$

$$\frac{D\epsilon}{Dt} = C_{\epsilon 1}\frac{\epsilon}{k}\frac{\tau_{ij}}{\rho}\frac{\partial U_i}{\partial x_j} + \frac{\partial}{\partial x_j}\left[(\nu + \frac{\nu_t}{\sigma_\epsilon})\frac{\partial \epsilon}{\partial x_j}\right] - C_{\epsilon 2} f_2 \frac{\epsilon^2}{k}. \tag{D.2}$$

The eddy viscosity is

$$\nu_t = C_\mu f_\mu \frac{k^2}{\epsilon}. \tag{D.3}$$

The model constants are

$$\begin{aligned} C_\mu = 0.09, \quad \sigma_k = 1.0, \quad \sigma_\epsilon = 1.3, \\ C_{\epsilon 1} = 1.44, \quad C_{\epsilon 2} = 1.92, \end{aligned} \tag{D.4}$$

and the damping functions

$$f_\mu = f_2 = 1. \tag{D.5}$$

In the model the transport equations are not integrated to the walls. Instead the production and dissipation of kinetic energy are specified in the near-wall cells, using the logarithmic law-of-the-wall. The value of ϵ is specified the same way. A more detailed description of the wall laws can be found in Sørensen [103].

D.2 Low Reynolds number $k-\epsilon$ model by Launder & Sharma

A low-Reynolds number $k-\epsilon$ model is presented by Launder & Sharma in [56]. A new variable $\tilde{\epsilon}$ is defined as

$$\epsilon = \tilde{\epsilon} + D \qquad D = 2\nu \left(\frac{\partial \sqrt{k}}{\partial n} \right)^2, \tag{D.6}$$

where n is the direction normal to the wall. Compared to ϵ, $\tilde{\epsilon}$ has the advantage of the natural boundary condition $\tilde{\epsilon} = 0$, at the walls. For addition, it is proposed by Launder & Sharma that the term

$$E = 2\nu\nu_t \left(\frac{\partial^2 U}{\partial y^2} \right)^2, \tag{D.7}$$

is added to the right-hand side of the transport equation for ϵ. The term is added to compensate for additional production and to further balance diffusion and dissipation in the vicinity of the walls. With the new variable appearing in (D.6) and the term (D.7), the transport equations for the turbulent variables become

$$\frac{Dk}{Dt} = \frac{\tau_{ij}}{\rho}\frac{\partial U_i}{\partial x_j} + \frac{\partial}{\partial x_j}\left[(\nu + \frac{\nu_t}{\sigma_k})\frac{\partial k}{\partial x_j} \right] - (\tilde{\epsilon} + D) \tag{D.8}$$

$$\frac{D\tilde{\epsilon}}{Dt} = C_{\epsilon 1}\frac{\tilde{\epsilon}}{k}\frac{\tau_{ij}}{\rho}\frac{\partial U_i}{\partial x_j} + \frac{\partial}{\partial x_j}\left[(\nu + \frac{\nu_t}{\sigma_{\tilde{\epsilon}}})\frac{\partial \tilde{\epsilon}}{\partial x_j} \right] - C_{\epsilon 2} f_2 \frac{\tilde{\epsilon}^2}{k} + E. \tag{D.9}$$

The eddy viscosity is

$$\nu_t = C_\mu f_\mu \frac{k^2}{\tilde{\epsilon}}. \tag{D.10}$$

The constants are

$$\begin{aligned} C_\mu = 0.09, \quad \sigma_k = 1.0, \quad \sigma_\epsilon = 1.3, \\ C_{\epsilon 1} = 1.44, \quad C_{\epsilon 2} = 1.92, \end{aligned} \tag{D.11}$$

and the damping functions are both functions of the turbulent Reynolds number

$$R_t = \frac{k^2}{\nu\tilde{\epsilon}}. \tag{D.12}$$

The damping function for the eddy viscosity is

$$f_\mu = \exp\left[\frac{-3.4}{(1 + \frac{R_t}{50})^2} \right], \tag{D.13}$$

and the damping function for the dissipation term in (D.9) is

$$f_2 = 1 - 0.3\exp(-R_t^2). \tag{D.14}$$

The boundary conditions at the walls are

$$k_w = 0 \quad \text{and} \quad \tilde{\epsilon}_w = 0. \tag{D.15}$$

D.3 Original $k-\omega$ model

Already in 1942 Kolmogoroff suggested the specific dissipation rate ω with dimension $time^{-1}$ as an alternative to ϵ. In 1988 Wilcox [110] presented his $k-\omega$ model based on the original transport equation by Kolmogoroff. The noteworthy property of this model is that the demand for damping functions in near-wall regions is rendered superfluous. The transport equations are

$$\frac{Dk}{Dt} = \frac{\tau_{ij}}{\rho}\frac{\partial U_i}{\partial x_j} + \frac{\partial}{\partial x_j}\left[(\nu + \sigma_{k1}\nu_t)\frac{\partial k}{\partial x_j}\right] - \beta^*\omega k \tag{D.16}$$

$$\frac{D\omega}{Dt} = \frac{\gamma_1}{\rho\nu_t}\tau_{ij}\frac{\partial U_i}{\partial x_j} + \frac{\partial}{\partial x_j}\left[(\nu + \sigma_{\omega 1}\nu_t)\frac{\partial \omega}{\partial x_j}\right] - \beta_1\omega^2. \tag{D.17}$$

The eddy viscosity is defined as

$$\nu_t = \frac{k}{\omega}, \tag{D.18}$$

and the model constants are

$$\sigma_{k1} = 0.5, \quad \sigma_{\omega 1} = 0.5, \quad \beta_1 = 0.0750, \quad \beta^* = 0.09,$$
$$\gamma_1 = \frac{\beta_1}{\beta^*} - \sigma_{\omega 1}\frac{\kappa^2}{\sqrt{\beta^*}}, \tag{D.19}$$

where $\kappa = 0.41$ The boundary conditions are

$$k_w = 0 \quad \text{and} \quad \omega_w = 10\frac{6\nu}{\beta_1(\Delta y)^2}, \tag{D.20}$$

where Δy is the distance from the wall to the nearest point. The first grid point above surface requires $y^+ < 3$, for (D.20) to be applicable. The boundary conditions are suggested by Menter [64], who also proposed that a limiter is applied to the production term in the k equation. This should relieve excessive production of turbulent kinetic energy and numerical 'wiggles'. The limiter takes the form.

$$\tilde{\mathcal{P}}_k = \min(\mathcal{P}; 20\mathcal{D}_k), \tag{D.21}$$

where $\mathcal{D}_k$ is dissipation of turbulent kinetic energy.

D.4 The $k-\omega$ BSL model

The $k-\omega$ model by Wilcox has the disadvantage of being highly sensitive to ω specified in the freest ream, see Menter [65]. For the same reason Menter [65] proposed the $k-\omega$ baseline (BSL) model, combining the $k-\omega$ model by Wilcox in the inner region of the boundary layer, and the standard $k-\epsilon$ in the outer region and the free stream. The transport equations for the baseline model by Menter are

$$\frac{Dk}{Dt} = \frac{\tau_{ij}}{\rho}\frac{\partial U_i}{\partial x_j} + \frac{\partial}{\partial x_j}\left[(\nu + \sigma_k\nu_t)\frac{\partial k}{\partial x_j}\right] - \beta^*\omega k \tag{D.22}$$

$$\frac{D\omega}{Dt} = \frac{\gamma}{\rho\nu_t}\tau_{ij}\frac{\partial U_i}{\partial x_j} + \frac{\partial}{\partial x_j}\left[(\nu + \sigma_\omega\nu_t)\frac{\partial \omega}{\partial x_j}\right] + 2(1-F_1)\sigma_{\omega 2}\frac{1}{\omega}\frac{\partial k}{\partial x_j}\frac{\partial \omega}{\partial x_j}. \tag{D.23}$$

The transport equations are obtained by transforming the $k-\epsilon$ model into a $k-\omega$ formulation, and using the blending function F_1. The blending function is designed to be one near walls and zero away from surfaces. Compared to the transport equation (D.17), equation (D.23) differs by the appearance of an additional cross-diffusion term. The eddy viscosity is

$$\nu_t = \frac{k}{\omega}. \tag{D.24}$$

The inner model constants are

$$\sigma_{k1} = 0.5, \quad \sigma_{\omega 1} = 0.5, \quad \beta_1 = 0.0750, \quad \beta^* = 0.09,$$
$$\gamma_1 = \frac{\beta_1}{\beta^*} - \sigma_{\omega 1}\frac{\kappa^2}{\sqrt{\beta^*}}, \tag{D.25}$$

which is similar to those of the $k-\omega$ model by Wilcox. The outer model constants are

$$\sigma_{k2} = 1.0, \quad \sigma_{\omega 2} = 0.856, \quad \beta_2 = 0.0828, \quad \beta^* = 0.09$$
$$\gamma_2 = \frac{\beta_2}{\beta^*} - \sigma_{\omega 2}\frac{\kappa^2}{\sqrt{\beta^*}}, \tag{D.26}$$

corresponding to the standard $k-\epsilon$ model. Both inner and outer model take $\kappa = 0.41$. The constants for the inner model, ϕ_1, and the outer model ϕ_2, are mixed to give ϕ using the blending function F_1. Thus,

$$\phi = F_1\phi_1 + (1 - F_1)\phi_2, \tag{D.27}$$

where

$$F_1 = \tanh(\arg_1^4). \tag{D.28}$$

Here

$$\arg_1 = \min\left[\max\left(\frac{\sqrt{k}}{0.09\omega y}; \frac{500\nu}{y^2\omega}\right); \frac{4\sigma_{\omega 2}k}{CD_{k\omega}y^2}\right], \tag{D.29}$$

where y is the distance to the wall and

$$CD_{k\omega} = max\left(2\sigma_{\omega 2}\frac{1}{\omega}\frac{\partial k}{\partial x_j}\frac{\partial \omega}{\partial x_j}, 10^{-20}\right). \tag{D.30}$$

The boundary conditions are

$$k_w = 0 \quad \text{and} \quad \omega_w = 10\frac{6\nu}{\beta_1(\Delta y)^2}, \tag{D.31}$$

identical to (D.20).

D.5 The $k-\omega$ SST model

The Shear Stress Transport (SST) model is identical to the baseline model, except that the constants for the inner model are changed to

$$\sigma_{k1} = 0.85, \quad \sigma_{\omega 1} = 0.5, \quad \beta_1 = 0.0750, \quad \beta^* = 0.09,$$
$$\gamma_1 = \frac{\beta_1}{\beta^*} - \sigma_{\omega 1}\frac{\kappa^2}{\sqrt{\beta^*}}, \tag{D.32}$$

where $\kappa = 0.41$. Further, the eddy viscosity used is

$$\nu_t = \frac{a_1 k}{\max(a_1\omega; \Omega F_2)}, \tag{D.33}$$

where $a_1 = 0.31$,

$$F_2 = \tanh(\arg_2^2) \tag{D.34}$$

and

$$\arg_2 = \max\left(2\frac{\sqrt{k}}{0.09\omega y}; \frac{500\nu}{y^2\omega}\right). \tag{D.35}$$

The modified eddy viscosity accounts for the transport of principal turbulent shear stress, τ. According to Menter [65], the new eddy viscosity leads to improvement in performance compared to the $k-\omega$ model by Wilcox, as well as the standard $k-\epsilon$ model.

D.6 The revised $k-\omega$ BSL model

The revised baseline model is similar to the baseline model, but the blending function has been adjusted. Using the original baseline it was found that the $k-\omega$ model dominates compared to the $k-\epsilon$ model for flows in enclosures. However the $k-\epsilon$ model is known to be more dissipative the $k-\omega$ model, for which reason it is desirable that the $k-\epsilon$ is covering most of the domain. Compared to the baseline model the blending function now takes the form

$$F_1 = \begin{cases} 1 & \text{if } y \leq 0.01 \\ 0 & \text{if } y > 0.01 \end{cases} \tag{D.36}$$

where y is the distance to the wall. This way of defining the blending function is ad hoc and using the model for other flows could be problematic. Further, the model suffers from being independent of the flow variables, and therefore the idea of letting the blending take place in the outer wake is lost.

Appendix E

Grid study for two-dimensional calculations of the airflow in the annex 20 case

Below a grid study using the low Reynolds number $k - \epsilon$ model is presented.

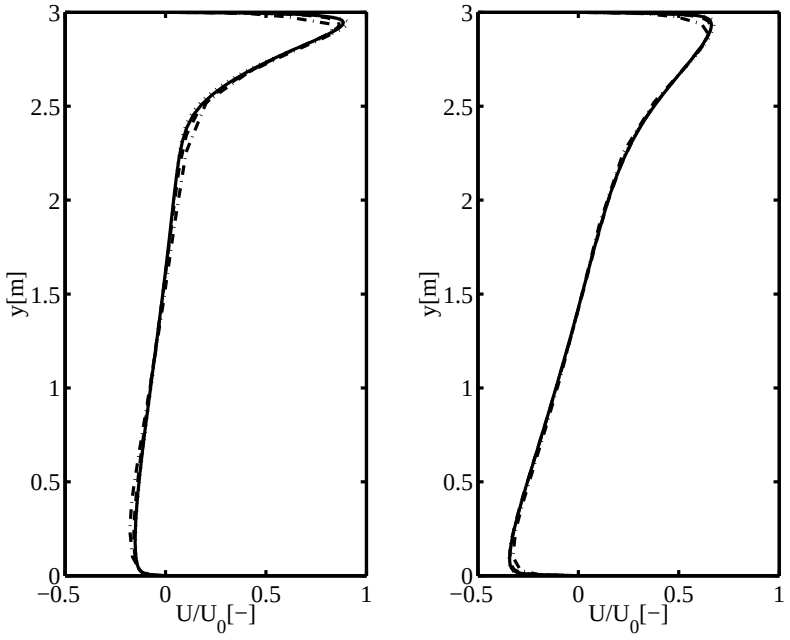

Figure E.1: Dimensionless horizontal velocities, u/u_0, along two vertical lines in the symmetry plane. Left: $x = 3\ m$. Right: $x = 6\ m$. Mesh sizes are: $- \cdot - \cdot -\cdot$: Blocks of 8×8 cells, $- \ - \ - \ -$: Blocks of 16×16 cells, ——: Blocks of 32×32 cells and $\cdots\cdots$: Blocks of 48×48 cells.

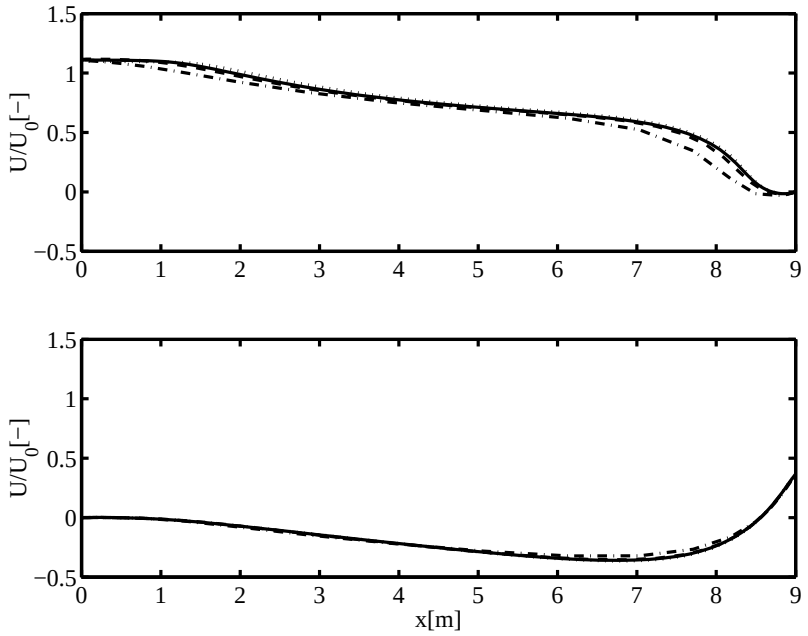

Figure E.2: Dimensionless horizontal velocities, u/u_0, along two horizontal lines in the symmetry plane. Lower: $y = 0.084\ m$. Upper: $y = 2.916\ m$. Interpretation of lines, see figure E.1.

Appendix F

Grid study for three-dimensional calculations of the airflow in the annex 20 case

Below a grid study using the low Reynolds number $k - \epsilon$ model is presented.

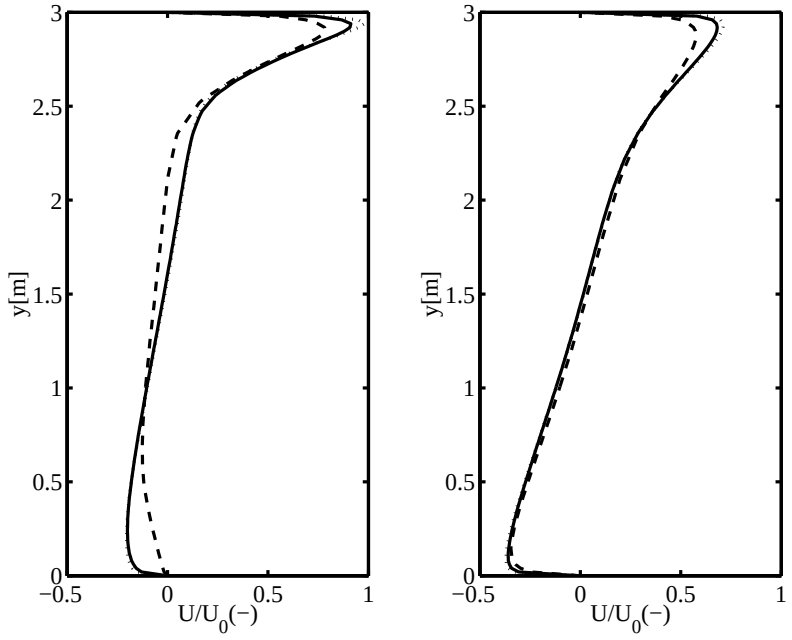

Figure F.1: Dimensionless horizontal velocities, $\frac{u}{u_0}(-)$, along two vertical lines in the symmetry plane. Left: $x = 3\ m$. Right: $x = 6\ m$. Mesh sizes are: $-\ -\ -\ -$: Blocks of $12 \times 12 \times 12$ cells (coarse mesh). ——: Blocks of $16 \times 16 \times 16$ cells (medium mesh). $\cdots\cdots$: Blocks of $24 \times 24 \times 24$ cells (fine mesh).

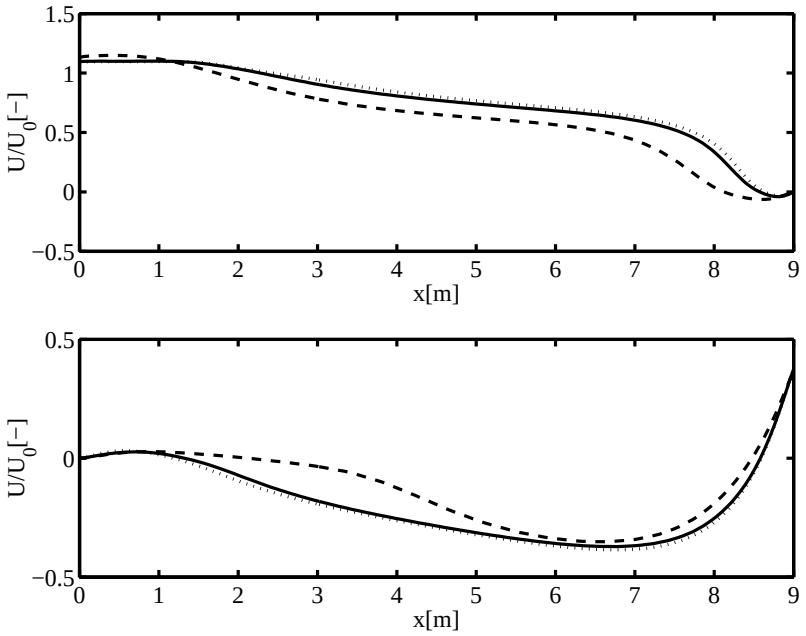

Figure F.2: Dimensionless horizontal velocities, $\frac{u}{u_0}(-)$, along two horizontal lines in the symmetry plane. Lower: $y = 0.084\ m$. Upper: $y = 2.916\ m$. Interpretation of lines, see figure F.1.

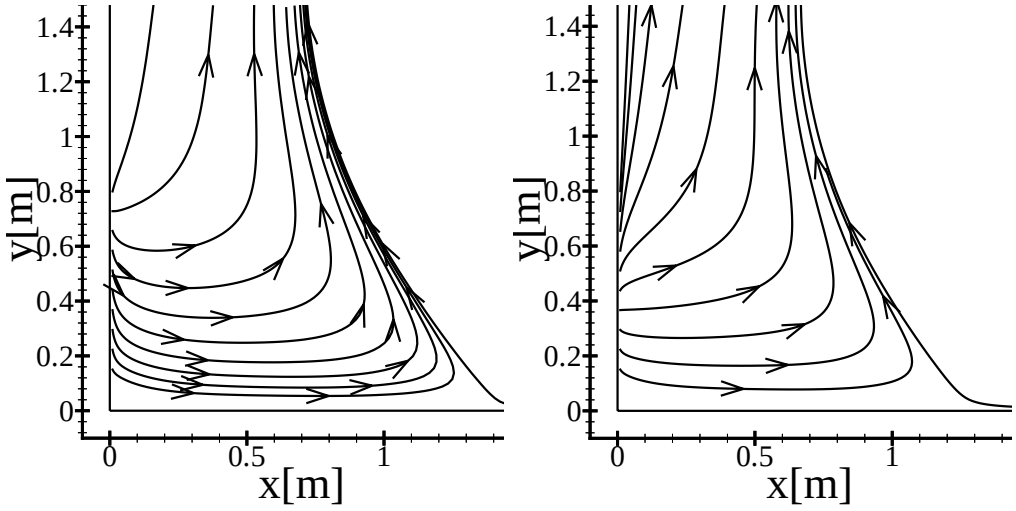

Figure F.3: Streamlines in lower left corner of the symmetry plane. Left: Medium mesh ($16 \times 16 \times 16$ cells). Right: Fine mesh ($24 \times 24 \times 24$ cells). The flow field was symmetric for the medium mesh and the fine mesh, but not for the coarse mesh.

Appendix G

Evaluation of solution for LES of airflow in the annex 20 case

For a LES of the airflow in the annex 20 2-D case, the averaging period and the influence from the grid is evaluated below.

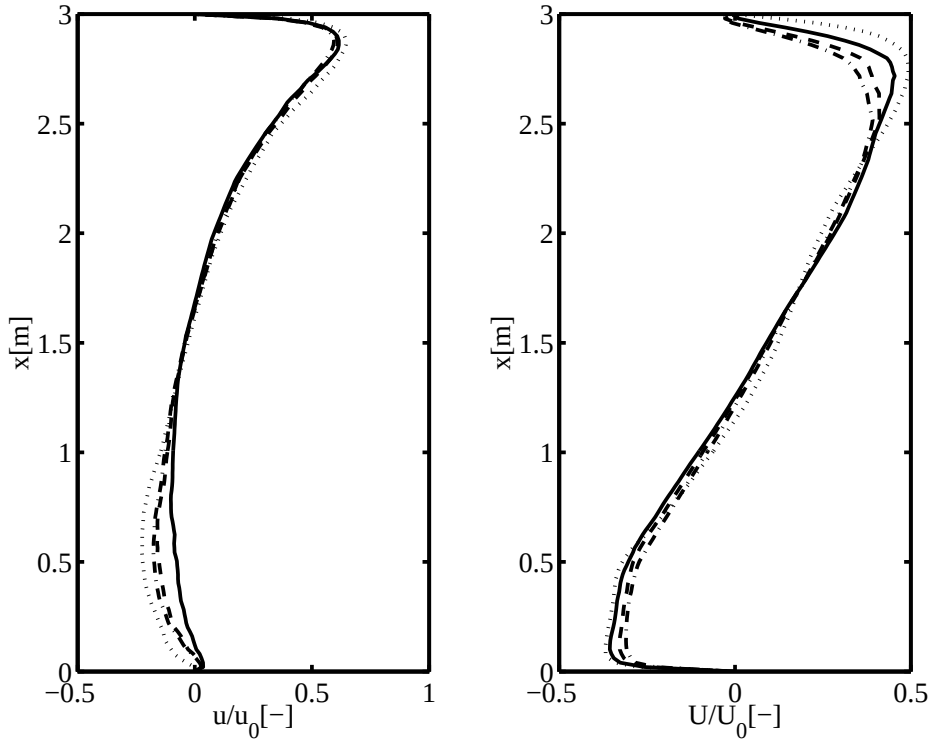

Figure G.1: Dimensionless horizontal velocities, $\frac{u}{u_0}$, along two vertical lines in the symmetry plane. Symbols are ———: Medium grid and $\Delta t = 100\ s$, − − − −: Medium grid and $\Delta t = 200\ s$, − · − · −·: Medium grid and $\Delta t = 300\ s$ and · · · · · · · : Fine grid and $\Delta t = 160\ s$.

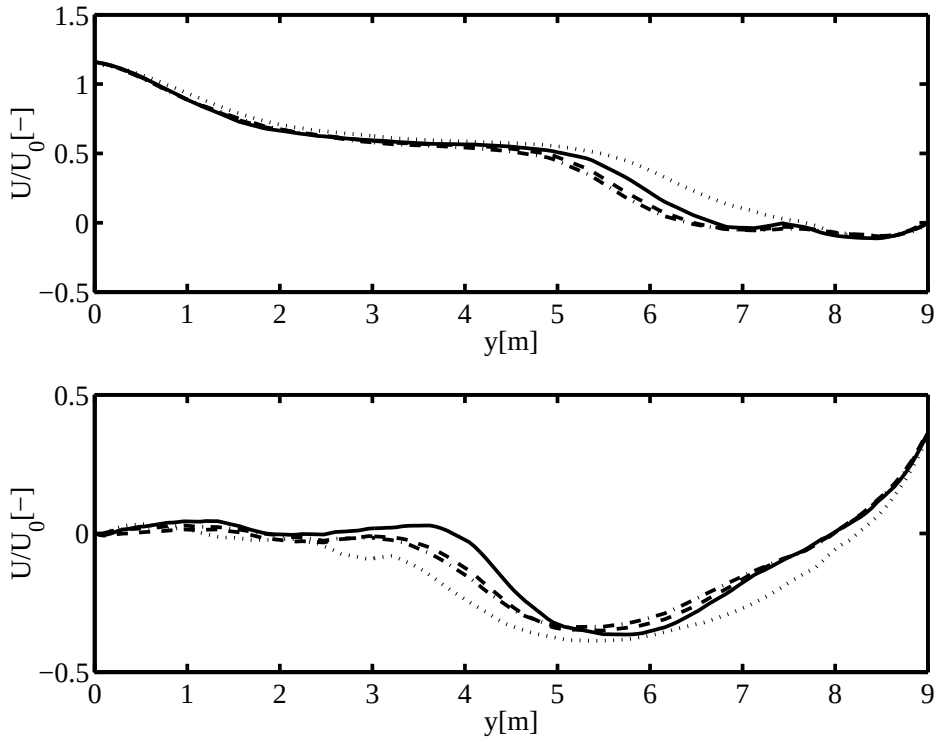

Figure G.2: Dimensionless horizontal velocities, $\frac{u}{u_0}$, along two horizontal lines in the symmetry plane. Symbols see figure G.1.

Appendix H

Grid study for calculations of the airflow in the annex 20 case with a heated wall

Below is presented a grid study for isothermal calculation of the airflow in the annex 20 test case with a heated wall, see figure H.1. The air exchange rate is $6^h{-}1$. The low-Reynolds number $k{-}\epsilon$ model was used for this study. Furthermore, the evolution of the velocities in a point is shown in figure H.2

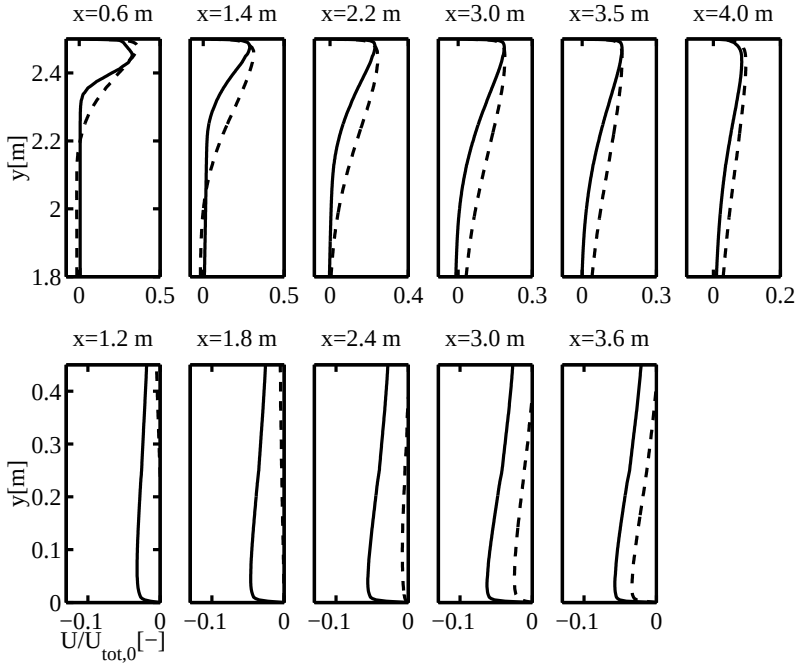

Figure H.1: Comparison of grid use for calculation of flow in isothermal annex 20 test case with a heated wall. Symbols are – – – –: Grid of $40 \times 72 \times 48$ cells, ——–: Grid of $80 \times 144 \times 96$ cells.

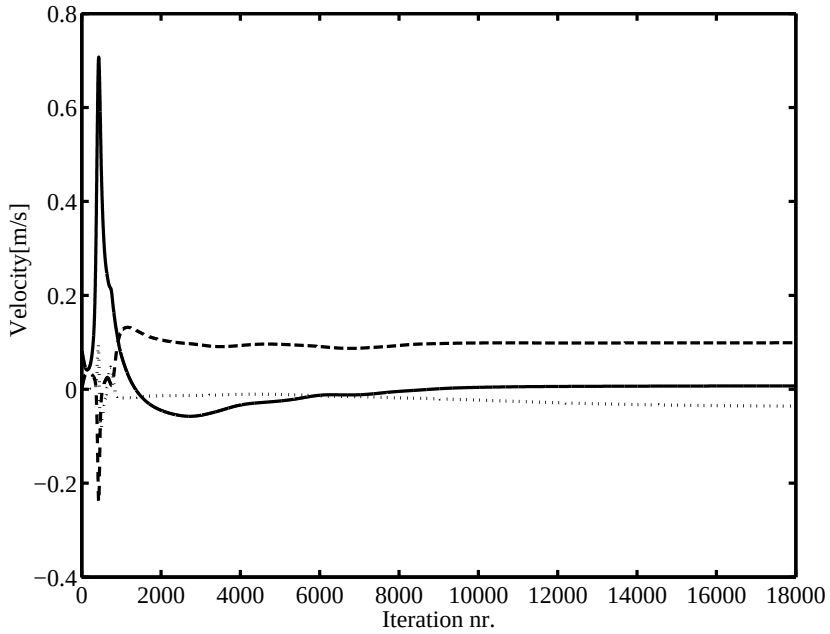

Figure H.2: Behaviour of velocity variables in monitor point $(x, y, z) = (0.44, 2.20, 0.06)$ using grid with blocks of $8 \times 8 \times 8$ cells. Symbols are: ———: u, $-\ -\ -\ -$:v, $\cdots\cdots$:w.

Appendix I

Driven cavity

I.1 Introduction

Buoyancy affected flows are of great interest when designing indoor climate. When using displacement ventilation a considerable insight into the effects of buoyancy on the flow field is required. One of the most simple configurations for studying buoyancy phenomena is the temperature driven cavity, which has been studied extensively over the past decades. For this benchmark case both experimental and numerical results exist.

Numerical investigation for laminar flow was carried out by Newell & Schmidt [77], who found that the logarithm of the average Nusselt number varies linearly on the logarithm of the Grashof number. In numerical studies of Henkes & Hoogendorn [45] the different flow topologies appearing in the laminar region were depicted, and further an extensive comparison with existing numerical results was carried out. The flow was described by direct numerical simulation, see Paolucci [86], from which detailed statistical information in the turbulent region was obtained. Calculations in the turbulent regime have been used for testing and developing existing turbulence model, e.g Henkes *et al* [44] and Peng & Davidson [89]. More sophisticated turbulence models have been developed see e.g. Davidson [22], where a hybrid of the $k-\epsilon$ and an algebraic Reynolds stress model was developed to incorporate non-isotropic effects in the two-equation model. The applicability of Boussinesq approximation was investigated by Farhangnia *et al* [35]. They found that this approximation is valid for buoyancy driven turbulent flows. A related area which is important for design of indoor climate, is the combined effect of radiation and natural convection. This was examined in terms of the rectangular cavity by Behnia *et al* [6].

The experiments available are mainly from the turbulent regime, see e.g. Bowles & Cheesewright [14] and Leong *et al* [58].

In the following the focus is on the implementation of the laminar transport equation for the temperature, Michelsen [69]. It was chosen to fix the Rayleigh number, Ra, at 10^6 and compare the results with other numerical results by Henkes & Hoogen-

doorn [45], Le Quéré [57] and de Vahl Davis [107]. A similar study for the old version of the *EllipSys* was carried out by Myllerup [72].

The computations presented below show good accordance with previously presented numerical results for three characteristic quantities of the flow: Averaged Nusselt number for the hot wall, maximum vertical velocity at half the height of the cavity and maximum horizontal velocity at half the width of the cavity. Further, the results are almost identical to those obtained with the old version of *EllipSys*. By visual inspection the behaviour of isotherms, the streamlines and the topology of the flow are in agreement with other numerical results.

I.2 Test case

The cavity used for evaluating the implementation of the temperature equation is quadratic, air filled with a hot and cold vertical wall, respectively, and two adiabatic horizontal walls, see figure I.1.

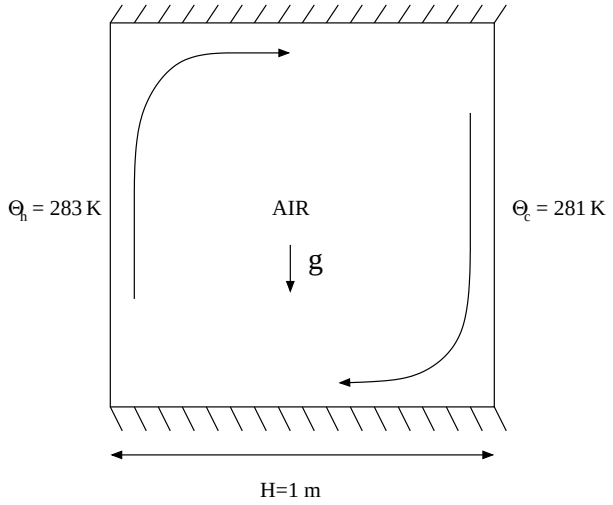

Figure I.1: Configuration of the temperature driven cavity. The domain is a square.

The governing parameter is the Ra defined by

$$Ra = \frac{g\beta\Delta\Theta H^3 Pr}{\nu^2}, \tag{I.1}$$

where $g = 9.82\ m/s^2$ is gravity, $\beta = 1/\Theta_{ref} = 1/(282\ K)$ is the thermal expansion coefficient, $\Delta\Theta = \Theta_h - \Theta_c = 2\ K$, $H = 1\ m$ is the height of the cavity, $Pr = 0.71$ is the Prandtl number and ν is the kinematic viscosity. The kinematic viscosity is adjusted to obtain the desired Ra. The equations for describing this flow are continuity, the laminar, steady, time-averaged Navier-Stokes equations with temperature

coupling and a transport equation for the temperature. The equations take the form

$$\begin{aligned}
\frac{\partial U_i}{\partial x_i} &= 0 \\
U_j\frac{\partial U_i}{\partial x_j} &= -\frac{1}{\rho}\frac{\partial P}{\partial x_i} + \frac{\partial}{\partial x_j}\left(\nu\frac{\partial U_i}{\partial x_j}\right) + \rho g_i\beta(\Theta - \Theta_{ref}) \\
U_i\frac{\partial \Theta}{\partial x_i} &= \frac{\partial}{\partial x_i}\left(\frac{\nu}{Pr}\frac{\partial \Theta}{\partial x_i}\right),
\end{aligned} \tag{I.2}$$

where $g_2 = -g$ and zero otherwise. Considering an ideal gas

$$\rho = \frac{pM}{R\Theta}, \tag{I.3}$$

and expressing the variation of ρ by using the thermal expansion coefficient

$$\beta = -\frac{1}{\rho}\left(\frac{\partial \rho}{\partial \Theta}\right)_p \approx -\frac{1}{\rho}\frac{\rho_{ref} - \rho}{\Theta_{ref} - \Theta}, \tag{I.4}$$

where Θ_{ref} is a reference temperature and ρ_{ref} is a reference density. It is important to note that the reference temperature and the reference density is related through equation (I.3) for an ideal gas. In the present calculations $T_{ref} = 282\ K$ is used, and thus $\rho_{ref} = 1.237$ is specified. With equation (I.4), the buoyancy term in (I.2) can be written as

$$\rho\beta(\Theta - \Theta_{ref}) \approx (\rho_{ref} - \rho), \tag{I.5}$$

which is used in the *EllipSys* code.

The grid was generated from

$$x_m = x_{max}\left(-0.5\tanh\left[\alpha\left(2\frac{m}{n} - 1\right)\right] / \tanh(-\alpha) + 0.5\right), \tag{I.6}$$

suggested by Davidson [21]. In equation (I.6) x_m is the coordinate for the m-th grid line, n is number of x-lines and α is a contraction factor set to 3.5.

I.3 Results

Several quantities could be compared, despite the simple geometry. It was chosen to focus on heat transfer, velocity, temperature distribution and topology.

In table I.1 the averaged Nusselt number was compared with measurements. The averaged Nusselt number is defined as

$$\int_0^1 Nu\ d\left(\frac{y}{H}\right), \tag{I.7}$$

with the local Nusselt number

$$Nu = -\frac{H}{\Delta\Theta}\left(\frac{\partial T}{\partial x}\right)_w, \tag{I.8}$$

where index w indicates that the derivative should be evaluated at the wall.

From table I.1 the scaled averaged Nusselt number, $\overline{Nu}Ra^{-1/4}$, found in the present calculation changes only 0.1 % from the medium mesh, 64×64 cells, to the fine mesh, 128×128 cells. Further the scaled maximum vertical velocity changes 0.5 % and the scaled maximum horizontal velocity changes 1.25 %. Thus it is assumed that using the medium mesh, the effects from the grid size is only a few percent on the considered quantities. It was not possible to obtain a converged solution with a mesh of 32×32 cells.

Comparing the results based on the medium mesh with the results obtained with the medium mesh by Henkes & Hogendoorn [45] the deviation of the three quantities, scaled Nusselt number, the scaled maximum vertical velocity and the the scaled maximum horizontal velocity were 0.2 %, 1.3 % and 1.7 %, respectively. For a similar comparison with the results presented by Myllerup [72], the deviations were 0.3 %, 0.7 % and 1.4 %. Comparing with results by de Vahl Davis [107] the differences were 0 %, 0.2 % and 1.4 %. Finally the discrepancies from the results obtained by Le Quéré [57] were 0.3 %, 0.7 % and 1.7 %. In all cases the deviation of the present results and other numerical results is in the order of 1 %. This is the same order of magnitude as the deviation between the present results based on the medium mesh and fine mesh, respectively. Thus it is concluded that the results obtained with the *EllipSys* code is acceptable. It is not known if there is a physical or numerical explanation for the largest deviation to occur for the maximum horizontal velocity.

The isotherms of the dimensionless temperature, defined as

$$\Theta_{dim} = \frac{\Theta - \Theta_c}{\Theta_h - \Theta_c}, \tag{I.9}$$

are presented in figure I.2. The isotherms show the expected symmetry around both the horizontal and vertical center axis. Further, by visual inspection, the result is in good agreement with the isotherms presented in Henkes and Hoogendoorn [45]. The streamline topology of the flow, shown in figure I.3, indicates the existence of two saddle points and three centres. This topology is also in agreement with the topology found by Henkes and Hoogendoorn [45] for the specified Ra.

Study	Grid	$\overline{Nu}Ra^{-1/4}$	$\frac{v_{max}}{\sqrt{g\beta\Delta\Theta H}}$	$\frac{u_{max}}{(g\beta\Delta\Theta\nu)^{1/3}}$
Henkes & Hoogendoorn	(60×60)	0.2789	0.2633	0.8145
	(120×120)	0.2790	0.2621	0.8144
Myllerup	(64×64)	0.2790	0.2616	0.8128
Present	(64×64)	0.2783	0.2599	0.8007
	(128×128)	0.2787	0.2613	0.8132
de Vahl Davis		0.2783	0.2603	0.8121
Le Quéré		0.2791	0.2618	0.8146

Table I.1: Comparison of scaled average Nusselt number at the hot wall, scaled maximum vertical velocity at half the centre height of the cavity and the scaled maximum horizontal velocity at half the cavity width. In the study by Henkes & Hoogendoorn [45], the study by Myllerup [72] and in the present study the finite volume approach were used. In the study by de Vahl Davis, [107], the finite difference method was used and finally Le Quéré, [57] employed the spectral method. The difference between the employed numerical techniques is emphasized by not indicating a grid size in the latter two studies.

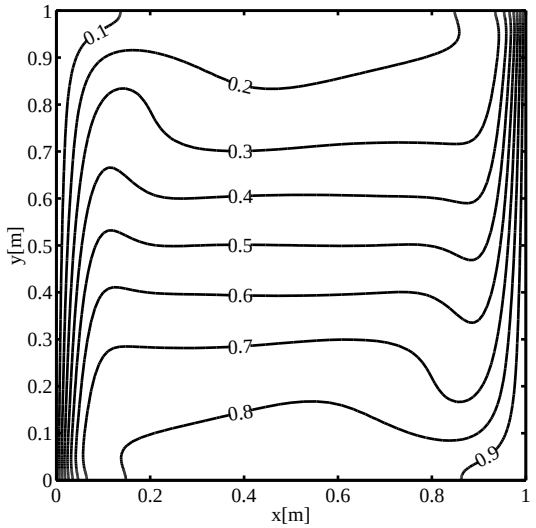

Figure I.2: Contours of dimensionless temperature $\frac{\Theta-\Theta_c}{\Theta_h-\Theta_c}$. Computations for the same Ra were carried out by Henkes & Hoogendoorn [45] and a similar distribution of contour lines was obtained.

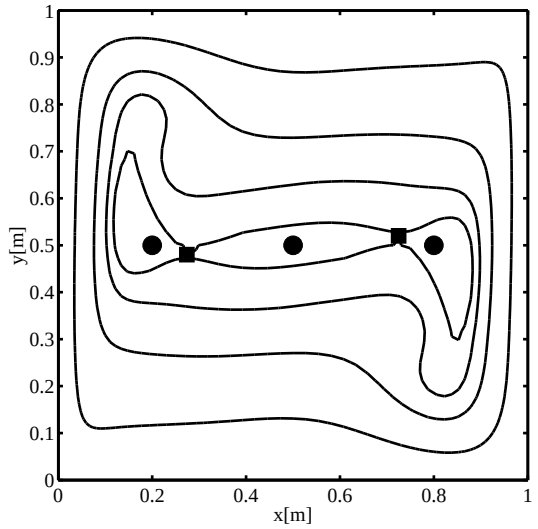

Figure I.3: Streamlines for $Ra = 10^6$. A '•' represents approximate location of centres and a '■' represents approximate location of saddle points. The topology is in agreement with the topology found by Henkes & Hoogendoorn [45].

I.4 Discussion

Calculations for the temperature driven cavity have been carried out. Comparison of the results for averaged Nusselt number, maximum vertical velocity at half the cavity height and the maximum horizontal velocity at half the cavity width showed good agreement with other numerical results. Further, the behaviour of the isotherms was compared with previous results. By visual inspection these were in good agreement with other numerical results. Finally, the topology found in the present calculation was similar to the topology obtained in earlier studies.

It can therefore be concluded that the implementation of the temperature equation leads to correct results for calculations of the flow in the temperature driven cavity.